EFFECT OF INDIUM-TIN OXIDE SURFACE MODIFICATIONS ON HOLE INJECTION AND ORGANIC LIGHT EMITTING DIODE PERFORMANCE

HUANG ZHAOHONG

(*B.Eng. Beijing University of Aeronautics and Astronautics*)

A THESIS SUBMITTED

FOR THE DEGREE OF DOCTOR IN PHILOSOPHY

DEPARTMENT OF MECHANICAL ENGINEERING

NATIONAL UNIVERSITY OF SINGAPORE

2009

ACKNOWLEDGMENTS

I would like to gratefully acknowledge the enthusiastic supervision of Prof. Jerry Fuh, Prof. E. T. Kang, and Prof. Lu Li during this work. In particular, I would like to thank Prof. E. T. Kang for the many insightful suggestions and the tacit knowledge which cannot be obtained through course work.

Special thanks also go to Dr. X. T. Zeng at Singapore Institute of Manufacturing Technology (SIMTech) for many helpful discussions regarding my research. I would also like to thank Ms. Y. C. Liu for a great deal of assistance through innumerable discussions over AFM used in performing my research. I am grateful to all my friends, Fengmin, Guojun, and Sam their cares and attentions.

Finally, I would like to thank my family for their support during these studies. In particular I would like to acknowledge my wife Xiaohui, my son Tengchuan, and my daughter Tengyue for their support and encouragement. I will always be indebted to Xiaohui for her tremendous sacrifices and unwavering commitment to support my work through these difficult times.

Abbreviations

AFM	Atomic force microscopy
Alq_3	Tris(8-hydroxyquinolato) aluminum
BE	Binding energy
CE	Calomel electrode
CuPc	Copper phthalocyanine
CV	Cyclic voltammetry
DC	Direct current
DFT	Density functional theory
DI	De-ionized
DOS	Density of states
EA	Electron affinity
EIL	Electron injection layer
EL	Electroluminescence
EML	Emission layer
ETL	Electron transport layer
ECT	Electrochemical treatment
FL	Fluorescence
HIL	Hole injection layer
HTL	Hole transport layer
HOMO	Highest occupied molecular orbital
IP	Ionization potential
ITO	Indium tin oxide
LB	Langmuir-Blodgett layer
LED	Light emitting diode
LUMO	Lowest unoccupied molecular orbital
L-I-V	Luminance-current-voltage
NPB	N,N'-bis(1-naphthyl)-N,N'-diphenyl-1,1'-biphenyl-4,4'-diamine
NHE	Normal hydrogen electrode
OLED	Organic light emitting diode
OP	Oxygen plasma
OPT	Oxygen plasma treatment
PANI	polyaniline
PE	Power efficiency
PEDOT:PSS	Poly(3,4-ethylenedioxythiophene) poly(styrenesulfonate)
PES	Photoelectron spectroscopy
PL	Phosphorescence
PTCDA	perylene-3,4,9,10-tetracarboxylic-3,4,9,10-dianhydride
RF	Radio-frequency
RMS	Root-mean-square
SAM	Self-assembly monolayer
SCE	Saturated calomel electrode
SEM	Scanning electron microscopy
S-G	Sol-gel

SHE	Standard hydrogen electrode
SPM	Scanning probe microscopy
SSCE	Silver-silver chloride electrode
TCO	Transparent conducting oxide
TE	Thermal evaporation
TEOS	Tetra ethyl orthosilicate
TPD	N, N'-diphenyl-N,N'-bis(3-methylphenyl)-(1,1'-biphenyl)-4,4'-diamine
UHV	Ultra-high vacuum
UPS	Ultraviolet photoelectron spectroscopy
UV	Ultraviolet
WF	Work function
XPS	X-ray photoelectron spectroscopy

List of Figures

List of Tables

Table 5.4. A comparison of key device performance indicators at 200 cd/m^2 between the OLED devices based on the ITO modified by TE, SAM and S-G SiO_2 buffer layers with the optimized thickness. V --- voltage, CE --- current efficiency, and PE --- power efficiency (lm/W).

List of Publications

Journal Papers:

1. Z. H. Huang, X. T. Zeng, X. Y. Sun, E. T. Kang, Jerry Y. H. Fuh, and L. Lu, "Influence of electrochemical treatment of ITO surface on nucleation and growth of OLED hole transport layer," Thin Solid Films, 517 (2009) 4180-4183.

2. Z. H. Huang, X. T. Zeng, X. Y. Sun, E. T. Kang, Jerry Y. H. Fuh, and L. Lu, "Influence of plasma treatment of ITO surface on the growth and properties of hole transport layer and the device performance of OLEDs," Organic Electronics, 9 (2008) 51-62.

3. T. Cahyadi, J. N. Tey, S. G. Mhaisalkar, F. Boey, V. R. Rao, R. Lal, Z. H. Huang, G. J. Qi, Z.-K. Chen, C. M. Ng, "Investigations of enhanced device characteristics in pentacene-based field effect transistors with sol-gel interfacial layer," Applied Physics Letters, 90 (2007) 122112

4. Z. R. Hong, Z. H. Huang, W. M. Su, X. T. Zeng, "Utilization of copper phthalocyanine and bathocuproine as an electron transport layer in photovoltaic cells with copper phthalocyanine/buckminsterfullerene heterojunctions: thickness effects on PV performances," Thin Solid Films, 515 (5) (2007) 3019-3023.

5. Z. H. Huang, X. T. Zeng, E. T. Kang, Jerry Y. H. Fuh and L. Lu, X. Y. Sun, "Electrochemical treatment of ITO surface for performance improvement of organic light-emitting diode," Electrochemical Solid State Letters, 9 (6) (2006) H39-H42.

6. Z. R. Hong, Z. H. Huang, X. T. Zeng, "Investigation into effects of electron transporting materials on organic solar cells with copper phthalocyanine/C60 heterojunction," Chemical Physics Letters, 425 (2006) 62-65.

7. Z. H. Huang, X. T. Zeng, E. –T. Kang, Y. H. Fuh, and L. Lu, "Ultra thin sol-gel titanium oxide hole injection layer in OLEDs," Surface and Coating Technology, 198 (1-3) (2005) 357-361.

Conference Papers and Presentations:

1. Z. H. Huang, X. T. Zeng, X. Y. Sun, E. T. Kang, Jerry Y. H. Fuh, and L. Lu, "Influence of electrochemical treatment of ITO surface on nucleation and growth of OLED hole transport layer," ThinFilms2008, 13-Jul-2008 to 16-Jul-2008, SMU, Singapore.

2. Z. H. Huang, W. M. Su and X. Zeng, "Application of C60 for black cathode in organic light emitting diode," 10th Asian Symposium on Information Displays (ASID'07), 02-Aug-2007 to 03-Aug-2007, Orchard Hotel, Singapore

3. D. Lukito, Z. H. Huang and X. Zeng, "Formation of integrated shadow mask using patternable sol-gel for passive matrix OLED displays," 10th Asian Symposium on Information Displays (ASID'07), 02-Aug-2007 to 03-Aug-2007, Orchard Hotel, Singapore

4. Z. H. Huang, X. T. Zeng, E. –T. Kang, Y. H. Fuh, and L. Lu, "Ultra thin TiO_2 hole injection layer in OLEDs," in: Proceedings of The 2nd International Conference on Technological Advances of Thin Films & Surface Coatings (ThinFilm2004), Singapore, 13-17 July 2004, 34-OTF-A973

Table of Contents

SUMMARY

The aim of this work is to investigate the influence of various surface modifications on, in turn, ITO surface properties, hole injection efficiency, and finally device performance. This research is expected to provide important information on good understanding of hole injection mechanisms in OLED devices.

In this study, extensive work involving surface modifications of ITO was carried out. These included gas plasma treatments, electrochemical treatments, and insulating buffer layer. In order to understand the governing factors of ITO surface properties, ITO samples were treated with different types of plasma (i.e., H_2, Ar, O_2, and CF_4) and characterized by in terms of surface morphology by AFM, surface chemical states by XPS, electron transfer kinetics by CV, and surface energy by contact angle measurements. Electrochemical process was first proposed as a new approach for ITO surface treatment. Similar to the plasma treatments, the electrochemically treated ITO surfaces were also characterized in surface properties. SiO_2 buffer layers produced by thermals evaporation, self-assembled-monolayer, and sol-gel processes were applied on to ITO surfaces as well. The SiO_2 buffered ITO surfaces were characterized by AFM and CV techniques. OLED devices based on the ITO electrodes modified by the different processes were fabricated and characterized in terms of L-I-V behaviour and EL efficiencies. More importantly, nucleation and initial growth of hole transport layer on the treated ITO surfaces were morphologically investigated to understand the influence of surface modification methods on interface property and therefore hole injection. Based on the results of surface

properties and device performance, phenomenal interface models were proposed for discussion of hole injection mechanism and the influence of hole injection on EL efficiency.

The results show that oxidative plasma and electrochemical treatments change ITO surface chemical states by decontamination, oxidation and surface etching. The resulted polar species alter the surface energy, especially its polar component. OLED device performance is correlated to the surface polarities of the ITO electrodes, namely, the higher the surface polarity, the more effective the hole injection. The improved device performance is attributed to the improved ITO/HTL interface properties (i.e., the good contacts between ITO and hole transporting layer) by refining the HTL deposit and reducing voids and defects at the interface. In contrast, all the insulating buffer layers block hole injection by reducing the effective contact areas at the ITO/HTL interface. For the same coating process, thicker buffer layers block more holes. Being of the similar thickness, the denser coating blocks more holes than the porous coating. More importantly, the electrochemical treatment of ITO surface was found to be capable of increasing not only hole injection but also EL efficiency at the same time.

Chapter 1

Introduction

Abstract

In this chapter, a brief overview of the organic light-emitting diodes (OLEDs) with the emphasis on device structure and electrical behavior, especially charge injection and transport is provided first. Background information related to charge injection and transport, including energy band diagram in OLED device and influence of surface properties on energy band diagram, are then introduced. Next, the influence of surface properties of indium tin oxide (ITO) on hole injection and thus on the performance of OLEDs is presented. After that, recent developments on ITO surface modifications are reviewed. Based on the literature review, research topics are proposed, and finally, the aims and outline of this thesis are addressed.

1.1 Organic Light-Emitting Diodes

1.1.1 Historical Background

Electroluminescence (EL) is the emission of light generated from the radiative recombination of electrons and holes electrically injected into a luminescent semiconductor. EL devices are conventionally made of inorganic direct-band gap semiconductors. Recently EL devices based on conjugated organic small molecules and polymers have attracted increasing attention. The operating principles of organic light-emitting diodes (OLEDs) are fundamentally distinct from conventional inorganic semiconductor-based light-emitting diodes (LEDs). The rectification and light-emitting properties of inorganic LEDs are due to the electrical junction between oppositely doped, p and n type regions of the inorganic semiconductor [1]. In contrast, OLEDs are formed using an undoped, insulating organic material, and the rectification and light-emitting properties of the OLED are caused by the use of asymmetric metal contacts.

Organic electroluminescence has been investigated since the 1950s [2], most notably in the works of Pope et al. and Helfrich et al. [3,4], which were observed on single crystals of anthracene, first published in the early 1960s. These initiated considerable efforts to achieve light-emitting devices from molecular crystals. In spite of the principal demonstration of an operating organic electroluminescent display incorporating even an encapsulation scheme similar to the ones used in nowadays commercial display applications [5], there were several draw-backs preventing practical use of these early

devices. For example, neither high enough current densities and light output nor sufficient stability could be achieved. The main obstacles were the high operating voltage as a consequence of the crystal thickness in the micrometer range together with the difficulties in reproducible crystal growth as well as preparing stable and sufficiently well-injecting contacts to them. Nevertheless, these investigations have established the basic processes involved in organic injection-type EL, namely injection, transport, capture and radiative recombination of oppositely charged carriers inside the organic material [6,7]. A further step towards applicable organic electroluminescent devices was made in the 1970s by the usage of thin organic films prepared by vacuum vapor deposition or the Langmuir–Blodgett technique instead of single crystals [8-10]. The reduction of the organic layer thickness well below 1 μm allowed the achieving of electric fields comparable to those which were applied to single crystals but now at considerably lower voltage. Apart from the morphological instability of these polycrystalline films, there arises the problem of fabricating pin-hole-free thin films from these materials. These problems could be overcome in the early 1980s by the usage of morphologically stable amorphous films, as demonstrated by Partridge's work on films of polyvinylcarbazole doped with fluorescent dye molecules [11]. However, the development of organic light-emitting device (or diode) known as today's OLED technology actually began 1980s by Tang and coworkers [12,13].

The development of organic multi-layer structures considerably improved the efficiency of light-emission by achieving a better balance of the number of opposite charge carriers and further lowered the operating voltage by reducing the mismatch of energy levels between the organic materials and the electrodes. Their research was followed by the disclosure of the doped emitter using the highly fluorescent organic dyes for color tuning

and efficiency enhancement. Since the late 1990s, OLEDs have entered the stage of commercialization and are considered as promising candidates for the next generation of large area flat-panel displays [14,15]. In addition, the first light-emitting devices containing luminescent polymer thin films were demonstrated in 1990 [16]. The polymeric materials have also been widely examined and are going to be commercialized with the same good prospects for display and lighting applications as the above-mentioned small molecules [17,18]. Since then, the development of polymeric LEDs and small molecular LEDs proceeded in parallel. The most considerable difference between theses two classes of molecular semiconductors is the degree of order and the subsequent macroscopic migration process. The mobility of photo-generated charges in small molecules is limited by the relatively small π overlap and hence electron hopping from molecule to molecule is dominant, while the intrinsic mobility on a conjugated polymer chain is determined by strong covalent intrachain interactions. Although the understanding of the device physics has proceeded in parallel for the two types of OLEDs, the conclusions presented are generally applicable to both molecular and polymeric LEDs [19].

1.1.2 Device Structure and Working Principle

In general, the basic processes occurring during OLED operation include: 1) charge carrier injection; 2) charge carrier transport; 3) electron-hole interaction (formation of excitons) and 4) radiative recombination [20]. The simplest organic electroluminescent device consists of a thin film of organic electroluminescent material sandwiched between two

metal contacts, at least one of which is transparent. Efficient hole and electron injection requires high work function metal to be the anode and low work function metal to be the cathode. When a voltage or bias is imposed onto the two electrodes, charge carriers (holes from anode and electrons from cathode) are injected into the organic layer and these carries are mobile under the influence of the high (> 10^5 V/cm) electric field. Some of these carriers may recombine within the emissive layer yielding excited electron-hole pairs, termed excitons. These excitons may be produced in either the singlet or triplet states and may radiatively decay to the ground state by fluorescence (FL) or phosphorescence (PL) pathways.

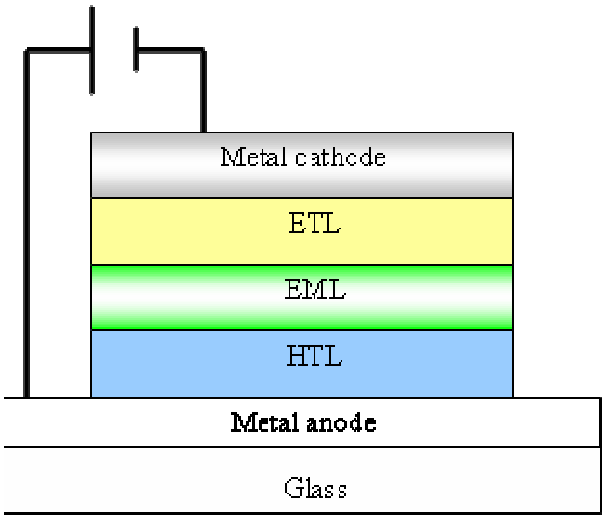

Figure 1.1 The structure of a typical multi-layer OLED device.

In reality, multilayer structure is frequently adopted, e.g., hole transport layer (HTL), emission layer (EML), and electron transport layer (ETL) in sequence from the anode to the cathode, as shown in Figure 1.1. The virtues of the multilayer device are the balanced transport of electrons and holes and the confinement of the emission region away from the

metal electrodes, which results in high efficiency and luminance at low operating voltages. In some cases, the bilayer device has been emphasized due to its simplicity, in which HTL is used for the transport of holes, and ETL is used for both the transport of electrons and emission of light [12].

1.1.3 Dependence of Device Performance on Charge Carrier Injection

Commercial applications of OLEDs require low driving voltage, high efficiency, and extended device lifetime. Since minimizing the driving voltage would increase the power efficiency, establish compatibility with conventional integrated circuitry, and also reduce both thermal heating and potential voltage-driven electrochemical degradation at the organic/metal interfaces, it would be favorable to drive the device at low voltage, preferably at the "turn-on" voltage. In reality, most OLEDs emit light of about 100 cd/m^2 (candela per square meter – luminance SI unit) at an operating voltage of two to four times the turn-on voltage [21]. Although it is not fully understood what causes this internal resistance and the subsequent voltage increase, there are reports indicating that driving voltage is closely related to both bulk properties of organic materials [22] and charge carrier injection [21-24]. In other words, in order to achieve the lowest possible voltage it is necessary to maximize the drift mobility of both types of carriers (hole and electron) and to have ohmic electrode/organic contacts. The former is highly reliant of organic materials, while the latter is controlled by the surface and interface properties.

Furthermore, charge injection across the electrode/organic interface also plays an important role in optimizing the device efficiency of an OLED [25-27]. This is because an unbalanced injection results in an excess of one carrier type that contribute to the current but not the light emission. Meanwhile, the unbalanced charge injection can also result in an enhanced non-radiative recombination due to the interactions of excitons with the excess charge carriers. Consequently, over the past decade, increasing research activities have focused on improving charge injection efficiency at both cathode/organic and anode/organic interfaces [28-33].

1.1.4 Issues at Electrode/Organic Interface

Ideally, the operating voltage of a LED should be close to the photon energy (E_g) divided by the elementary charge (q), i.e. E_g/q, which has been reached for inorganic semiconductor LEDs. This condition is generally not achieved in OLEDs mainly due to non-ideal charge carrier injection limited by the formation of barriers at the interfaces of electrode/organic [34], therefore, questions about the nature of these interfaces arise. Over the past decade, surface science has begun to play a key role in developing a deeper fundamental understanding of electrode/organic interfaces, particularly with respect to the way electronic structure and chemistry relate to charge carrier injection [35-40].

Photoelectron spectroscopy has been extensively employed to determine the electronic structure and chemistry at the metal/organic interfaces. Dipoles, chemical reaction, and atomic diffusion are readily observed in the near interface region. As a consequence, the

determination of the carrier injection barrier is not just a simple matter of calculating the difference between the metal work function and the energy levels of the organic solid owing to the presence of interfacial dipoles and chemical reaction. For almost all the interfaces formed by depositing organic materials on metal surfaces under ultrahigh vacuum conditions, a dipole layer is formed at metal–organic interface, due to various origins such as charge transfer across the interface, redistribution of electron cloud, interfacial chemical reaction, and other types of rearrangement of electronic charge [41]. The interface dipole scenario was originally proposed by Seki and his coworkers [38,42] and has received extensive support from other research groups [23,43]. Experiments by a number of research groups indicate that dipoles are found at all metal–organic interfaces, while the dependence of the interface dipole magnitude on the metal work function varies from organic to organic [42, 44].

Although the dipole theory has been extensively used to describe the organic-on-metal interfaces at high vacuum conditions, it is still questionable for the theory to be used in actual systems formed at low vacuum or environmental conditions such as the fabrication of polymeric LEDs. Furthermore, various surface modifications make the interfacial structure more complex. Therefore, a deep understanding of the interfacial nature and the charge injection mechanism, especially in the case of surface modifications, is necessary and meaningful for further improvement of OLED device.

1.2 Theory of Charge Carrier Injection and Transport

1.2.1 Difference between Organic and Inorganic Diodes

A fundamental understanding of how charge is injected from a metal to a conjugated organic system is essential to the design and operation of organic electronic devices. Although significant advances have been made in the understanding of injection EL on the inorganic p-n junctions, the studies of organic systems have lagged behind due to the complexities of the organic solids. In the case of crystalline inorganic diodes, charge carrier injection and transport processes can be described by the Schottky-Mott energy band model [45,46]. On a microscopic scale, however, charge-carrier transport in molecular solids is different from the conduction mechanisms in "classic" inorganic semiconductors [25].

Unlike crystalline inorganic semiconductor material, most polymeric or low-molecular weight materials used in OLEDs form disordered amorphous films without a macroscopic crystal lattice. Furthermore, since organic semiconductors are absent of extended delocalized states, charge transport is usually not a coherent motion in well-defined bands but rather a stochastic process of hopping between localized states. This results in the typically observed carrier mobility (μ) in the range of 10^{-3} ~ 10^{-7} cm^2/Vs, which is at least 3 orders lower than that of inorganic semiconductors. Consequently, excitations are only localized on either individual molecules or a few monomeric units of a polymer and usually have a large exciton binding energy of some tenths of an eV. Additionally, many

of the materials in OLEDs are wide-gap materials with energy gaps of 2–3 eV, sometimes even more. Therefore the intrinsic concentration of thermally generated free carriers is generally negligible ($<10^{10}$ cm^{-3}) and from this viewpoint the materials can be considered more as insulators than as semiconductors. Although impurities exist in organic semiconductors due to the residuals from the synthesis of the material, structural imperfects, and oxygen or moisture, they usually act as traps rather than as sources of extrinsic mobile charge carriers.

Therefore, direct transfer of the inorganic semiconductor physics to organic solids is generally a very poor approximation and has been shown to be quantitatively incorrect for many interfaces involving organic EL materials [39,47,48]. This suggests that the classical band theory can give only a qualitative understanding of the charge carrier injection and transport processes in OLEDs. Even so, conventionally the Mott-Schottky energy band model is still used as a theoretical basis for investigation on the charge injection and transport in OLEDs, because a specific theory for organic-based LEDs has not been established.

1.2.2 Energy Band Diagram

1.2.2.1 Flat Band Diagram

As stated in the ideal Schottky-Mott model [45], charge carrier injection is believed to be limited by the formation of barriers at the metal/semiconductor interface, which can be

identified on an energy band diagram. To construct such diagram, the energy band diagrams of the metal and the semiconductor without contact are first considered, and then they are aligned using the same vacuum level as shown in Figure 1.2(a). When the metal and the semiconductor are brought together, the Fermi energies of them do not change right away. This yields the flat-band diagram of Figure 1.2(b). In the absence of doping, interface dipoles and other interfacial effects and assuming vacuum level alignment, the barrier height (Φ_B) is defined as the potential difference between the Fermi energy of the metal (E_{FM}) and the band edges where the charge carriers reside (E_C for electrons and E_V for holes). As a result, the metal-semiconductor junction will therefore form a barrier for electrons and holes if E_{FM} as drawn on the flat band diagram is somewhere between E_C and E_V.

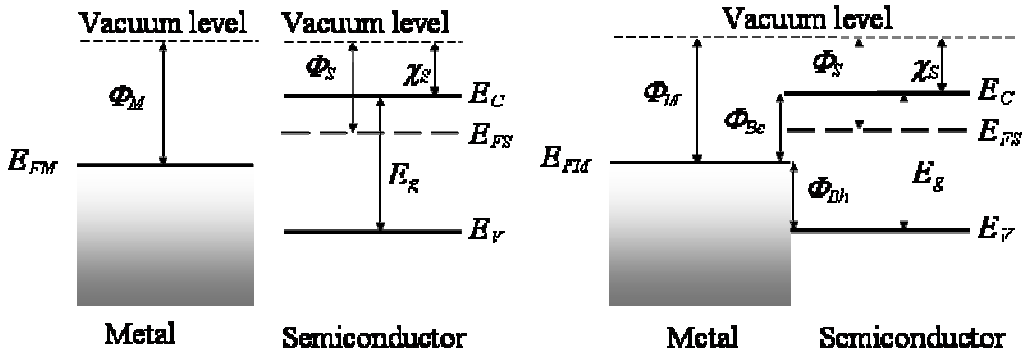

Figure 1.2 Energy band diagram of the metal and the semiconductor before (a) and after (b) contact is made.

According to the flat band diagram, the energy barrier (Φ_B) to charge carrier injection is determined by the work function of the metal (Φ_M) and the electron affinity (χ_S) or ionization potentials (IP) of the semiconductor and can be expressed as

$$\Phi_{Be} = \left| \chi_S - \Phi_M \right| \tag{1.2.1}$$

for electrons, and

$$\Phi_{Bh} = \left| \Phi_{IP} - \Phi_M \right|$$

$$= \left| E_g + \chi_S - \Phi_M \right| \tag{1.2.2}$$

for holes, respectively, where E_g is the band gap energy of the semiconductor. This indicates that if the Schottky-Mott rule is valid, the barriers to electron injection (Φ_{Be}) and hole injection (Φ_{Bh}) should be linear functions of Φ_M.

It should be noted that the values of χ_S and Φ are dominated by the bulk cohesion of the atoms, but are affected by the following surface phenomena:

- reconstruction, where the surface atoms rearrange in the surface plane
- relaxation, where the atoms move slightly away from their bulk positions
- surface states
- impurities at the surface
- dipole layer due to charge leakage out of the surface (i.e., electron spill-off)

1.2.2.2 Band Bending

Since the Fermi energy in the metal differs from that in the semiconductor, the flat band diagram shown in Figure 1.2(b) is not in a thermal equilibrium. When the metal and the semiconductor are put into contact, both the Fermi levels and the vacuum levels need to align up. Having different work functions, this dual alignment is obtained by shifting some electrons from one material to the other to create a dipole with an electrical potential

equal to the difference in Fermi levels, $V_{bi}=\Phi_M - \Phi_S$, which is so-called built-in potential at the junction.

For example, electrons in the *n*-type semiconductor can lower their energy by traversing the junction. As the electrons leave the semiconductor, a positive charge due to the ionized donor atoms, stays behind. This charge creates a negative field and lowers the band edges of the semiconductor. Electrons flow into the metal until equilibrium is reached between the diffusion of electrons from the semiconductor into the metal and the drift of electrons caused by the field created by the ionized impurity atoms. This equilibrium is characterized by a constant Fermi energy throughout the structure. As a result, the energy bands of the n-type semiconductor exhibit upward bending, as shown in Figure 1.3(a). In contrast, the downward band bending occurs for metal p-type semiconductor contact, as shown in Figure 1.3(b).

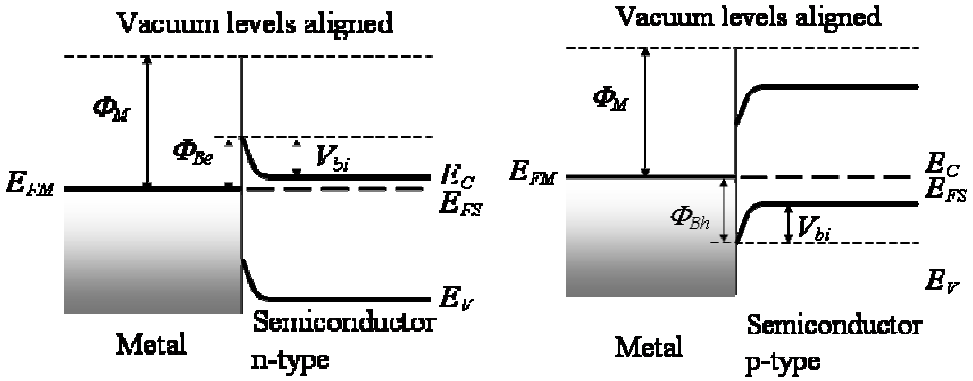

(a) (b)

Figure 1.3 Energy band diagram of (a) metal n-type semiconductor contact and (b) metal p-type semiconductor contact.

Compared with flat band model, band bending model does not change the barriers to charge injection. However, the band bending model is valid only if free charges exist in

the semiconductor. It should be noted that most of organic semiconductors are used with high purity and are intrinsic semiconductors. Therefore, free charge density is very small and can be neglected. In other words, organic semiconductors can be treated as insulators in many cases. This means that band bending rarely occur at organic/metal interface because no charge transfer exists [49].

1.2.2.3 Energy Band Diagram of Single Layer OLED Device

One of fundamental processes occurring in OLEDs is charge injection from the metal contacts into the organic semiconductor thin film. The charge injection can be qualitatively understood by considering the electronic energy structure of the thin organic film. In the limit of no interaction between an electrode and an organic film in physical contact, energy barrier to hole injection is specifically defined as difference between the Fermi level of the anode and the highest occupied molecular orbital (HOMO) band of the organic thin film. Similarly, energy barrier to electron injection is defined as difference between the Fermi level of the cathode and the lowest unoccupied molecular orbital (LUMO) band of the organic film [39, 48].

To realize optimal injection, HOMO and LUMO of organic materials should lie as close as possible to Fermi levels of anode and cathode, respectively. Consequently, this becomes the basis for selection of electrode materials, that is, high work function metals (e.g., Au, and indium tin oxide) serve as anodes and low work function metals (e.g., Al, Mg, Ba or Ca) as cathodes.

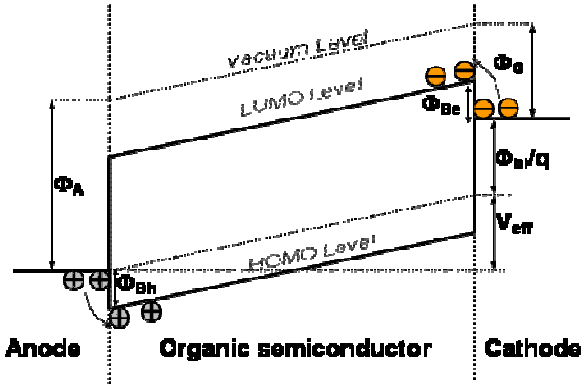

Figure 1.4 Energy band diagram of single layer OLED.

Figure 1.4 schematically shows the energy band diagram of a single layer OLED device, which is generally accepted by most researchers. Although organic semiconductors are disordered materials without a well-defined band structure, for simplicity, the spatial variation of the molecular energy levels is usually drawn in a band-like fashion. In addition, this diagram also does not include polaronic effects, i.e. the fact that due to a structural relaxation the energy levels of charged molecules are different from the neutral state levels. The luminescent organic systems are often treated as intrinsic semiconductors with a rigid band structure [50,51]. This treatment is reasonable because of low carrier mobilities and negligible free carrier densities [50].

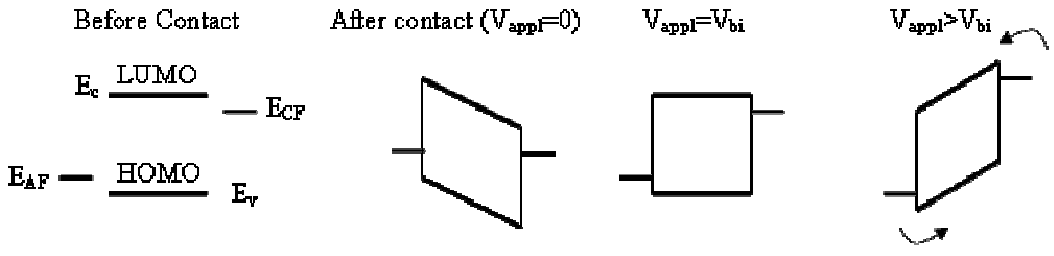

Figure 1.5 Schematic illustration of energy band diagram of a single layer OLED in different conditions, i.e., before contact, after contact, $V_{appl}=V_{bi}$, and $V_{appl}>V_{bi}$.

As shown in Figure 1.5, the two electrodes with different work functions (E_{AF} for Fermi level of anode and E_{CF} for Fermi level of cathode) are necessary in order to obtain double-carrier injection in OLEDs, but lead to the presence of a non-negligible built-in voltage (V_{bi}) across the organic layer. Neglecting energy level shifts due to various interface phenomena, V_{bi} is equal to the contact-potential difference of the two metal electrodes, i.e. $V_{bi} = (E_{AF} - E_{CF})/q$, which is presented by Φ_{bi}/q in Figure 1.4. The physical importance of V_{bi} is that the applied external voltage (V_{appl}) is reduced in terms of effectiveness such that a net drift current in forward bias direction can only be achieved if V_{appl} exceeds V_{bi}, as shown in Figure 1.5. The effective voltage, V_{eff}, can be presented as $V_{appl} - V_{bi}$ across the organic layer under forward bias conditions.

Although the built-in potential can be obtained by photoconductivity measurements [52], the barrier height difference is the parameter to be considered only if no interaction occurs at the interface [53], which is rarely satisfied in reality. Care should be taken when using the work functions of pure metals measured in ultra-high vacuum (UHV), as the preparation conditions of OLEDs are usually not clean enough to exclude the oxidation of low work function metals or the formation of adsorbate layers even on noble metals. In addition, chemical reactions between the organic layer and the metals can lead to the formation of an interfacial layer with different properties than the bulk materials which in turn significantly modifies the energetics at the injecting contact [42,54].

1.2.3 Influence of Interface Dipole on Energy Barrier

The Schottky-Mott model was based on the hypothesis of no interaction taking place at the metal/semiconductor interface. Unfortunately, experimental barrier heights often differ from the ones calculated using *Eq*. (1.2.1) or *Eq*. (1.2.2) due to the non-ideal interface between metal and semiconductor in reality. Numerous photoelectron studies and Kelvin probe measurements have demonstrated that the charge injection barrier is affected by the dipole D_{int} at the conjugated material/metal interface [38,41,44,55-57].

An interface dipole with its negative pole pointing toward the organic layer and its positive pole toward the metal increases the HOMO energy of the organic layer by adding an electrostatic energy and decrease the Fermi energy (i.e. increases the metal work function). As a result, the hole injection barrier Φ_{Bh} is reduced. Accordingly, reversing the direction of the interface dipole reduces the electron injection barrier Φ_{Be}. Thus, increased work function of anode and decreased work function of cathode are associated with improvement of hole and electron injections, respectively [58].

The origins of the interface dipole are still in dispute. One of the explanations is that when the organic molecules are adsorbed on the metal surface, the surface electrons are compressed back into the sample surface [58,59]. The metal work function is considered to be composed of two parts: bulk electronic structure and surface dipole contributions. A neutral metal surface in a vacuum presents a surface dipole because a deficit of electronic density exist inside the metal close to the surface, while an excess of electronic density is

obtained outside the surface. As a consequence, the electrostatic potential jumps from its bulk value (inner potential) to a higher value outside the metal (outer potential). The difference between the inner and outer electrostatic potentials defines the metal surface dipole potential energy, which can reach several eVs [58,60].

With a compression of the surface electrons in presence of the adsorbed (chemisorbed or physisorbed) organic molecules, the metal work function will decrease. The interface dipole barrier increases the energy difference between Fermi level of the metal and the HOMO of the organic molecules, leading to higher hole injection barrier. In addition, when the molecules are actually chemisorbed on the metal surface, their electron density interacts with that of the metal such that new chemical bonds can be formed. Bond formation is accompanied by an electron density flow through the atoms involved in a newly formed bond, whose direction depends on the relative electronegativity. This partial charge transfer between metal and adsorbate constitutes the second contribution to the interface dipole [58]. Another explanation about the formation of interface dipole is free charge transfer, rather than the partial charge transfer in formation of chemical bonding [61,62].

However, the charge transfer explanation is not supported by other experimental results [49,63], since most organic semiconductors are of large band gap and lack of enough free charge, charge transfer cross the metal/organic semiconductor junction is not expected, as mentioned previously.

1.2.4 Vacuum Level Shift

It is commonly accepted that the vacuum level shift (Δ) is attributed to an interfacial dipole between metal and semiconductor [41]. Other origins of the vacuum level shift were also proposed, including image force and the tailing of electron clouds of metal into vacuum [63,64].

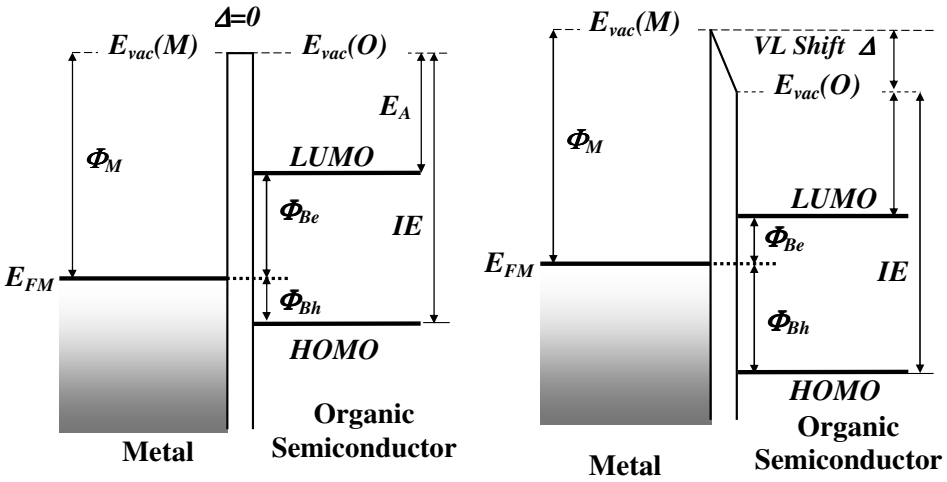

Figure 1.6 Schematic of an organic-metal interface energy diagram without (a) and with (b) vacuum level shift.

Due to the vacuum shift, energy band diagram of metal/organic semiconductor will be different from that of metal/inorganic semiconductor. The Fermi level alignment between metal and organic semiconductor relies on the vacuum shift instead of the band bending because no charge transfer occurs, as shown in Figure 1.6. Such Fermi level alignments have been observed at some metal/organic interfaces such as C60/metal [65], PTCDA/metal [44], and TPD/metals (Cu, Mg, Ag) [49].

1.3 Indium Tin Oxide as an Anode

The primary requirements for an anode in OLEDs are that its work function should be high enough to enable good injection of holes and that it must be sufficiently transparent to permit the exit of light from the organic light-emitting layer. Up to now, the most prevalent materials used for the anode is indium-tin-oxide (ITO), which has low resistivity (~$2X10^{-4}$ Ω cm) [91], high optical transmittance over the visible wavelength region (> 90% at 550 nm) [92], excellent adhesion to the substrates, stable chemical property, relatively high work function (4.5-5.0 eV) [93,94], and easy processibility (for patterning) [12].

The properties of ITO films are strongly dependent on the preparation method. The techniques employed to produce ITO films include RF (radio-frequency) magnetron sputtering, direct-current (DC) magnetron sputtering, reactive evaporation, reactive sputtering, electron beam evaporation, as well as spray pyrolysis. Among them, DC magnetron sputtering is the most used process for mass production of ITO films, since the process can provide homogeneous ITO films with low resistivity and good reproducibility [95].

1.3.1 Conduction Mechanism

Electrical conductivity (σ) depends on concentration (N) and mobility (μ) of the relevant free carrier as follows:

$\sigma = N \mu e$,

where e is the electron charge. In order to obtain films with high conductivity, high carrier concentration and mobility should be simultaneously realized.

The electrical properties of the oxides depend critically upon the oxidation state of the metal component (stoichiometry of oxide) and on the nature and quantity of impurities incorporated in the films, either intentionally or inadvertently. Perfectly stoichiometric oxides are either insulator or ionic conductor. The later is of no interest as a transparent conductor due to the high activation energy required for ionic conductivity.

In_2O_3 has the cubic bixbyte structure in which O^{2-} ions occupy, in an ordered manner, three-fourths of the tetrahedral interstices of a face-centered-cubic In^{3+} - ion array [96]. The indium oxide has a filled O^{2-}:2*p* valence band that is primarily oxygen 2*p* in character [97]. The In:3*d* core lies below the valence-band edge E_v. The conduction band is the metal-5*s* band with an edge E_c about 3.5 eV above E_v [98]. The next higher band is the metal-5*p* band. As prepared, indium oxide generally lacks stoichiometry due to oxygen-array vacancies V_O. At high V_O concentration, a V_O impurity band forms and overlaps E_c at the bottom of the conduction band producing a degenerate semiconductor. The oxygen vacancies act as doubly ionized donors and contribute at a maximum two electrons to the electrical conductivity as shown in the following equation:

$$O_O^X \rightarrow V_O + 2e^- + \frac{1}{2} O_2(g)$$

The material composition can be represented as In_2O_{3-x}. In addition to providing conduction electrons, the oxygen vacancies also allow for O^{2-} ion mobility. Therefore,

In_2O_{3-x} should be a mixed conductor, having both electronic and O^{2-} ion conduction [97], although the latter is negligible when compared to the electronic conduction.

ITO is essentially formed by substitutional doping of In_2O_3 with Sn (Tin) which replaces the In^{3+} atoms from the cubic bixbyte structure of the parent oxide. Sn thus forms an interstitial bond with oxygen and exists either as SnO or SnO_2, accordingly having a valency of +2 or +4, respectively. This valency state has a direct bearing on the ultimate conductivity of ITO. The lower valence state of SnO results in a net reduction in carrier concentration since a hole is created, which acts as a trap and reduces conductivity. On the other hand, predominance of the SnO_2 state means Sn^{4+} acts as an n-type donor releasing electrons to the conduction band. However, the good conductivity of ITO is attributed to both Sn dopants and oxygen vacancies [97,99,100]. The non-stoichiometric oxide semiconductor contains several percent of the oxygen sites in vacant, leading to degenerate n-type doping [100].

Each vacancy is an electron donor, providing two electrons (difference in charge between an oxygen anion and the vacancy). Oxygen vacancies and dopant Sn atoms form donor levels, which account for the carrier density in the conduction band. Since ITO inherently contains a large number of defects, the Sn atoms, as well as the randomly located vacancies, the conductivity also depends on details of sample preparation and thermal history as well as on the degree of crystallization.

Achievement of the lowest possible resistivity of ITO is of practical significance in the respect that it provides some flexibility in selecting the film thickness in order to achieve

high optical transmission while still retaining low sheet resistance. However, transparency in the visible region is strongly affected by the electrical properties of the film [101], because the mechanisms of electrical conduction and optical transmission are very much interdependent. As a result, the electrical properties are usually achieved at the expense of transmission. The direct optical bandgap of ITO films is generally in a range of values from 3.5 to 4.06 eV [97,102]. The high optical transmittance of these films is a direct consequence of them being a wide bandgap semiconductor. The fundamental absorption edge generally lies in the ultraviolet of the solar spectrum and shifts to shorter wavelengths with increasing carrier concentration, N. This is because the bandgap exhibits an $N^{2/3}$ dependence due to the Moss-Burstein shift [103].

1.3.2 Morphology and Crystallographic Orientation

As-deposited ITO film by DC magnetron sputtering features with a so called "grain-subgrain" surface morphology and polycrystalline structure, as shown in Figure 1.7(a) (height mode) or Figure 1.7(b) (phase mode). Each "grain" (200-600 nm in size) consists of a cluster of 10-40 nm sized subgrains, which are highly aligned in crystalline orientation. More discussions on their crystalline features are reported in literature [95,99].

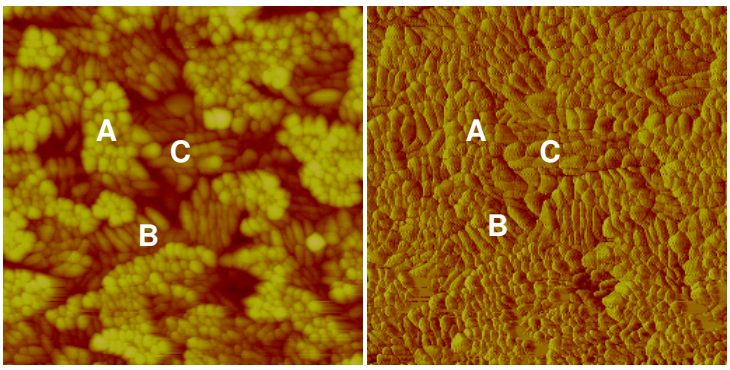

(a) (b)

Figure 1.7 AFM image of as-clean ITO thin film deposited by DC magnetron sputtering: (a) height mode and (b) phase mode, showing three different types of grains marked by A, B, and C, oriented respectively with their <400>, <222> and <440> axes normal to the substrate surface. The scan area is $1 \times 1\ \mu m^2$.

These grains are generally classified into three groups: (A) square subgrains, (B) triangular subgrains, and (C) rectangular subgrains with film thickness in the order of A>B>C. According to Kamei et al. [95], A, B, and C were confirmed to be oriented respectively with their <400>, <222> and <440> axes, normal to the substrate surface. However, only (400) planes are always exposed at the surface for the above mentioned three axes due to higher durability of (400) planes against re-sputtering during film growth, resulting in the difference in the height of grains with different orientations [95,99]. The difference in height seems to be a factor in describing surface roughness of ITO films. The domains with different morphology have different heights, and thus many protrusions and steps are expected to be formed on the surface. The root-mean-square (RMS) roughness value is in the range of 2-4 nm [104].

1.3.3 Chemical and Electrochemical Stabilities of ITO Film

ITO is usually considered to be redox inert as a substrate. In general, ITO is insoluble in alkaline solutions but is vulnerable to chemical attack in aqueous acid. This behavior has been utilized, for example, in the pattern-wise etching of ITO, which is indispensable for the fabrication of all kinds of display devices. The etching kinetics for thin film ITO in aqueous acidic solution has been well investigated [105,106]. Like the situation of chemical etching, ITO is somewhat unstable electrochemically [107]. Cathodic reduction of oxides into metals on ITO surface has been reported in electrolytes with various pH values [108-110].

In a general way, oxides are expected to be stable against oxidative processes when the metal cation is at its highest oxidation state. However, there are examples in literature of anodic corrosion not brought on by a reduction mechanism but occurred through the breaking of the surface bonds without change in the metal valence state [111a,111b,112]. The anodic corrosion occurs only at potentials in the range of 0.9-1.3 V vs. saturated calomel electrode (SCE), where chlorine is oxidized rather than oxygen is released [111a,111b]. Therefore, the stability of ITO against electrochemical process is related to not only the imparted potential, but also the type of electrolyte. It is known that when proper aqueous electrolyte and potential are selected, oxygen evolution will take place by electrolysis of water without anodic corrosion. The highly active oxygen atom will then oxidize any unsaturated states of the metal atoms on the ITO surface.

1.3.4 Faults of ITO as Hole Injection Electrode

The physi-chemical and morphological properties of the ITO substrate, for example work function, roughness, surface energy and polarity are of crucial importance in improving the OLED device performance [27,113-115]. Work function has particularly been identified as the most important surface property, as the HOMO of most organic materials lies more than 5 eV below vacuum, even at around 6 eV for some organics. The significant energy barrier to hole injection due to the insufficient high work function of bare ITO results in hole-limited devices characterized with high driving voltage [35,41,116,117]. Moreover, abnormal device behaviors such as shorting, and unstable current-voltage characteristics have been observed in OLEDs with bare ITO surfaces [118]. In order to mitigate these problems, modifications of ITO surface have been proposed, as reviewed in next section.

1.4 ITO Surface Modifications

1.4.1 Surface Treatments

Previous theoretical and experimental work shows that hole injection into organic layer is mainly influenced by the properties of ITO anode, especially work function. As it is known, work function is a surface property and it is possible to alter its value by proper surface modification processes. Many ITO surface treatment processes have been reported, including ultraviolet (UV) ozone exposures [13,119-122], gas plasma treatments [113,123,124], Aquaregia (70wt%HNO_3:30wt%HCl:DI = 1:3:20) [93] acid and base adsorption [37,57,125,126]. Experiences showed that reducing treatments, such as hydrogen plasma, increases the required drive voltage whereas oxidative treatments, such as UV-ozone and oxygen plasma, decrease it [113]. This is consistent with the generally observed result that oxygen adsorption increases metallic work functions [127]. Although a long-term stability of ITO treated by oxygen plasma was reported [93], a common problem of the above ITO surface treatments is instability. It was found that the modified surface work function degrades slowly back to its initial value in a few hours or minutes [120,128].

Some theories and physical models were proposed to explain the increase in ITO work function by the surface treatments, such as removal of the surface carbon contamination[93,94,113,129], metal depletion on treated ITO surface [113,130], surface defects [131], and formation of dipoles [115,131,132].

1.4.2 Insertion of Hole Injection Buffer Layer

One of the methods to control the hole injection is the insertion of a buffer layer between ITO anode and HTL film. Nanometer thick high work function metallic films, such as Pt [23], Au [133] and Ni [114], have been capped on the ITO anode as hole injection layer (HIL), which results in lowering of the operation voltage and increasing of hole injection current, but with no observable improvement in power efficiency [23,114]. Clearly, this implies reduced quantum efficiencies. Furthermore, such metals are only semitransparent, hence there are diminishing gains in efficiencies resulting from the high work functions.

On the contrary, the integration of an organic buffer layer between anode and HIL has resulted in enhanced luminous efficiency and device duration. Organic semiconductors, such as copper phthalocyanine (CuPc) [119], starburst amine [134], and polyaniline (PANI) [116] are the widely used buffer materials with suitable HOMO energy levels. However, disadvantages of the organic buffer layers are significant, such as incompatibility to fabrication processes and substantial increase of drive voltage. Inorganic semiconductors, such as CuO_x [135,136], NiO [132,137], WO_3 [138], VO_x and MoO_x [139], have been successfully utilized as HIL. The turn-on voltage is reduced to 3-4 V, and the brightness is also greatly improved. Unfortunately, the optical transmittance of the inorganic semiconductor films is not very high, rendering the difficulty to realize the most optimal performance.

Insertion of an insulating buffer layer between the ITO and an organic medium has been widely reported to improve OLED device performance. Modification of ITO surface by Langmuir-Blodgett (LB) layers and self-assembled monolayers (SAMs) were reported for manipulating the energy level offset at ITO-HTL interface [57,134,140-143]. With polar adsorbate molecules oriented outward from ITO surface, an artificial dipolar layer is formed and ITO work function is increased [133,144]. With molecules carrying a high dipole moment oriented perpendicular to the metal surface, it has been observed that the total interface dipole can be rather easily tuned by changing the magnitude of the molecular dipole moment chemically [40,145,146]. The dipolar SAMs provide a method of tuning the work function of ITO electrode to the HOMO of the HTL, thus improving device performance. However, the dipolar property of the monolayer on ITO surface may change with the deposition of HTL, leading to a recovery of the modified ITO work function [147].

A more interesting finding is the modification of ITO surface with ultra thin SAMs that have less dipolar effect, such as n-butylsiloxane [148] and octachlorotrisiloxane [149]. This ultra thin buffer layer enhances hole injection and charge recombination efficiency, while blocking electron transport to the anode. Unlike the atomically flat crystal surfaces used in most investigations with SAMs, ITO has a rugged surface, which is expected to limit adsorbate mobility and disrupt the circulation of solution over the surface, which are necessary for achieving long-range order. In addition, most SAMs could not be used in polymeric OLEDs as the monolayer on ITO is subjected to the strong solution process. Therefore, another approach was proposed to improve hole injection efficiency by the insertion of an insulating hole injection buffer layer between the ITO and an organic

medium, such as Al_2O_3 [150], SiO_2 [151], Pr_2O_3 [152], Si_3N_4 [153], Teflon [154,155] and even LiF [156].

1.5 Disputes over Hole Injection Mechanisms

1.5.1 Energy Barrier Theory

Although physical and chemical properties of ITO surfaces treated by various processes have been investigated in order to understand the effect of the surface treatments on hole injection, majority of the research work had been concentrated on work function. A general understanding of the hole injection mechanism is that the increased work function by the surface treatments reduces the energy barrier for hole injection, and therefore the driving voltage [93,122,131,148,157,158], as shown in Figure 1.8.

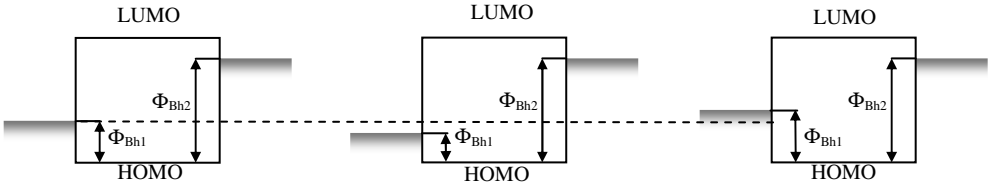

Figure 1.8 Energy diagrams showing the influence of change in work function on energy barrier. Compared with a sample without surface treatment (a), hole injection barrier will be either decreased (b) or increased (c), depending on the shift of Fermi level of the anode.

Unfortunately, the change in work function could not perfectly explain the improvements in EL efficiency and device stability [93,159]. Some experimental results showed that oxygen-plasma treatment of the ITO anodes gives the highest operational stability and

efficiency of polymer LEDs, even when an aqueous based PEDOT:PSS [=poly(3,4-ethylenedioxythiophene) poly(styrenesulfonate)] is used as the hole injection layer [115]. This result also challenges the work function hypothesis because the formation of hydroxyl groups on treated ITO surface in this case has a negative effect on ITO work function.

Moreover, the work function elucidation has been intensively questioned partially due to the invalidity of Schottky-Mott model for organic semiconductors, which is mainly caused by vacuum shift at the ITO/organic interface [41,44] and no charge transfer cross the junction [49,63]. The work function hypothesis is further challenged by the findings that showed markedly different performance on the devices with ITO films being of similar work functions [160], and less influence of energy barrier on hole injection efficiency [161]. Tadayyon et al. recently concluded that the increased ITO work function by dipoles did not influence the energy barrier because the dipoles also shift the vacuum level [162].

1.5.2 Image Force Model

The effect of insulator-buffered ITO surface on hole injection has been attributed to the reduced charge back scattering and improved charge balance. It is generally accepted that an image force model is applicable to charge injection from electrodes into organic solids. Hence, injected charges induce counter charges on the electrode surface which in turn exerts a force on charges being injected away from the electrode. This so-called image force effect has both negative and positive characteristics with respect to charge injection.

At close proximities to the electrode (≤ 1 nm), the charge back-scattering region, charges experience Coulombic forces attracting them back to the electrode, thereby retarding injection. If the charge escapes this region, they experience a lower barrier and injection is facilitated [163]. However, this model has not been quoted as widely as tunneling theory.

1.5.3 Tunneling Theory

Tunneling theory was used to explain the enhancements in hole injection efficiency of the devices with the insulating buffer layer. On the other hand, the improvement in luminance efficiency was attributed to balanced carrier injection due to the blocking effect of the insulating buffer layer on injected holes. The conflict explanations are clearly unable to improve the device performance in both hole injection and EL efficiency.

It is obvious that both image force and tunneling theories requires an assumption that the insulating buffer layer is a continuous ultra thin film sandwiched between the electrode and the organic. In reality, neither dry vapor deposition nor wet SAM process can produce full coverage of ITO by an ultra thin film with nominal thickness less than 1 nm, due to the poor uniformity of ITO surface in chemical composition and morphology. Instead, previous experimental work demonstrates that once ITO surface was fully covered by an insulating layer, the operating voltage of OLED based on the modified ITO surface was significantly increased [149]. Based on the partially covered ITO surface, it is puzzling that charge injection prefers the more insulating area instead of the more conductive uncovered ITO. Therefore, the previously proposed explanations to the effects of

insulating buffer layer on OLED performance are suspected to be invalid. Further investigations are needed to have good understanding of the mechanism.

1.6 Scope of This Thesis

1.6.1 Possible Topics of Investigation

As a transparent electrical conductor, ITO shows exceptional properties that have been exploited in both displays and solar cells. In particular, it has been widely used as an anode in OLEDs for hole injection. As mentioned above, the ITO/organic interface properties significantly influence the performance of OLED devices. The interface properties are verified to have been changed with ITO surface modifications.

The mechanisms behind the improved device performance by ITO surface modifications are still disputed. Changes in work function and therefore the energy barrier for carrier injection have been the major concern in most reports. However, the work function elucidation is impuissant in some device physics, such as enhanced efficiency and extended lifetime. There are virtually no systematic experimental investigations of these and many other effects, and many areas remain as current or future research topics for organic-based electronic devices.

Despite many ITO surface modification methods such as acidic etching, gas plasma, UV ozone, and ultra thin buffer coatings being proposed and characterized, electrochemical treatment of ITO surface has not been reported.

More importantly, few studies have been done to morphologically characterize the hole transport layer on modified ITO surfaces, thus the influence of thin film morphology on device performance is poorly characterized. Being more specific, there are almost no studies that describe the nucleation and growth of hole transport layer on the modified ITO surfaces and the importance of the interface evolution in understanding the microscopic mechanisms of ITO surface modifications.

1.6.2 Aims and Objectives

The aim of this work is to investigate the influence of various surface modifications on, in turn, ITO surface properties, hole injection efficiency, and finally device performance. This research is expected to provide important information on good understanding of hole injection mechanisms in OLED devices.

With this goal in mind, extensive work involving surface modifications of ITO was carried out. These included gas plasma treatments, electrochemical treatment, and insulating buffer layers. In order to understand the governing factors of ITO surface properties, ITO samples were treated with different types of plasma (i.e., neutral, reductive and oxidative) and characterized by in terms of surface morphology, chemical states, electron transfer kinetics, and surface energy. Electrochemical process was proposed as a new approach for ITO surface treatment. Similar to the plasma treatments, the electrochemically treated ITO surfaces were also characterized in surface properties. Insulating buffer layers produced by wet and dry processes were applied on to ITO

surfaces as well, which are expected to influence hole injection in a different way from plasma and electrochemical treatments. More importantly, nucleation and initial growth of hole transport layer on the treated ITO surfaces were morphologically investigated to understand influence of the surface modification methods on interface property and therefore hole injection. Based on the results of surface properties and device performance, a physical interface model was proposed for discussion of hole injection mechanism.

1.6.3 Layout of Thesis

Chapter 2 will briefly describe the major surface characterization techniques used in this study, including atomic force microscopy for morphological study of interface evolution, X-ray photospectroscopy for analysis of chemical states, cyclic voltammetry for characterization of surface electron transfer kinetics, and contact angle measurements for estimation of surface energy. In addition, general procedures for sample preparation, device fabrication and characterizations are also described in this chapter.

Chapter 3 contains studies of various plasma treatments of ITO electrodes and their effects on the surface properties of ITO and device performance.

Chapter 4 proposes the electrochemical methods for modifying the ITO surface. The electrochemically treated ITO electrodes were characterized by various analytical techniques.

Chapter 5 presents the effects of insulating buffer layers on hole injection.

Chapter 6 involves morphological investigation into the effects of surface modification on nucleation and growth of hole transport layer on the treated ITO surface.

Chapter 7 discusses the mechanism of hole injection and its effect on EL efficiency by proposing phenomenal models.

Chapter 8 summarizes the important findings and conclusions and proposes a few research topics worth of following up.

Chapter 2

Experimental and Characterization Techniques

Abstract

In this chapter, an overview of the instrumentation and characterization techniques that are specifically used for studying ITO surface properties, including atomic force microscopy, photoemission spectroscopy, electrochemical analysis, and estimation of surface energy by contact angle measurements, is provided.

2.1 Atomic Force Microscopy

2.1.1 Introduction

Atomic force microscopy (AFM), as a member of scanning probe microscopy (SPM) family, was invented by G. Binnig et al. in 1986 [164]. By measuring the distance dependent forces between the surface and a molecular-sized tip as a sensor, one probes the topography of both conducting and isolating samples on a fine scale, down to the level of molecules and groups of atoms. AFM can produce images of materials as small as 1 nm and provide a true three-dimensional surface profile. Most AFM modes can work perfectly well in ambient air and samples viewed by AFM do not require any special treatments (such as metal coatings).

In this section, AFM is briefly introduced in terms of system set up and operation modes. Details on the AFM technique can be found in literature [165-172].

2.1.2 AFM System

An AFM system, as schematically shown in Figure 2.1, consists of a surface having structural and physicochemical characteristics, an interaction processing characteristic strength and range, and a probe (also called cantilever) which can be located and controlled in the spatial and temporal domains, with its own characteristics [168]. The flexible cantilever made of silicon or silicon nitride has a sharp tip on its free end. The

curvature radius of the sharp tip is on the order of nanometers, normally in the range of 3-50 nm. The operation of an AFM is based on the measurement of the force between the sample surface and the sharp probe. When the tip is brought into close proximity of a sample surface, the short-range attractive or repulsive force ($<10^{-9}$ N) between the tip and the sample, such as *van der Waals* force, leads to a vertical deflection of the cantilever from its equilibrium position according to *Hooke's* law. A laser beam focused on the top of the cantilever is reflected from the cantilever to a four segment photo-detector that is position-sensitive, and the deflection (in the sub-angstrom range) is measured by changes in differential voltage signal. The feedback circuit regulates the z-control in order to achieve a constant deflection signal from the photo-detector while the sample is raster scanned.

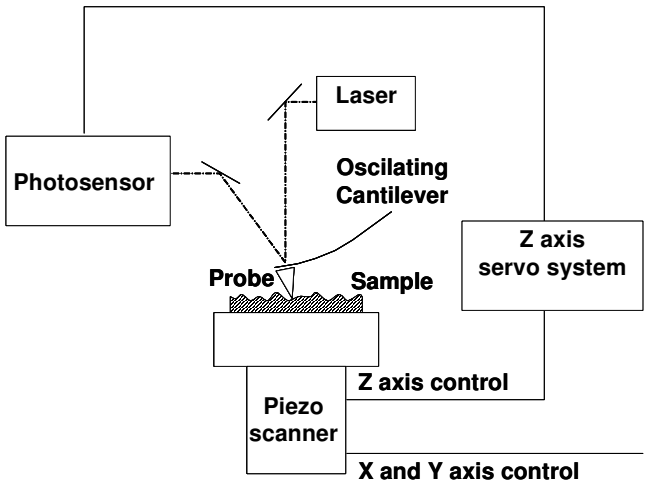

Figure 2.1 Basic principle of the AFM technique after Myhra [168].

Generally, the sample is mounted on a piezoelectric tube that can move the sample in the z direction for maintaining a constant force, and the x and y directions for scanning the sample. By scanning the tip parallel to the surface, either the local variation of the tip-

surface repulsive force or the z-scanner position required for maintaining a constant force is converted into an atomic-scale height or deflection (force) image. A scan may cover a distance of over 100 micrometers in the x and y directions and 4 micrometers in the z direction, which is an enormous range.

2.1.3 Operation Modes

Depending on the distance between the tip and surface (i.e. on the interaction strength between the two), AFM can be divided in three main operation modes: (1) contact mode, (2) noncontact mode, and (3) tapping mode, which is a transition mode between the contact and noncontact modes, as shown in Figure 2.2.

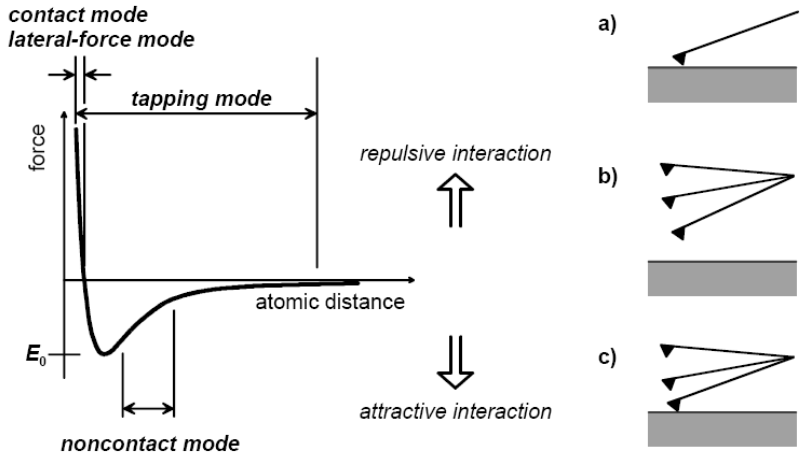

Figure 2.2 Schematic illustration of the region for contact (a), non-contact (b) and tapping mode (c) AFM, after Magonov [169] and Howland [170].

Contact mode means that the tip comes through the fluid layer on the sample surface, and thus, directly contacts the surface. Under ambient air conditions, most surfaces are covered by a layer of adsorbed gases (condensed water vapor and other contaminants)

which is typically several nanometers thick. When touching this layer, the tip meets two additional forces pulling it down into the layer, thus increasing the overall force on the sample: A higher surface tension results from capillary actions that cause a meniscus to form, and trapped electrostatic charges both on the tip and sample contribute to additional adhesive forces, that lead to hysteresis in the force-vs-distance curve. Consequently, the scanning tip can exert strong vertical and lateral shear forces on the sample. The later may cause inelastic or elastic surface deformations or the removal of weakly bounded and defective layers, thus probing mechanical properties (e.g. indentation, adhesion or friction) of sample. During imaging in contact mode, changes in cantilever deflection are monitored. Maintaining a constant deflection, i.e. a constant repulsive force between tip and sample, the height profile displays the vertical movement of the z-scanner at each (x, y) data point.

In noncontact mode, the surface is tracked with a tip oscillating above the fluid layer with amplitude of a few nanometers. In this way, neither tip nor sample can be contaminated during scanning, and no force is exerted to the surface. The height profile results of the spatial variation of the attractive long-range van der Waals forces as measured by a decrease of the resonance frequency of the cantilever. Usually, noncontact mode only works with low scan rates (1-2 Hz) on very flat, extremely hydrophobic surfaces, where the adsorbed fluid layer is at a minimum.

Theoretically, any type of sample can be scanned by AFM. However, scanning soft samples (like oligomers, polymers, biological samples) in contact mode may cause damage of the sample. On the other hand, because most samples develop a liquid

meniscus layer, keeping the probe tip close enough to the sample for these inter-atomic forces to become detectable while preventing the tip from sticking to the surface presents a major hurdle for noncontact mode in ambient conditions. To bypass these problems, a new probe scanning technique with dynamic contact or semi-contact was developed, in which the cantilever is oscillated such that it comes in contact with the sample with schemes for noncontact. The cantilever oscillates vertically at its resonance frequency or close to it (typically values are found in the range of 50 kHz to 500 kHz) with an amplitude ranging from 20 nm to 100 nm. Mechanical oscillations of the cantilever are excited by the piezo-driver that has a direct contact with the cantilever substrate. The particular feature of this mode is that the oscillating tip slightly knocks the sample surface during the scanning only in the lowest point of its amplitude. In the same time, during the most of its oscillation period the cantilever does not touch the surface and their interaction level is relatively low.

Dynamic contact operations include frequency modulation and the more common amplitude modulation. In frequency modulation, changes in the oscillation frequency provide information about a sample's characteristics. In amplitude modulation, better known as tapping mode, changes in the oscillation amplitude yield topographic information about the sample. Additionally, changes in the phase of oscillation under the tapping mode can be used to discriminate between different types of materials on the surface. In tapping mode, soft surfaces are less modified than during imaging in contact mode.

2.2 X-ray Photoelectron Spectroscopy

2.2.1 Theoretical Background

Photoelectron spectroscopy (PES) is widely used to examine the composition and chemical state distribution of species at solid surfaces. The basis of this technique is the so called photoelectric effect discovered already in 1887 by Hertz and theoretically explained in 1905 by Einstein. This effect simply consists in the emission of electrons from a surface upon irradiation with electromagnetic radiation with a known energy E (usually presented in electron volt, eV) given by the Einstein relation:

$$E = h\nu, \qquad (2.2.1)$$

where h is Planck constant (6.62×10^{-34} J s), and ν is frequency (Hz) of the radiation.

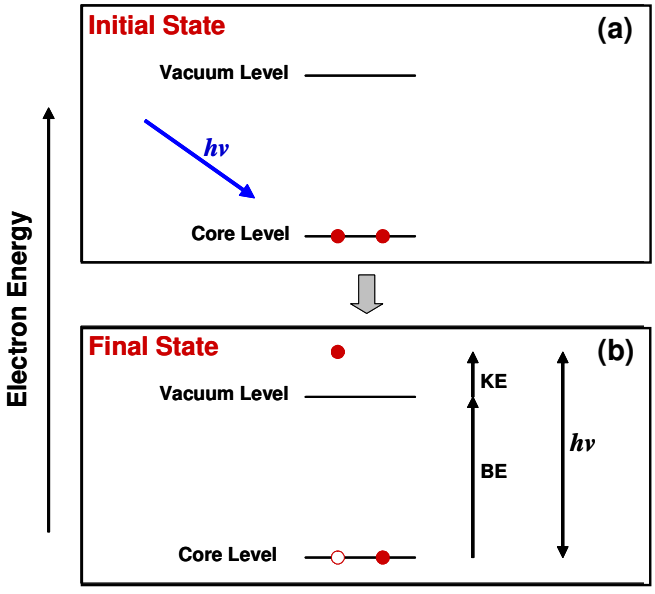

Figure 2.3 Working principle of photoemission spectroscopy (after Hoflund [173])

PES is carried out by illuminating a sample with electromagnetic radiation and analyzing the kinetic energy distribution of the photoelectrons. In this process, the excitation radiation is chosen to be monochromatic. An incident photon of known energy (*hv)* is used to impart energy on an electron, as shown in Figure 2.3(a). The electron uses this energy to overcome the binding energy (*BE*) holding it to the atom and the electron's remaining energy is in the form of kinetic energy (*KE*), as shown in Figure 2.3(b). *KEs* of the emitted electrons forming the spectral peaks are measured using an electrostatic charged-particle energy analyzer, from which *BEs* of these electrons can be calculated from the following equation [173]:

$$KE = hv - BE + \phi_s \qquad (2.2.2)$$

where ϕ_s is the work function of the spectrometer rather than the specimen.

The *KE* of the photoelectrons usually varies from a few electron volts up to a few hundred electron volts, depending on the photon energy used. The *BE* of the photoelectrons depends strongly on the excited atoms and therefore gives elemental information. In order to excite the electrons from their bound states in the sample, different sources of electromagnetic radiation, operating at various energies, can be used. Generally two regimes are identified: XPS for energies $hv > 100$ eV and ultraviolet photoelectron spectroscopy (UPS) for energies $hv < 100$ eV. Electromagnetic radiation can penetrate deep into the sample but only electrons emitted in a region very close to the surface can leave it and reach detector. Although conceptually similar, XPS and UPS measurements offer different kinds of information about the sample. In XPS, the photons are absorbed by atoms in solid, leading to ionization and emission of core (inner shell) electrons. By

contrast, in UPS the photons interact with valence levels of the solid, leading to ionization and emission of these valence electrons.

2.2.2 Instrumentation and Resolution of XPS

The schematic illustration of an XPS instrument is given in Figure 2.4(a). In a typical XPS experiment, an X-ray beam strikes the sample surface, giving photoelectron radiation. These electrons pass the electron optics and enter the hemispherical analyzer. At the other end of the analyzer electrons are detected, counted, and a spectrum of photoelectron intensity versus binding energy is displayed. An ion gun (not shown here) is frequently attached for ion bombardment of the sample surface to obtain composition profile in depth.

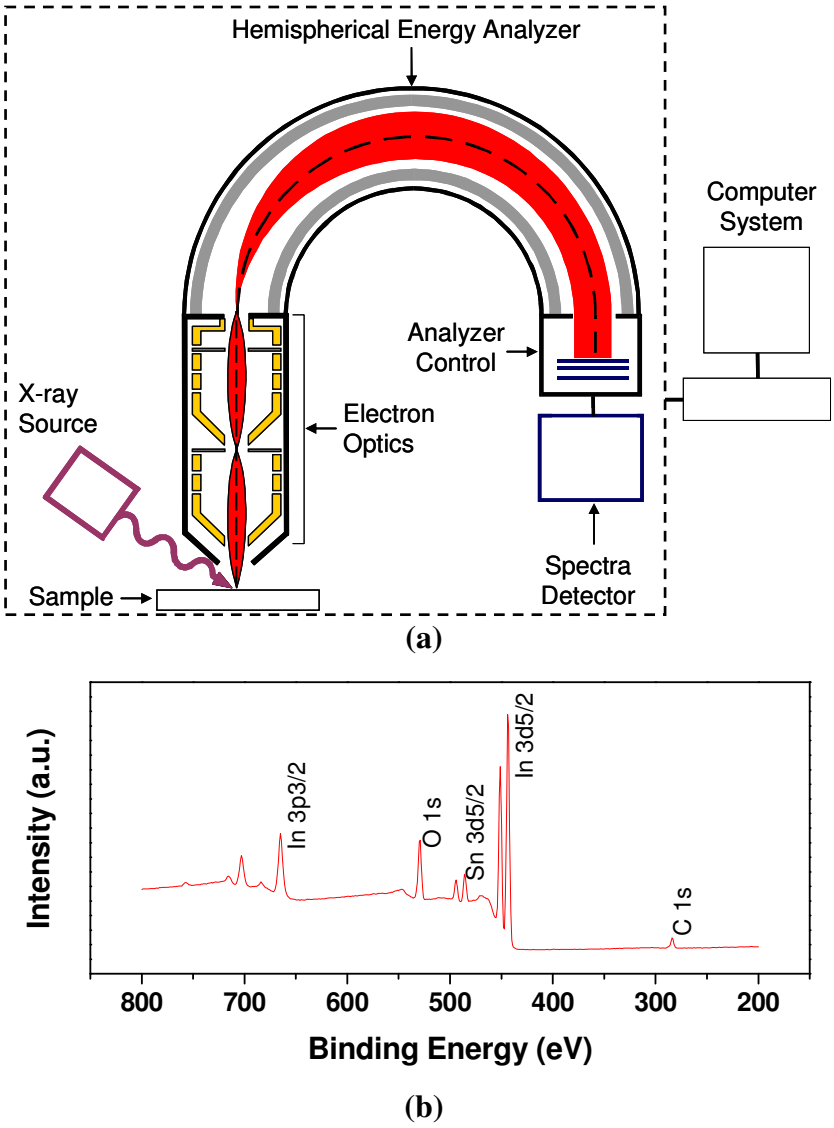

Figure 2.4 Schematic XPS instrumentation (a) and a typical XPS spectrum of an ITO surface (b).

XPS is commonly carried out with either monochromatic Al K_α radiation ($h\nu$ = 1486.6 eV) or Mg K_α ($h\nu$ = 1253.6 eV) sources. A typical XPS survey spectrum consists of well-defined spectral peaks on a large background of inelastically scattered electrons formed during transport of photoelectrons to the surface, as shown in Figure 2.4(b). The electrons

comprising the spectral peaks carry most of the useful information although the fraction of these electrons in the total emission yield is very small (<< 1 %). The primary peaks arise from the valence-band structure, which is not shown in Figure 2.4(b), from shallow core levels (BE < 50 eV), from deeper core levels and from Auger processes for each of the elements present at or above the detection levels in the near-surface region of the sample. X-rays have a low absorption cross section in solids so that most penetrate many hundreds of nm. However, most of the photoelectrons having *KEs* between 100 and 1500 eV travel only a few nm before losing energy by suffering an inelastic collision, then becoming part of the broad background rather than contributing to the elemental peaks [173].

Diagram of a basic, typical PES instrument used in XPS, where the radiation source is an X-ray source. When the sample is irradiated, the released photoelectrons pass through the lens system which slows them down before they enter the energy analyzer. The analyzer shown is a spherical deflection analyzer which the photoelectrons pass through before they are collected at the collector slit.

Hence although X-rays penetrate to a depth of several micrometers, ejected photoelectrons generally come from only the first several nanometers of material. Thus, XPS is very much a surface technique. The sampling depth in XPS is in the range of 1-5 nm, corresponding to 4 - 20 atomic or molecular monolayers, depending upon the attenuation length of the photoelectrons being collected. The distribution of photoelectrons in depth tails exponentially into a solid, which means that the composition determined from XPS data is a weighted average over the region being examined and the near-surface layers contribute more intensity to the total signal. The imaged and analyzed area varies between

2 and 500 μm with a sensitivity limit of 0.1 ~ 1 % of a monolayer corresponding to 10^{12} ~ 10^{13} atoms/cm^2 within the analyzed volume [171].

In addition to analysis of surface composition and chemical states, XPS can also be used for composition variation with depth of thin film, although which is not used in this study. One of the most frequently used techniques is the destructive depth profiling, which is realized by bombardment of the film surface with Ar^+ ions at controlled power and timing. After certain time of this "bombardment erosion", the composition is analyzed before next bombardment starts. Thus a composition depth profile is obtained.

2.2.3 Information Disclosed by XPS

The information sought from XPS data is normally that of composition and/or chemical state. Because no two elements have the same set of *BEs*, the photoelectron spectrum from an element will be characteristic of that element. The presence of peaks at particular *BEs* therefore indicates the presence of a specific element in the sample under study. Furthermore, the intensity of the peaks is related to the concentration of the element within the sampled region, which is therefore used to determine the sample stoichiometry at the surface. Thus, the technique provides a quantitative analysis of the surface composition through calculation of the peak areas with appropriate sensitivity factors.

More importantly, XPS is a powerful analysis technique to identify chemical states on the sample surface, as the *BE* is dependent on the chemical environment of the atom.

Different chemical environments often induce slight modifications of the core level positions. These modifications, also known as chemical shifts, can be detected by XPS and can be interpreted in terms of the interactions between the different chemical species present at the surface. This information is of special interest when investigating adsorbate as it allows to evaluate the adsorbate coverage and to learn about its interaction with the substrate. Chemical-state assignments are usually based on the most prominent peaks because they have the highest delectability, but some of the less prominent peaks often exhibit larger shifts in *BE* for a given chemical state, so it is useful in such cases to base chemical-state analysis on them. Information on *BEs* and peak shapes for various chemical states has been well documented in literature [174-177].

In practice, however, the binding energies of elemental species may be so closely spaced that XPS is unable to distinguish between them. This difficulty is complicated further by the presence of more than two overlapping chemical states. In these cases, peak separation is necessary by fitting the spectra with a nonlinear least-squares algorithm, such as Gaussian and Lorentzian functions. The curve-fittings could separate a spectrum into several sub-peaks, which is helpful to determine the different chemical states of the discussed elements on a sample surface.

2.2.4 Spectra Calibration of XPS

For accurate XPS analysis, spectra calibration is necessary. Many calibration methods have been reported for different applications [173]. One popular method is to assign the energy of the C 1s peak due to carbon contamination (referred to as adventitious carbon)

on the sample to the internationally accepted value of 284.6 eV, which then allows the *BEs* of all other features to be found [176]. In the ideal case, this carbon consists only of hydrocarbons in electrical contact with all surface species. Although this method has serious drawbacks, it has been used more often than all others. The drawbacks include the facts that the adventitious carbon is not well characterized, that it may not be in electrical contact with the species being examined, and that it may consist of several different chemical states of carbon leading to a complex peak shape.

To solve the problems, an empirical method is frequently used based on internal spectral self-consistency. Instead of assigning the *BE* of an alleged contamination peak to the C 1s value given above, a peak from one of the major constituents in the sample is chosen, and on the basis of the probable chemical state of that constituent (from other evidence) a *BE* is assigned to that peak. With this trial assignment, the *BEs* of all other features can then be assigned, at which point self-consistency must be examined. If the assignment is correct, then not only will the assignment of a C 1s peak to adventitious carbon appear reasonable, but the interpretation of all the other spectral features will be compatible with published values of *BEs*. If consistency is not obtained in that interpretation, then either an adjustment must be made to the trial *BE* or another element selected and the procedure repeated.

2.3 Cyclic Voltammetry

2.3.1 Introduction

Cyclic voltammetry (CV) is an electrochemical equilibrium technique for the study of redox processes that occur in an electrochemical cell containing electrodes, electrolyte(s) and analyte(s). In a cyclic voltammetry experiment, a potential is applied to the system, and the current response over a range of potentials (a potential window) is measured. The electrode potential follows a linearly ramping potential vs. time as shown in Figure 2.5(a). The potential is increased linearly with time to some specified potential value and then decreased over the same period of time back to the initial potential. These data are then plotted as current vs. potential, as shown in Figure 2.5(b).

As the waveform shows, the forward scan produces a current peak for any analytes that can be reduced through the range of the potential scan. The current will increase as the potential reaches the reduction potential of the analyte, but then falls off as the concentration of the analyte is depleted close to the electrode surface. As the applied potential is reversed, it will reach a potential that will reoxidize the product formed in the first reduction reaction, and produce a current of reverse polarity from the forward scan. This oxidation peak will usually have a similar shape to the reduction peak. As a result, information about the redox potential and electrochemical reaction rates of the compounds is obtained.

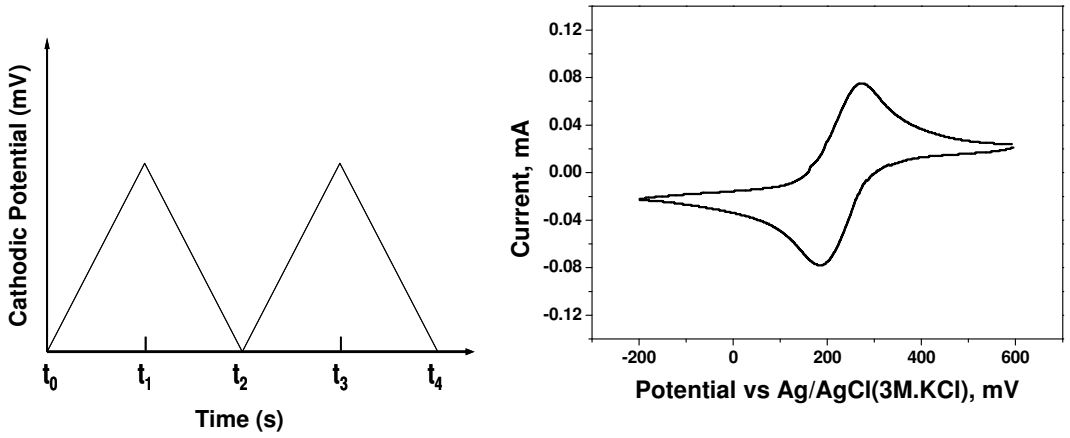

(a) (b)

Figure 2.5 Cyclic voltammetry potential waveform (a) and the corresponding CV graph (b).

CV is a fast and simple method for initial characterization of a redox-active system. In addition to providing an estimate of the redox potential, CV can also provide information about the rate of electron transfer at the electrode-solution interface, and the stability of the analyte in the electrolyzed oxidation states. More importantly, characteristics of the CVs are dependent on the electrode employed and, in return, studies of CVs reveal properties of the electrode surface. In this respect, the ITO films modified by plasma treatments, electrochemical process, and ultra thin insulating films were used as an electrode for CV.

2.3.2 Electrical Double-Layer and Charging Current

The changing arrangement of ions, solvent, and electrons in the electrode/solution interfacial region near the electrode surface has been the focus of considerable

investigation [178]. The electrical double-layer is associated with an ideally polarized electrode in which no charge transfer can occur regardless of the potential imposed by an external voltage source, as schematically shown in Figure 2.6. The specific nature of the structure and the interactions of the electrical double-layer should be considered in the interpretation of electroanalytical data. Various models have been proposed describing the interface region near the electrode surface, such as Helmholtz double-layer model, Gouy-Chapman diffuse double-layer model, Stern model, etc [179-181].

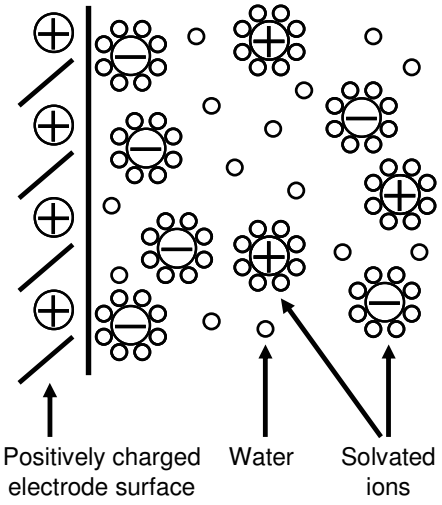

Figure 2.6 Schematic diagram of electrical double layer found at a positively charged electrode [181].

Helmholtz parallel-plate capacitor model [182,183] is widely used to interpret some phenomena occurs at electrode/solution interface due to its simplicity, although it does not account for the possible specific adsorption or random motion of ions. Based on this parallel-plat capacitor model, a current is required to change the potential applied to the electrode, and this is referred to as the charging current. Since the potential in a cyclic voltammetry experiment is constantly changing, there is an (approximately) constant

charging current throughout the experiment that makes a major contribution to the background current.

2.3.3 Faradic Current and Nernst Equation

Since the real power of CV technique lies in its ability to investigate mechanisms and potentials of electrode reactions, the CV experiment is usually carried out under the conditions where charging current is much small, compared to the current from transfer of electrons between the energy levels of the working electrode and the molecular energy levels of the species under study. This current is often referred to as the faradic current. Transfer of electrons from filled electrode orbitals to vacant molecular orbitals is referred as reduction, whereas transfer of electrons from filled molecular orbitals to vacant electrode orbitals is referred to as oxidation. Whether oxidation or reduction can occur depends upon the relative energies of the Fermi level of the electrode (i.e., the energy of the highest occupied electrode orbital) and the frontier molecular orbitals of the studied species. For example, reduction can occur if the Fermi level is higher than the lowest unoccupied molecular orbital, whereas oxidation requires that the Fermi level is lower than the highest occupied molecular orbital.

Faradic current depends on two things: the kinetics of electron transfer and the rate at which the redox species diffuses to the surface. In the case of reduction, for instance, oxidized specie (O) diffuses to the electrode surface, receives an electron becoming reduced specie (R), and diffuses away from the electrode surface. Current at the surface is

generated by the transfer of electrons from the electrode to the oxidized species (*O*). In solution current is carried by migration of ions.

The Nernst equation describes the fundamental relationship between the potential applied to an electrode and the concentration of the redox species at the electrode surface. If an electrode is at equilibrium with the solution in which it is immersed, the electrode will have a potential, invariant with time, which is thermodynamically related to the composition of the solution. In solution, species *O* is capable of being reduced to *R* at the electrode by the following reversible electrochemical reaction: $O + ne^- \leftrightarrow R$. If the kinetics of electron transfer is rapid and so is not current-limiting at any potential, the concentrations of *O* and *R* at the electrode surface can be assumed to be at equilibrium with the electrode potential. Hence, the concentrations of *O* and *R* at the electrode surface are governed by the Nernst equation [181]:

$$E = E^{0'} + \frac{RT}{nF} \ln \frac{C_O^S}{C_R^S} \tag{2.3.1}$$

where *E* is the applied potential (in *V*), $E^{0'}$ is the formal redox potential, *R* (8.31451 J/K•mol) is the universal gas constant, *T* is the temperature (in Kelvin), *F* (96484.6 C/mol) is the Faraday constant, *n* is the number of electrons transferred, and C^S is a surface concentration (it is assumed in this equation that the diffusion coefficients of *O* and *R* are equal). Such a redox process is frequently referred to as reversible. For specific conditions, such as at 25 ^{o}C, the equation can also be written as [181]:

$$E = E^{0'} + \frac{0.0591}{n} \log \frac{C_O^S}{C_R^S} \tag{2.3.2}$$

According to the Nernst equation, the concentration of the oxidized species at the surface will decrease as the potential becomes more negative. Assuming that the electron transfer rate is very rapid, the current i measured as the potential is decreased will be directly related to diffusion rate of oxidized species to the electrode surface:

$$i = nFAJ \tag{2.3.3}$$

where n is the number of electrons, F is Faraday's constant, A is the area of the electrode surface and J is the flux of the oxidized species to that surface. The flux is governed by Fick's law:

$$J = -D\left(\frac{dC}{dx}\right)_{x=0} \cong D\frac{(C^* - C_{x=0})}{\Delta x} \tag{2.3.4}$$

where, D is the diffusion coefficient of the species, x the distance from the electrode surface, $(dC/dx)_{x=0}$ is the concentration gradient at the surface, C^* the concentration of the oxidized species in the bulk solution, and $C_{x=0}$ its concentration at the surface. It is obvious that the greater the concentration gradient, the greater the flux J and therefore the greater the cathodic current.

2.3.4 Experimental Setup

A typical experimental setup for CV scans is schematically shown in Figure 2.7. First, a potentiostat is required for controlling the applied potential, and a current-to-voltage converter is required for measuring the current. A user interface is required to define the way the potential is applied - the potential waveform. There are a number of different potential waveforms, and these are referred to by characteristic names; for example, cyclic

voltammetry, and differential pulse voltammetry. The potentiostat must be connected to the electrochemical cell.

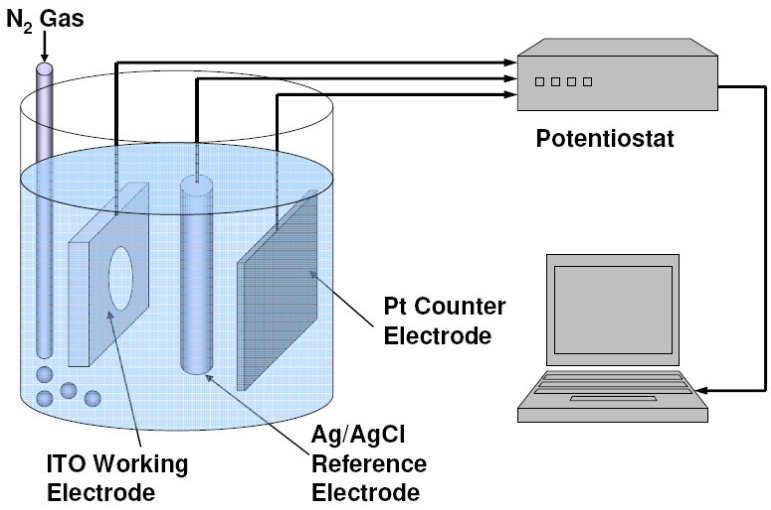

Figure 2.7 Schematic construction of electrochemical cell used for electrochemical treatment and analysis.

In a cyclic voltammetry experiment, an external potential is applied to the cell, and the current response is measured. Better potential control is achieved using a potentiostat and a 3 electrode system, in which the potential of one electrode (the working electrode) is controlled relative to the reference electrode, and the current passes between the working electrode and the third electrode (the auxiliary electrode).

The working electrode is the one at which the electrochemical phenomena being investigated takes place. The working electrode materials should be electronically conductive and electrochemically inert over a wide potential range (the potential window). Commonly used working electrode materials for cyclic voltammetry include platinum, gold, silver, and glassy carbon. Other materials, e.g., semiconductors, ITO glass, and other

metals, are also used for more specific applications. Various surface treatments and ultra thin coatings are also applied to the working electrode for investigating the effects of the surface modifications on the electrochemical properties of the electrode, such as electron transfer rate across the electrode-solution interface.

The reference electrode has such a property that it can be taken as the reference standard against which the potentials of the other electrodes present in the cell can be measured. Silver-silver chloride electrode (SSCE) and calomel electrode (CE) are frequently used for CV scans. SSCE and CE in a saturated potassium chloride solution at 25 ^{o}C develop potentials of 199 mV and 244 mV vs. the normal (or standard) hydrogen electrode (NHE) (or SHE), respectively [184].

The third functional electrode is the counter or auxiliary electrode that serves as a source or sinks for electrons so that current can be passed from the external circuit through the cell. The auxiliary electrode is typically a platinum wire or glassy carbon. In order to support the current generated at the working electrode, the surface area of the auxiliary electrode must be equal to or larger than that of the working electrode.

Electrolyte solutions can be aqueous or non-aqueous. A wide range of salts can be used for aqueous electrolyte solutions. The electrolyte solution must be able to dissolve the analyte (redox couple), must be chemically and electrochemically inert over a wide potential range, and must be pure.

2.3.5 CV Graph and Interpretations

Figure 2.8 shows a typical CV spectrum based on the electrochemical system where ITO as a working electrode and $Fe^{III}(CN)_6^{3-}/Fe^{II}(CN)_6^{4-}$ as an redox couple in 0.1 mol KNO_3 electrolyte. At the start of the experiment, the bulk solution contains only *R* so that at potentials lower than the redox potential, there is no net conversion of *R* into *O*. As the redox potential is approached, there is a net anodic current which increases exponentially with potential. As *R* is converted into *O*, concentration gradients are set up for both *R* and *O*, and diffusion occurs down these concentration gradients. At the anodic peak, the redox potential is sufficiently positive that any R that reaches the electrode surface is instantaneously oxidized to *O*. Therefore, the current now depends upon the rate of mass transfer to the electrode surface, resulting in an asymmetric peak shape.

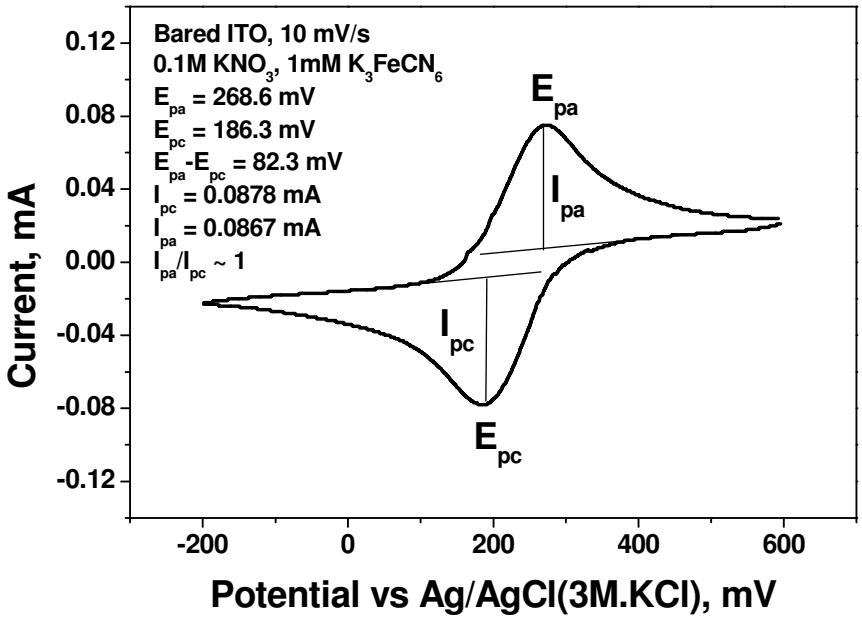

Figure 2.8 A typical plot of current vs. potential in a CV experiment.

Upon reversal of the scan, the current continues to decay until the potential nears the redox potential. At this point, a net reduction of *O* to *R* occurs which causes a cathodic current which eventually produces a peak shaped response. Further decrease of potential results in reduced cathodic current that is governed by mass transfer, until the end of the cycle.

The parameters of greatest interest for a CV are the peak anodic potential (E_{pa}), the peak cathodic potential (E_{pc}), the peak anodic current (I_{pa}), and the peak cathodic current (I_{pc}). If a redox system remains in equilibrium throughout the potential scan, the electrochemical reaction is said to be reversible. In other words, equilibrium requires that the surface concentrations of *O* and *R* are maintained at the values required by the Nernst Equation. Under reversible condition, the peak potential separation ΔE_p (= E_{pa} - E_{pc}) = (58/n) mV at all scan rates at 25 ^{o}C, where n is the number of electrons transferred. In practice, the difference is typically 70-100 mV. Meanwhile, the ratio of anodic to cathodic peak currents approaches unity, i.e., I_{pa}/I_{pc}=1. However, a larger peak separation than (58/n) mV and a remarkable deviation of the I_{pa}/I_{pc} ratio from unity indicate the redox system is in an irreversible condition due to the retarded electron transfer kinetics, which the important evidences of surface passivation.

2.4 Contact Angle Measurements and Surface Energy

2.4.1 Introduction

Surface energy is an underlying concept in thin film science, which determines whether one material wets another and forms a uniform adherent layer. For example, a material with very low surface energy will tend to wet a material with a higher surface energy. On the other hand, if the deposited material has a higher surface energy it tends to form clusters or "ball up" on the low-surface-energy substrate. The mechanism behind the phenomena is the reduction of system free energy. Consequently, as observed in nature, a liquid tends to ball up to reduce its surface area, and crystals tend to facet in order to expose those surfaces being of the lowest energy. As surface energy is related to bond energy and to the number of bonds broken in creating the surface, and in turn is related to the binding energy of the material [186], the surface property is a direct manifestation of intermolecular forces. The surface of a solid, like that of a liquid, possesses additional free energy, but owing to the reduced molecular mobility this free energy is not directly observable, and it must be measured by indirect methods. For this purpose, measurement of contact angles is a practical technique. Although the contact angle method is also changed with surface heterogeneity, roughness, adsorption/desorption, inter-diffusion, and/or surface deformation, the method has been accepted and widely used for estimation of solid surface energies.

2.4.2 Concept of Contact Angle and Young's Equation

Thin film deposition on a solid generates new interfaces between dissimilar materials and involves considerations of wettability, spreading, interface evolution, and adhesion. The wettability of a solid by a liquid is characterized in terms of the angle of contact that the liquid makes on the solid [187]. The contact angle (θ) is the angle at which a liquid/vapor interface meets the solid surface, as illustrated in Figure 2.9. Contact angle measurements characterize the surface with respect to wetting properties and surface tension.

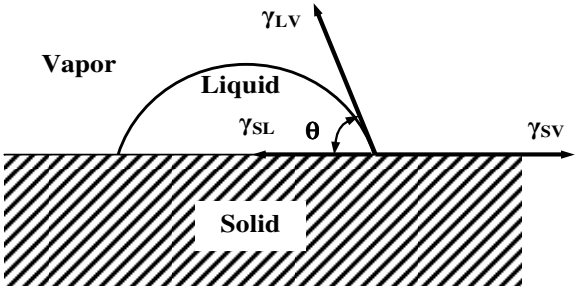

Figure 2.9 The shape of the droplet is determined by the Young-Laplace equation.

When a liquid drop is in contact with an ideally smooth, homogeneous, rigid and insoluble solid, the bare surface of the solid absorbs the vapor of the liquid until the volatility of the absorbed material is equal to that of the liquid. With the establishment of the equilibrium, there is a liquid-solid interface between the two phases. The tensions at the three phase contact point are indicated such that LV is the liquid/vapor point, SL the solid/liquid point, and SV the solid/vapor point.

Young [188] first proposed treating the contact angle (θ) of the liquid in equilibrium as the resultant of the three surface tensions:

$$\gamma_{SV} - \gamma_{SL} = \gamma_{LV} \cos\theta \quad (2.4.1)$$

where γ is the surface tension (or surface free energy), and the subscripts refers to the three different interfaces. The Young's equation was approximately presented by [189-193]

$$\gamma_{LV}(1+\cos\theta) = \gamma_S + \gamma_{LV} - \gamma_{SL}, \quad (2.4.2)$$

where, γ_S is the surface energy of the solid in vacuum. This equation indicates that from the contact angle measurement with a liquid of known γ_{LV}, only ($\gamma_S - \gamma_{SL}$) can be obtained.

Models have been developed during past few decades to provide approximate answers by giving us another equation with which to separate γ_S and $\gamma_{SL,}$ such as Zisman plot [193], equation of state [194], geometric mean [195,196], harmonic mean [197], and acid-base [198]. These five models are often called by different names, so it becomes tedious to keep track of all of them. It is very important to understand that these are, indeed, very approximate. The models are based on independent knowledge of how liquids and solids adhere to one another. Each model does better with one type of surface or another, but there is no recognized "correct" answer.

Although controversies concerning the correctness of these methods exist in the literature, the estimation of solid surface energy is still bothering people. Primarily researchers would like to characterize surfaces without having to explicitly describe the test fluid. The right hand side of Young's equation (Eq. 2.4.1) is the product of the test liquid surface tension and the contact angle, so surface energy is more "fundamental," even if it cannot be accurately measured with today's understanding. Secondly, the surface energy description mimics the surface tension description for liquids, so similar terminology is

used for both. Thirdly, the inaccuracies in today's models are acceptable to some. The real issue now is choosing a model. Careful reviews on these approaches indicate that geometric mean and harmonic mean methods are more widely used. The basics of the two methods are the same and the only difference exists between them in mathematic treatment.

2.4.3 Estimation of Solid Surface Energy

2.4.3.1 Geometric Mean Method

Fowkes [199] first proposed that the surface free energy of a pure phase could be represented by the sum of the contributions arising from different types of force components, such as dispersion force, polar force, hydrogen bonding force, induction force (Debye), and acid/base force. At least seven components have been identified by Fowkes [200], but Schultz et al. [201] suggested that the surface free energy may be generally expressed by two terms, namely a dispersion component and a polar component. Fowkes then proposed that the geometric mean of each force component is a reliable prediction of the interaction energies at the interface caused by the two force components. After a lot of theoretical and experimental work [194,196,202-204], a new expression of Young's equation (Eq. 2.4.1) has been deduced for a solid-liquid system by eliminating the interfacial free energy (γ_{SL}) [205]

$$1+\cos\theta = \frac{2(\gamma_S^d)^{1/2}(\gamma_{LV}^d)^{1/2}}{\gamma_{LV}} + \frac{2(\gamma_S^p)^{1/2}(\gamma_{LV}^p)^{1/2}}{\gamma_{LV}}, \qquad (2.4.3)$$

where the superscript d refers to the dispersion (non-polar) component due to instantaneous dipole moments, and p refers to the polar (non-dispersion) component, including all the interactions established between the solid and liquid, such as dipole-dipole, dipole-induced dipole and hydrogen bonding, etc. [206].

In the geometric mean approach, measuring the contact angle θ for liquids 1 and 2 with known values of γ_{LV}^{d} (dispersive component) and γ_{LV}^{p} (polar component) on a given substrate, the surface energy components γ_S^{p} and γ_S^{d} can then be determined from the following simultaneous equations:

$$\frac{1+\cos\theta_1}{2} = \frac{(\gamma_{LV1}^{d})^{1/2}}{\gamma_{LV1}}(\gamma_S^{d})^{1/2} + \frac{(\gamma_{LV1}^{p})^{1/2}}{\gamma_{LV1}}(\gamma_S^{p})^{1/2} \tag{2.4.4}$$

$$\frac{1+\cos\theta_2}{2} = \frac{(\gamma_{LV2}^{d})^{1/2}}{\gamma_{LV2}}(\gamma_S^{d})^{1/2} + \frac{(\gamma_{LV2}^{p})^{1/2}}{\gamma_{LV2}}(\gamma_S^{p})^{1/2} \tag{2.4.5}$$

The total surface energy of the solid surface, γ_S, is then simply the sum of the two components, i.e., $\gamma_S = \gamma_S^{p} + \gamma_S^{d}$.

2.4.3.2 Harmonic Mean Method

In the harmonic mean method [197,207,208], it is assumed that the solid-liquid interfacial free energy is equal to the harmonic mean of free energy of solid and liquid. Applying the harmonic mean method in Young's equation (Eq. 2.4.1), one has

$$(1+\cos\theta)\gamma_{LV} = 4\left(\frac{\gamma_S^{d}\gamma_{LV}^{d}}{\gamma_S^{d}+\gamma_{LV}^{d}} + \frac{\gamma_S^{p}\gamma_{LV}^{p}}{\gamma_S^{p}+\gamma_{LV}^{p}}\right). \tag{2.4.6}$$

Identical to the geometric mean method, two probing liquids are needed in order to solve for the two unknowns, the dispersive and polar components of surface energy. In the same way as with using the geometric mean, the harmonic mean may be used to calculate the dispersive and polar components of the surface energy by measuring the contact angles of liquids, 1 and 2, on a solid. The two simultaneous equations,

$$\gamma_{LV1}(1+\cos\theta_1) = \frac{4\gamma_{LV1}^d\gamma_S^d}{\gamma_{LV1}^d+\gamma_S^d} + \frac{4\gamma_{LV1}^p\gamma_S^p}{\gamma_{LV1}^p+\gamma_S^p} \tag{2.4.7}$$

$$\gamma_{LV2}(1+\cos\theta_2) = \frac{4\gamma_{LV2}^d\gamma_S^d}{\gamma_{LV2}^d+\gamma_S^d} + \frac{4\gamma_{LV2}^p\gamma_S^p}{\gamma_{LV2}^p+\gamma_S^p} \tag{2.4.8}$$

are then solved for γ^d_S and γ^p_S.

2.4.3.3 Limitations

According to Wu et al. [207], the harmonic mean is better suited for low energy surfaces such as polymers than geometric mean. Since ITO surface energy is generally higher than that of polymers, in this study geometric mean is used.

It should be pointed out that for thermodynamic equations used in the above mentioned methods to be valid, surfaces must be atomically flat, chemically homogenous and there must be no chemical interaction between the solid and liquid. In reality, the two former conditions are very rare and therefore any surface energy calculated on common surfaces is only an estimate. Therefore, the estimated surface energy is on a relative basis in the final analysis.

2.5 Sample Preparation and Film Thickness Calibration

2.5.1 ITO Sample Cleaning

In this study, the commercial ITO-coated glass (Präzisions Glas & Optik GmbH) with an initial sheet resistance of 20 Ω/ were used as the substrates. Prior to their use, the ITO substrates were routinely cleaned by a sequence of sonications in detergent solution, ethanol and de-ionized (DI) water each for 10 min, and finally dried in a flow of nitrogen. The ITO sample just after the routing clean is denoted as "as-clean", which was used as a control for comparison.

2.5.2 Si Wafer Sample Cleaning

Silicon (111) substrates (Semiconductor Processing Co.) were cleaned by immersing them in an H_2O_2 + sulfuric acid mixture (70 vol.% concentrated H_2SO_4, 30 vol.% H_2O_2) at 90 ^oC for 30 min. This strongly oxidizing combination removes all organic contaminants on the surface, but does not disturb the native silicon oxide layer. The wafer samples were then rinsed repeatedly with DI water and finally blown dry under a stream of nitrogen.

2.5.3 Calibration and Measurements of Coating Thickness

For thermally evaporated coatings, the film thickness was monitored by a quartz thickness monitor after precise calibration by using a profilometer. However, precise calibration of

solution-coated thin film thickness on ITO surface is difficult due to its rougher surface. Therefore, cleaned silicon wafer substrates were used to calibrate wet coating thickness in combination with ellipsometric measurements, according to the procedures described in literature [209,210].

Chapter 3

Plasma Treatment

Abstract

In this chapter, various plasma treatments of ITO electrodes and their effect on the surface properties of ITO and device performance are described. A brief overview of the effect of plasma treatments of ITO surface on hole injection efficiency will be given with the emphasis on the hole injection mechanisms behind the surface treatment. Different types of plasmas, namely, hydrogen (H_2-P), argon (Ar-P), oxygen (O_2-P), and carbon tetrafluoride (CF_4-P) were used to treat the ITO surface. Chemical composition, surface energy, and charge transfer across interface were investigated by X-ray photoelectron spectroscopy (XPS), contact angle goniometer, and cyclic voltammetry (CV), respectively. Luminance-current-voltage (L-I-V) characteristics of the OLED devices based on the surface treated ITO electrodes, in configuration of ITO/NPB(60nm)/Alq_3(60nm)/LiF/Al, [NPB=N,N'-bis(1-naphthyl)-N,N'-diphenyl-1,1'-biphenyl-4,4'-diamine and Alq_3=tris(8-hydroxyquinolato) aluminum] were also presented. The atomic force microscopy (AFM) results showed that change in surface morphology was not distinguishable after the plasma treatments under the treatment conditions employed in this study. Compared with the pristine ITO surface, plasma treatments, in particular O_2-P and CF_4-P, significantly increased the peak potential separation and reduced the peak current in the cyclic voltammograms, implying a suppressed electron transfer across the solid-solution

interface. More importantly, plasma treatments showed significant effect on the surface composition, surface energy and device performance.

3.1 Introduction

Oxygen plasma treatment of ITO surface has been widely reported to improve OLED device performance, in particular, driving voltage and device stability [113,115,124]. Although various physical and chemical properties of the plasma treated ITO surfaces have been investigated to understand the effect of the surface treatments on hole injection, the majority of discussion was concentrated on the change in work function. A general understanding of the hole injection mechanism is that the increased work function by the surface treatments reduces the energy barrier for hole injection, and therefore the driving voltage [93,122,131,148,157,158]. However, the effect of electrode work function has been questioned by many researchers [41,44,49,63,160-162]. They believed that, instead of work function, other surface properties such as surface energy [115], and morphology [160,161] may play a more important role in manipulating the device performance [124,211,212]. Being short of a systematic investigation on this aspect, more experimental work is clearly needed to understand the mechanisms behind the improved device performance by plasma treatments.

In this chapter, four different types of plasmas, viz., hydrogen (H_2-P), argon (Ar-P), oxygen (O_2-P) and carbon tetrafluoride (CF_4-P) plasmas, were used to treat ITO surfaces. Chemical composition, surface energy, and charge transfer kinetics across solid-solution interface were investigated by XPS, contact angle goniometry, and CV, respectively. L-I-V characteristics of the OLED devices based on the treated ITO surfaces were also presented. This work aimed at studying the effects of plasma treatment on ITO surface

properties and therefore the device performance. The experimental results will provide further support to the discussions on hole injection mechanisms in later chapters.

3.2 Experimental

ITO-coated glass samples were firstly cleaned as described in Section 2.5. Next, the plasma treatment of ITO samples was carried out in a parallel plate type plasma system (MARCH PX-1000) at room temperature using the working gases of Ar, H_2, O_2, and CF_4 (denoted as Ar-P, H_2-P, O_2-P, and CF_4-P), respectively. In the plasma treatment chamber, two electrode plates were fixed at a distance of 10 mm, and the samples were placed on the bottom plate. All the samples were plasma treated for 3 min at an RF (13.56 MHz) power of 600 W, and a pressure of 30 Pa. The gas flow rates of 300 sccm were used for the H_2 and CF_4 gas plasmas, and 600 sccm for Ar and O_2 gas plasmas. The treated ITO samples were subsequently stored in a portable desiccator with at the pressure of 30 Pa for further experimental work. The treated ITO samples were exposed to atmosphere about 2 min when being transferred from the plasma treatment chamber into the desiccator, or from the desiccator into the vacuum chambers for surface analyses and device fabrication.

3.3 Results and Discussion

3.3.1 Surface Morphology

The surface morphology of the as-clean and plasma-treated ITO samples was examined using a Digital Instruments Nanoscope IIIA AFM. More information about AFM technique can be found in Section 2.1.

The AFM images of as-clean and plasma-treated ITO samples were compared by measuring the RMS roughness and the "grain-subgrain" features [95,99]. The RMS roughness values measured by AFM fall in the range of 3-4 nm for all the plasma treated ITO samples, and are thus similar to the as-clean ITO. The surface morphology is also not sensitive to the plasma-treatment time in the range of 0-10 min that is frequently adopted in the fabrication of OLED devices, as shown in Figure 3.1. The results are consistent with the conclusions made by other research groups [213,214], in which no change in the microstructure of the electrode surface was observed even after 30 min of plasma treatment [213], and no effect was found on the surface composition after 10 min of plasma treatment [214].

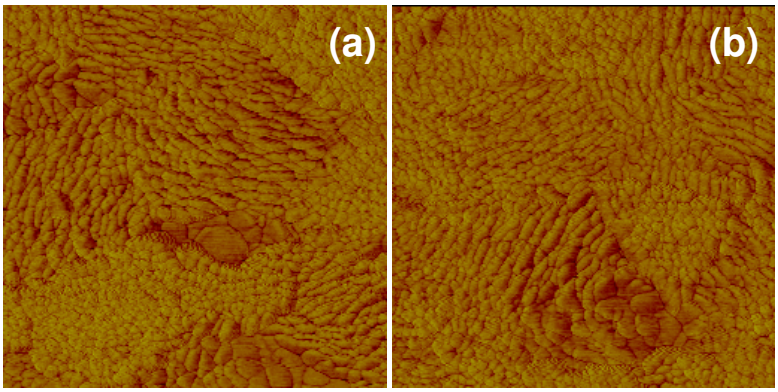

Figure 3.1 AFM (phase mode) images of (a) the as-clean ITO surface, and (b) the ITO surface treated by Ar plasma for 10 min under the treatment conditions described in Section 3.2. The scan area is 1×1 μm^2.

The results, however, are clearly not conclusive, as a dramatic increase in ITO surface roughness after Ar plasma has also been reported by Kim et al. [215] Obviously, various operating conditions, such as plasma generation (microwave or RF), power, gas flow rate, treatment time and others, have been used by different research groups for ITO surface plasma treatment. It is, therefore, not difficult to understand the conflicting reports on the effect of plasma treatment on ITO topography. As the operating conditions of plasma treatment used in this study do not result in measurable change of the ITO surface morphology, the study on nucleation and growth of HTL over the plasma-treated ITO surfaces can be carried out independent of the topographic factor.

3.3.2 Surface Analysis by XPS

XPS was used to characterize the chemical compositions and states of ITO surfaces treated by plasma. All XPS experiments were performed in a VG ESCALAB 220i0XL instrument. All spectra were recorded in the constant pass energy mode of the analyzer

using a monochromatic Al Kα X-ray source (1486.7 eV) at a photoelectron take-off angle of 90°. Survey spectra were recorded with pass energy of 150 eV and step width of 1 eV and high-resolution spectra were recorded with pass energy of 20 eV and step width of 0.1 eV. With a linear background correction, the relative atomic concentration of each element on ITO surface was calculated according to their peak areas corrected with the empirical sensitivity factors, the instruments transmission function and the specific mean free path lengths. More information about XPS technique can be found in Section 2.2.

3.3.2.1 Calibration of XPS Spectra

The detected XPS spectra are usually shifted due to surface charging, and the binding energy values directly obtained from the spectra could not be used for qualitative or quantitative analysis. Therefore, a proper calibration of the XPS spectra is essential for meaningful discussions. The C 1s binding energy (~285 eV) of atmospheric carbon contaminants, normally in aliphatics, is most frequently used as a reference to calibrate the spectra obtained from ITO surfaces [176]. For the as-clean, O_2-P, Ar-P, and H_2-P samples, the XPS spectra can be calibrated by the main C 1s peak, as the major carbon source in these cases is atmospheric aliphatic contamination. However, spectra calibration is troublesome for CF_4 plasma treated ITO, because new carbon compounds may be created during the treatment. Moreover, we could not assure the existence of the measurable amount of aliphatic sequences on the heavily fluorinated surfaces [216].

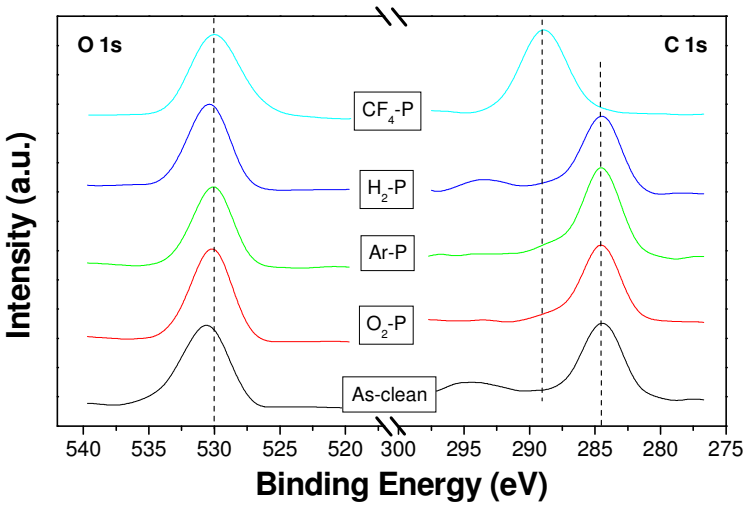

Figure 3.2 C 1s and O 1s survey spectra of ITO surfaces after different plasma treatments

Therefore, another reference must be identified to complete the spectra calibration. O 1s is a promising candidate as the second reference for spectra calibration. For Ar-P and CF_4-P plasma treatments, it is reasonable to assume that most of the oxygen containing contaminants, such as O-H (including water) and C-O/C=O species, will be removed by the plasmas. On the other hand, the situation in recontamination, i.e., exposure to atmosphere after the plasma treatments, is in the same way for all the treated samples in this study. Therefore, the oxygen species on ITO surfaces treated by the two plasmas and thus the locations of O 1s peaks should have non detectable difference. Based on this assumption and deduction, O 1s obtained from Ar-P sample is used as the second reference for calibration of XPS spectra obtained from the ITO sample after CF_4 plasma treatment, as shown in Figure 3.2.

3.3.2.2 Overview of XPS Spectra and Composition

Wide-scan XPS spectra (from 200 to 800 eV) of the untreated and various plasma-treated ITO substrates are shown in Figure 3.3. The most significant photoelectron signals of F, O, Sn, In and C were detected. The peaks at the binding energies of about 687, 530, 493, 486, 452, 444, 285 eV correspond to F 1s, O 1s, Sn $3d_{3/2}$, Sn $3d_{5/2}$, In $3d_{3/2}$, In $3d_{5/2}$, and C 1s core-level spectra, respectively.

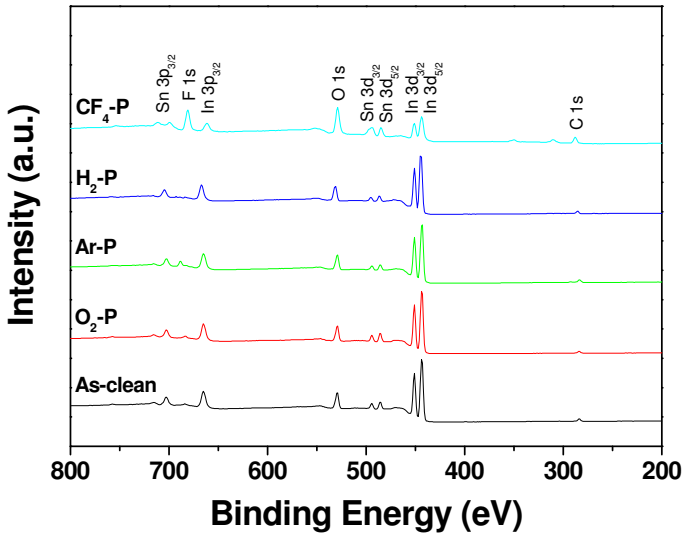

Figure 3.3 Wide-scan XPS survey spectra of different ITO surfaces: as-clean, plasma treatments with oxygen (O_2-P), argon (Ar-P), hydrogen (H_2-P), and carbon fluoride (CF_4-P).

Most of the core-level spectra are asymmetrical and broad, indicating that each spectrum contains multi components with different binding energy shifts. For the sample treated by CF_4 plasma, C 1s spectrum was shifted considerably to the higher binding energy. It was also quite evident that the relative intensities of In 3d and Sn 3d peaks were dramatically reduced on the CF_4-plasma treated ITO surface, compared to those of other samples. This was attributed to the presence of O- and/or F-rich compound layer. Similar results were

reported when ITO surface was treated with phosphoric acid, which was attributed to a acid layer formed on the substrate [126].

Assuming surface composition remains homogeneous, the chemical composition of various ITO surfaces can then be calculated based on the core-level peak component areas and their relative sensitivity factors. Table 3.1 summarizes the XPS analysis results of these spectra obtained from ITO surfaces before and after various plasma treatments, in terms of atomic concentration and ratios. The results showed that plasma treatment can significantly change the surface composition, in particular, the oxygen and carbon contents.

Table 3.1. Chemical composition of ITO surfaces under different plasma treatments.

ITO	Chemical Composition in at.%					Ratio	
Sample	O	In	Sn	F	C	In:Sn	O:In
As-clean	43.8	24.0	10.5	-	21.7	2.3	1.8
H_2-P	40.1	27.0	11.8	-	21.0	2.3	1.5
Ar-P	45.7	27.0	11.7	-	15.6	2.3	1.7
O_2-P	49.8	25.6	10.7	-	14.0	2.4	1.9
CF_4-P	32.8	9.4	3.7	23.2	30.9	2.5	3.5

Compared to that of the as-clean sample surface, the relative concentration of carbon on the ITO surfaces changed from 21.7% to 21.0, 15.6, 14.0, and 30.9 % after H_2, Ar, O_2 and CF_4 plasma treatments, respectively. The relative oxygen content was increased by O_2 and Ar plasma treatments but decreased by H_2 and CF_4 plasma treatments, from 43.8% of the control to 49.8 and 45.7, 40.1, and 32.8%, respectively. The results demonstrated that the relative oxygen content changes reversely with carbon. Although no extra oxygen is added in Ar plasma treatment, the increase in relative oxygen content is obviously owing to the

partial removal of the surface contaminants by the argon ion bombardment and the possible atmospheric oxidation after the plasma treatment. Furthermore, O:In on the Ar-P sample surface was decreased. It is also noted that the oxygen reduction by CF_4 plasma treatment is along with a presence of high content fluorine. Although having the lowest absolute value of oxygen content, the highest O:In ratio was obtained on CF_4 plasma treated surface, and the sum of F and O was found to be much higher than the oxygen content on the O_2 plasma treated ITO. The In:Sn ratios for all samples are in the range of 2.3 – 2.5, which are clearly much lower than that of the ITO stoichiometry (about 9:1). This indicates that the ITO surface is rich in Sn. The data also show that the Sn concentration was reduced after O_2 and CF_4 plasma treatments. Selective etching of Sn was ever reported [217], especially for the Ar plasma treatment, where a stronger plasma bombardment was used for the surface cleaning. However, the change in In:Sn ratios among different plasma treatments in this study is not significant enough to conclude that the Sn was selectively etched by O_2 and CF_4 plasma.

It is obvious that the chemical composition analysis is still too coarse for us to obtain a good understanding of the surface properties. For example, possible contributions to the measured oxygen content on the ITO surface include chemical species of In-O, Sn-O, OH, H_2O, C-O, C=O, etc., being of different in binding energies. Unfortunately, it is usually not easy to assign the oxygen-containing compounds based on an O 1s XPS spectrum, due to overlaps in their binding energies. Therefore, deconvolution of XPS spectra has frequently been used for differentiating the chemical species under discussion.

3.3.2.3 Carbon Contamination and New Carbon Species Created by CF_4-P

As shown in Table 3.1, a large amount of carbon was detected for all treated and untreated ITO samples, which is inevitable for samples handled in the ambient [176,218]. Entire removal of the contaminants seems impossible, even in high vacuum environment. More importantly, once exposed to atmosphere the treated surfaces will be re-contaminated by varied amount of carbon-containing substances, depending on the type of treatment process. Furthermore, some surface treatments, such as CF_4-P, may precipitate new carbon species. Therefore, discussions on decontamination effect based on the measured carbon contents may result in incorrect conclusions. By careful deconvolution analysis, it is possible to identify peaks corresponding to carbon atoms bound to different atoms, which is helpful for us to trace the carbon sources.

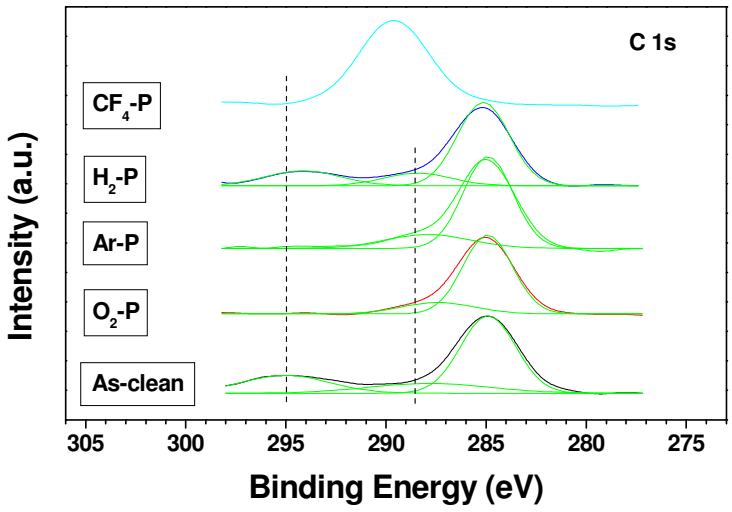

Figure 3.4 C 1s XPS survey spectra of ITO surfaces treated by different plasmas.

C 1s photoemission lines of the as-clean and plasma treated ITO surfaces are compared in Figure 3.4. For the as-clean and H_2-P samples, besides the main peak at about 285 eV, a carbon compound at about 295 eV is found, which is denoted as CF_3 species [173,174]. The carbon fluorides on the two samples possibly originate from the CF_4-contaminated plasma treatment chamber or the sample handling nearby. According to previous reports, oxygen plasma is an effective process to remove the carbon contaminants [93,113,222]. Therefore, the carbon detected after O_2 and Ar plasma treatments is mainly from the atmosphere, i.e., carbon recontamination. The C 1s spectra of the atmospheric contaminants are fitted using two bands: a strong main peak of C-C-H at 284.7 eV, and a weak widen peak with a binding energy of 288.5 eV, which is related to the formation of oxygen to carbon single bonds C-O (chemical shift about 2 eV) and to carbon double bonds C=O groups (chemical shift about 3 eV) [176,223,224].

For CF_4 plasma treatment, the C 1s peaks at 285 eV (C-C-H bonds) are not discernible. Instead, a widen C 1s peak appears at about 290 eV. The results of Table 3.1 show that the carbon content on the CF_4-P treated surface is higher than that of as-clean ITO, suggesting that new carbon compounds are introduced by the treatment. However, the carbon species with high binding energies on the ITO surface treated by CF_4 plasma are difficult to confirm directly, as the binding energies for C-O, C=O, and C-F species have been reported from 286 eV to 293 eV [176,225-229].

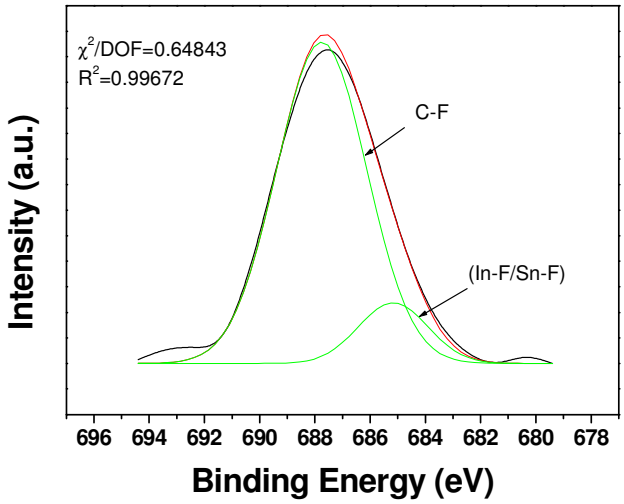

Figure 3.5 F 1s core level spectrum from an ITO surface after CF_4 plasma treatment and exposure to atmosphere, and the Gaussian-fitted sub-peaks illustrating the presence of two chemical sates of fluorine (C-F and In/Sn-F).

Figure 3.5 shows that the F 1s core-level of the CF_4 plasma-treated ITO can be resolved into two peak components with binding energies at about 685 and 688 eV, attributed to In/Sn-F [219,247] and C-F [176] chemical species, respectively. It is noted that the C:F ratio is about 1.33, as shown in Table 3.1. As In/Sn-F compounds reduce the number of F bound to C, it is reasonable to expect the presence of C_2F species on the ITO surface after CF_4P treatment. It is the surface fluorination that causes the missing C-C-H peak after CF_4 plasma treatment and exposure to atmosphere, as the fluorinated surfaces are not easily contaminated by the atmospheric hydrocarbons [216].

3.3.2.4 Asymmetry of O 1s Spectra

It is well known that indium oxide generally lacks stoichiometry due to oxygen vacancies [97,217], i.e., the existence of $In_2O_{x<3}$ and $SnO_{x<2}$ species, implying that O:In ratio in the bulk ITO is less than 1.5. Table 3.1 shows that, except for the H_2-P sample, the O:In ratios

are higher than that of stoichiometrical In_2O_3, indicating presence of additional oxygen sources on the ITO surfaces. The O:In ratio on the H_2-P sample is lower than that of as-clean sample, which is attributed to the reductive effect of hydrogen plasma on ITO surface. It is easy to understand the high O:In ratio on the O_2-P sample surface due to the oxidation effect of the oxygen plasma. In the case of CF_4-P, however, the highest O:In ratio up to about 3.5 was obtained. This can be attributed to the etching effect of CF_4 plasma, as the In 3d and Sn 3d signals on the CF_4-P sample surface are every weak, as shown in Figure 3.2. It is obvious that both In and Sn were etched out by the CF_4 plasma at a similar etching rate, as In:Sn ratio does not increase significantly. It should be pointed out that the samples after plasma treatments were exposed to atmosphere before the XPS analysis in this work. A varied amount of oxygen-containing contaminants from atmosphere are expected to adsorb onto the treated ITO surfaces. The unknown oxygen contributions from the contaminants make the O:In ratio cramped. Therefore, O:In ratio measured by XPS analysis after exposure of the treated samples to atmosphere may not be a reliable data to quantitatively explain the effect of surface modifications, although the ratios measured under similar conditions have frequently been used for discussions on the ITO surface properties after various treatments [93,113].

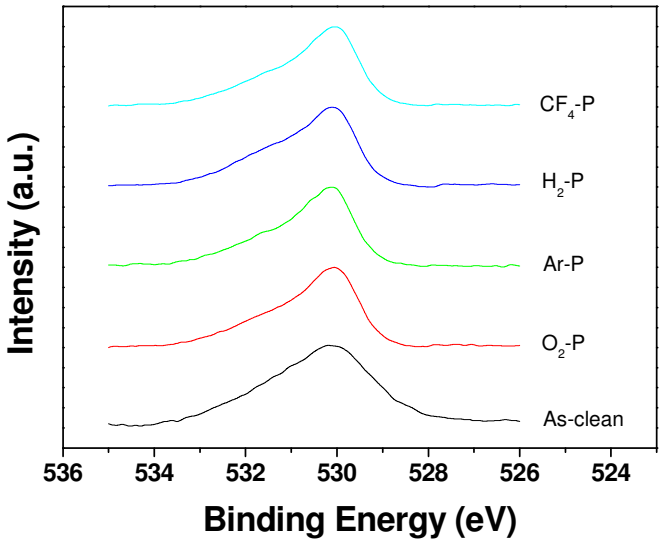

Figure 3.6 O 1s XPS high-resolution spectra of ITO surfaces treated by different plasmas

Figure 3.6 shows the O 1s high-resolution spectra detected from the ITO surfaces after different plasma treatments, with normalization to the spectrum of the as-clean sample. It can be seen that the O 1s peaks are positioned at *BE* of about 530 eV, but all the spectra are broaden and asymmetric, indicating multiple oxide components included. The O 1s *BEs* of pure ITO, hydroxides of metals (i.e., Sn and In) and H_2O have been reported in the range of 528–533 eV [97,217,230-232]. In this regard, the chemical shifts between the different chemical species can be so small that their O 1s peaks are heavily overlapped, and therefore that the BE alone is generally insufficient to discriminate between them.

As it is well known, for an element with high negativity, reduced BE means reaction with elements having lower electronegativity. It is generally believed that the O 1s peak at lower binding energy (about 530 eV) is derived from the O bonded to In and/or Sn atoms being of lower electronegativity. However, once samples are exposed to atmosphere, H_2O will be present on the ITO surface in a form of either molecular absorbent or metallic

hydroxides of (i.e., In-OH and Sn-OH species) [233,234]. O 1s peak is therefore expected to be shifted to the higher *BE* region due to the O-H bond in the hydroxides, and especially the absorbed water [217]. According to the previous reports, the O 1s at about 530 eV is due to the oxygen in bulk ITO [235], but the O 1s at about 532 eV is originated from the oxygen in hydroxyl groups at the outermost surface as well as adsorbed water [158,236,237]. However, Fan et al. [97] believed that the O 1s due to the chemisorbed H_2O should be at 533 eV. Nevertheless, the high *BE* shift and broadening of O 1s peaks in this work are mainly attributed to the hydroxyl groups and adsorbed water. In particular, the water adsorption onto the CF_4-P sample surface may promote In-F/Sn-F.xH_2O compounds [238], leading to the highest O:In ratio. This is also the possible reason why the heavily fluorinated ITO surface is still hydrophilic.

3.3.2.5 Oxidation States of In and Sn Atoms on ITO Surfaces

The O 1s, In 3d and Sn 3d core level spectra for the as-clean and plasma-treated films are shown in Figure 3.7. The results show that the In $3d_{5/2}$ and Sn $3d_{5/2}$ peaks measured from the as-clean sample are located at the lower binding energies of 443.6 and 485.7 eV, respectively, corresponding to In or $In_2O_{x<3}$, and Sn or $SnO_{x<2}$ [176,230,239,240].

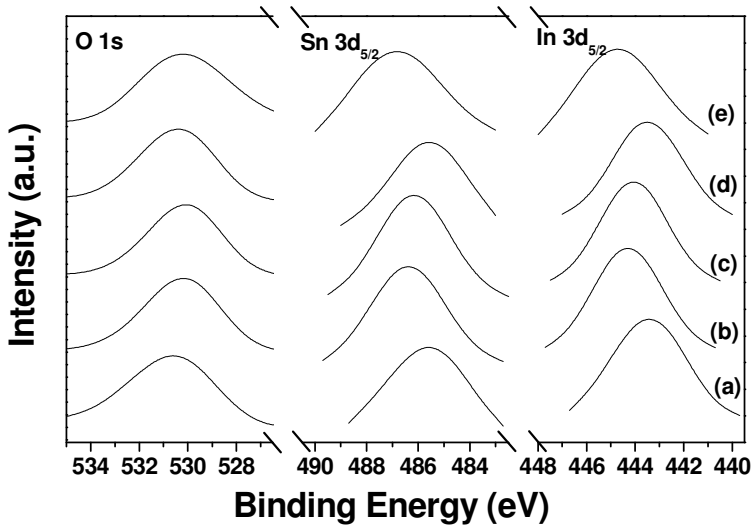

Figure 3.7 XPS spectra of O 1s, Sn $3d_{5/2}$, and In $3d_{5/2}$ for different treatments: (a) as-clean, (b) O_2-P, (c) Ar-P, (d) H_2-P, and (e) CF_4-P.

According to the previous reports, metal In/Sn and $In_2O_{x<3}/SnO_{x<2}$ species might be reduced during ITO sputtering process [223,241-244], which results in the lower binding energy peaks of the as-clean sample. Theoretically, H_2-P treatment would reduce ITO surface layer to either metals (In/Sn) or nonstoichiometric oxides ($In_2O_{x<3}/SnO_{x<2}$) [240]. Compared to the as-clean sample, however, no significant change in the bonding states of both In and Sn after H_2-P treatment was found in this study. This is likely because the reduced species are partially re-oxidized and/or hydrolyzed once the treated sample is exposed to the atmosphere. For Ar-P and O_2-P samples, the binding energies of In $3d_{5/2}$ (444.3 eV) and Sn $3d_{5/2}$ (486.3 eV) compare very well with those reported for oxides of In and Sn [97,246-248]. In this case, the two peaks correspond to the saturated oxidation states of the two metals, i.e., In^{3+} from In_2O_3 and Sn^{4+} from SnO_2, respectively [176,217,230].

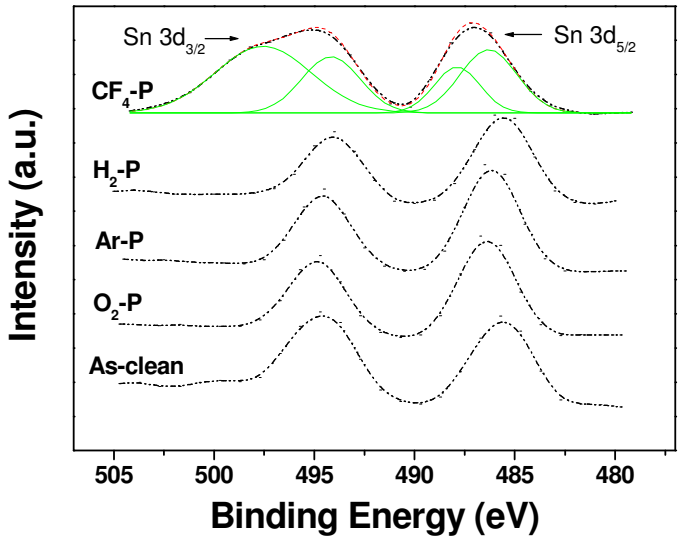

Figure 3.8 XPS spectra of Sn $3d_{5/2}$ and Sn $3d_{3/2}$ obtained from the ITO samples after different surface treatments. Each of the two spectra obtained from CF_4P treated sample is Gaussian-fitted with two sub-peaks.

More interestingly, CF_4-P treatment results in a *BE* shift (~ 0.5 eV) of In $3d_{5/2}$ and Sn $3d_{5/2}$ peaks to the higher energy band, compared to the O_2-P treatment. This is obviously related to the formation of In-F, especially Sn-F species, as F is more electronegative than O. This is further confirmed by deconvolutions of the Sn $3d_{5/2}$ and Sn $3d_{3/2}$ spectra, as shown in Figure 3.8. Compared with those obtained from other plasma treatments, the Sn 3d spectra obtained from CF_4 plasma-treated ITO are broad and each of them, especially the Sn $3d_{3/2}$, is clearly composed of two components at the lower and higher binding energies, corresponding to the metal oxides and the metal fluorides, respectively.

3.3.3 Surface Analysis by Cyclic Voltammetry

CV scans were carried out using a potentiostat (Solatron Instruments) and a standard three-electrode electrochemical cell. Ag/AgCl (3 M KCl) with electrode potential of 210

mV vs. NHE [185] was used as the reference electrode and Pt wire as the auxiliary electrode. The ITO working electrode area (0.93 cm^2) was defined by the size of a rubber o-ring. The CV data were obtained in a solution containing 0.1 M KNO_3 (supporting electrolyte) and 1.0 mM $K_4Fe(CN)_6$ (redox couples) at room temperature and a scan rate of 100 mV/s, and in a potential range from -200 to +800 mV. All potentials were reported with respect to Ag/AgCl (3M KCl). Before any CV scan, the electrolyte was nitrogen bubbled for 30 min to reduce the oxygen content in the electrolyte. More information about CV technique can be found in Section 2.3.

The voltammograms of the as-clean and plasma-treated ITO electrodes in a solution of 1 mM $[Fe(CN)_6]^{3-/4-}$ redox couple in 0.1 M KNO_3 supporting electrolyte are compared in Figure 3.9. Peak voltages and peak currents are summarized in Table 3.2. It is clearly seen that the electrochemical processes for all samples are irreversible because the peak potential separations ($\Delta E_p = E_{pa} - E_{pc}$) are much larger than 58 mV and the I_{pa}/I_{pc} ratio is smaller than unity. These findings clearly imply surface passivation by contamination or oxidation, which are discussed in details below. Compared with the CV data obtained from the as-clean ITO sample, peak potential separation is almost unchanged for the H_2-P sample, slightly decreased for the Ar-P sample, but significantly increased for the O_2-P sample and, in particular, the CF_4-P sample. Similarly, the peak current is also changed with the plasma treatments, but in the opposite way.

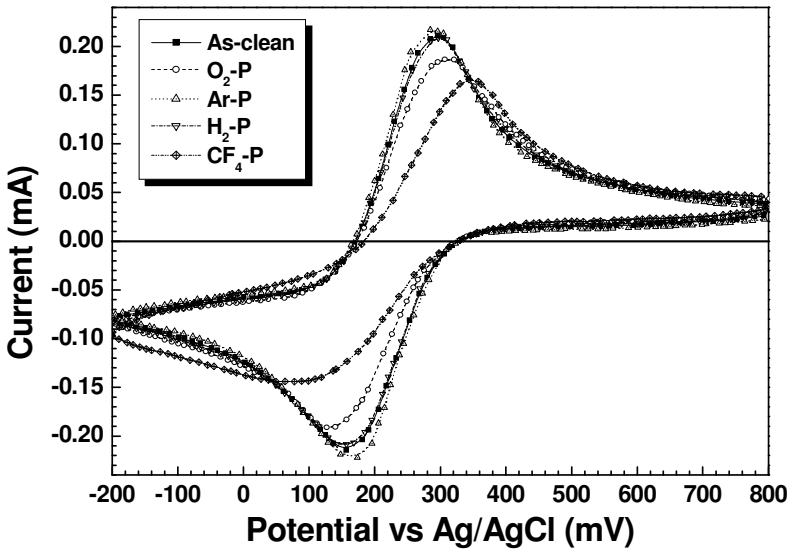

Figure 3.9 Cyclic voltammograms for ITO electrodes with different surface conditions: As-clean, Ar-P, H_2-P, O_2-P, and CF_4-P. Electrolyte: 1.0 mM $Fe(CN)_6^{3-/4-}$ in 0.1 M KNO_3. Reference electrode: Ag/AgCl (3 M KCl). Scan rate: 100 mV/s.

As well known, Faradic current depends on two things: the kinetics of electron transfer and the rate at which the redox species diffuses to the surface. There are three major causes for the irreversible behavior, viz., slow electron transfer kinetics, chemical reactions of redox couples, and uncompensated solution resistance. It is reasonable to assume that there is no chemical reaction of redox couples on the ITO surfaces during the CV scans. In this work, the operating conditions, such as electrolyte and redox couple, scanning rate, temperature, etc., were kept the same for all the ITO samples. The change in peak potential separation and peak current is therefore attributed to the different plasma treatments. In other words, plasma treatment is the only reason causing the change in electron transfer kinetics. It is simply noted that peak potential separation is a function of the rate constant for electron transfer, which decreases as redox couples are unable to reach the electrode surface.

Table 3.2. Summary of CV characteristics extracted and calculated from Figure 3.9, including peak anodic potential (E_{pa}), peak cathodic potential (E_{pc}), peak potential separation (ΔE_p) formal redox potential (E_{pa}+E_{pc})/2, peak cathodic current (I_{pc}), peak anodic current (I_{pa}), and I_{pa}/I_{pc} ratio.

ITO Sample	E_{pa} (mV)	E_{pc} (mV)	ΔE_p (mV)	$(E_{pa}+E_{pc})/2$ (mV)	I_{pa} (mV)	I_{pc} (mV)	I_{pa}/I_{pc}
As-Clean	298	157	141	227.5	0.217	0.239	0.908
O_2-P	321	130	191	225.5	0.196	0.215	0.912
Ar-P	283	165	118	224.0	0.230	0.245	0.939
H_2-P	300	158	142	229.0	0.215	0.236	0.911
CF_4-P	350	73	277	211.5	0.151	0.165	0.915

The reduced peak currents and increased peak potential separations in the cyclic voltammograms with the $Fe(CN)_6^{3-/4-}$ redox couple are possibly caused either by the partially blocking of ITO electrode surface or by hindering of the redox couple diffusion to the electrode surface. The XPS results have revealed that the as-clean ITO surface is contaminated by substantial amounts of adventitious carbon. In addition, the complete hydrolysis products of the ITO surface, i.e., $In(OH)_3$-like species, may not be strongly bound to the ITO lattice [214]. The presence of the hydrocarbon contaminants and the insulating hydroxides on ITO surface reduce the effective surface area for electron transfer. Liau and co-workers [212] also found that the ITO surface contains electrochemical "hot spots" and "dead regions", which are attributed to the inhomogeneous distribution of oxygen vacancies [213]. However, the electrochemical dead regions are obviously related to the areas covered by the insulating contaminants or hydroxides.

The XPS results in the previous section reveal that H_2-P is not effective in removing the hydrocarbon contaminants. This is further verified by the CV results, as no remarkable

change in cyclic voltammogram after H_2-P treatment was observed. In comparison, the reduced peak potential separation and increased peak current for the Ar-P sample imply the removal of the contaminants, at least to a certain extent, which is consistent with the results from XPS. However, the hydrocarbon recontamination owing to the exposure of sample to atmosphere may cover up the cleaning effect of the Ar-P treatment, as the difference in cyclic voltammogram between the as-clean and the Ar-P samples is not substantial.

On the contrary, the larger peak potential separation and lower peak current of the O_2-P and CF_4-P samples indicate that electron transfer rate at the ITO surfaces are notably suppressed by the two plasma treatments, especially the CF_4-plasma. It is obvious that the highly electronegative species in the plasmas, such as O and F atoms, can effectively remove the carbon contaminants and the hydroxides. Because of the same environment after plasma treatments for all samples, the lower electron transfer rates suggest that electrochemical "hot spots" have been destroyed by the oxidative plasma treatments. As above mentioned, the oxygen vacancies contribute to the good conductivity of ITO films [97,217]. However, the oxygen vacancies also imply the existence of $In_2O_{x<3}$ and $SnO_{x<2}$ species [176,230,239,240]. During O_2 and CF_4 plasma treatments, the reactive O and F are expected to react with the unsaturated oxides on the ITO surfaces and therefore decrease the oxygen vacancies, which therefore provide ITO surface with low conductivity due to the reduced free electrons [157]. In other words, the oxidative plasma treatments could result in an insulating oxide layer, which is clearly an obstacle against the electron transfer of the redox couple at the surface. In particular, the most electronegative F atoms could

more significantly remove the oxygen vacancies by etching of In and Sn at the ITO surface, and therefore lead to the lowest electron transfer rate.

Another cause for the sluggish electron transfer kinetics is the increase in negative charge of the ITO surface resulting from exposure of the surface to the oxidative plasmas [249]. The negative charge would repel the highly negatively charged $Fe(CN)_6^{4-}$ from the surface and further impede electron transfer. However, this negative surface charge speculation is short of supporting evidence, as both anodic and cathodic peaks are positioned in the positive potential region. Furthermore, it can be argued that the negative charges formed during oxygen plasma treatment due to the dangling bonds (e.g., In-$O^{\bullet}$ or Sn-$O^{\bullet}$) still exist once the ITO surface is in contact with the aqueous electrolyte [222]. In addition, the much larger peak potential separation caused by CF_4-P treatment in our study obviously do not support the negative surface change elucidation, because there are no dangling bonds available in the Sn-F or In-F species.

Interestingly, the peak cathodic current is larger than the anodic peak current for all samples, as shown in Table 3.2. The common phenomenon of the larger cathodic current in our CV experiments is speculated to be related to the double layer formed at the ITO-solution interface. Refer to Figure 2.7, when ITO electrode is positively polarized, negative charges in the electrolyte (NO_3^- in this study) will be accumulated on the electrode surface, forming a double layer. For redox reactions, $Fe(CN)_6^{4-}$ is oxidized into $Fe(CN)_6^{3-}$ by giving off an electron for anodic current, and $Fe(CN)_6^{3-}$ is reduced into $Fe(CN)_6^{4-}$ by capturing an electron for cathodic current. The negative charges of the

double layer repel more intensely against $Fe(CN)_6^{4-}$ than $Fe(CN)_6^{3-}$, leading to lower anodic current and higher cathodic current.

3.3.4 Contact Angle Measurements and Estimation of Surface Energy

The contact angle measurements are carried out using a Ramé-Hart contact angle goniometer (Model 100-22) by the sessile drop technique [208] at 20 ^oC and 60% relative humidity. At the first, a substrate placed on the sample stage of the goniometer, and a liquid drip of 0.045 cm^3 is delivered onto a horizontally oriented substrate from a micro-syringe placed at a fixed height approximately 2 cm above the sample. Contact angle measurements are carried out by magnifying the cross-section of the sessile drop by a traveling microscope with a miniature protractor eyepiece. In this process, digital images of the contact angles are obtained by a CCD camera fit into the ocular of the microscope. Images are captured after a minimum of 10 s to allow the liquid and solid surfaces to interact completely. Both the displayed left and right angles are recorded and the average of them is taken to be the characteristic contact angle of the liquid droplet. To minimize statistical variation, the characteristic contact angle is measured for five droplets per sample. The average of the characteristic contact angles is then used to calculate the surface energy being analyzed. The error associated with the contact angle measurements is $\pm 2^o$. Three samples for each treatment are prepared and the surface energy for the treated surface is the average value from the three samples.

The surface energy (γ_s), sum of the dispersive (γ_s^p) and polar (γ_s^p) components, are calculated based on the geometric-mean method [205]. DI water and glycerol (from Aldrich Chem. Co.) are used as the probe liquids in this work, and their respective surface tensions (γ) and the corresponding polar component (γ^p) and dispersive component (γ^d) are given in Table 3.3.

Table 3.3. Surface tensions (γ) and the corresponding polar component (γ^p) and dispersive component (γ^d) of water and glycerol, where γ is the sum of γ^p and γ^d.

Probe Liquid	γ^p **(mJ/m^2)**	γ^d **(mJ/m^2)**	γ **(mJ/m^2)**
Water	**51.0**	**21.8**	**72.8**
Glycerol	**26.4**	**37.0**	**63.4**

More information about the estimation of surface energy based on the contact angle data can be found in Section 2.4. Surface polarities (χ_p), defined as the ratio of the polar component (γ_s^p) to total surface energy (γ_s) [115], i.e., $\chi_p = \gamma_s^p / \gamma_s$, were also calculated.

3.3.4.1 Change in Surface Energy and Polarity with Plasma Treatments

Table 3.4 summarizes the contact angles, calculated surface energies and polarities of ITO samples treated with different plasmas. The details on estimation of surface energy by contact angle measurements have been described in Section 2.4. The results show that, γ_s

of ITO was remarkably increased by Ar-P, O_2-P and CF_4-P treatments, but slightly reduced by H_2-P treatment, compared to the as-clean ITO sample. It should be noted that the Ar-P, O_2-P and CF_4-P increase γ_s^p, in the order of CF_4-P>O_2-P>Ar-P, but decrease γ_S^d. On the contrary, H_2-P renders the highest γ_S^d and the lowest γ_s^p. CF_4-P yields the maximum χ_p of 0.87 and hydrogen plasma, on the opposite end, the minimum χ_p of 0.62, compared to 0.65 of the as-clean ITO.

Table 3.4. Contact angles, calculated surface energies and polarities for different plasma treatments of the ITOs. The total surface energy (γ_s) is the sum of the polar (γ_s^p) and dispersive (γ_s^d) components ($\gamma_s = \gamma_s^p + \gamma_s^d$) and the polarity ($\chi_p$) is the ratio of the polar component to the total surface energy ($\chi_p = \gamma_s^p/\gamma_s$).

Sample	**Contact angle (°)**		γ_s^p	γ_s^d	$\gamma_s=\gamma_s^p+\gamma_s^d$	$\chi_s=\gamma_s^p/\gamma_s$
	Water	Glycerol	(mJ/m^2)	(mJ/m^2)	(mJ/m^2)	
As-Clean	40.7	34.3	36.6	19.8	56.4	0.65
H_2-P	42.6	34.8	34.1	21.2	55.3	0.62
Ar-P	23.0	21.3	50.2	17.1	67.3	0.75
O_2-P	7.9	21.8	62.4	11.8	74.2	0.84
CF_4-P	11.9	27.3	65.1	9.5	74.6	0.87

3.3.4.2 The Factors Governing Surface Polarity

The results in Table 3.4 show that plasma treatments change ITO surface energy mainly through its polar component. It is interesting to understand how the plasma treatment changes the surface polarity. It is generally accepted that there are two origins of the polar component (γ_s^p) in surface energy (γ_s), the surface dipole and the hydrogen bonding. The

former is the predominating factor in influencing work function [222]. As-clean ITO surface is suspected to have various chemical species [128,232], such as M, M-O-M, M-OH, as well as CH_x, where M denotes metallic atoms (i.e., In and Sn in this study) and CH_x the organic contaminants. These species collectively contribute to the polar component in surface energy.

M-O-M bond is more hydrophobic [215] than its corresponding metallic bond due to its symmetric structure and resulting low polarity. Experimental studies showed that M-O-M has a tendency to be incompletely hydrolyzed [250-252]. Therefore, considerable quantities of OH groups are present on ITO surface, and have been estimated to be in the order of 1 OH group per 1 nm^2 of ITO surface [253]. The polarity of M-OH bond is believed to be in the same order of M, which is supported by the fact that work function of ITO is independent of dehydoxylation and rehydroxylation [222]. In addition, hydrogen bonds have considerable contribution to the ITO surface energy [130] due to the existence of oxygen-containing species, such as M-O-M and M-OH. In addition, contamination of ITO surface must be considered, which might also influence the ITO surface energy [115,120,122]. The organic contaminants are insulating and have lower polarity due to their more covalent bond features. A fractional coverage of ITO surface with such hydrocarbon contaminants will decrease surface energy through reducing the exposure of M-O-M and M-OH species.

For Ar plasma treatment, there should be no chemical reaction due to the inert property of Ar. However, decontamination effect of the Ar ion bombardment has been confirmed by the XPS results (as shown in Table 3.1). Although Ar plasma has also removed OH group

(i.e., dehydroxylation), the treated sample is easily rehydrolyzed in presence of water [222], leading to limited change in OH group concentration once exposed to humid air. Therefore, the increase in polarity after Ar plasma treatment can be attributed to the decontamination effect instead of dehydroxylation and rehydroxylation. An increase of about 37.2% in polar component of surface energy after Ar plasma, as shown in Table 3.4, indicates that the as-clean ITO surface used in this study is heavily contaminated. The decontamination by Ar plasma has been confirmed to promote hole injection [113,254,255], although it does not change work function [113,124,130].

When the reductive H_2 plasma is applied, physical adsorption of a hydrogen atom onto M-O-M surface may result in a negative dipole as well. As shown in Table 3.4, however, minor change of the surface polarity after H_2 plasma (lowered by only 0.3) implies that a fraction of M-O-M or M-OH has been reduced into M with higher surface energy that partially compensate the negative effect of the plasma treatment on polarity, which is supported by the lowest O:In ratio for the H_2-P sample, as shown in Table 3.1. This is further supported by the fact that the dispersive component of surface energy (γ_s^d) is raised after H_2 plasma, by about 1.4 mJ/m^2. Because the dispersive component of surface energy is directly related to London-van der Waals dispersion forces [199] that increase with the size of surface molecules/atoms in question [221], higher concentration of larger metals such as In and Sn firmly results in higher dispersive component of surface energy and lower work function due to the relative deficiency of oxygen atoms. Significant decrease in ITO work function by H_2 plasma treatment has been reported by several research groups [256-258].

In contrast, hydrocarbon contaminants on ITO surface can be effectively removed by the O_2 plasma treatment [255], which contributes to the high surface polarity for the same reason as the Ar plasma treatment. More importantly, O_2 plasma converts the M-OH or M-OOH into M-O$^{\bullet}$ through OH group oxidation chemistry [222]. Because M-O$^{\bullet}$ can be stabilized by ‘‘resonance’’ delocalization of unpaired spin density among lattice oxygen, it would be expected to be stable even in the presence of water [222]. As a consequence, this oxidation increases the ITO surface dipole layer, leading to higher polarity. Other hypotheses have also been proposed to explain the increase in polarity by the O_2 plasma treatment, such as adsorption of oxygen anions and water [122,130]. However, hydroxylation or dehydroxylation has been proved not to be a primary factor in determining the work function of ITO, which is related predominantly to surface dipole [222]. Therefore, the O_2 plasma treatment increases the surface polarity possibly through removing contaminants and producing highly polar and stable M-O$^{\bullet}$ species. It should be noted that this speculation has not been proven experimentally.

Compared to the case of O_2-P, CF_4-P is more effective for removing hydrocarbon contaminants from ITO surfaces. Furthermore, the XPS results show that the released fluorine atoms or ions during CF_4-P treatment produce M-F bond, as shown in Figure 3.5 and Figure 3.8. The higher negativity of F and asymmetric structure of M-F bond provide ITO surface with more positive dipole and stronger hydrogen bonding than M-O$^{\bullet}$, which might be the reason causing the highest surface polarity (χ_p) of 0.87, as shown in Table 3.4.

3.3.4.3 A Comparison with Si Sample

To further understand the influencing factors on surface polarity, Si wafer samples with 2 nm native oxide (SiO_2) were also treated by the same plasmas as described above and the surface energies are listed in Table 3.5.

Table 3.5. Surface energies and polarities of the Si wafer sample with 2 nm native oxide (SiO_2) and the ITOs after different plasma treatments. The total surface energy (γ_s) is the sum of the polar (γ_s^p) and dispersive (γ_s^d) components, i.e., $\gamma_s = \gamma_s^p + \gamma_s^d$, and the polarity ($\chi_p$) is the ratio of the polar component to the total surface energy, i.e., $\chi_p = \gamma_s^p/\gamma_s$.

Silicon Sample	**Contact angle (°)**		γ_s^p	γ_s^d	$\gamma_s=\gamma_s^p+\gamma_s^d$	$\chi_s=\gamma_s^p/\gamma_s$
	Water	Glycerol	(mJ/m^2)	(mJ/m^2)	(mJ/m^2)	
S1-Clean	23.0	21.3	50.2	17.1	67.3	0.75
S2-Ar-P	9.1	4.3	54.0	18.1	72.1	0.75
S3-H_2-P	23.0	25.3	53.3	14.5	67.8	0.79
S4-O_2-P	5.3	7.0	55.9	17.0	72.9	0.77
S5-CF_4-P	43.1	44.0	42.8	12.1	54.9	0.78

It was found surprisingly that unlike ITO, minor changes in surface polarity of SiO_2 were observed after various plasma treatments. As Si has the similar electronegativity (in Pauling scale) as those of In and Sn, i.e., 1.8 for Si vs. 1.7 for In and 1.8 for Sn, minor difference in permanent dipole should exist between Si-O-Si and In-O-In or Sn-O-Sn. This suggests that other factors also contribute to the formation of dipole layer and/or the surface polarity. Besides their crystal structures, the most significant difference between SiO_2 and ITO is that SiO_2 is an insulator but ITO a conductor with considerable amount of free electrons. Therefore, the high sensitivity of ITO surface polarity to plasma treatment is related to its high conductivity. Furthermore, poly-crystalline ITO contains more defects

than single crystal Si wafer, which may also influence the responsive behavior of ITO to plasma treatment.

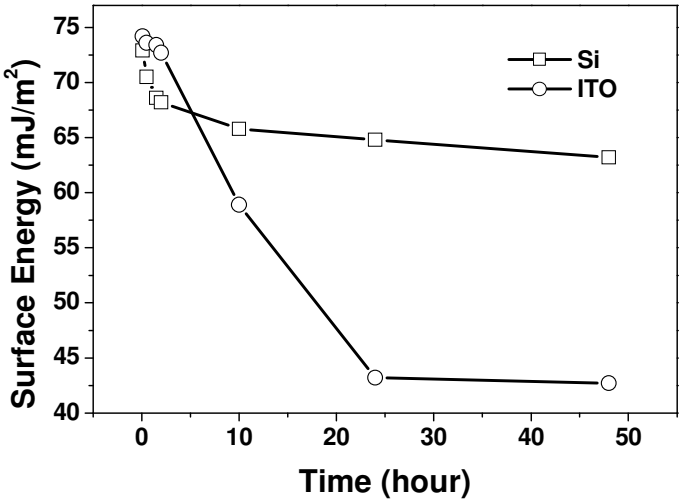

Figure 3.10 Dependence of surface energy on atmospheric exposing time after oxygen plasma treatment for Si wafer and ITO samples.

This speculation can be further verified by comparing ITO sample with Si wafer in surface energy decay with exposing time to the air, as shown in Figure 3.10. Compared with Si wafer, a greater drop in surface energy with time is detected for ITO sample, suggesting that ITO surface is inclined to the atmospheric carbon contaminants. The high energy defects on ITO surface are the preferential sites for adsorption of hydrocarbon molecules, leading to fast decay in surface energy. On the contrary, the surface energy decay of single crystal Si wafer is much slow due to its shortage of such high energy defects.

3.3.5 Effect of Plasma Treatments on Device Performance

3.3.5.1 Device Configuration and Fabrication

The ITO-coated glasses (Präzisions Glas & Optik GmbH, 20 Ω/) were routinely cleaned according to Section 2.5, followed by different plasma treatments as described in Section 3.2. Based on the as-clean and plasma-treated ITO substrates, the OLED devices with a configuration of ITO/NPB(60nm)/Alq_3(60nm)/LiF/Al [NPB=N,N'-bis(1-naphthyl)-N,N'-diphenyl-1,1'-biphenyl-4,4'-diamine and Alq_3=tris(8-hydroxyquinolato) aluminum] were fabricated by subsequent deposition of the functional layers using the conventional thermal evaporation technique at a pressure of 5×10^{-4} Pa. According to the ITO surface conditions, the fabricated OLED devices were denoted in the same way as Section 3.2, viz., as-clean, Ar-P, O_2-P, H_2-P, and CF_4-P, respectively. The deposition process starts with the evaporation of 60 nm thick NPB as the hole transport layer, followed by 60 nm thick Alq_3 as the electron transport and light emissive layer emitting in the green with a broad emission peaking at 530 nm [12]. The deposition rate for the two organic semiconductor layers is 0.2 nm/s. After the deposition of organic layers, a 0.6 nm thick LiF electron injection layer and a 150 nm thick Al layer were deposited immediately as the cathode at rates of 0.03 nm/s and 0.3 nm/s, respectively. The aluminum cathodes were deposited through a shadow mask to form devices with active area of 0.09 cm^2. The film thickness was monitored by a quartz thickness monitor. To ensure the valid comparison of the experimental results, all the functional layers were deposited successively on the differently treated samples during one vacuum run.

3.3.5.2 *L-I-V* Characteristics

Basic characterization of the OLED devices involved measuring the device luminance (L) having a unit of candela per square meter (cd/m^2) and current density (I) having a unit of milliamp per square centimeter (mA/cm^2) as a function of the applied voltage (*V*), viz., luminance-current-voltage (*L-I-V*). The voltage was supplied by a computer driven Keithley 2400 source using a linear staircase of 0.2 V with a 0.2 s delay between measurements, and the current was measured by a Keithley 2000 multimeter. The luminous output from the light emission area of 0.09 cm^2 was collected with a calibrated silicon photodiode. In addition, current efficiency having unit of candela per ampere (cd/A) and power efficiency (also called luminous efficacy) having unit of lumen per watt (lm/W), where lumen is SI unit of luminous flux and can be calculated by cd×sr, were obtained using the same system. All the *L-I-V* characteristics were carried out in a dark box and ambient atmosphere at room temperature.

Figure 3.11(a) and 3.11(b) show, respectively, the *I-V* and *L-V* characteristics of the devices with ITO substrates pre-treated by different plasmas. In comparison with the control sample (as-clean), both the *I-V* and *L-V* curves shift to the lower voltage region for the devices with ITO pre-treated by Ar-P, O_2-P and CF_4-P, but to the higher voltage region for the device with H_2-plasma treated ITO. For instance, the operating voltages at luminance of 200 cd/m^2 are 4.1, 5.6, 6.4, 7.0, and 7.2 V for the samples of CF_4-P, O_2-P, Ar-P, as-clean, and H_2-P, respectively.

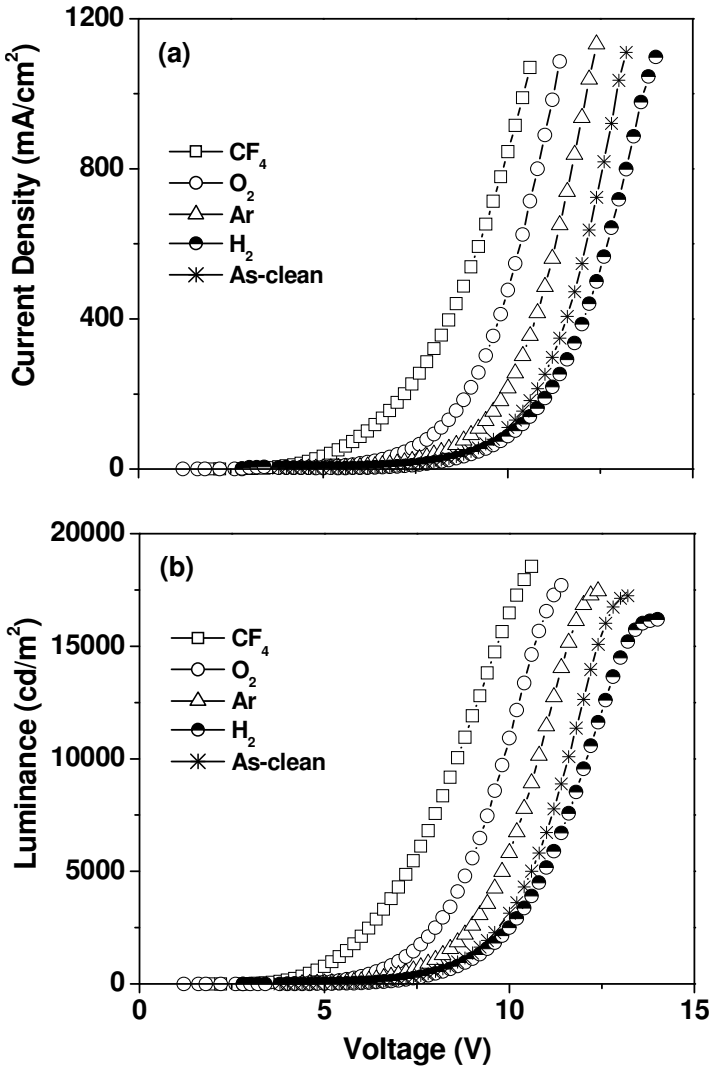

Figure 3.11 *I-V* (a) and *L-V* (b) characteristics of the OLED devices made with ITOs treated by different plasmas, with a device configuration of ITO/NPB(60nm)/Alq_3(60nm)/LiF/Al.

In the present study, *I-V* curve shift can be viewed as a direct indicator of the change of hole injection efficiency. The results in Figure 3.11(a) suggest that O_2 and CF_4-P treatments promotes the hole injection from ITO to HTL, while H_2-P treatment depressed the hole injection efficiency, which is consistent with the previous findings that reducing treatments increase the required drive voltage whereas oxidative treatments decrease it [124]. In comparison, Ar-P is moderately helpful to enhance the hole injection, which is

similar to the results reported by Wu et al. [113], although there were other reports showing the negligible or even negative effect [115,124].

Figure 3.12(a) shows the current efficiency (cd/A) versus current density (mA/cm^2) of the devices. Compared with the as-clean sample, current efficiency is in principle unchanged for Ar-P and H_2-P treatments, but lowered by O_2-P and CF_4-P treatments. For instance, at a given current density of ~30 mA/cm^2, current efficiencies of devices with as-clean, Ar-P, H_2-P, O_2-P, and CF_4-P treated ITO substrates are 2.88, 2.84, 2.80, 2.55 and 2.34 cd/A, respectively. It is interesting to note that these results do not agree with those reported in the literature [124], where current efficiency is raised by O_2-P and lowered by H_2-P.

In contrast to current efficiency, the power efficiency (lm/W) shows totally different effect, as shown in Figure 3.12(b). The device with CF_4-P treatment is prominent over the measurable current density range. At about 11 mA/cm^2, maximum power efficiencies are obtained for the devices with as-clean, Ar-P, H_2-P, and O_2-P treated ITO substrates in an order of O_2-P (1.25 lm/W) > Ar-P (1.22 lm/w) > as-clean (1.14 lm/W) > H_2-P (1.09 lm/W). However, the corresponding power efficiency for device with CF_4-P treatment is up to 1.67 lm/W which is ~34% higher than that of O_2-P, although the value is not the maximum point of power efficiency.

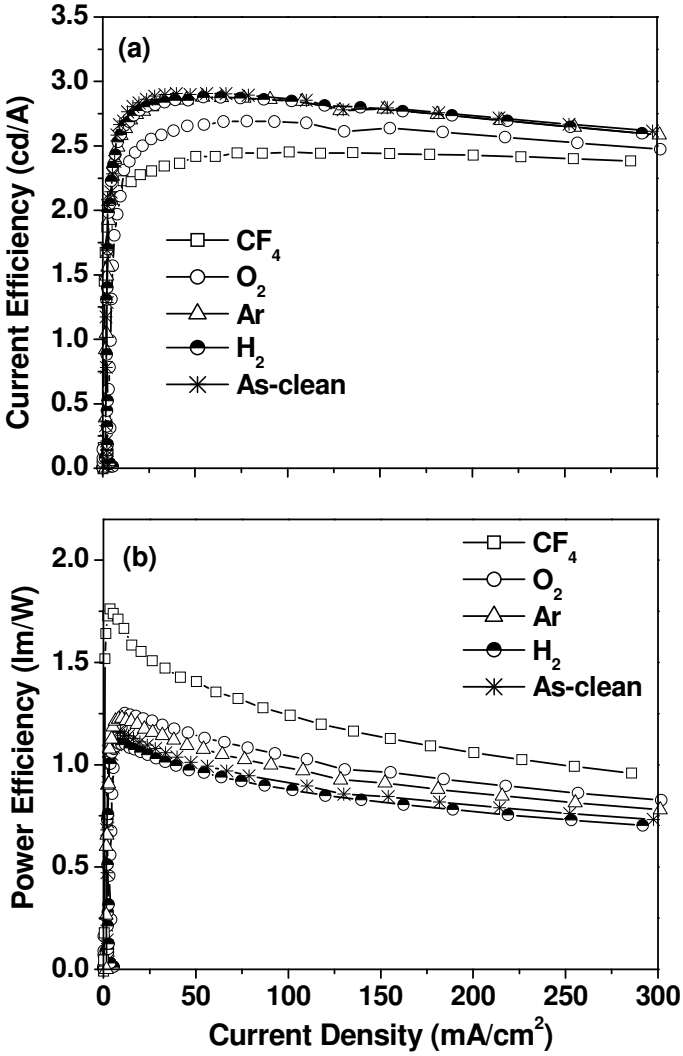

Figure 3.12 Current efficiency (a) and power efficiency (b) vs. current density curves of OLED devices made with ITOs treated by different plasmas, with a device configuration of ITO/NPB(60nm)/Alq_3(60nm)/LiF/Al.

For an electron injection limited device, excess hole injection will contribute to the device current but not the electron-hole recombination, leading to a lower current efficiency. The significant decrease of the operating voltage by the O_2-P and CF_4-P treatments of ITO indicates a remarkable improvement of hole injection, as shown in Figure 3.11. A comparison between Figure 3.11(a) and Figure 3.12(a) shows that the devices in this study are electron injection limited, as hole injection was improved by O_2-P and CF_4-P

treatments at the expenses of current efficiency. Therefore, the excess hole injection should be responsible to the lower current efficiencies due to the unbalanced charge injection and/or the recombination zone shift closer to the Al cathode [143]. For a hole injection limited device, the influence of plasma treatments on efficiency may be concluded differently, where the treatments raising hole injection should enhance the current efficiency of OLED devices. This may explain the controversial reports in literatures on the dependence of efficiency upon the same surface treatment.

Power efficiency is another important performance indicator of OLED devices. It is clear that with the same luminance, power efficiency depends on not only the current density but also the driving voltage. Lowered driving voltage can significantly raise power efficiency, which causes the difference between current and power efficiencies in this study, as shown in Figure 3.12(a) and Figure 3.12(b), respectively. For instance, compared with the as-clean sample, the operating voltage (at 200 cd/m^2) after CF_4-P treatment is reduced by about 2.9 V. The considerable drop of driving voltage overwhelms the negative effect from the excess hole injection, leading to significant increase of power efficiency from 1.14 lm/W to 1.67 lm/W, or ~46%.

3.3.5.3 Effect of Surface Properties on Hole Injection

The AFM results in Section 3.3.1 have revealed that the plasma treatments under the operating conditions used in this study do not result in measurable change of the ITO surface morphology. XPS results in Section 3.3.2 show that the plasma treatments have significant effects on the ITO surface chemical states, which was further verified by the

CV results in Section 3.3.3. As discussed in Section 3.3.4, the concentration of polar species, such as OH, M-O•, and M-F dominates the surface energy (γ_s), especially its polar component (γ_s^p), and therefore the surface polarity ($\chi_p = \gamma_s^p/\gamma_s$). Refer to Table 3.4, the calculated surface polarities of the different samples are in the sequence of CF_4-P(0.87) > O_2-P(0.84) > Ar-P(0.75) > as-clean(0.65) > H_2-P(0.62). Compared to the *I-V* curves in Figure 3.11(a), the sequence in surface polarity is surprisingly identical to that of hole injection efficiency. In comparison, the ranking in operating voltage at luminance of 200 cd/m^2 are exactly conversed, viz., CF_4-P(4.1V) < O_2-P(5.6V) < Ar-P(6.4V) < as-clean(7.0V) < H_2-P(7.2V). This suggests that hole injection of the OLED devices in this study is controlled by the ITO surface polarity.

In the OLED device fabrication, the hole transport material, NPB, is first deposited onto an ITO surface, and the ITO/NPB interface comes into being. As described in Section 3.3.5.1, the cathode for electron injection was the same in all the devices based on the different ITO substrates, and the devices were fabricated in the same batch. The marked changes in hole injection are obviously attributed to the plasma treatments that have modified the ITO surfaces and then the ITO/NPB interfaces. O_2-P and CF_4-P significantly increase the surface polarities, which is expected to enhance hole injection through improving the adhesion of NPB onto the ITO surfaces and then forming good electric contacts [115]. This speculation will further be verified in Chapter 6 and discussed in Chapter 7.

3.5 Conclusion

In this chapter, the plasma-treated ITO surfaces were investigated in morphology, surface composition and chemical states, electron transfer kinetics, and surface energy by AMF, XPS, CV, and contact angle goniometer, respectively. OLED devices based on the plasma treated ITO, in a structural configuration of ITO/NPB(60nm)/Alq_3(60nm)/LiF/Al substrates, were also fabricated and characterized in luminance and electrical properties. The effect of plasma treatments on ITO surface properties and thus the hole injection efficiency across ITO/NPB interface, as well as their relations were discussed.

AFM observations showed that the rms roughness values measured by AFM fall in the range of 3-4 nm for all plasma treated ITO samples, being similar with the as-clean ITO. The surface morphology is also not sensitive to the plasma-treating time in the range of 0-10 min. XPS analysis revealed that as-clean ITO sample was heavily contaminated by substantial amounts of adventitious hydrocarbon. The H_2-P treatment could not remove the carbon contaminants, but the Ar-P treatment was moderately effective for carbon decontamination. In comparison, O_2-P was extremely effective to remove the adventitious hydrocarbon. For CF_4-P treatment, carbon recontamination was not observed but new carbon species were found on the ITO surface. High O:In ratios on the O_2-P and CF_4-P ITO surfaces were attributed to surface oxidation and etching, respectively. The resulted polar surface species make the ITO surface less conductive, which was further verified by CV scans.

Based on the contact angle measurements, the calculated surface polarities on the different plasma treated samples are correlated to the hole injection efficiency of the OLED devices. More specifically, the higher the surface polarity, the higher the hole injection efficiency. The plasma treatments modify the ITO surfaces and then the ITO/NPB interfaces. O_2-P and CF_4-P significantly increase the surface polarities, which is expected to enhance hole injection through improving the adhesion of NPB onto the ITO surfaces and then forming good electric contacts.

Chapter 4

Electrochemical Treatment

Abstract

In this chapter, a brief overview on various ITO surface treatment processes for enhancement of hole injection efficiency, with the emphasis on stability issues, is first given. A new surface treatment method using electrochemical process is then proposed for hole injection improvement, with optimized treating parameters. Surface properties of the electrochemically treated ITO substrates are characterized in terms of morphology, surface composition and chemical states, electron transfer kinetics, as well as surface energy, with help of AFM, XPS, CV, and contact angle goniometer. OLED devices based on the electrochemically treated ITO surfaces, in configuration of ITO/NPB(60nm)/Alq_3(60nm)/LiF/Al, are fabricated and characterized in term L-I-V behaviors and electroluminescence (EL) efficiencies. The aim of the present work is to understand the dependence of ITO surface properties on treatment parameters and their influence on device performance. The results show that surface composition and surface energy are sensitive to the treatment applied voltage. Substantial improvement in hole injection and EL efficiencies was observed in devices based on the electrochemically pre-treated ITO substrates at an optimized treatment voltage. The mechanisms behind this performance enhancement were discussed.

4.1 Introduction

In Chapter 3 it was found that total surface energy of ITO was changed considerably by plasma treatment through its polar component, and the polar component of the ITO surface energy is affected more significantly than the dispersion component by oxygen plasma treatment. We therefore proposed that oxidative plasma treatments, such as O_2-P and CF_4-P, significantly increased the ITO surface polarity via decontamination and formation of more dipolar species. The plasma surface treatments demonstrate their effectiveness, to a certain extent, in improving device performance. According to the previous report, however, the plasma treated ITO surfaces are highly sensitive to the environment. For example, the increased work function due to plasma treatment decays over time and returns to its original value within hours [120,128,259]. In fact, the surface instability is a common problem observed for all the surface treatments reported so far. For those surface treatments reported using chemical means [256,260,261], their effectiveness was found to be very sensitive to the type and the concentration of the solutions used, leading to difficulties in consistency and efficiency for process control. The limitations of the reported processes in reproducibility and stability of the resulting surfaces suggest that more effective and robust processes are required for ITO surface treatment.

In this chapter, we report an electrochemical method for the surface modification of ITO film. Surface morphology, chemical composition, electron transfer kinetics and surface energy of the electrochemically treated ITO films are characterized by AFM, XPS, CV, and contact angle goniometer, with an emphasis on the correlation between the surface

properties and the treatment voltages. OLED devices based on the electrochemically treated ITO surfaces, with configuration of ITO/NPB(60nm)/Alq_3(60nm)/LiF/Al, are fabricated and characterized in term L-I-V behaviors and electroluminescence (EL) efficiencies. The aim of the present work is to understand the dependence of ITO surface properties on treatment parameters and their influence on device performance. The results show that surface composition and surface energy are noticeably sensitive to the treatment voltage. The performance of OLEDs can be significantly improved when the electrochemically treated ITO at an optimized treatment voltage is used as the anode material. The device turn-on voltage has been remarkably reduced and the EL efficiency has been notably increased, in comparison with the corresponding devices fabricated with the untreated ITO film.

4.2 Experimental

Electrochemical treatment was performed in the same electrochemical processing system used for CV test, as illustrated in Figure 2.7, but the counter electrode in this case is a Pt plate with an active area of 30X30 mm^2. ITO glass sheet (25X25 mm) with an exposed area of 0.93 cm^2, defined by the size of a rubber o-ring, was used as the working electrode. The ITO sheet and the Pt counter electrode were arranged in parallel and the distance between the two electrodes was kept in 10 mm. The electrolytes were 0.1 M aqueous solutions of NaCl, KCl, NaOH, Na_2CO_3, Na_2WO_4, Na_3PO_4, $K_4P_2O_7$, and $Na_4P_2O_7$. The applied voltages were set and reported vs. NHE.

At the first, the electrolyte and potential window were screened out for the electrochemical treatments with criteria of low water contact angle and invisible morphological change on the treated ITO surfaces, by using goniometer and AFM, respectively. After the screening work, the ITO samples were positively polarized in the selected electrolyte for 30 s at varied voltages from 1.2 to 2.8 V with a interval of 0.4 V, denoted as ECT+1.2V, ECT+1.6V, ECT+2.0V, ECT+2.4V, and ECT+2.8 V, correspondingly. An ITO sample was immersed in the selected electrolyte under the same working conditions without polarization (denoted as ECT+0.0V) to serve as the control for comparison. All the treated samples were thoroughly rinsed, via sonication in DI water, to remove the residual electrolyte, before the final drying by blowing with nitrogen.

The electrochemically treated samples were then characterized in terms of morphology by AFM, chemical bonding status by XPS, electron transfer kinetics by CV, and surface energy by contact angle methods. OLED devices based on the electrochemically modified ITO substrates, in configuration of ITO/NPB(60nm)/Alq_3(60nm)/LiF/Al, were fabricated and characterized in terms of L-I-V behaviors and EL efficiencies. The detailed information on the experimental procedures for ITO sample pre-cleaning, surface property characterization, as well as device fabrication and characterization are similar to those in Chapter 3.

4.3 Results and Discussion

4.3.1 Selection of Electrolyte and Potential Window

Table 4.1 summarized the contact angles (with probe liquid of DI water) of ITO samples positively polarized at a voltage of 2 V for 30 s in 0.1 M electrolytes of NaCl, KCl, NaOH, Na_2CO_3, Na_2WO_4, Na_3PO_4, $K_4P_2O_7$, and $Na_4P_2O_7$, respectively. θ_0 in the table denotes the water contact angles measured instantly after the treatments, and θ_{24} the values obtained after keeping of 24 hours in air. The angle difference between the two measurements, $\Delta\theta = \theta_{24} - \theta_0$ was also calculated and listed in the table.

Table 4.1. Contact angles (with probe liquid of DI water) measured on the electrochemically-treated ITO surfaces at +2 V in different electrolytes and with different keeping time after the treatments.

Contact Angle (^{o})	**As-Clean**	**KCl**	**NaOH**	**Na_2CO_3**	**Na_2WO_4**	**Na_4PO_4**	**NaP_2O_7**	**$K_4P_2O_7$**
θ_0	**41.0**	**29.8**	**13.0**	**19.5**	**13.6**	**13.6**	**<5***	**<5***
θ_{24}	**41.5**	**34.0**	**48.0**	**40.0**	**33.0**	**35.5**	**25.0**	**15.5**
$\Delta\theta$	**0.5**	**4.2**	**35.0**	**20.5**	**19.4**	**21.9**	**20.0**	**10.5**

*Note: The measurable limit of the contact angle goniometer used in this study is 5^o, and the value was used for calculation of $\Delta\theta$ in the cases of $K_4P_2O_7$, and $Na_4P_2O_7$.

The contact angles of the ITO surfaces measured immediately after the electrochemical treatment varied from 5 to 29.8^o, with the maximum from KCl and the minimum from both $Na_4P_2O_7$ and $K_4P_2O_7$, which are significantly lower than that of the as-clean sample (41^o). This result suggests that electrochemical treatment is an effective method for improvement

of ITO surface hydrophilicity or wetting property that is an important factor affecting the adhesion between a thin film and the substrate. Considering the ability to reduce contact angle, the electrolytes listed in the table can be ranked in descending sequence as $Na_4P_2O_7$ = $K_4P_2O_7$ > NaOH > Na_4PO_4 = Na_2WO_4 > KCl. It can be seen that electrochemical treatments at +2 V in both $Na_4P_2O_7$ and $K_4P_2O_7$ electrolytes results in a contact angle less than 5^o, which implies that pyrophosphate anions may take a role in the treatment. Contact angle decay, $\Delta\theta = \theta_{24} - \theta_0$, provides the direct evidence about the stability of the corresponding treated surface. A comparison in contact angle decay ($\Delta\theta$) demonstrates that $K_4P_2O_7$ is a superior electrolyte, by the smallest θ_0 and $\Delta\theta$. Therefore, 0.1 M $K_4P_2O_7$ electrolyte will be selected for electrochemical treatment of ITO surfaces and the electrochemical experiments in the later part of the chapter are all based on the selected electrolyte.

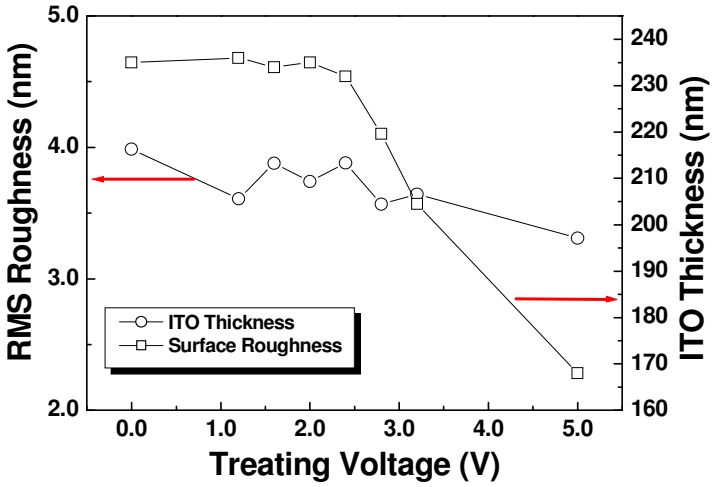

Figure 4.1. Changes in thickness and roughness of ITO films electrochemically treated at varying voltages in 0.1 M $K_4P_2O_7$ electrolyte.

ITO samples were electrochemically treated in 0.1 M $K_4P_2O_7$ by varying voltage from 0 to +5 V. The thickness and RMS roughness of the treated ITO surfaces were measured by

using ellipsometry and AFM, respectively, and plotted versus the treatment voltages in the Figure 4.1. It can be seen that the values of rms roughness for all the samples fall in a range from 4.0 nm for 0V to 3.3 nm for +5 V. Although the fluctuated changes in roughness with treatment voltage, a down trend in the gross can be observed with increasing voltage. However, the variation in surface roughness is not significant enough to differentiate the treatment voltages, because the measurements for the untreated ITO films drop in the same range, i.e. 3-4 nm. On the other hand, thickness measurements present a different scenario, where the changes in thickness are trivial for the samples treated at a voltage below +2.4 V, but considerable when a higher voltage is applied. More specifically, the measured variation of thickness is within 4 nm for the samples treated at voltages in between 0 and +2.4V, but as high as 64 nm of thickness reduction was found when the treatment voltage was increased from +2.4 V to +5.0 V. This result implies a noticeable etching of the ITO films, which has been verified in both low and high pH value solutions [111a,111b]. It is believed that ITO is etched in acidic (e.g., HCl) solutions through the breaking of surface bounds without change in the metal valence state, rather than by a reduction mechanism [112,262], which has widely used for ITO patterning. However, the electrolyte used in this study is basic in nature, suggesting that DC sputtered polycrystalline ITO film is electrochemically unstable even in basic solution. This is further supported by AFM observation.

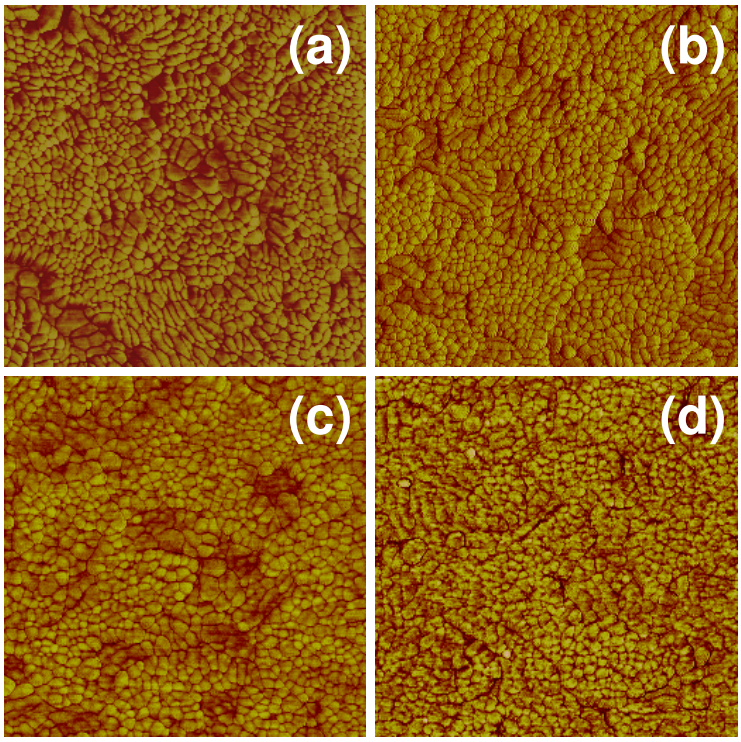

Figure 4.2. AFM (phase mode) images of ITO surfaces electrochemically treated at 0 V (a), +2.0 V (b), +2.8 V (c), and +3.2 V (d) in 0.1 M $K_4P_2O_7$ electrolyte. The scan area is 1×1 μm^2.

AFM phase mode (see Section 2.1) images of the ITO surfaces electrochemically treated at 0, +2.0, +2.8, and +3.2 V were obtained using a Digital Instruments Nanoscope IIIA AFM and shown in Figure 4.2. Compared with the untreated ITO sample, no significant change in grain-subgrain textures [95,99] (Refer to Section 1.3.2 for details) is observed for the sample treated at +2.0V. It seems that the subgrains are slightly leveled after the treatment. However, the grain-subgrain textures on ITO surface are trailing off after the treatment at +2.8 V, even disappearing when a voltage of +3.2 V is applied. The AFM observations are consistent with the measurements in RMS roughness and thickness, shown in Figure 4.1. These results demonstrate that ITO surfaces were electrochemically etched at treatment voltages of $\geq$ +2.8 V.

4.3.2 Surface Analysis by XPS

XPS was used to characterize the chemical compositions and states of ITO surfaces pre-treated by electrochemical process. The C 1s binding energy (~285 eV) of atmospheric carbon contaminants was used as a reference [176] to calibrate the spectra obtained from the electrochemically treated ITO surfaces. The XPS experimental details are similar to Section 3.3.2.

4.3.2.1 XPS Spectra and Chemical Compositions

Wide-scan XPS spectra (from 100 to 800 eV) of the untreated and electrochemically treated ITO substrates are shown in Figure 4.3. Ssignificant photoelectron peaks at the BEs of 530, 445, 486, and 285 eV, corresponding to O 1s, In $3d_{5/2}$, Sn $3d_{5/2}$, and C 1s core-level signals, respectively, are clearly detected. Other peaks, such as In $3d_{3/2}$, In $3p_{3/2}$, Sn $3d_{3/2}$, Sn $3p_{3/2}$, as well In 4s, are also marked for reference. More importantly, weak peaks (displayed as insets in the figure) at about 133, 292, and 295 eV are detected on some surfaces, which are assigned to P $2p_{3/2}$, K $2p_{3/2}$ and K $2p_{1/2}$, respectively.

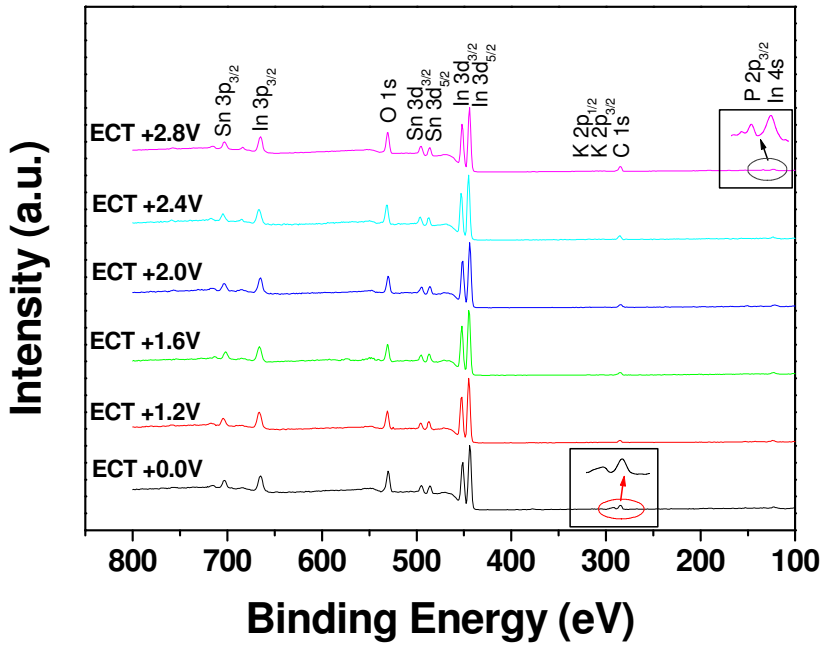

Figure 4.3. Wide-scan XPS spectra of ITO surfaces electrochemically treated at varying voltages in 0.1 M $K_4P_2O_7$ electrolyte.

With the assumption that the ITO surface was homogeneous in chemical composition within the XPS sampling area and depth, the chemical compositions of various ITO surfaces were calculated by using the core level peak areas and their relative sensitivity factors. In practice, the calculation work was carried out by a build-in program of the XPS system. Table 4.2 summarizes the XPS analysis results of these spectra obtained from ITO surfaces pre-treated at different voltages, in terms of the atomic concentration and ratios. The results clearly show the changes in surface composition after the electrochemical treatments.

Carbon content changes from 16.4% of the sample without imposing voltage (i.e., ECT+0.0V) to 11.3, 12.6, 12.7, 15.5 and 20.6 % after electrochemical treatments at voltages between +1.2 and +2.8 V with an interval of 0.4 V, respectively. The relative

oxygen content was increased from 49.4% of ECT+0.0V to 51.6, 53.5, 54.0, 55.3 and 50.7%, correspondingly. Notably, it was found that element P was found on both ECT+0.0V and ECT+2.8V, but element K on ECT+0.0V only.

Table 4.2. Changes in surface atomic concentrations (derived from the relative XPS O 1s, Sn $3d_{5/2}$, In $3d_{5/2}$, C 1s, P $2p_{3/2}$, and K $2p_{3/2}$ spectral area ratios) for ITO substrates electrochemically treated at different voltages in 0.1 M $K_4P_2O_7$ electrolyte.

ITO	Chemical Composition in at.%						Ratios	
Sample	O	In	Sn	K	P	C	In:Sn	O:In
ECT+0.0V	49.4	25.7	2.7	3.6	2.4	16.4	9.72	1.92
ECT+1.2V	51.6	32.7	3.4	-	-	11.3	9.69	1.61
ECT+1.6V	53.5	30.7	3.2	-	-	12.6	9.54	1.74
ECT+2.0V	54.0	30.2	3.2	-	-	12.7	9.52	1.79
ECT+2.4V	55.3	26.4	2.9	-	-	15.5	9.19	2.10
ECT+2.8V	50.7	24.2	2.8	-	1.8	20.6	8.50	2.10

The XPS analysis reveals that the electrochemical treatment is an effective method to remove the adventitious carbon contaminants adsorbed on the ITO surfaces. The high O:In ratio on the ECT+0.0 surface is attributed to the presence of the pyrophosphate contaminant. The O:In and O:Sn ratios increase with the treatment voltage, implying the presence of unsaturated oxidation states of In and Sn on the pristine ITO surface, such as $In_2O_{x<3}$ and $SnO_{x<2}$, as reported by other research groups [176,230,239,240]. Another reason causing the increase in O:In and O:Sn ratios is electrochemical etching. Furthermore, the decrease in In:Sn ratio with moving up the treatment voltage suggests that more In than Sn atoms were etched out from the ITO surfaces by the electrochemical process. In particular, the In:Sn ratio decreases from 9.71 of ECT+0.0V to 8.50 of ECT+2.8. The electrochemical etching leads to remarkable change in topography of the ITO surface, as shown in Figure 4.2.

It should be noted that such a chemical composition analysis is too coarse to provide good understanding of the surface properties. For example, possible contributions to the measured oxygen content on the ITO surface include ITO, metal hydroxides, carboxylic compounds, water, as well as phosphates as contaminants or new chemical species. Therefore, the information disclosed by the atomic percentages is limited. However, the atomic composition is helpful for investigating the chemical bonding status when it is used in combination with the analysis of chemical shifts.

4.3.2.2 Analysis of Surface Contamination

As shown in Table 4.2, a large amount of carbon was detected for all the electrochemically-treated ITO samples. The presence of carbon residues is inevitable because the electrochemical treatments were carried out in the ambient. Furthermore, the treated samples were exposed to the atmosphere prior to XPS analysis, as in the case of plasma treatments. Compared with the E+0.0V sample, the carbon decontamination by the electrochemical treatments at voltages from +1.2 to +2.4 V is discernible, but not significant. This is obviously related to the recontamination of the electrochemically treated ITO samples. In comparison, ECT+2.8V sample surface adsorbs more carbon contaminants, which can be attributed to the existence of P-containing compounds.

According to previous reports, oxidative treatments such as oxygen plasma and UV-ozone are effective processes for removing the carbon contaminants adsorbed on the ITO surfaces [93,113,222]. For electrochemical treatments, the carbon decontamination is clearly related

to the high density of oxygen released from the positively polarized ITO surface. A similar electrochemical decontamination was also reported by Comninellis et al [263,264], where SnO_2 was used as an anode for waste water treatment. They observed that organic pollutants were destroyed by electro-oxidation at a potential more positive than 1.0 V against SCE.

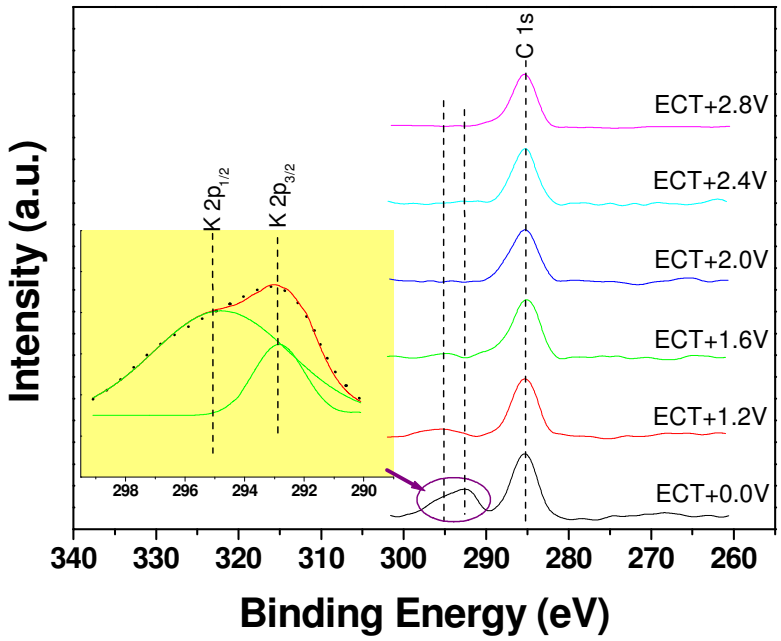

Figure 4.4. XPS C 1s, K $2p_{3/2}$ and K $2p_{1/2}$ spectra of the ITO surfaces electrochemically treated at different voltages in 0.1 M $K_4P_2O_7$ electrolyte, normalized to the spectrum of ECT+0.0V sample.

Figure 4.4 shows that besides the main peak at about 285 eV that serves as a BE reference, a weak and broad higher energy component with BE > 290 eV is also discernible for ECT+0.0V. The wider and asymmetric peak is obviously due to spectra overlap. The peak was Gaussian-fitted using two sub-peaks at 295.1 and 292.9 eV, being assigned to K $2p_{1/2}$ and K $2p_{3/2}$ ($K_4P_2O_7$) [174], respectively. The presence of $K_4P_2O_7$ on ECT+0.0V surface is supported by the fact that P $2p_{3/2}$ peak (at the BE of 132.6 eV) were detected on the same sample, as shown in Figure 4.5. The adsorbed $K_4P_2O_7$ [265] contaminant originates from

the electrochemical treatment solution, most likely due to the insufficient rinsing after the treatment (i.e., immersing without applied voltage).

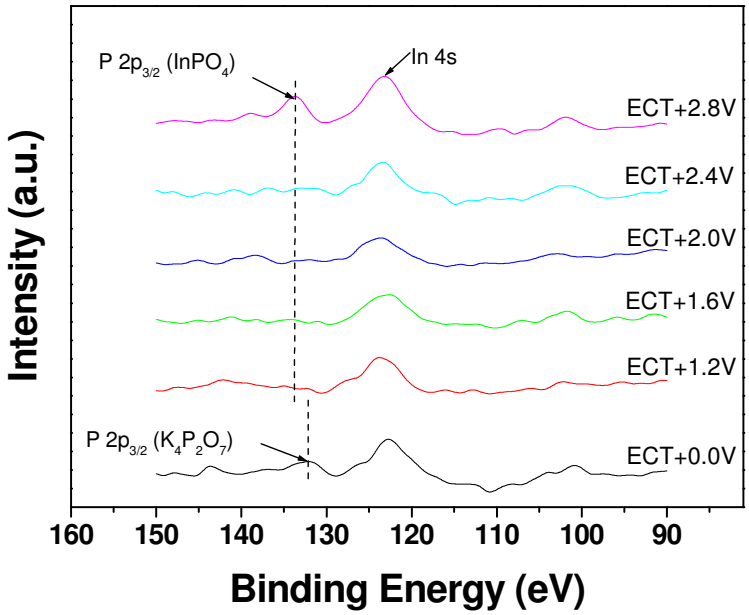

Figure 4.5. XPS In 4s and P $2p_{3/2}$ spectra of the ITO surfaces electrochemically treated at different voltages in 0.1 M $K_4P_2O_7$ electrolyte.

A comparison between Figure 4.4 and Figure 4.5 shows that the P $2p_{3/2}$ peak (at 134 eV) is also discernible for ECT+2.8V, but no K signal was detected on the sample surface. This suggests that a new P-containing compound rather than $K_4P_2O_7$ was formed on the ITO surface. Compared with ECT+0.0V, the P $2p_{3/2}$ peak had shifted about +1.4 eV (from 132.6 to 134 eV), indicating that $InPO_4$ could have been formed [266].

4.3.2.3 Elucidation of Oxygen Content and O 1s Spectra

Figure 4.6 shows the O 1s spectra detected from the ITO surfaces after electrochemical treatment at different voltages, normalized to the spectrum of ECT+0.0V sample. Two O

1s peaks were found, one positioned at the lower BE (about 530 eV) for all the samples, the other at the higher BE (about 531.5 eV) for ECT+0.0V and ECT+2.8V samples only. The O 1s peak at 530.1 eV is derived from the O bonded to In and/or Sn atoms (i.e. bulk ITO), as discussed in Chapter 3. The O1s peak at higher binding energy for ECT+0.0V and ECT+2.8V samples is obviously attributed to the existence of phosphates, as P is more electronegative than In an Sn. Compared with ECT+0.0V sample, the O 1s peak at higher BE for ECT+2.8V is shift slightly (about +0.4 eV) to the higher energy band, likely due to the higher Pauling-scale electronegativity of In (1.7) than K (0.9).

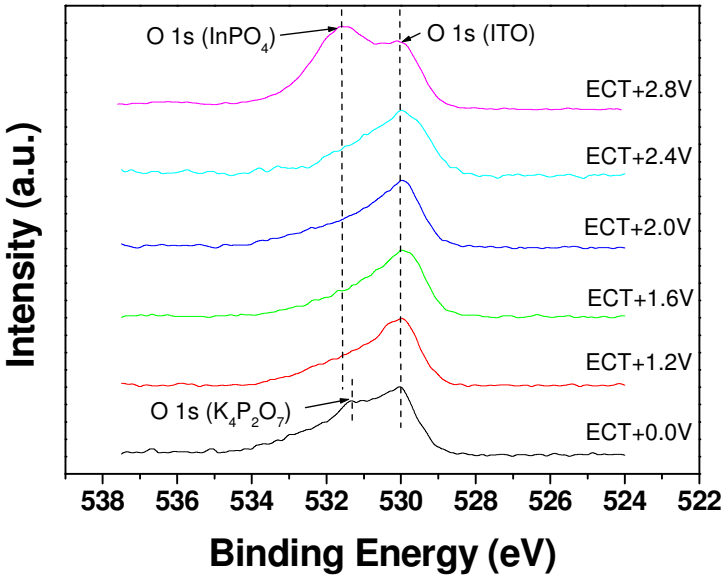

Figure 4.6. XPS O 1s spectra of the ITO surfaces electrochemically treated at different voltages in 0.1 M $K_4P_2O_7$ electrolyte, normalized to the spectrum of ECT+0.0V sample.

From Figure 4.6, it is also noted that all the O 1s spectra are asymmetric and their long tails extend to higher BE bands, indicating more oxygen-containing species are included besides those from phosphates and ITO, which is similar to those in the case of plasma treatments. However, their assignments are difficult due to the extensive overlap of the corresponding O 1s spectra. As the aqueous electrolyte was used for the electrochemical

treatment, it was unavoidable for H_2O to be present on the ITO surfaces in a form of either molecular absorbent or metallic hydroxides (i.e., In-OH and Sn-OH species) [233,234]. As the electronegativity of element H is 2.1 (in Pauling-scale), which is higher than those of In and Sn, the BEs of O 1s peaks for H-O-H, In-O-H, and Sn-O-H are expected to be located at higher BE regions than that for pure ITO (BE = 530.2 eV). For example, BEs from 532.1 to 533 eV have been attributed to the oxygen in hydroxyl groups at ITO surface as well as adsorbed water [97,158,236,237]. Nevertheless, the high energy extension of O 1s peaks in this study is mainly due to the existence of O-H bonds on the ITO surfaces.

4.3.2.4 Oxidation States of In and Sn Atoms

The In $3d_{5/2}$ and Sn $3d_{5/2}$ core-level spectra for the electrochemically pre-treated ITO samples are shown in Figure 4.7. The results show that the In $3d_{5/2}$ and Sn $3d_{5/2}$ peaks measured from ECT+0.0V and ECT+1.2V samples are located at the lower BEs of 443.6 and 485.7 eV, respectively, corresponding to the metal In and Sn, as well as the nonstoichiometric oxide species (e.g., $In_2O_{x<3}$ and $SnO_{x<2}$) [176,230,239,240]. The shoulders on the higher BE bands for the two samples are attributed to In_2O_3 and SnO_2 [239,240]. According to the previous reports [223,241-244], metal In/Sn and $In_2O_{x<3}$ and $SnO_{x<2}$ might be reduced from ITO during sputtering process, which results in the lower binding energy peaks of ECT+0.0V and ECT+1.2V samples. The similarity in spectral lineshape from the two samples suggests that the electrochemical pretreatment at voltages $\leq$ +1.2 V did not change the oxidation states of In/Sn atoms on the ITO surface in this work.

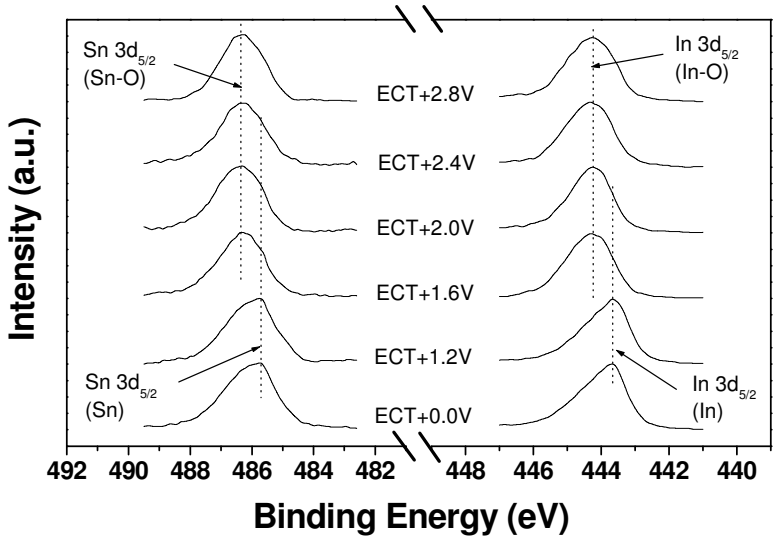

Figure 4.7. XPS spectra of Sn $3d_{5/2}$ and In $3d_{5/2}$ for ITO surfaces electrochemically treated at different applied voltages in 0.1 M $K_4P_2O_7$ electrolyte.

When the treatment voltage is higher than +1.6 V, the peaks of In $3d_{5/2}$ and Sn $3d_{5/2}$ appear at the higher BEs of 444.3 eV and 486.4 eV, respectively. In these cases, the two peaks correspond to the saturated oxidation states of the two metals, i.e., In^{3+} from In_2O_3 and Sn^{4+} from SnO_2, respectively [97,176,217,230,246,257,247]. Compared to the ECT+0.0V and ECT+1.2V samples, the chemical shift of about +0.7 eV implies that surface oxidation took place in the electrochemical treatments at voltages $\geq$ +1.6V.

4.3.2.5 Oxidative Processes Controlled by Treatment Voltage

In the present study, positive voltages were imposed on ITO samples in the $K_4P_2O_7$ electrolyte. If ITO and $P_2O_7^{4-}$ in the electrolyte are stable in the potential window (0~+2.8V against NHE), half-cell reactions listed below at the positively polarized electrode are likely to take place under certain conditions, according to the literature [267].

$O_2(g) + H_2O + 2e^- \rightleftharpoons HO_2^- + OH^-$		+0.076
$O_2(g) + 2H_2O + 4e^- \rightleftharpoons 4OH^-$		+0.401
$O_2(g) + 2H^+ + 2e^- \rightleftharpoons H_2O_2$		+0.682
$O_2(g) + 4H^+ + 4e^- \rightleftharpoons 2H_2O$		+0.815 ($[H^+] = 10^{-7}$ mol dm^{-3})
$HO_2^- + H_2O + 2e^- \rightleftharpoons 3OH^-$		+0.88
$O_2(g) + 4H^+ + 4e^- \rightleftharpoons 2H_2O$		+1.229
$O_3(g) + H_2O + 2e^- \rightleftharpoons O_2(g) + 2OH^-$		+1.24
$O_3(g) + 6H^+ + 6e^- \rightleftharpoons 3H_2O$		+1.501
$H_2O_2 + 2H^+ + 2e^- \rightleftharpoons 2H_2O$		+1.776
$O_3(g) + 2H^+ + 2e^- \rightleftharpoons O_2(g) + H_2O$		+2.076

It can be seen that when the treatment voltage is below +1.229 V, less oxygen will be released because the concentration of OH^- and/or H^+ species in the electrolyte is small, which is the case where a voltage of +1.2 V is applied in the present study. It is expected that a treatment voltage between 0 V and +1.229 V may not result in intense oxidation of the ITO surface and therefore ineffective in decontamination. As a result, no significant change in surface oxidation states is observed after electrochemical treatment at +1.2 V, as shown in Figure 4.7. However, a different situation appears when the treatment voltage reaches +1.229 V, where concentrated oxygen atoms are released on the anode surfaces due to the electrolysis of water. Moreover, with the increase of the treatment voltage from +1.24 V to +2.07 V, more reactions will take place on the anode surface with the formation of oxidative species, such as O_3 and H_2O_2. The highly active oxygen atoms released on the anode surface are expected to effectively remove the organic contaminants on the ITO surface. More importantly, the pre-treatments at voltages from +1.6 to +2.8 V can oxidize some $In_2O_{x<3}$ and $SnO_{x<2}$ species into their saturated oxidation states, i.e., In_2O_3 and SnO_2 [97,176,217,230,246,257,247], respectively, as shown in Figure 4.7. As mentioned previously, however, higher treatment voltages of $\geq$ +2.8 V leads to serious electrochemical etching.

4.3.3 ITO Surface Passivation by Electrochemical Treatments

In Figure 4.8, current was plotted against treatment voltage for ITO samples with different treatment time from 5 to 30 s in an aqueous electrolyte containing 0.1 M $K_4P_2O_7$. It can be seen that at +1.2 V, current was not responding to the treatment time. Starting from +1.6 V the current flow decreases with the treatment time, in particular for high voltage. During the electrochemical treatments, two sources of current can be anticipated. The first is the current required to charge the capacitive interface between the electrolyte and the working electrode. It is obvious that a time of more than 5 s is most likely enough to complete the charging processes. This is supported by the fact that at the treatment voltage of +1.2 V, no significant change in current is observed with increasing treatment time from 5 s to 30 s. The second is the Faradic current originated from transfer of electrons across the interface between the electrolyte and the ITO working electrode under study, implying the existence of redox reactions near and/or on the electrode surface, e.g. electrolysis of water. The very low current at the treatment voltage of +1.2 V is likely to have been generated by the presence of atmospheric oxygen in the electrolyte, which can promote water electrolysis at lower applied voltage, as described in last section. In other words, a voltage of +1.2 V is lower than the electrochemical potential required for the main redox reactions.

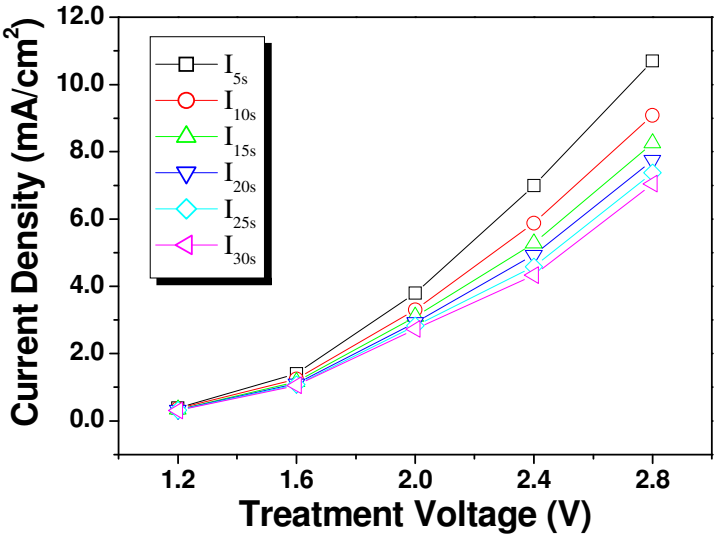

Figure 4.8. Current-voltage curves for ITO samples with 2×2mm active area, treated in an aqueous electrolyte containing 0.1 M $K_4P_2O_7$ for varied treatment time from 5 to 30 s.

The decreased current with treatment time indicates an increased resistance against the charge transfer across the interface, which is likely attributed to the passivation of the ITO surface. It is also noted that the current-voltage behaviors do not follow the Nernst equation. This is because there is no exotic redox couples existed in the electrolyte and the redox reactions rise from the electrolysis of H_2O in the electrolyte. Therefore, the concentration of conducting ions is positively changed with increasing treatment voltage.

In order to confirm the existence of passivation on ITO surface during the electrochemical treatment, a Pt plate was used to replace the ITO sample and treated under the same conditions. A comparison of the current-voltage curves between the two samples treated for 30 s is shown in Figure 4.9. It can be seen that when treated at +1.2 V, the current flows for both Pt and ITO samples are close to zero. However, with increasing voltage, the current flows for Pt and ITO samples are increased but at different rates, i.e., the more current flows through Pt than ITO for the voltage window used in this study. It appears that

the higher the treatment voltage, the lager the difference. As Pt is chemically and electrochemically inert in the working conditions, it is reasonable to assume that no oxide that can significantly change the Faradic current is formed in the working conditions of this study. It is then expected that the lower current flow through ITO sample is due to the lower conductivity in the bulk and surface of ITO. Assuming that the bulk conductivity of ITO is constant in this study, the lower rates of current change with treatment voltage for the ITO sample is clearly related to the higher resistance against charge transfer across the ITO/electrolyte interface, which indicates that ITO surface has been passivated.

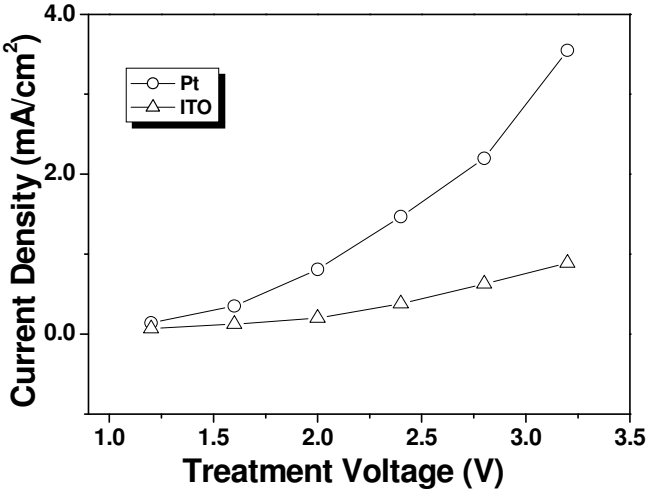

Figure 4.9. Current-voltage curves for Pt and ITO samples with 2×2 mm active area, treated in an aqueous electrolyte containing 0.1 M $K_4P_2O_7$ for 30 s.

Conductivity of ITO films is attributed to both Sn dopants and oxygen vacancies of the oxide lattice (duo to the presence of $In_2O_{x<3}$ and $SnO_{x<2}$ species) [97,99,100]. The change in surface conductivity of ITO films during electrochemical treatment is attributed to the surface oxidation by the oxygen released due to water electrolysis and the electrochemical etching of the ITO surface, which have been verified by the XPS results. Both the causes

lead to the lower conductivity by reducing the surface oxygen vacancies [97,100]. In addition, the surface passivation could be severer when insulating metal phosphates are formed on the ITO surface, as discussed in the last section.

CV scans were carried out using a potentiostat (Solatron Instruments) and a standard three-electrode electrochemical cell. Experimental details of the CV scans are similar to those in Section 3.3.3. The voltammograms of the electrochemically treated ITO electrodes at different treatment voltages in a solution of 1 mM $[Fe(CN)_6]^{3-/4-}$ redox couple in 0.1 M KNO_3 supporting electrolyte are shown in Figure 4.10. Peak potentials and peak currents are summarized in Table 4.3. Similar to the plasma treatments, the peak potential separations ($\Delta E_p = E_{pa} - E_{pc}$) for all the electrochemically treated samples are much larger than 58 mV and the I_{pa}/I_{pc} ratios deviate from unity, implying irreversible electrochemical conditions. Compared with that of the ECT+0.0V sample, peak potential separation is almost not changed after electrochemical treatment at +1.2V, slightly decreased for the ECT+1.6V sample, slightly increased for the ECT+2.0V and ECT+2.4V samples, but significantly increased for the ECT+2.8V. Similarly, the peak current is also changed with the treatment voltage, but in the opposite way.

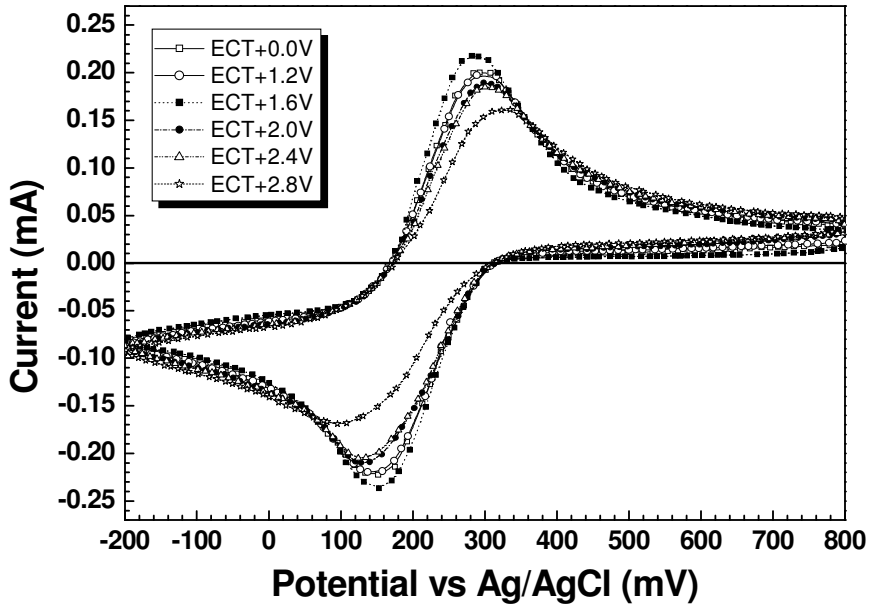

Figure 4.10. Cyclic voltammograms for ITO electrodes electrochemically treated at voltages from 0 to 2.8 V. Electrolyte: 1.0 mM $Fe(CN)_6^{3-/4-}$ in 0.1 M KNO_3. Reference electrode: Ag/AgCl (3 M KCl). Scan rate: 100 mV/s.

As mentioned in Chapter 3, peak potential separation is a function of the rate constant for electron transfer, which decreases as redox couples are unable to reach the electrode surface. If the CV test parameters are kept the same for all samples, the major factor causing the difference in peak potential separation can be attributed to the varied electrode surface conditions. The reduced peak currents and increased peak potential separations in the cyclic voltammograms with the $Fe(CN)_6^{3-/4-}$ redox couple are possibly caused by either partial blocking of the ITO electrode surface or hindering of the redox couple diffusion to the electrode surface. The XPS analysis reveals that ECT+0.0V sample surface was contaminated by substantial amounts of adventitious carbon. In addition, the complete hydrolysis products of the ITO surface, i.e., $In(OH)_3$-like species, may not be strongly bound to the ITO lattice [214]. The presence of the hydrocarbon contaminants and the insulating hydroxides on ITO surface reduce the effective surface area for electron transfer.

Liau and co-workers [212] also found that ITO surface contained electrochemical "hot spots" and "dead regions", which can be attributed to the inhomogeneous distribution of oxygen vacancies [213]. However, the electrochemical dead regions in this study are obviously related to the areas covered by the insulating contaminants or hydroxides.

Table 4.3. Summary of CV characteristics extracted and calculated from Figure 4.10, including peak anodic potential (E_{pa}), peak cathodic potential (E_{pc}), peak potential separation (ΔE_p)formal redox potential (E_{pa}+E_{pc})/2, peak anodic current (I_{pa}), peak cathodic current (I_{pc}), and I_{pa}/I_{pc} ratio.

ITO Sample	E_{pa} (mV)	E_{pc} (mV)	ΔE_p (mV)	$(E_{pa}+E_{pc})/2$ (mV)	I_{pa} (mV)	I_{pc} (mV)	I_{pa}/I_{pc}
ECT+0.0V	290	145	145	217.5	0.232	0.243	0.955
ECT+1.2V	290	146	144	218.0	0.236	0.246	0.959
ECT+1.6V	282	143	139	212.0	0.241	0.255	0.945
ECT+2.0V	313	129	184	221.0	0.215	0.223	0.964
ECT+2.4V	315	126	189	220.5	0.209	0.216	0.968
ECT+2.8V	325	100	225	212.5	0.166	0.175	0.949

The XPS results also demonstrate that the electrochemical treatments at voltages ≤ +1.2 V were not effective to remove the hydrocarbon contaminants. This is further verified by the CV results, as no significant change in cyclic voltammogram occurred after electrochemical treatment at +1.2 V. In comparison, the reduced separation of peak potential and increased peak current for the ECT+1.6V sample imply the removal of the contaminants, at least to a certain extent, which is consistent with the results from XPS analysis. With further increase in the treatment voltage, more reactions will take place on the anode surface with the formation of oxidative species, such as O_3 and H_2O_2 [267]. The oxidative species released on the ITO surfaces are expected to oxidize not only the carbon

contaminants but also the nonstoichiometric oxide species, such as $In_2O_{x<3}$ and $SnO_{x<2}$. Therefore, the larger peak potential separation and smaller peak current observed for the ITO pre-treated at voltages from 2.0 to 2.8 V imply the existence of obstacles against the electron transfer of the redox couple at the pre-treated ITO surface. This is possibly due to the surface oxidation and electrochemical etching, which have been proved by the results in Figure 4.8 and Figure 4.9. This is consistent with the increase in O:In ratio and the decrease in In:Sn ratio with treatment voltage, as shown in Table 4.2. Besides the surface oxidation and the electrochemical etching, other causes may contribute the largest peak potential separation and the lowest peak current for ECT+2.8. XPS results show the presence of insulating metal phosphates on the sample surface, which should also be responsible to the CV behaviors.

4.3.4 Contact Angle and Estimation of Surface Energy

The contact angle measurements were carried out using a Ramé-Hart contact angle goniometer (Model 100-22) with DI water and glycerol as the probe liquids. The surface energies (γ_s), sum of the polar (γ_s^p) and dispersive (γ_s^d) components, i.e., $\gamma_s = \gamma_s^p + \gamma_s^d$, are calculated by the geometric-mean method [205] using the measured contact angles. More information about the estimation of surface energy based on the contact angle data can be found in Section 2.4. Surface polarities (χ_p), defined as the ratio of the polar component (γ_s^p) to the surface energy (γ_s) [115], i.e., $\chi_p = \gamma_s^p / \gamma_s$, were also calculated.

4.3.4.1 Changes in Surface Energy with Treatment Voltage

Table 4.4 summarizes the γ_s^p, γ_s^d, γ_s, and χ_p of the ITO samples electrochemically treated at different voltages. The corresponding contact angles, based on which the surface energies were calculated, are also listed in the table for reference. The results show that surface wettability (i.e., water contact angle), γ_s^p, γ_s^d, γ_s, and χ_p are strongly dependent on the treatment voltage.

Table 4.4. Surface energies and polarities of ITO samples pre-treated at different voltages, based on contact angle measurement and calculation by geometric mean method. The total surface energy (γ_s) is the sum of the polar (γ_s^p) and dispersion (γ_s^d) components ($\gamma_s = \gamma_s^p + \gamma_s^d$) and the polarity χ_p is the ratio of the polar component to the total surface energy ($\chi_p = \gamma_s^p/\gamma_s$).

ITO	Contact angle (°)		γ_s^p	γ_s^d	$\gamma_s=\gamma_s^p+\gamma_s^d$	$\chi_p=\gamma_s^p/\gamma_s$
Sample	Water	Glycerol	(mJ/m^2)	(mJ/m^2)	(mJ/m^2)	
ECT+0.0V	49.4	35.2	24.1	28.8	52.9	0.46
ECT+1.2V	51.5	36.8	22.2	29.6	51.8	0.43
ECT+1.6V	23.8	18.9	47.8	18.9	66.8	0.72
ECT+2.0V	16.9	29.7	63.6	9.4	72.9	0.87
ECT+2.4V	13.8	21.9	59.1	12	72.1	0.82
ECT+2.8V	50.2	34.4	22.3	30.9	53.2	0.42

From Table 4.4, it can be seen that the electrochemical treatment at +1.2 V results in negligible change in γ_s, as it decreases from 52.9 mJ/m^2 for the ECT+0.0V sample to 51.8 mJ/m^2. With increasing the treatment voltage, γ_s increases until the maximum value of 72.9 mJ/m^2 is reached for ECT+2.0 V, which is comparable to that from the oxygen plasma treatment (74.2 mJ/m^2). However, further increase of the treatment voltage from +2.0 V to +2.8 V significantly reduces γ_s from 72.9 mJ/m^2 to 53.2 mJ/m^2. It is also found that the

electrochemical treatments change both γ_s^p and γ_s^d in a reverse manner, and a higher χ_p normally corresponds to a higher γ_s^p and a lower γ_s^d. For instance, +2.0 V treatment yields the maximum χ_p of 0.87 with γ_s^p = 63.6 mJ/m^2 and γ_s^d = 9.4 mJ/m^2, while +2.8 V treatment gives the minimum χ_p of 0.42 with γ_s^p = 22.2 mJ/m^2 and γ_s^d = 29.6 mJ/m^2. In short, the most polar surface can be obtained by the electrochemical treatment at a treatment voltage near +2.0 V, while treatments at a voltage of $\leq$ +1.2 V or $\geq$ +2.8 V may cause the surface polarity to change less or to decrease.

4.3.4.2 Surface Energy Controlled by Chemical States

It is interesting to understand how the electrochemical treatment changes the surface energy of ITO films. Table 4.4 has shown that surface energy is closely correlated to the treatment voltage used for the electrochemical treatment of ITO surface. In fact, the apparent dependence of the surface property on the treatment voltage is determined by the changes in chemical bond of ITO surface. As mentioned above, contamination and oxidation state are the two major factors controlling γ_s, especially γ_s^p.

The organic contaminants are insulating in nature and have lower χ_p due to their more covalent chemical bonds. A fractional coverage of ITO surface by CH_x contaminants will decrease γ_s, through reducing the exposure of M-O-M and M-OH polar species, and therefore the dipoles and hydrogen bonds, as described in Chapter 3. Thus, the low γ_s of ECT+0.0V (see Table 4.4) is partially related to the adventitious carbon species. As mentioned above, the voltage used for the electrochemical decontamination must be higher

than +1.229 V (i.e., the potential required for oxygen release), which is experimentally supported by other research groups [263,264]. This is the reason why no significant change in surface polarity is observed after the electrochemical treatment at +1.2V.

It is generally accepted that there are two origins of the γ_s^p in γ_s, the surface dipole and the hydrogen bonding. Extensive hydroxylation of the ITO surface may take place by positive polarization in the aqueous electrolyte. In such a way, a substantial amount of M-OH species, which is more hydrophilic than M-O-M species [215], will be formed on the ITO surface during the electrochemical process. In addition, hydrogen bonds can considerably contribute to the ITO surface energy [130] due to the existence of M-OH species. It is obvious that hydrogen bonding is present for the M-OH species rather than M and CH_x species. As a consequence, a surface covered with a high concentration of M-OH species shows high polarity, which is increased with treatment voltage.

It should be noted that when the treatment voltage is higher than +2.4 V (e.g., +2.8 V in this study), indium phosphate may be generated and adhered onto the ITO surface, as shown in Figure 4.5 and Table 4.2. Similar to the hydrocarbon contaminants, the metal phosphate layer stops the formation of the polar M-OH bonds. In addition, the highest carbon content of 20.55 at.% was detected on ECT+2.8, which is clearly related to the presence of the metal phosphates. As a consequence, the surface energy was reduced.

4.3.5 Effect of Electrochemical Treatments on Device Performance

4.3.5.1 Device Configuration and Fabrication

The ITO-coated glasses (Präzisions Glas & Optik GmbH, 20 Ω/) were routinely cleaned according to Section 2.5, followed by electrochemical treatment at different voltages as described in Section 4.2 and Section 4.3.1. Based on the electrochemically pre-treated ITO substrates, the OLED devices with a configuration of ITO/NPB(60nm)/Alq_3(60nm)/LiF/Al were fabricated using the same procedures and deposition parameters described in section 3.3.5.1. According to the treatment voltages of +0.0, +1.2, +1.6, +2.0, +2.4, and +2.8 V, the fabricated OLED devices were denoted in the same way as the ITO samples, viz., ECT+0.0V, ECT+1.2V, ECT+1.6V, ECT+2.0V, ECT+2.4V, and ECT+2.8V, respectively.

4.3.5.2 *L-I-V* Characteristics

Figures 4.11(a) and 4.11(b) show, respectively, the current-voltage (*I-V*) and luminance-voltage (*L-V*) characteristics of the OLED devices made with ITO substrates electrochemically treated at various voltages. In comparison with the control sample (ECT+0.0V), both the *I-V* and *L-V* curves shift to the lower voltage region for the devices with ITO pre-treated with voltages in the range of +1.6 to +2.4 V. However, higher turn-on voltages are observed for the devices with ITO pre-treated at the low voltage of +1.2 V and

high voltage of +2.8 V. The *I-V* and *L-V* behavior for the devices with pre-treatments at +2.0 V and +2.4 V are similar.

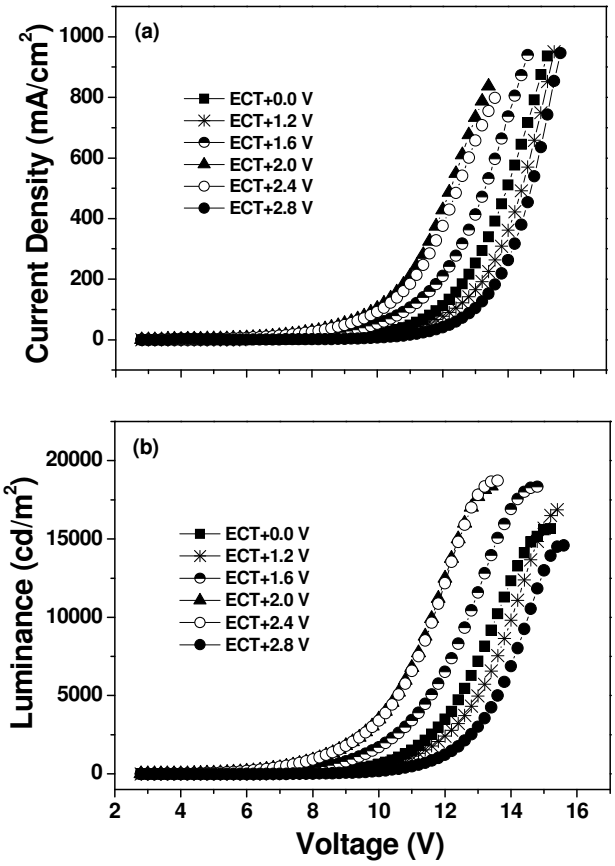

Figure 4.11. *I-V* (a) and *L-V* (b) characteristics of the OLED devices made with ITO electrochemically treated at different voltages, with a configuration of ITO/NPB(60nm)/Alq_3(60nm)/LiF/Al.

Figure 4.12(a) and 4.12(b) show, respectively, the current efficiency and power efficiency versus current density of the devices. Compared to the control device, both the current efficiency and power efficiency are enhanced with the increase in treatment voltage from +1.6 V to +2.4 V, although the enhancement of current efficiency at lower current densities is not as significant as that at higher current densities. On the contrary, remarkable lower efficiencies are observed for the device with ITO pre-treated at +2.8 V. For the device with

ITO pre-treated at +1.2 V, the efficiencies remain almost unchanged, except for the decline at small current densities.

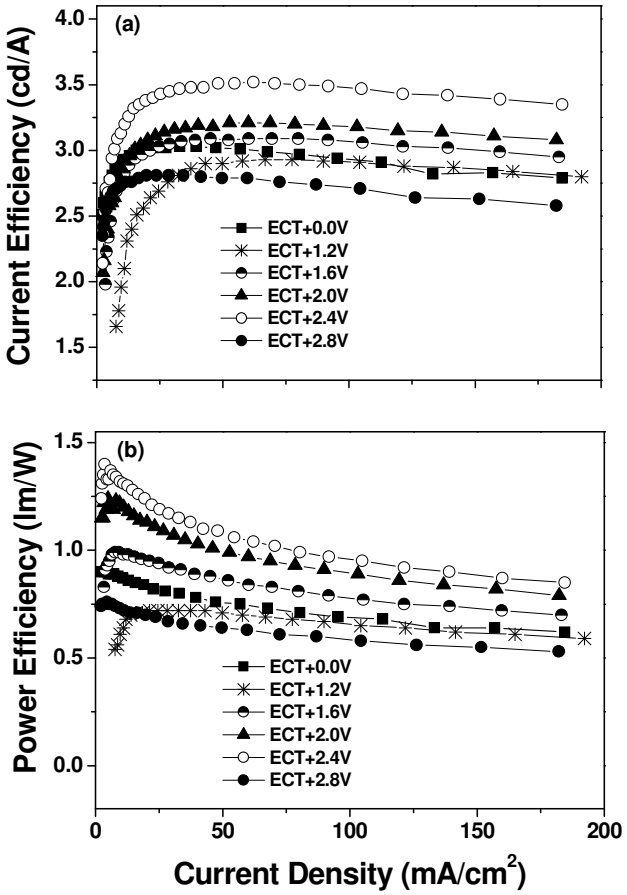

Figure 4.12. Plots of current efficiency (a) and power efficiency (b) vs. current density for the OLED devices made with ITO electrochemically treated at different voltages, with a configuration of ITO/NPB(60nm)/Alq_3(60nm)/LiF/Al.

In general, the devices based on ITO substrate electrochemically-treated at voltages from +1.6 V to +2.4 V exhibit improved EL performance, especially at the treatment voltage of +2.4 V. For the devices with ITO treated at +1.6, +2.0, and +2.4 V, the device turn-on voltages are reduced correspondingly to about 4.1, 2.8, and 2.9 V, from about 5.3 V for the control device. The corresponding operating voltage at 200 cd/m^2 is also reduced to about 7.0, 5.6, and 5.8 V, from about 8.4 V. It can be noted that treatments in the voltage range

from +1.6 to +2.4 V provide devices with higher current and power efficiencies. For instance, at a given current density of 20 mA/cm^2, the current efficiency and power efficiency of the device with treatment at +2.0 V are as high as 3.4 cd/A and 1.24 lm/W, respectively. These values are 13% and 48% higher than those of the corresponding values in the device ECT+0.0V. It is concluded that the optimized electrochemical treatment voltage is about +2.0 V, as the treatment leads to the highest surface polarity of ITO and the best device performance.

4.3.5.3 Effect of Surface Properties on Hole Injection

XPS results in Section 4.3.2 show that the electrochemical treatment voltage has significant effects on the ITO surface chemical states, which was further verified by the CV results in Section 4.3.3. More specifically, the concentration of polar species (e.g., M-OH), which depends on the treatment voltage, dominates the surface energy (γ_s), especially its polar component (γ_s^p), and therefore the surface polarity ($\chi_p = \gamma_s^p/\gamma_s$). Refer to Table 4.4, the calculated surface polarities of the different samples based on the contact angle measurements are in the sequence of ECT+2.0V(0.87) > ECT+2.4V(0.82) > ECT+1.6V(0.72) > ECT+0.0V(0.46) > ECT+1.2V(0.45) > ECT+2.8V(0.42). Compared to the *I-V* curves in Figure 4.11(a), the sequence in surface polarity is surprisingly identical to that of hole injection efficiency. In comparison, the ranking in operating voltage at luminance of 200 cd/m^2 are exactly conversed, viz., $V_{ECT+2.0V} < V_{ECT+2.4V} < V_{ECT+1.6V} < V_{ECT+0.0V} < V_{ECT+1.2V} < V_{ECT+2.8V}$. This suggests that hole injection of the OLED devices in

this study is correlated to the ITO surface polarity that is controlled by the surface chemical states.

In the OLED device fabrication, the hole transport material, NPB, is first deposited onto an ITO surface, and the ITO/NPB interface comes into being. As described in Section 4.3.5.1, the cathode for electron injection was the same in all the devices based on the ITO substrates electrochemically treated at different voltages, and the devices were fabricated in the same batch. The marked changes in hole injection are obviously attributed to the electrochemical treatments that have modified the ITO surfaces and then the ITO/NPB interfaces. Electrochemical treatments at voltages from +1.6 to +2.4 V, especially the optimized +2.0 V, significantly increase the surface polarities, which have enhanced hole injection through improving the adhesion of NPB onto the ITO surfaces and then forming good electric contacts [115]. However, the electrochemical treatment at +1.2 V did not improve the device performance due to less change in surface polarity. Furthermore, treatment at higher than +2.4 V lead to the lower surface polarity that deteriorates the ITO/NPB interface, and therefore the hole injection is significantly decreased. The interface evolution and its effect on hole injection will be discussed in Chapter 6.

Notably, the results show that electrochemical treatment of ITO surface is able to improve not only hole injection but also EL efficiency, which is not attainable by the plasma treatment in the present study. This difference will be discussed in Chapter 7.

4.4 Conclusion

In this chapter, electrochemical process was developed to modify ITO surface for improving OLED device performance. Effect of the electrochemical treatments on surface morphology, composition and chemical state, surface passivation status and electron transfer kinetics, and surface energy were investigated by AFM, XPS, CV, and contact angle goniometer, respectively, with an emphasis on the correlation between the surface properties and the treatment voltages. The influence of the electrochemical treatments on the ITO surface properties and thus the hole injection efficiency across ITO/HTL interface, as well as their relations were discussed.

AFM observations show that no visible change in morphology and ITO film thickness was observed when a treatment voltage below +2.4 V was used. However, when treatment voltage is larger than +2.4 V, the ITO film thickness is substantially reduced, suggesting electrochemical etching.

XPS analysis revealed that the electrochemical treatment is an effective method to remove the adventitious carbon contaminants adsorbed on the ITO surfaces. With increase in the electrochemical treatment voltage, the ITO surfaces the nonstoichiometric oxide species on were oxidized into their saturated oxidation states. However, In:Sn ratio is decreased with increase in treatment voltage, suggesting electrochemical etching took place on the ITO surfaces, especially for the treatment voltages higher than +2.4 V. The electrochemical etching leads to remarkable change in topography of ITO surface. The electrochemical

etching of In and Sn from ITO surface also contributes to the high O:In and O:Sn ratios. In addition, when the treatment voltage of +2.8 V was applied, metal phosphates were promoted.

ITO surface passivation by the electrochemical treatment was detected and varied with treatment time and voltage. Cyclic voltammograms of the ITO electrodes electrochemically treated at different voltages further confirmed the ineffectiveness of treatment at a voltage below +1.2 V. The significantly reduced electron transfer rates by the treatment at a voltage higher than +2.0 V implies that insulating surface layers were formed by the electrochemical treatments. This is attributed to the surface oxidation and electrochemical etching, as well as the formation of insulating metal phosphate formed at treatment voltage higher than +2.8 V.

Surface energy study of ITO film demonstrated that the treatment voltage can affect the polarity of ITO surface. Starting from +1.2 V, with increase in treatment voltage, the surface polarity is increased up to +2.0 V and then decreased. The maximum polarity of 0.87 and the minimum polarity of 0.42 are obtained by the treatments at +2.0 and +2.8 V, respectively. The increased surface polarity is attributed to the decontamination and surface oxidation, leading to more polar surface species. However, severe electrochemical etching takes place if the treatment voltage is higher than +2.0 V, leading to the deterioration of the surface properties. In addition, the presence of metal phosphate on ECT+2.8V also contributes to its lowest polarity.

Based on the OLED devices with a configuration of ITO/NPB(60nm)/Alq_3(60nm)/LiF/Al, the turn-on voltage was reduced from 5.3 V for device with the pristine ITO electrode to 2.8 V for device with the ITO electrode pre-treated at +2.0 V. The current efficiency and power efficiency at 20 mA/cm2 were increased, correspondingly, from 3.0 cd/A and 0.84 lm/W to 3.4 cd/A and 1.24 lm/W. These show that the electrochemical treatment of ITO surfaces at the optimized voltage is effective in reducing the device turn-on and operating voltages of the OLEDs, implying significant improvement of hole injection. The hole injection efficiency is correlated to the surface polarity. With the moving up the surface polarity of the ITO electrodes, the operating voltage is decreased correspondingly. In other words, the higher the surface polarity, the higher the hole injection efficiency. The electrochemical treatments modify the ITO electrode surfaces and then the ITO/NPB interfaces. The treatment at about +2.0 V significantly increases the surface polarity that is controlled by the surface chemical states. Similar to the plasma treatment, the high surface polarity enhances the hole injection through improving the adhesion of NPB onto the ITO electrode surfaces and then forming good electric contacts.

Chapter 5

Insulating Buffer Layers

Abstract

In this chapter, a brief overview on the effect of insulating buffer layer between ITO and HTL on hole injection and therefore device performance is first given. ITO surfaces are coated with SiO_2 thin films deposited by E-beam thermal evaporation (TE), self-assembled monolayer (SAM), and sol-gel (S-G) processes, respectively. The buffer layer coated ITO surfaces are then characterized using AFM and CV to understand the influence of coating processes and film thickness on the coating morphology and the electron transfer kinetics. OLED devices with a configuration of ITO/SiO_2/NPB(60nm)/Alq_3(60nm)/LiF/Al are fabricated and characterized in terms of L-I-V behaviours. The results show that insulating buffer layers sufficiently block hole injection of the devices based on the modified ITO surfaces due to the reduction of effective contact areas between ITO and NPB. The effects of the coating processes and the buffer layer thickness on the device performance are also discussed.

5.1 Introduction

It is generally accepted that the optimization of charge injection and transport processes is of critical importance for a bright and efficient OLED device. Besides surface treatments, such as plasma and electrochemical treatments, ultra thin insulating buffer layers have been inserted between ITO and HTL by various processes for controlling hole injection. Kurosaka et al. [150] used Al_2O_3 as a buffer layer in a device with configuration of ITO/Al_2O_3/TPD/Alq_3/Mg:Ag. Such device exhibited a doubled quantum efficiency (0.6% against 0.35%) compared to the device based on a bare ITO substrate. However, this improvement in EL efficiency was obtained at a cost of higher turn-on voltage, which was increased from 10 V in the device without the Al_2O_3 layer to 20 V in the device with such a buffer layer. A high bright and efficient device was fabricated by Deng et al. [151] through insertion a 1-nm-thick SiO_2 film as a hole injection layer. Although the EL efficiency was improved, the turn-on voltage in the device was still not lowered down sufficiently. In addition, Pr_2O_3 [114] and other non-oxide insulating layers, such as Si_3N_4 [153], Teflon [152], and even LiF [156] were also used for this purpose.

The device performance by insertion of the insulating buffer layer has been elucidated in the basis of tunneling model by the most researchers [114,151-153,269-271], which request the buffer layer to be uniform and continuous. It is noted that most of the insulating buffer layers were deposited by vacuum vapor deposition processes, although SAM SiO_2 [149] and sol-gel TiO_2 [268] were also reported. As it is known, in vapor deposition processes, deposition starts from nucleation and growth. In most cases, the

morphology of the deposit at the beginning of deposition stage appears in the form of isolated islands. As a result, the substrate is not fully covered until the islands are linked together. The optimized thickness of the insulating buffer layers for the best device performance has been estimated to be about 1 nm [114,151,271] using image force model. However, the minimum thickness of the insulating buffer layer for fully covering ITO surface is much larger than 1 nm [114,156]. In addition, the anisotropic nature of the vapor deposition processes also enlarges the minimum film thickness for the full coverage, especially for rough and flawed surfaces such as ITO. As a consequence, the use of tunneling theory in these cases is questionable due to the insufficient coverage of ITO surface by the dielectric materials. Therefore, it is meaningful to further investigate the effect of the insulating buffer layers.

In this study, SiO_2 buffer layers with varied thickness were deposited on ITO surfaces using thermal evaporation (TE), self-assembled-monolayer (SAM), and sol-gel (S-G) processes. The buffer layer coated ITO surfaces were characterized by AFM and CV to understand the influence of coating morphology and thickness on electron transfer kinetics. OLED devices based on the buffer modified ITO surfaces, with configuration of ITO/SiO_2/NPB(60nm)/Alq_3(60nm)/LiF/Al, were fabricated and characterized in terms of L-I-V behaviors.

5.2 Experimental

Substrate cleaning: After pre-cleaning by sonications, Si and ITO substrates were exposed to Ar plasma for 3 min to eliminate the influence by the adventitious carbon contaminants. The details of sonication cleaning and plasma treatment can be found in Chapter 2.

E-beam evaporated buffer layers: SiO_2 layers with different thickness in the range 0–15 nm were deposited onto the cleaned ITO or Si wafer substrates at a deposition rate of 0.1–0.2 Å/s and a pressure of 5×10^{-4} Pa by an e-beam evaporation system from a tungsten crucible.

Self-assembled SiO_2: The cleaned ITO and Si(111) substrates were heated in air at 125 °C for 15 min and placed into a antechamber of a glove box, where a vacuum of 25-50 mTorr was applied for 20 min to remove excess surface moisture. The samples were then transferred into a reaction vessel in the glove box with highly purified nitrogen. A 50 mM solution of tetrachlorosiloxane in freshly distilled heptane was added to the reaction vessel in sufficient quantity to totally immerse the substrates. The substrates were allowed to react with the stirring siloxane solution for 30 min. Following removing from the siloxane solution, the substrates were rinsed and sonicated two successive times in freshly distilled dry pentane in the same glove box. The substrates were then removed from the glove box, washed, sonicated with acetone, and subsequently dried in air at 125 °C for 15 min. This process was repeated to form SAM SiO_2 thin films being of incremental thickness. The experimental procedures and the chemical reaction mechanism for SAM SiO_2 coating on

ITO surface was proposed, as shown in Figure 3.1, which is similar to that in the literature [149].

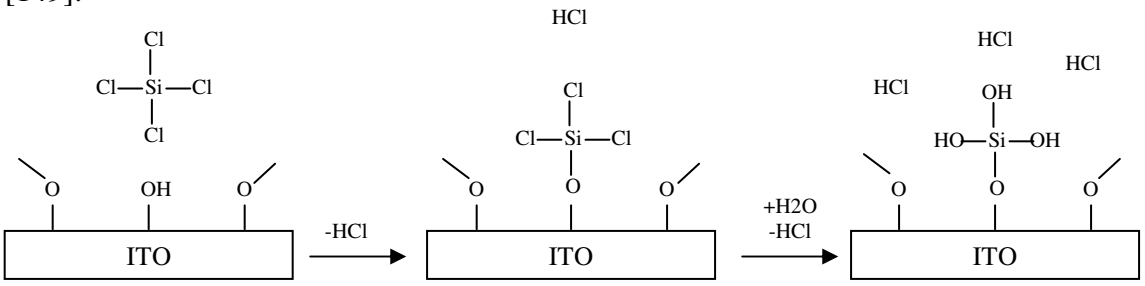

Figure 5.1. Schematic diagram showing the experimental procedures and the chemical reaction mechanism for SAM SiO_2 coating on ITO surface.

Sol-gel deposited SiO_2: The precursor for silicon dioxide sol-gel solutions was tetra ethyl orthosilicate (TEOS) [$(C_2H_5O)_4Si$]. The sol-gel solutions with different concentrations of Si were prepared following the method reported in literature [273]. The sol-gel solution was filtered using 0.2 μm Teflon filter to remove big gel particles. A sol-gel SiO_2 layer was then deposited onto the prepared ITO and Si wafer substrates by spin-casting process at a speed of 2500 rpm, followed by drying in air at 150 ^oC for 30 min. This process was repeated to form SiO_2 layers being of incremental thickness. The experimental procedures and the chemical reaction mechanism for sol-gel SiO_2 coating on ITO surface was proposed, as shown in Figure 5.2, based on the sol-gel theory in the literature [273].

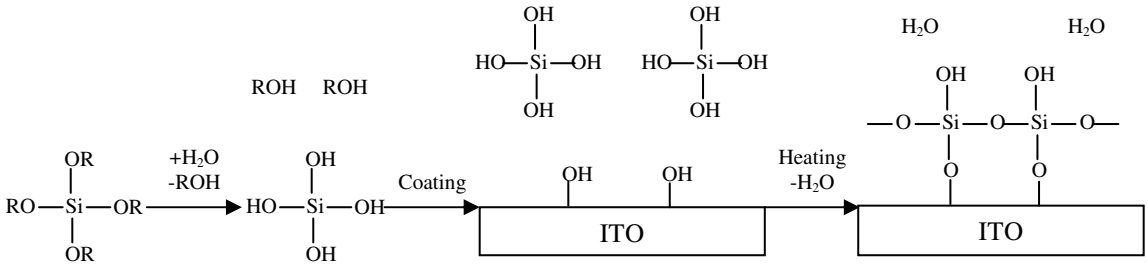

Figure 5.2. Schematic diagram showing the experimental procedures and the chemical reaction mechanism for sol-gel SiO_2 coating on ITO surface.

5.3 Results and Discussion

5.3.1 Influence of Coating Process on Buffer Layer Morphology

5.3.1.1 Thermal Evaporation Process

AFM observation of ITO surfaces coated with TE SiO_2 layers: The morphology of the TE SiO_2 is in isolated-islands growth mode, as shown in Figure 5.3. The scattered-particle feature of the dielectric coating is more clearly presented on Si substrate (refer to Figure 6.10(b)). A uniform distribution of the deposited SiO_2 particles is clearly seen, which means that nucleation of the SiO_2 film is not sensitive to the topographic conditions of ITO surface. With further deposition, the number of the SiO_2 particles is increased, but the size of the particles is not increased significantly. The ITO surface feature disappears after coated with 5 nm SiO_2 and the coating is in a particle-stack structure with clearly porous features.

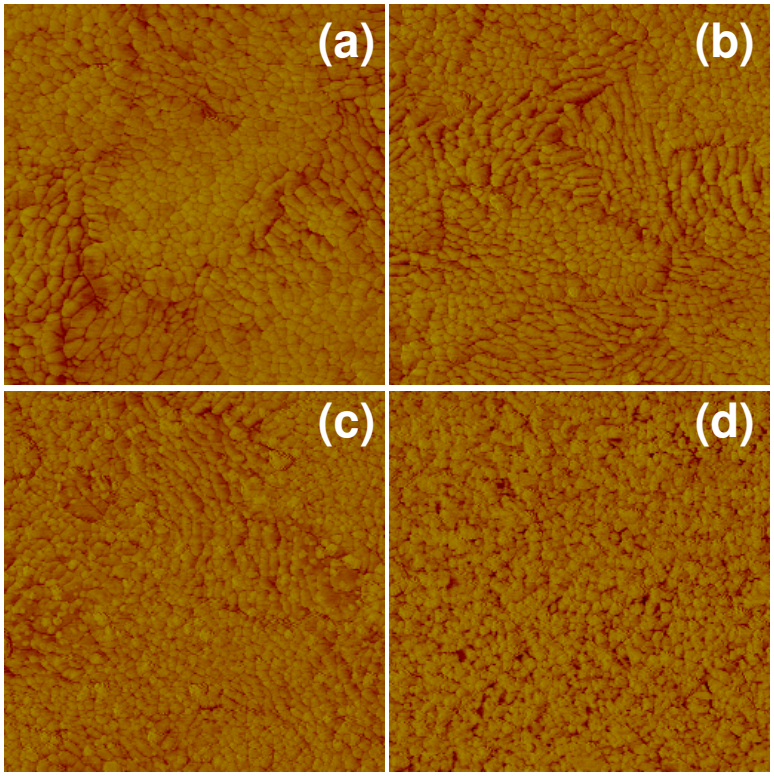

Figure 5.3. AFM phase mode images of the ITO surfaces modified by TE SiO_2 buffer layers with different thickness: (a) 0.5 nm, (b) 1.0 nm, (c) 2.0 nm, and (d) 5.0 nm. The scan area is 1×1 μm^2.

5.3.1.2 SAM Process

Calibration of SAM SiO_2 thickness: To make a more uniform and denser coating of SiO_2 on a rough ITO substrate, SAM process is also exercised. Figure 5.4 shows spectroscopic ellipsometer measurements on a series of self-assembled SiO_2 layers on Si(111) substrates. The plot of thickness vs. number of coating layers shows that film thickness increases monotonically with repeated layer depositions. From the slope of the least-squares line, it can be inferred that the thickness of each SAM SiO_2 layer is about 0.24 nm, under the deposition conditions employed in this study. The linear relation of thickness to the number of coating layers provides us with great convenience in tailoring the cumulative

dielectric thickness on not only the Si substrates but also the ITO films.

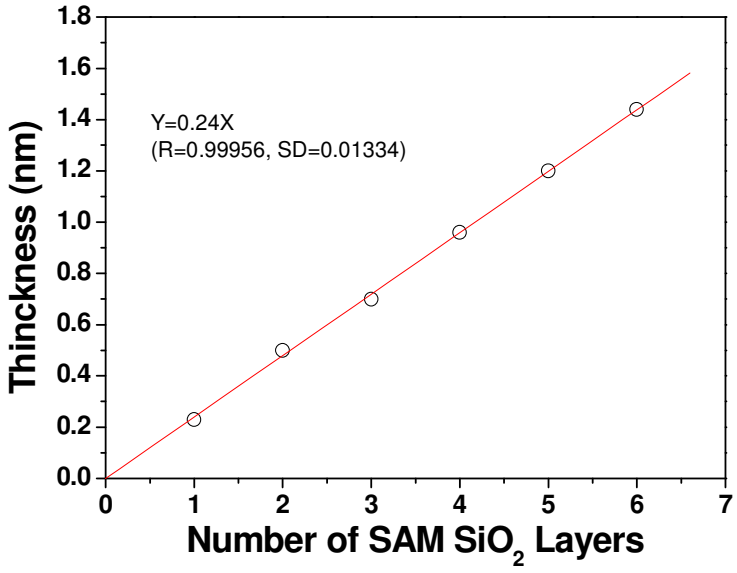

Figure 5.4. Spectroscopic ellipsometer measured thickness of SAM SiO_2 films vs. the number of layers deposited on single-crystal Si(111), showing the monotonic increase in total film thickness with number of depositions. The line is a least-squares fit to the data.

AFM observation of ITO surfaces coated with SAM SiO_2 layers: A morphological comparison between ITO surfaces without coating and with 6-layer SAM SiO_2, as shown in Figure 5.5, reveals that SAM SiO_2 buffer layers are essentially featureless and extremely smooth, with no indication of island growth, film cracking, or pitting. The featureless characteristic of SAM SiO_2 on ITO surface was reported by Malinsky et al. [149], where their SAM SiO_2 coating is per layer much thicker than ours due to a different precursor applied. From the AFM images, the SAM coatings are indistinguishable from its ITO substrate. Nevertheless, the existence of SAM SiO_2 on ITO surfaces has been verified by the above spectroscopic ellipsometer measurements and will be further confirmed by the previously discussed CV results. It is therefore expected that SAM process is more suitable for depositing smooth, uniform and dense thin films on ITO surfaces.

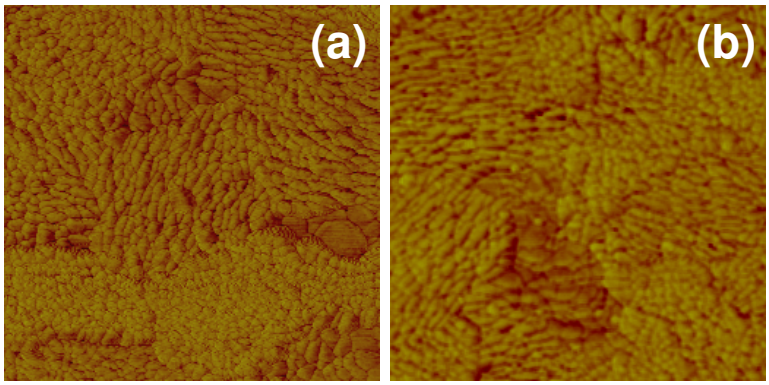

Figure 5.5. AFM phase mode images showing a morphological comparison between (a) the as-clean ITO film and (b) the ITO surface modified by 6 layers of SAM SiO_2. The scan area is 1×1 μm^2

5.3.1.3 Sol-gel Process

Calibration of sol-gel SiO_2 thickness: Spectroscopic ellipsometer measurements (Figure 5.6) on a series of S-G SiO_2 coated Si(111) substrates indicate that the total deposited film thickness increases monotonically with repeated layer depositions. From the slope of the least-squares line, it can be inferred that each S-G spin-coat results in a SiO_2 layer with a thickness of about 0.6 nm. This linearity in the S-G SiO_2 deposition process affords considerable precision in tailoring the cumulative dielectric thickness on Si(111) substrate. The thickness calibration results obtained from Si wafer substrate are also used to estimate the S-G coating thickness on ITO surface in this study.

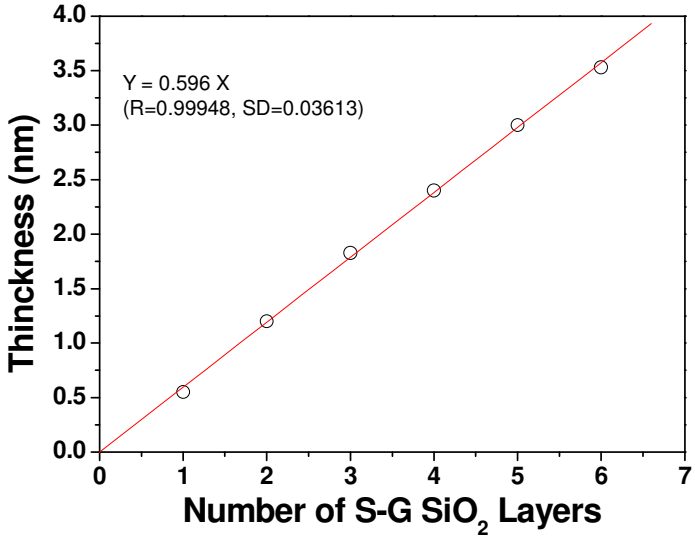

Figure 5.6. Spectroscopic ellipsometer measured thickness data for S-G SiO_2 layers spin-coated on single-crystal Si(111), showing the monotonic increase in total film thickness with number of coats. The line is a least-squares fit to the data.

AFM observation of Si surfaces coated with S-G SiO_2 layers: AFM images of Si (111) spin-coated with varied number of S-G SiO_2 layers in Figure 5.7 demonstrates that the S-G SiO_2 films on Si wafer substrate grow in an "islands-lakes" mode. After the first coat, a network of S-G SiO_2 (named as "islands" in this study) is established on the Si substrate. With repeating the spin-coating process, the number of "islands" or "lakes" (i.e., the exposed Si substrate) does not change significantly and the surface coverage increases through extension of the S-G "islands". With increasing the sol-gel layers, the small sol-gel particles in the lake areas are increased. It is clearly seen that the number of S-G SiO_2 layers requested for fully covering the Si substrate under the present coating conditions seems more than 6, which corresponds to a thickness of about 3.4 nm. The discontinuous feature of the S-G coating also suggests that the coating thickness measured by spectroscopic ellipsometer is only an approximation. The citation of coating thickness in the context should be, therefore, read with focusing on the differentiation in thickness,

rather than its absolute value.

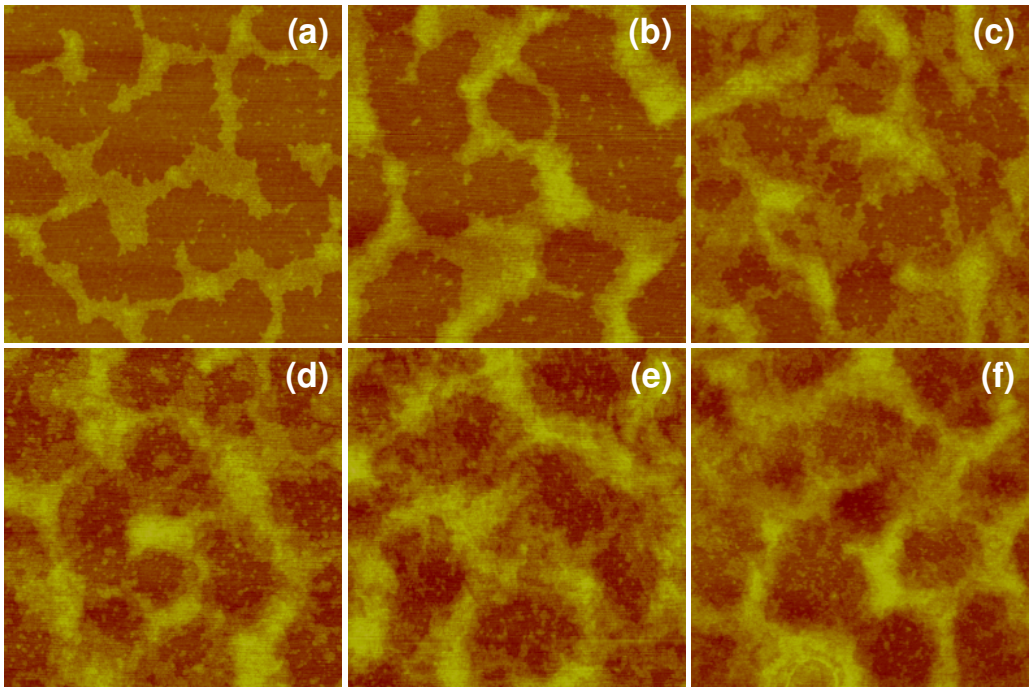

Figure 5.7. AFM height mode images of Si (111) surfaces modified by varied number of S-G SiO_2 layers: (a) 1 layer, (b) 2 layers, (c) 3 layers, (d) 4 layers, (e) 5 layers, and 6 layers. The scan area is 1×1 μm^2.

AFM observation of ITO surfaces coated with S-G SiO_2 layers: The "islands-lakes" morphology of S-G SiO_2, however, does not appear on ITO surfaces and a smoother coating is obtained, as shown in Figure 5.8. This is attributed to the rougher surface of the ITO film (RMS ~ 4 nm), compared with the Si substrate (RMS ~ 0.3 nm). The AFM images show that the S-G SiO_2 covers the grain and/or subgrain boundaries first. It inferred that the noticeable peak-valley feature of the ITO films has an obstacle effect to prevent the S-G coating from phase conglomeration that results the "islands-lakes" coating morphology on the Si substrates.

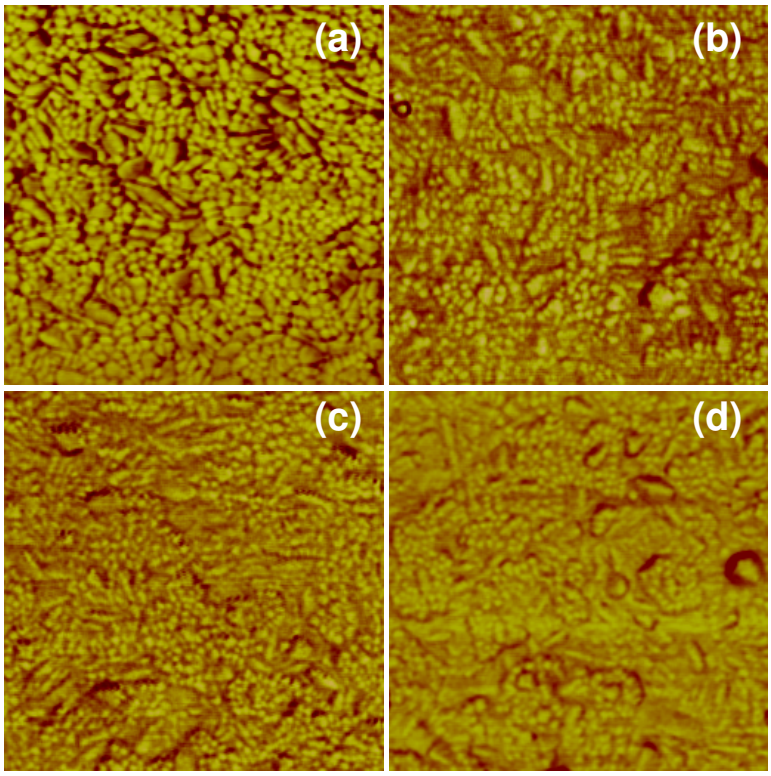

Figure 5.8. AFM phase mode images of ITO surfaces modified by S-G SiO_2 buffers with varied number of layers: (a) 1 layer, (b) 2 layers, (c) 4 layers, and (d) 6 layers. The scan area is 1×1 μm^2

5.3.2 Analysis of Buffer Layer Coated ITO Surfaces by Cyclic Voltammetry

CV scans were carried out using a potentiostat (Solatron Instruments) and a standard three-electrode electrochemical cell. Ag/AgCl (3 M KCl) with electrode potential of 210 mV vs. NHE [185] was used as the reference electrode and Pt wire as the auxiliary electrode. The ITO working electrode area (0.93 cm^2) was defined by the size of a rubber o-ring. The CV data were obtained in a solution containing 0.1 M KNO_3 (supporting electrolyte) and 1.0 mM $K_4Fe(CN)_6$ (redox couples) at room temperature and a scan rate of 100 mV/s, and in a potential range from -200 to +800 mV. All potentials were reported

with respect to Ag/AgCl (3M KCl). Before any CV scan, the electrolyte was nitrogen bubbled for 30 min to reduce the oxygen content in the electrolyte. More information about CV technique can be found in Section 2.3.

5.3.2.1 Thermal Evaporation SiO_2 Buffer Layers

Figure 5.9 shows cyclic voltammograms for $Fe(CN)_6^{3-/4-}$ redox couple using an as-clean ITO surface and a series of ITO surfaces coated by thermal evaporation (TE) SiO_2 thin films with different thickness from 0 to 15 nm. All of the voltammograms display relatively facile electron transfer kinetics, with peak potential separations ranging from 140 to 160 mV. Interestingly, thickness of the dielectric film has little effect on the voltammetric response (i.e., peak potential separation and peak current), as the TE SiO_2 buffer layers yield CV plots similar to that obtained from as-clean ITO. The AFM images in Figure 5.3 clearly show that ITO surface can be fully covered by 5 nm SiO_2 film being of particle-stack feature. The less reduction in peak current with increasing coating thickness measured for the fully covered ITO sample demonstrates that the particle-stacked dielectric films contain connected pores, which provide channels for electrolyte approaching ITO surface. Therefore, the Faradic current is sensitive to the density of the dielectric deposit, although apparent surface coverage has frequently been used for discussion in electron transfer across coated ITO/solution interface. This can be further verified by producing a denser buffer layer on ITO surface.

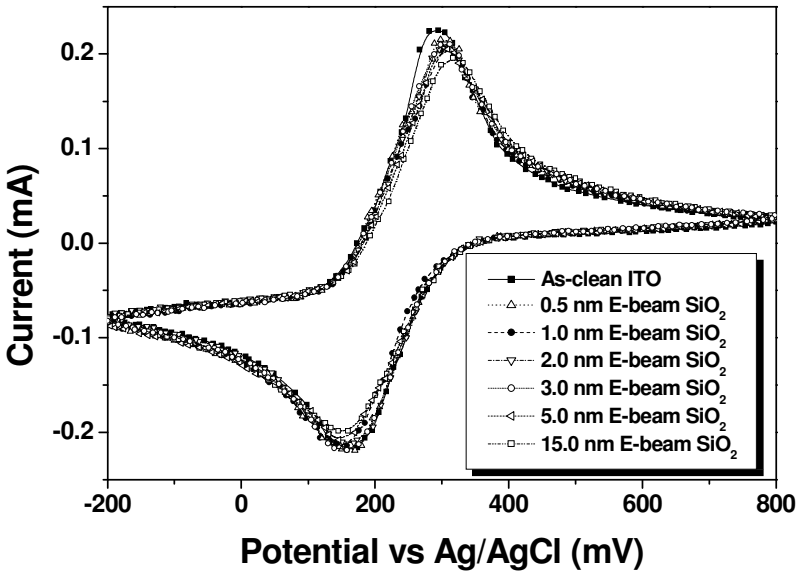

Figure 5.9. Cyclic voltammograms of 1.0 mM $[Fe(CN)_6]^{3-}$ in 0.1 M KNO_3 supporting electrolyte at an as-clean ITO film and a series of ITO surfaces coated with 0.5, 1, 3, 5, and 15 nm TE SiO_2. The sweep rate is 100 mV/s and the working electrode area is 0.93 cm^2. The lines through the data points are drawn as a guide to the eye.

5.3.2.2 SAM SiO_2 Buffer Layers

CV tests were carried out on the ITO surfaces modified by SAM SiO_2 films with varied number of layers from 0 to 6, as shown in Figure 5.10. As judged by both the separation between anodic and cathodic potential peaks, and by the overall magnitude of current flowing at any potential, there is a successive passivation of the ITO surface toward this redox chemistry as the buffer layer thickness is increased. The reduced peak current and large peak potential separation with only one to two layers of the dielectric material demonstrates that the redox processes are significantly suppressed by the SAM dielectric coatings. Furthermore, the electron transfer is totally blocked when the ITO surface is covered by 4- and 6-layer SAM coatings, because no Faradic (peak) current is detected for the two samples, as shown in Figure 5.10. This is an indirect evidence to confirm the

existence of SAM coatings on ITO surface, although they are not clearly visible in AFM images, as shown in Figure 5.5. From the plots in Figure 5.4, it can be seen that the thickness of the 4-layer SAM SiO_2 film is only about 1 nm. This implies that SAM process is much superior to TE process in terms of film density and ITO passivation effect.

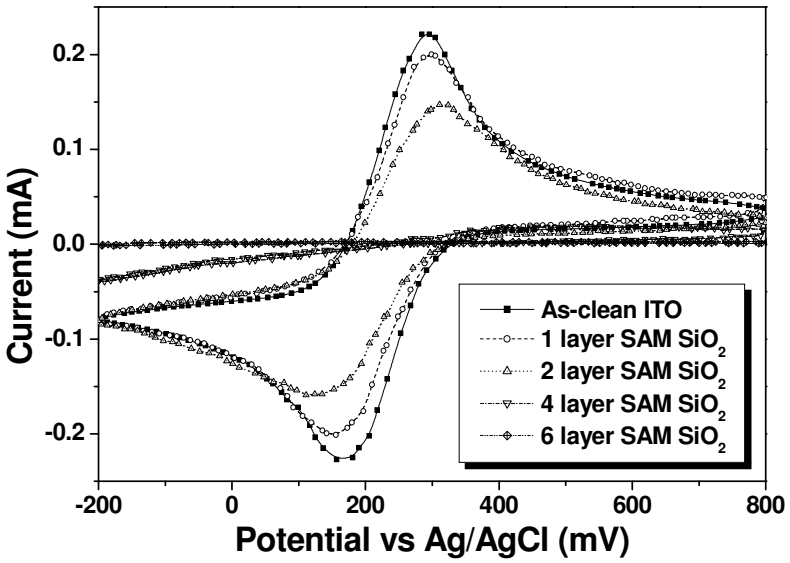

Figure 5.10. Cyclic voltammograms of 1.0 mM $[Fe(CN)_6]^{3-}$ in 0.1 M KNO_3 supporting electrolyte at an as-clean ITO film and a series of ITO surfaces coated with one layer, two layers, four layers, and six layers of self-assembled SiO_2. The sweep rate is 100 mV/s and the working electrode area is 0.93 cm^2.

5.3.2.3 S-G SiO_2 Buffer Layers

The electrochemical performance of S-G SiO_2 coated ITO surfaces with varied number of coating layers from 0 to 6 is displayed in Figure 5.11. All the voltammograms obtained from the S-G coated ITO surfaces exhibit larger peak potential separation values (ΔE_p) than that of the as-clean ITO sample, more specifically, the peak potential separation enlarges with increasing the buffer thickness. Meanwhile, the peak current is dropped,

correspondingly.

In contrast, the change in peak current and peak potential separation with the increased S-G SiO_2 layers is not large as expected. From Figure 5.8, it can be seen that the ITO surface feature almost disappears after coated with 6-layer S-G SiO_2 film, suggesting the majority of the ITO surface is covered by the dielectric film. On the other hand, the less reduction in peak current obtained from the 6-layer coated ITO surface is conclusive proof of the existence of substantial ITO surface areas in contact with electrolyte. This reveals that the S-G SiO_2 film is highly porous in microscopic point of view.

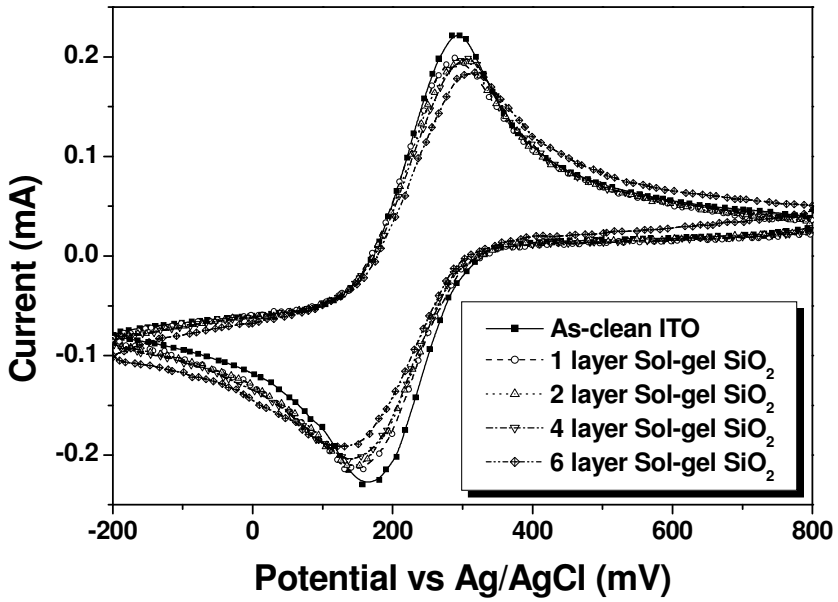

Figure 5.11. Cyclic voltammograms of 1.0 mM $[Fe(CN)_6]^{3-}$ in 0.1 M KNO_3 supporting electrolyte at an as-clean ITO film and a series of ITO surfaces coated with one layer, two layers, three layers, and four layers of S-G SiO_2. The sweep rate is 100 mV/s and the working electrode area is 0.93 cm^2. The lines through the data points are drawn as a guide to the eye.

5.3.2.4 Apparent Coverage versus Film Density

As it is commonly known, the performance of ITO used in electrochemical applications is primarily determined by electron-transfer kinetics. Since the process of electron transfer is confined to the interface between the electrode and the electrolyte, the redox kinetics will be influenced by the effective surface area, i.e., density of active electron-transfer sites. Peak potential separation and peak current are the two indicators to present electron transfer rate, which decreases as redox couples are unable to reach the electrode surface. Insulating buffer layers are definitely barriers against electron transfer at the ITO/solution interface. According to the conventional discussions, the electrochemical performance of the coated ITO surface is mostly affected by the buffer layer coverage. However, the findings in this study indicate that the film density, depending on the coating processes, plays a more critical role in the electrochemical performance of the coated ITO surfaces than the apparent coating coverage.

5.3.3 OLED Device Performance

The ITO-coated glasses (20 Ω/) were routinely cleaned according to Section 2.5, followed by buffer coating by different coating processes, as described in Section 5.2. To remove the effect of surface contamination due to the buffer layer coating processes and exposing to the atmosphere, all the ITO surfaces were treated by Ar plasma, according to the procedures in Section 3.2, prior to the OLED fabrications. The device based on the ITO surfaces without coatings are denoted as 0nm or 0L, depending on the coating

process adopted. Based on the ITO substrates (with and without coatings), the OLED devices with a configuration of ITO/SiO_2/NPB(60nm)/Alq_3(60nm)/LiF/Al were fabricated using the same procedures and deposition parameters described in section 3.3.5.1.

5.3.3.1 OLED Device Based on ITO Modified by Thermal Evaporated SiO_2

The *L-I-V* measurements of the OLED devices are similar to Section 3.2.5. Figure 5.12 shows the L-I-V curves measured from the OLED devices based on ITO surfaces coated by TE SiO_2 buffer layers. Some critical data presenting the device performance are summarized in Table 5.1. It is clearly seen that the TE SiO_2 buffer layers with varied thickness from 0.5 to 15 nm render no benefit to the device performance in terms of improved hole injection and EL efficiencies. Compared with the device without buffer layer, for example, L-I-V curve moves to the right (high driving voltage) side for 0.5 nm thick buffer, and then to the left (low driving voltage) side for 1.0 nm thick buffer with ceiling of the control sample (0.0nm), but to the right side again for 2.0 nm thick buffer. Further increasing the buffer thickness, e.g., in the cases of 5 and 15 nm, unidirectional and prominent right shifts of the L-I-V curves are observed. The left-right swing phenomenon of the L-I-V curve for the devices with ultra thin films was frequently reported in literature [114,138,151].

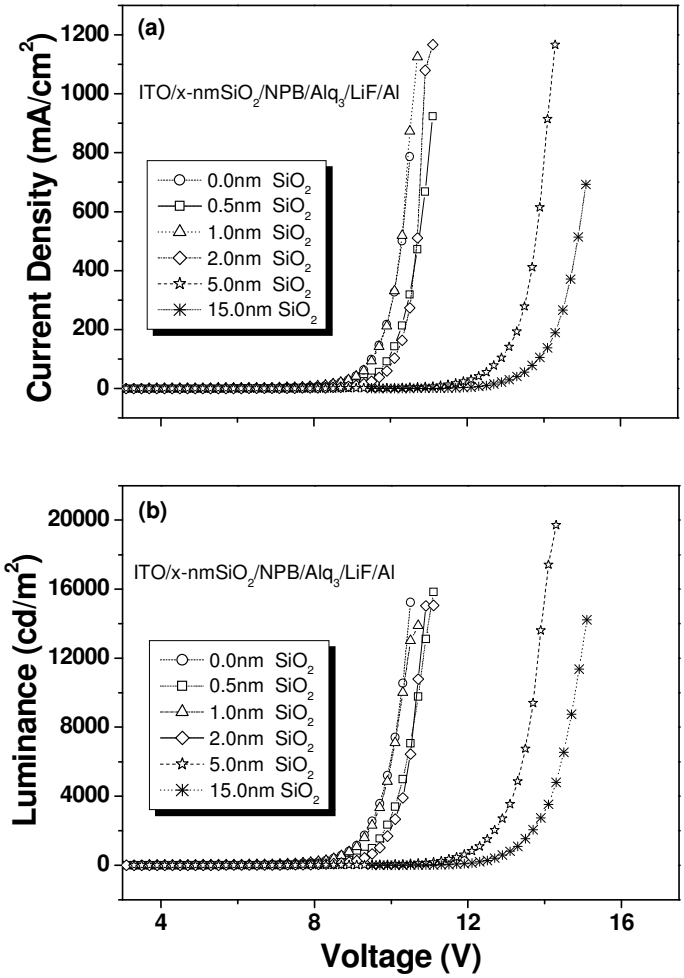

Figure 5.12. Current density (a) and luminance (b) vs applied voltage plots for OLED devices made with thermal evaporated SiO_2 buffer layers in configuration of ITO/SiO_2/NPB/Alq_3/LiF/Al, showing the effect of buffer layer thickness on L-I-V characteristics. The lines through the data points are drawn as a guide to the eye.

More specifically, the turn-on voltage is increased from 4.3 V for the coating free sample to 4.5, 4.6, 5.1, 6.7 and 10.1 V for the devices with 0.5, 1, 2, 5 and 15 nm SiO_2 thin films, respectively. The operating voltage for a luminance of 100 cd/m^2 is also increased from 7.5 V to 8.3, 7.7, 8.6, 10.7 and 12.0 V, correspondingly. This means that hole injection is inversely related to the coating thickness. The results in the present study are clearly in disagreement with those reported by other groups [114,138,151,156], where the device performance was more or less improved. The inconsistent results is likely to be due to the

different pre-cleaning processes, as solvent sonication was used in this study but plasma cleaning processes were adopted by them.

Table 5.1. Summary of L-I-V characteristics for the devices with TE SiO_2 buffer layers with varied thickness. V --- voltage (V), I --- current density (mA/cm^2), CE --- current efficiency (cd/A), PE --- power efficiency (lm/W)

	0nm	**0.5nm**	**1nm**	**2nm**	**5nm**	**15nm**
Turn-on V	4.3	4.5	4.6	5.1	6.7	10.1
Turn-on I	0.7	0.4	0.7	0.6	0.5	0.5
V@100cd/m^2	7.5	8.3	7.7	8.6	10.7	12.0
I@100cd/m^2	4.0	3.8	4.2	4.1	3.8	4.1
CE@100cd/m^2	2.6	2.7	2.5	2.6	2.6	2.7
PE@100cd/m^2	1.07	1.02	1.04	0.95	0.76	0.71
Max.CE	2.77@9.3V	2.75@8.9V	2.66@9.3V	2.80@9.9V	2.73@12.5V	2.75@13.5V
Max.PE	1.27@4.5V	1.50@4.7V	1.17@5.3V	1.50@3.5V	1.40@5.7V	0.75@11.1V

Note: "Turn-on" voltage and current are defined as those corresponding to a luminance of 1 cd/m^2.

Figure 5.13 shows the changes of current (a) and power (b) efficiencies with current density for the six different devices. Again, the devices with TE SiO_2 buffer layers are inferior to that without buffer layers in both current and power efficiencies. The right-moving L-I-V curve and the reduced current efficiency evidently imply the blocking of hole injection by the coatings.

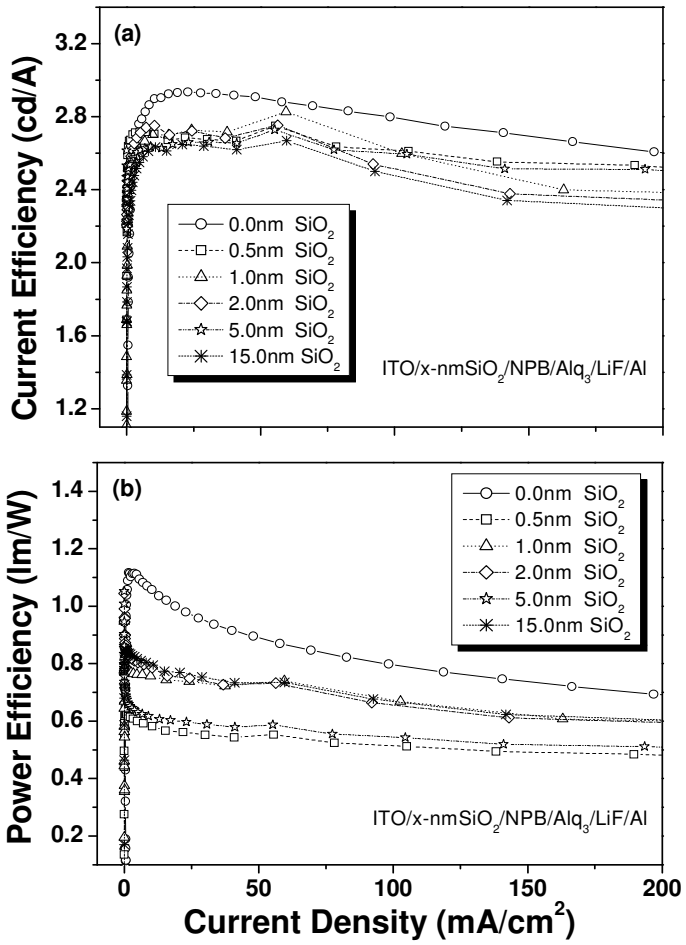

Figure 5.13. Current (a) and power (b) efficiency vs current density plots for OLED devices made with thermal evaporated SiO_2 buffer layers in configuration of ITO/SiO_2/NPB/Alq_3/LiF/Al, showing the effect of buffer layer thickness on device efficiency.

5.3.3.2 OLED Device Based on ITO Modified by SAM SiO_2

Figure 5.14 shows the L-I-V curves for the OLED devices based on the SAM SiO_2 coated ITO surfaces with varied number of coating layers (from 0 to 6). A summary of the device performance for different samples is given in Table 5.2.

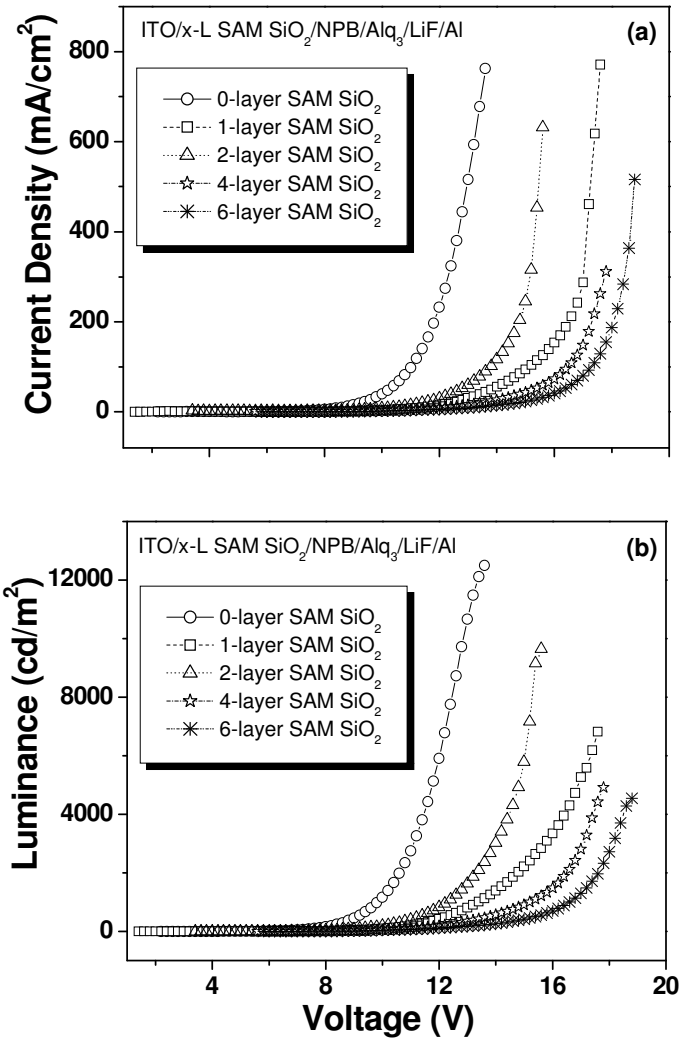

Figure 5.14. Current density (a) and luminance (b) vs applied voltage plots for OLED devices with SAM SiO_2 buffer layers in configuration of ITO/SiO_2/NPB/Alq_3/LiF/Al, showing the effect of the layer thickness on L-I-V characteristics.

It can be seen that L-I-V curves obtained from the devices with SAM SiO_2 buffer layers behave in the similar way to the TE SiO_2 samples. Figure 5.14(a) shows that at a given current density, the change in driving voltage with the number of coating layers (denoted as xL, x =0, 1, 2, 4, and 6) is in the order of $V_{0L} < V_{2L} < V_{1L} < V_{4L} < V_{6L}$. The same trend is also observed for the L-V plots, as shown in Figure 5.14(b).

Table 5.2. Summary of L-I-V characteristics for devices with varied number of SAM SiO_2 buffer layers. V --- voltage (V), I --- current density (mA/cm^2), CE --- current efficiency (cd/A), PE --- power efficiency (lm/W)

	0L	**1L**	**2L**	**4L**	**6L**
Turn-on V	3.9	5.5	5.0	6.8	7.2
Turn-on I	0.58	0.75	0.64	0.77	0.24
V@100cd/m^2	7.6	10.1	9.2	11.1	11.4
I@100cd/m^2	3.7	3.8	4.7	5.1	5.4
CE@100cd/m^2	2.70	2.60	2.16	2.05	1.91
PE@100cd/m^2	1.10	0.82	0.74	0.58	0.51
Max.CE	2.93@9.4V	2.68@11.8V	2.73@12.4V	2.19@13.0V	1.91@11.6V
Max.PE	1.12@6.8V	0.85@9.2V	0.77@10.6V	0.58@11.2V	0.57@11.2V

Note: "Turn-on" voltage and current are defined as those corresponding to a luminance of 1 cd/m^2.

Compared with the reference device based on the as-clean ITO, however, the devices with the SAM buffer layers need higher driving voltages to achieve the same value of luminance. Specifically, the turn-on voltage is increased from 3.9 V for the reference device to 5.5, 5.0, 6.8, and 7.2 V for the devices with 1, 2, 4, and 6 buffer layers, respectively, as shown in Table 5.2. The operating voltage for a luminance of 100 cd/m^2 is also increased from 7.6 V to 10.1, 9.2, 11.1, and 11.4 V, correspondingly. This means that hole injection is significantly suppressed by insertion of a SAM buffer layer between ITO and HTL, which is in agreement with the results obtained by Malinsky et al [149].

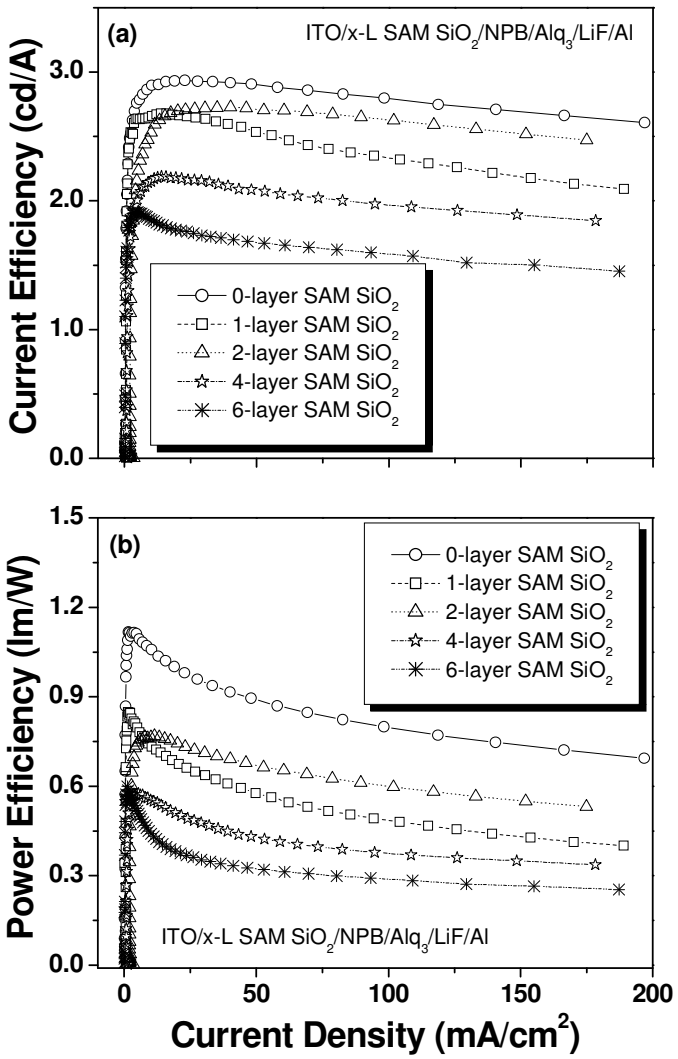

Figure 5.15. Current (a) and power (b) efficiency vs current density plots for OLED devices made with SAM SiO_2 buffer layers in configuration of ITO/SiO_2/NPB/Alq_3/LiF/Al, showing the effect of buffer layer thickness on device efficiency. One layer is approximately corresponding to 0.24 nm.

As shown in Figure 5.15 and Table 5.2, the severe hole blocking by SAM SiO_2 buffer layers in the present study lead to noticeable drops in both current and power efficiencies. For example, at the driving voltage (for 100 cd/m^2), the current efficiency is decreased from 2.7 cd/A for the reference device to 2.6, 2.16, 2.05, 1.91 cd/A for 1, 2, 4, and 6 layers, respectively. Meanwhile, the power efficiency is also dropped from 1.10 lm/W to 0.82, 0.74, 0.58 and 0.51 lm/W, correspondingly. Compared to the devices with TE SiO_2, it can

be found that the SAM SiO_2 buffer layers are much more effective in hole blocking, which is possibly attributed to the high density of SAM coatings.

5.3.3.3 OLED Devices Based on ITO Modified by Sol-Gel SiO_2

Figure 5.16(a) and 5.16(b) show L-I-V curves for the OLED devices based on the ITO surfaces coated with varied number of S-G SiO_2 layers (from 0 to 4). The L-I-V curves for the devices based on as-clean ITO surface (i.e., without Ar plasma treatment and coatings) are shown here for comparison. Some critical characteristics of the devices are summarized in Table 5.3.

It is clearly seen that when the S-G SiO_2 buffer layer is thinner than about 1.2 nm (2 layers) the device performance can be significantly improved, compared with the as-clean device. For the samples with buffer layer thicknesses of 0.6 nm (1 layer) and 1.2 nm (2 layer), the turn-on voltage is reduced from 4.2 V for the device without buffer layer to 2.6 V and 3.2 V, respectively.

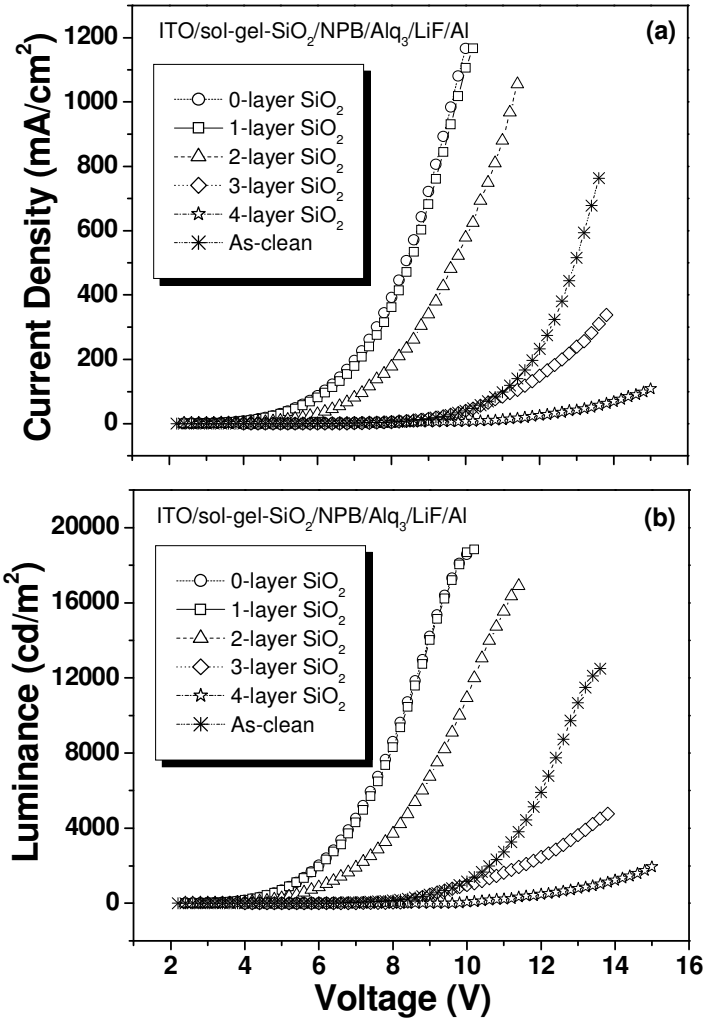

Figure 5.16. Pots of current density (a) and luminance (b) vs. applied voltage for OLED devices based on the ITO substrates modified by S-G SiO_2 layers in configuration of ITO/SiO_2/NPB/Alq_3/LiF/Al, showing the effect of buffer thickness on L-I-V characteristics. One layer is approximately corresponding to 0.6 nm in thickness.

Similarly, the operating voltage (at 100 cd/m^2) was also reduced from 7.6 V to 3.8 V and 4.4 V, respectively. The best L-I-V performance was observed from the device modified by 1 layer S-G SiO_2, which is comparable with that of the device based on the control device with Ar plasma pre-treatment. Compared with the as-clean sample, the I-V and L-V curves for thinner buffer layers (0.6 nm and 1.2 nm in this study) shift towards the lower voltage region, suggesting improved hole injection. In contrast, thicker buffer layers

(1.8 nm and 2.4 nm in this study) obviously deteriorated the device performance, as both I-V and L-V curves move to the higher voltage regions than that of the buffer layer free device.

Table 5.3. Summary of L-I-V characteristics for devices with varied number of S-G buffer layers. V --- voltage (V), I --- current density (mA/cm^2), CE --- current efficiency (cd/A), PE --- power efficiency (lm/W)

	0L	1L	2L	3L	4L	As-clean
Turn-on V	2.5	2.6	3.2	6.4	6.6	4.2
Turn-on I	0.24	0.37	0.53	0.67	0.86	0.50
V@100cd/m^2	3.8	3.8	4.4	8.4	10.2	7.6
I@100cd/m^2	5.6	5.5	4.3	7.8	8.6	3.7
CE@100cd/m^2	1.84	1.99	2.53	1.28	1.30	2.70
PE@100cd/m^2	1.52	1.65	1.85	0.48	0.04	1.11
Max.CE	2.33@6.6V	2.24@6.2V	3.00@5.8V	3.00@9.2V	2.00@11.6V	2.93@9.0V
Max.PE	1.55@4.2V	1.65@3.8V	1.88@4.2V	1.03@9.0V	0.56@10.8V	1.12@6.8V

A good OLED device should possess not only the high luminance but also the high luminance efficiency. The results shown in Figure 5.17(a) reveal that, in comparison with the as-clean sample and in the current density range of < 25 mA/cm^2, current efficiency is increased for the devices with 1.2 and 1.8 nm thick buffer layers, but decreased for the rest, including the Ar plasma treated sample. It should be pointed out that the selected current density range in the comparisons is meaningful because the current density for a typical operating luminance, e.g. 100 cd/m^2 for display and 1000 cd/m^2 for lighting, is much smaller than 25 mA/cm^2. In contrast, power efficiency shown in Figure 5.17(b) change with coating thickness in a different way, in which the devices with 1.0 nm and 1.2 nm thick buffer layers as well as Ar plasma treatment possess better performance, but the devices with thicker buffer layers perform worse. As well-known, luminance (lm) is candela per square meter (cd/m^2). According to the definitions of current efficiency (cd/A)

and power efficiency (lm/W), the only difference between the two efficiencies is that, other than current density, driving voltage is also considered in the later. With increasing coating thickness, the driving voltage requested to achieve a certain current density is significantly increased, as more ITO surface is covered by the thicker insulating SiO_2. The increased driving voltage is the direct cause for the declined power efficiency with increasing coating thickness.

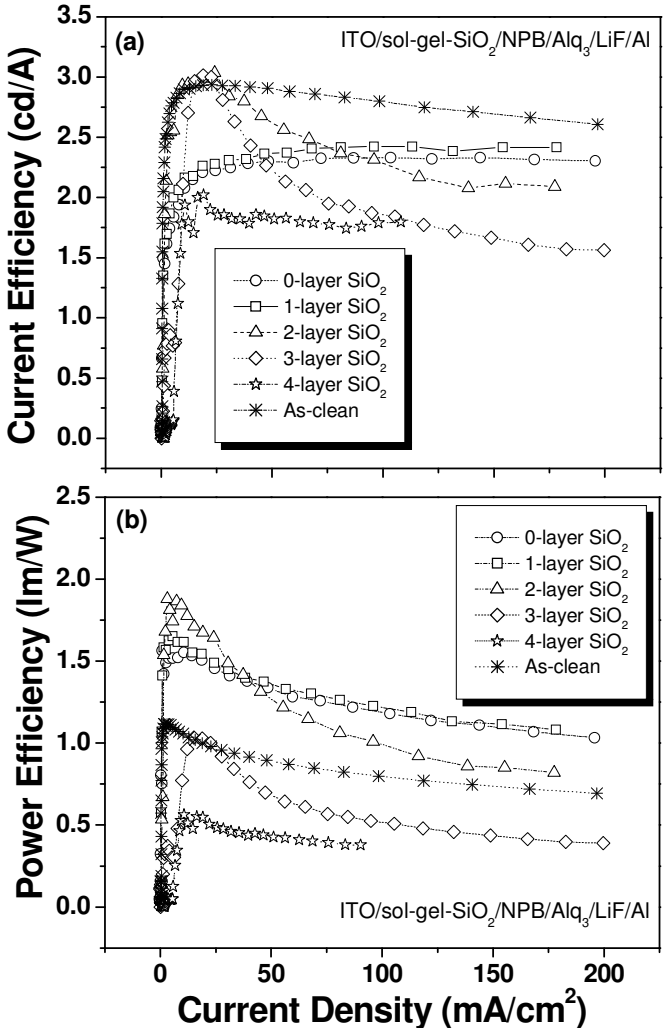

Figure 5.17. Current (a) and power (b) efficiency vs current density for OLED devices based on the ITO substrates modified by S-G SiO_2 layers in configuration of ITO/SiO_2/NPB/Alq_3/LiF/Al, showing the effect of buffer layer thickness on device efficiency. One layer is approximately corresponding to 0.6 nm in thickness.

As mentioned above, the reference device is a hole injection limited device. The enhancement in both hole injection and current efficiency in the cases of, e.g., 1.2 and 1.8 nm thick buffer layers, indicates that there is an opportunity for the reference device to further enlarge hole population so as to enhancing current efficiency. More importantly, the results in Table 5.3 show that at an operating voltage of 100 cd/m^2, the highest current efficiency of 2.53 cd/A and power efficiency of 1.85 lm/W were simultaneously achieved for the sample with 1.2 nm buffer layer, which is much better than the reference device.

5.3.3.4 Effect of Coating Processes on Device Performance

The results reveal that insulating buffer layers block hole injection by reducing the effective contact areas at the ITO/NPB interface. For the same coating process, thicker buffer layers block more holes. The hole blocking effect is also related to the coating process adopted. For example, more holes were blocked by the SAM SiO_2 than TE SiO_2 and S-G SiO_2 buffers, with similar coating thickness. This is attributed to the denser thin films produced by SAM process than TE and S-G process in this work, which has been verified by the CV results.

For an easy comparison, Table 5.4 listed some key device performance indicators from the OLED devices based on the ITO modified by TE, SAM and S-G SiO_2 buffer layers with optimized coating thickness. It is clearly seen that the device based on 2-layer (~1.2 nm thick) S-G SiO_2 buffer in combination with Ar plasma post-treatment shows the lowest turn-on voltage and operation voltages, and the highest current and power efficiencies.

Table 5.4. A comparison of key device performance indicators at 200 cd/m^2 between the OLED devices based on the ITO modified by TE, SAM and S-G SiO_2 buffer layers with the optimized thickness. V --- voltage, CE --- current efficiency, and PE --- power efficiency (lm/W).

	Turn-on V	**V@200cd/m^2**	**CE@200cd/m^2**	**PE@200cd/m^2**
TE SiO_2 – 1 nm	4.6	10.2	2.60	0.80
SAM SiO_2 – 2L	5.0	10.1	2.44	0.77
S-G SiO_2 – 2L	3.2	4.8	2.85	1.87

Section 5.3.1 revealed that buffer layer morphology was significantly different from one coating process to another, in particular the ultra thin S-G SiO_2 layer showing the netted texture. Buffer layer morphology is suspected to affect the formation of ITO/NPB interface and therefore the OLED device performance, which will be studied in Chapter 6 and discussed in Chapter 7.

5.4 Conclusion

The aim of this work is to study the effect of ITO electrodes modified by SiO_2 buffer layers on OLED device performance. E-beam thermal evaporation (TE), self-assembled-monolayer (SAM), and sol-gel (S-G) processes were used to modify ITO surface.

The TE SiO_2 thin films on ITO surfaces are in particle-stacked structure, more specifically, discontinuous and very porous. The AFM images of SAM SiO_2 coatings on ITO surfaces are featureless, implying high density and uniformity of the coatings. The SiO_2 coatings on ITO surface by S-G process are continuous and porous in the form of network. The CV results reveal that substantial amount of pores exist in the TE and S-G thin film, leading to less sensitivity of electron transfer rate to the film thickness. In contrast, 1nm thick SAM SiO_2 film sufficiently suppresses the electron transfer rate, which is another evidence to verify the high density of the SAM coatings.

The L-I-V characteristics of the OLED devices based on the ITO modified by the SiO_2 buffer layers reveal that insulating buffer layers block hole injection by reducing the effective contact areas at the ITO/NPB interface. For the same coating process, thicker buffer layers block more holes. Being of the similar thickness, the denser SAM SiO_2 blocks more holes than the porous TE SiO_2 and S-G SiO_2. By comparison, an ultra thin (~1 nm thick) S-G SiO_2 provides OLED device with the best performance, which is related to the netted texture of the S-G coated oxide film.

Chapter 6

Morphological Study of ITO/NPB Interface

Abstract

In this chapter, nucleation and growth process of the NPB hole transport layers on the ITO surfaces modified by different surface modifications are investigated using AFM to find out the factors controlling the evolution of ITO/organic interface. It is found that surface polarity is responsible for the density and distribution of NPB nucleation sites on plasma and electrochemically treated surfaces. The verdict is supported by deposition ultra thin NPB onto the Si wafer samples treated by different plasmas, where similar NPB morphologies were observed on the surfaces with similar polarities. The results obtained by deposition of NPB films on the ITO surfaces coated with insulating buffer layers, however, demonstrate that the confinement effect of the scattered buffer deposits on NPB nucleation and growth is significant.

6.1 Introduction

Although plasma treatments change both surface energy and work function of ITO electrodes [122,148], no direct correlation between the surface energy and the work function has been found and the dominant factor controlling hole injection is still under dispute. For instance, Ar plasma increases ITO surface energy rather than work function as documented in literature [115,148]. Moreover, oxidative plasma treatments of ITO improve the devices stability, which could not be explained by the work function hypothesis.

Recent experimental work [160,161] showed that OLED devices fabricated on ITO substrates with similar work functions but different surface morphologies (e.g. roughness) exhibited markedly different performance. Chen et al. [161] reported their experimental results using different HILs with different HOMOs, and concluded that the energy barrier difference at the ITO/HIL interface was not the main factor in determining the hole injection efficiency from the ITO anode to HIL. Instead, they proposed that the morphology of HIL and therefore the contact between HIL and hole transport layer (HTL) would play a decisive role in the device performance.

The results in previous chapters show that ITO surface modifications impose their influence on device performance through changing ITO surface compositions and/or morphology. In this chapter, the nucleation and growth process of NPB hole transport

layer on the modified ITO surfaces are investigated to find out the factors controlling the evolution of ITO/organic interface and its relation with hole injection.

6.2 Thin Film Growth Modes

For thin film growth on a substrate, three possible modes are distinguished [274,275]. In the “island growth”, or *VOLMER-WEBER* mode, small clusters are nucleated directly on the substrate surface and then grow and form “islands” of the condensed phase. This happens when the deposited molecules are more strongly bound to each other than to the substrate, where the cohesion energy between atoms of the deposit is larger than the adhesion energy between atoms of the substrate and the deposit. Therefore, this mode is displayed by many systems of higher surface energy materials on lower surface energy substrates, such as metals growing on insulator including many metals on alkali halides, graphite or compounds like mica.

The “layer-by-layer”, or *FRANK-VAN DER MERVE* mode, displays the opposite characteristics. In this case, the adhesion energy is much larger than the cohesion energy. Since the molecules are strongly bound to the substrate than to each other, the first molecules that condense form a complete monolayer on the surface. Subsequently, this first layer is covered by a somewhat less tightly bound second layer. This growth mode is observed in the case of adsorbed gases, such as several rare gases on graphite and on several metals in some metal-metal systems, and in semiconductor growth on semiconductors.

The “layer plus island” or *STRANSKI-KRASTANOV*, growth mode is an intermediate case. After forming the first monolayer, or a few monolayers, subsequently layer growth is

unfavorable and islands are formed on top of the intermediate layer. There are many possible reasons for this mode to occur and almost any factor which disturbs the monotonic decrease in binding energy characteristics may be cause.

Many factors influence the growth mode of thin films. One of the important factors is surface and/or interface energy. In general, a higher surface energy of the substrate is beneficial to a smooth growth of the film (i.e. layer growth mode) and a strong bonding of the film to the substrate, whereas an island growth mode is corresponding to a relatively low surface energy of the substrate. In most thin film deposition processes, nucleation of the product phase occurs heterogeneously at some preferential sites on the substrate, such as grain boundaries [279], subgrain boundaries [280], dislocations [281], or other surface defects [282-284], where the surface energy is remarkably higher than the rest of the surface. When the substrate is not uniform in surface energy, the adsorbed molecules are locked or irreversibly trapped on to the surface defects and grow into stable nuclei [283,285] because the energy barrier for nucleation is significantly lower at high surface energy areas. On the other hand, the arrived species on the lower surface energy sites tend to migrate towards the active sites and finally add onto the stable nuclei. In this case, the bonding energy between two deposited atoms is greater than the average bonding energy between a deposited atom and a substrate atom [286], leading to thin film growth in island mode [287,288].

6.3 Experimental

ITO glass and Si(111) wafer were used as the substrates for the morphological study. After the surface modifications, as described in Section 3.2 for plasma treatments, Section 4.2 for electrochemical treatments, and Section 5.2 for insulating buffer layers, NPB films with different thickness ranging from 2 to7 nm were deposited onto the modified ITO and Si substrates by thermal evaporation at a deposition rate of 0.2 nm/s and a pressure of 5×10^{-4} Pa from a quartz crucible. The film thickness was monitored by a quartz thickness monitor.

The surface morphology of the ultra thin NPB films on ITO surfaces were characterized using a Digital Instruments Nanoscope IIIA AFM. The images for the morphological studies had a scan area of 1×1 μm^2. Non-contact AFM with tapping mode was used, as the contact mode is not appropriate due to its constant force applied which is sufficient to physically distort the organic films. All AFM results are shown in phase modulation to provide a clearer picture of the organic film morphology. More information about sample pre-cleaning processes and AFM technique can be found in Chapter 2.

6.4 Results and Discussion

6.4.1 NPB Morphology on Plasma Treated ITO Surfaces

Figure 6.1 shows the AFM images of 2 nm NPB thin film (i.e., the dark phase on the images) deposited on the as-clean ITO surface (a), and the pre-treated ITO surfaces by Ar-P (b), H_2-P (c), CF_4-P (d), and O_2-P (e). It can be seen that the coverage percentage (φ) of ITO surface by the 2 nm thick NPB depends on the type of plasma treatment, in the sequence of $\varphi_{CF4\text{-}P} > \varphi_{O2\text{-}P} > \varphi_{Ar\text{-}P} > \varphi_{as\text{-}clean} > \varphi_{H2\text{-}P}$. For the as-clean, Ar-P and H_2-P treated ITO surfaces, island-like morphology (i.e., *VOLMER-WEBER* growth mode) is observed, although there are slight differences in shape and distribution. Basically, the islands discontinuously distribute along grain boundaries, but the wetting features of NPB on the three substrates are clearly different, with wettability in an order of Ar-P>as-clean>H_2-P. On the contrary, CF_4-P and O_2-P treatments of ITO led to more uniform NPB thin film coverage without conglomeration, and the NPB films grow in a mode similar to *FRANK-VAN DER MERVE* mode. In this case, NPB film covers not only the grain boundaries but also the sub-grain boundaries, although subgrains are not fully covered. It is observed that the CF_4-P treatment led to more subgrains covered by the 2 nm thick NPB film than the O_2-P treatment. Considering the fact that deposition rate and substrate temperature strongly influence the surface morphology of organic films [277,278], the NPB of a given thickness was deposited onto the ITO samples in discussion in the same batch and thus the morphological difference is caused by the different plasma treatments.

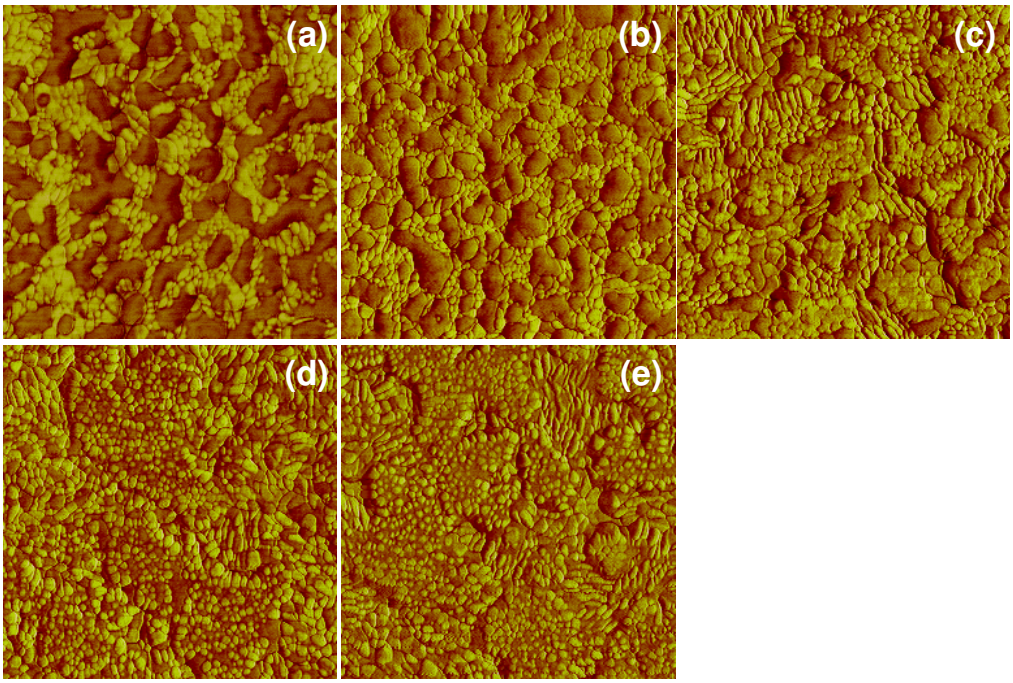

Figure 6.1. AFM (phase mode) images of 2 nm thick NPB on the ITO surfaces with different plasma treatments: (a) as-clean; (b) Ar-P; (c) H_2-P; (d) CF_4-P; (e) O_2-P. The dark phase on the images is NPB thin film. The scan area is 1×1 μm^2.

Figure 6.2 shows that, except for the H_2-P treated sample, 7 nm thick NPB almost fully covers the ITO surfaces pre-treated by Ar-P, O_2-P and CF_4-P plasmas. Once the ITO surface is fully covered by the NPB deposit, the interface evolution is completed and the growth of NPB thin film is then dependent of the NPB film surface conditions and the temperature rather than the film-substrate interaction [289]. In other words, the effect of ITO surface properties on NPB growth mode is gradually diminished and eventually disappeared with the increasing NPB thickness. This can be clearly seen by comparing Figure 6.1 and Figure 6.2.

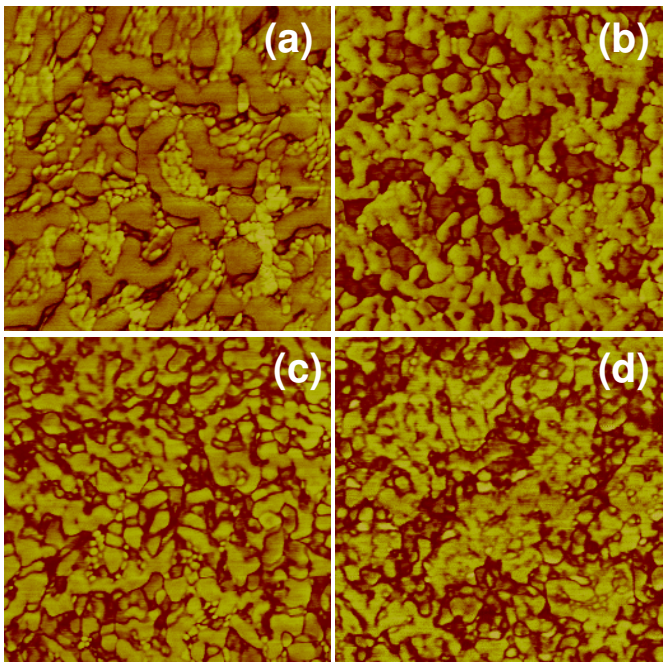

Figure 6.2. AFM (phase mode) images of 7 nm thick NPB on the ITO surfaces with different plasma treatments of H_2 plasma (a); Ar plasma (b); CF_4 plasma (c); and O_2 plasma (d). The dark phase on the images is NPB thin film. The scan area is 1×1 μm^2.

6.4.2 NPB Morphology on Electrochemically-Treated ITO Surfaces

Figure 6.3 shows the phase AFM images of 2 nm NPB thin film deposited on the ITO surfaces treated by 0V (a), +1.2 V (b), +1.6 V (c), +2.0 V (d), +2.4 V (e), and +2.8 V (f), respectively. It can be seen that the surface covering of the 2 nm thick NPB depends on the treating voltage. Island-like morphology is observed for all the electrochemically treated ITO surfaces, although there are differences in shape and distribution. Basically, the NPB islands discontinuously distribute along grain boundaries. It is obvious that +2.0 V and +2.4 V treatments lead to more uniform covering of NPB thin film on the ITO surface. In comparison, the pre-treatment at +2.0 V is preferred due to the indiscernible

conglomeration of the NPB phase on the sample surface. Similar to the case of plasma treatment, the deposition of NPB on all the ITO samples was carried out in the same batch, and thus the morphological difference is attributed to the different treating voltages.

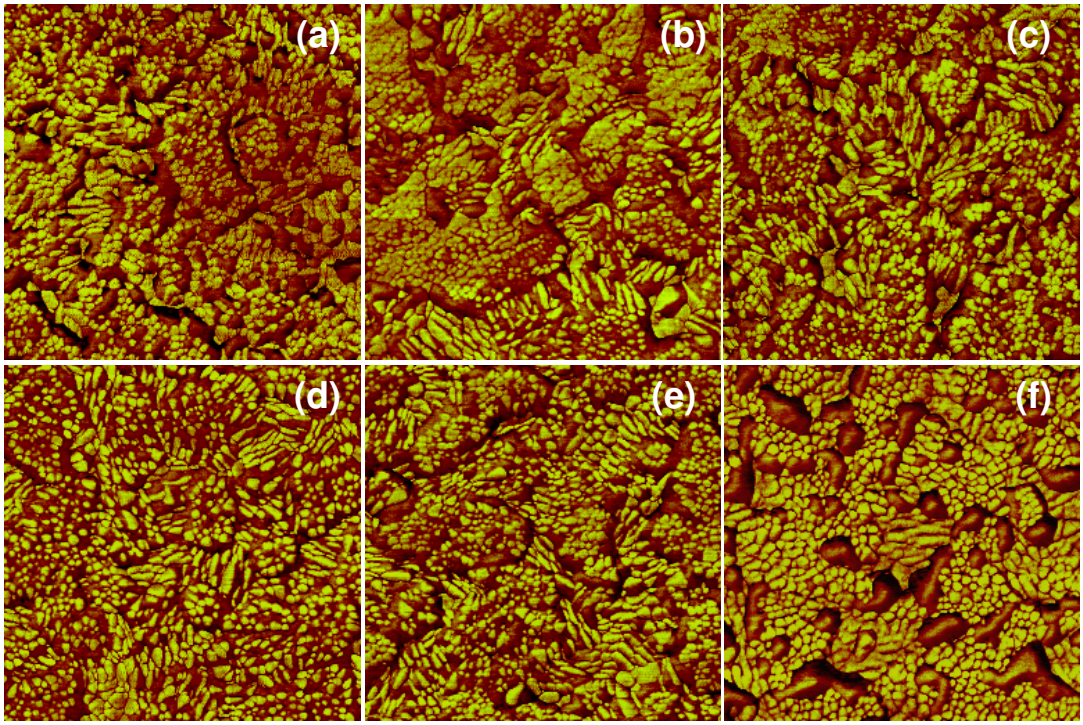

Figure 6.3. AFM (phase mode) images of 2 nm thick NPB on the ITO surfaces pretreated at different voltages: (a) 0 V; (b) +1.2 V; (c) +1.6 V; (d) +2.0 V; (e) +2.4 V; (f) +2.8 V. The NPB deposits are the dark areas on the images. The dark phase on the images is NPB thin film. The scan area is 1×1 μm^2.

Figure 6.4 shows that 5 nm thick NPB almost fully covers the electrochemically treated ITO surfaces. However, their dissimilarities in morphology become more considerable. For example, a fine and continuous layer of 5 nm thick NPB thin film was observed on the ITO surface treated by +2.0 V, whereas coarse and large islands become the dominant feature for the samples treated by 0 V, +1.2 V and +2.8 V. Compared with the case of 2 nm NPB, it can be found that the nucleation sites do not significantly increased with

further deposition and that the increase in surface coverage relies on NPB lateral growth of the nuclei until they coalesce. Therefore, morphology of the first layer NPB depends on the interaction between the organic molecules and the substrate until the ITO surface is fully covered by the NPB clusters. In practice, a few layers of uniform film may be required to disencumber the influence from the substrate [289], as the ITO surface is highly uneven in properties.

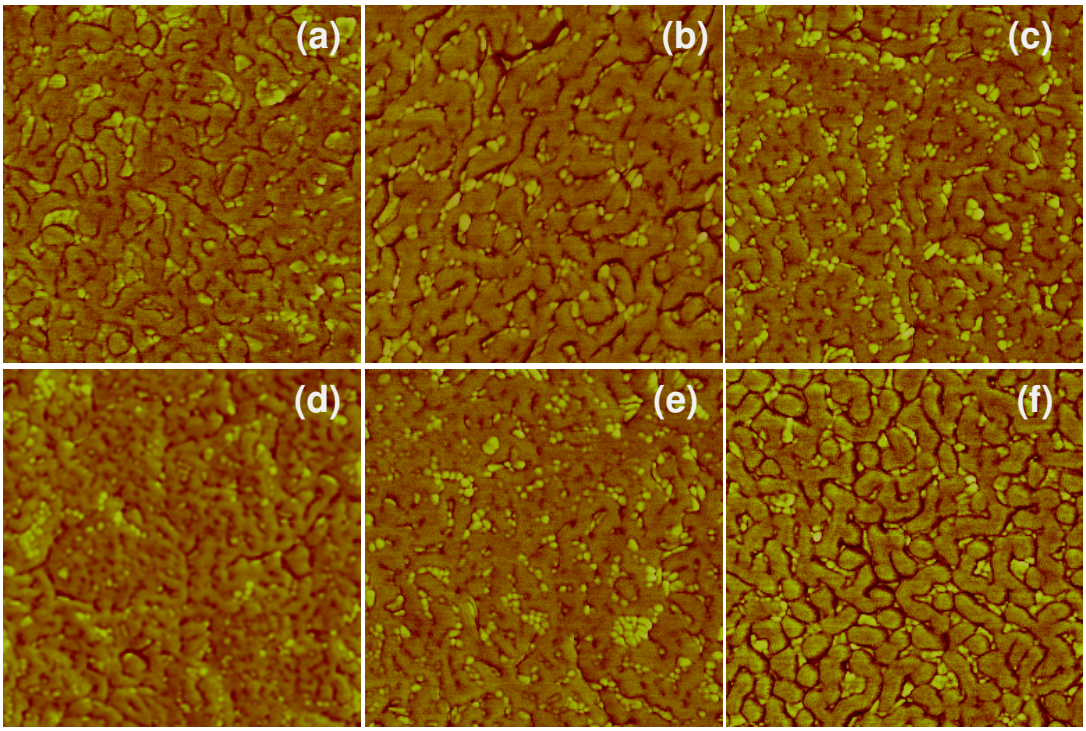

Figure 6.4. AFM (phase mode) images of 5 nm thick NPB on the ITO surfaces treated with at voltages: (a) 0 V; (b) +1.2 V; (c) +1.6 V; (d) +2.0 V; (e) +2.4 V; (f) +2.8 V. The dark phase on the images is NPB thin film. The scan area is 1×1 μm^2.

6.4.3 Influence of Surface Energy and Polarity

The results in Chapter 3 and Chapter 4 demonstrate that the electrochemical and plasma treatments significantly change the ITO surface polarity, χ_P. Comparisons of the surface polarities in Table 3.3 and Table 4.5 with the AFM images in Figure 6.1 and Figure 6.3, respectively, a conclusion is reached that the polarity of ITO surface is correlated to the morphology of NPB thin film via governing the NPB nucleation and growth, and the higher the surface polarity, the more uniform the NPB thin film. For example, the higher polarity for the samples electrochemically treated at +2.0 V (χ_P=0.87) and plasma treated with CF_4 (χ_P=0.87) is corresponding to fine NPB thin film and high covering of the ITO surface, whereas the lower polarity for the samples electrochemically treated at +2.8 V (χ_P=0.42) and treated by H_2 plasma (χ_P=0.62) lead to coarse NPB thin film and low covering of the ITO surface.

To further verify the conclusion, 2 nm thick NPB was deposited on Si wafers treated by Ar, H_2, CF_4, and O_2 plasmas, respectively. The corresponding AFM images are shown in Figure 6.5. The values of total surface energy (γ_S) and surface polarity (χ_P) are also given in the figures. Different plasmas cause a change of 33% in γ_S, from the minimum of 54.9 mJ/m^2 for CF_4-P to the maximum of 72.9 mJ/m^2. However, only 5% difference in χ_P is found between the minimum and the maximum values. On the other hand, the morphologies of 2 nm thick NPB on the four samples wondrously resemble, in terms of shape, distribution and surface coverage. It is surface polarity that control the nucleation and initial growth of NPB film on ITO and Si substrates.

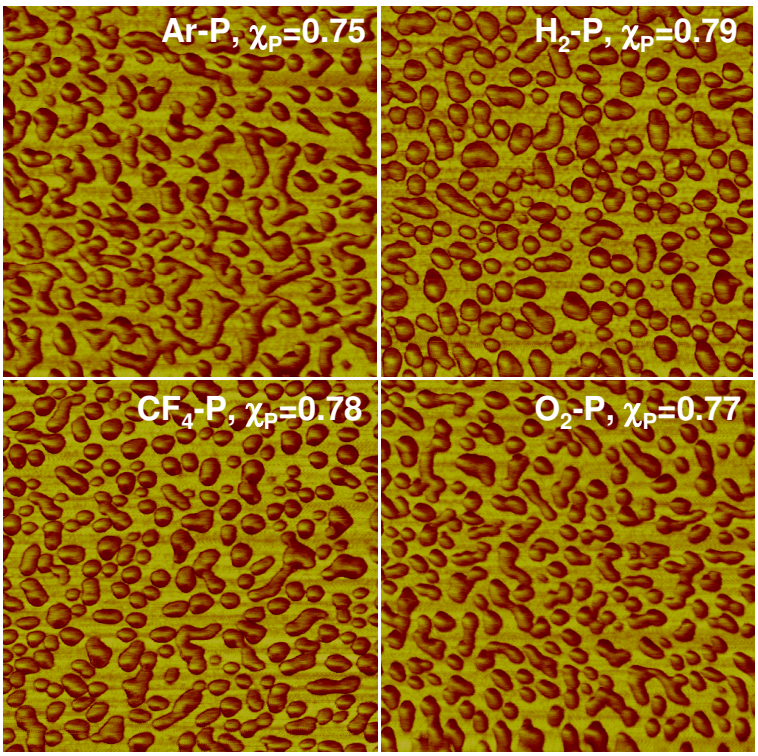

Figure 6.5. AFM (phase mode) images of 2 nm thick NPB on the Si wafer surfaces treated by different plasmas marked on the images. The values of surface polarity (χ_p) displayed on the images are from Table 3.4. The dark phase on the images is NPB thin film. The scan area is 1×1 μm^2.

6.4.4 Ultra Thin Buffer Layers and Their Influence on NPB Morphology

Figure 6.6 shows the AFM images of 2 nm NPB thin film on ITO surfaces modified by Ar plasma and coated by sol-gel (S-G) SiO_2 with different thicknesses: (a) Ar-P, (b) 1.2 nm, (c) 1.8 nm, and (d) 2.4 nm. It should be noted that the particles with size of 80-100 nm are discernible, which are suspected to originate from sol-gel solution and pass through the 0.2 μm filter.

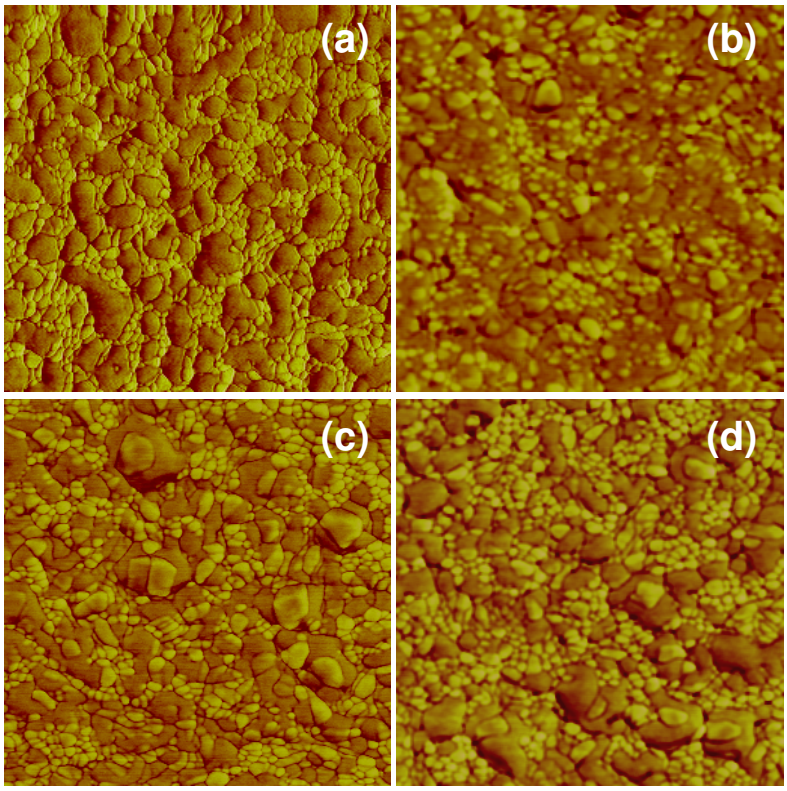

Figure 6.6. AFM (phase mode) images of 2 nm thick NPB thin film on the ITO surfaces modified by Ar plasma and S-G SiO_2 with different thicknesses: (a) Ar-P, (b) 0.6 nm, (c) 1.2 nm, and (d) 1.8 nm. The dark phase on the images is NPB thin film. The scan area is $1\times1\ \mu m^2$.

Compared with the isolated NPB islands on the Ar-P sample surface shown in Figure 6.6(a), the uniformity of NPB film is significantly improved on the ITO surface coated with 1.2 nm S-G SiO_2, as shown in Figure 6.6(b). In particular, no island-like morphology is observed. However, with increasing S-G layer thickness, the continuity of the NPB film becomes worse, as shown in Figure 6.6(c) and 6.6(d). This implies that the ITO surface areas without coating are the preferential sites for NPB film nucleation. This can be further confirmed by the morphology of thicker NPB deposits.

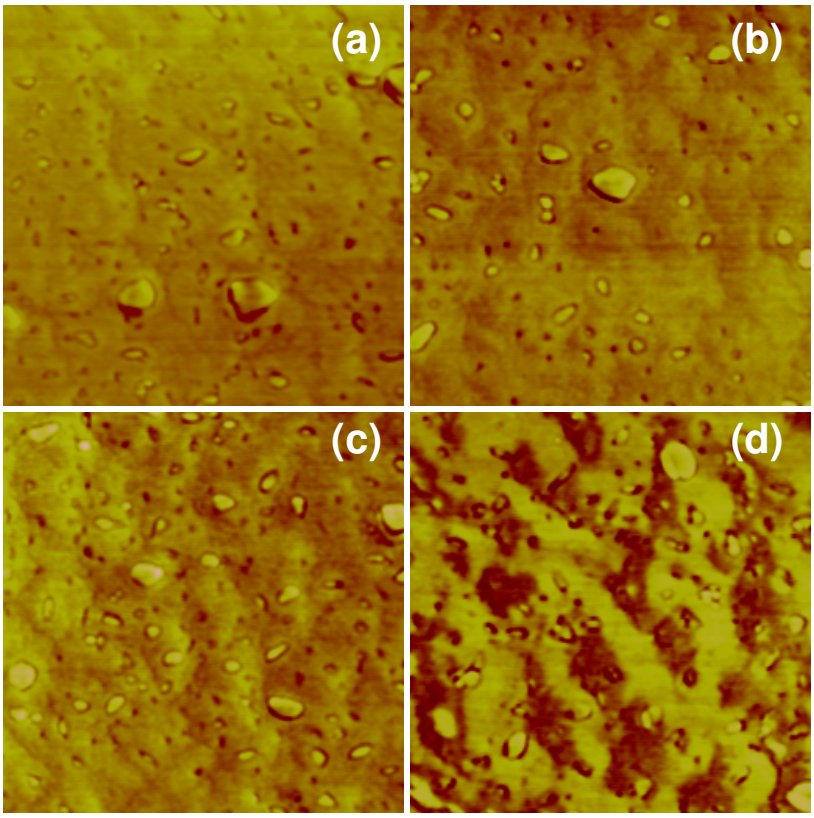

Figure 6.7. AFM (phase mode) images of 7 nm thick NPB thin film on the ITO surfaces modified by S-G SiO_2 buffer layers with different thicknesses: (a) 0.6 nm, (b) 1.2 nm, (c) 1.8 nm, and (d) 2.4 nm. The dark phase on the images is NPB thin film. The scan area is 1×1 μm^2.

The S-G modified ITO surfaces were coated with 7 nm thick NPB film, as shown in Figure 6.7. It is obvious that the thicker S-G layer means higher coverage of SiO_2 deposit on ITO surface, and more NPB thin film is therefore deposited on SiO_2 film than ITO surface. It is clearly seen that the NPB films become coarser with increasing S-G layer thickness from 0.6 to 2.4 nm. In particular, a distinctly wavy NPB film can be observed on the 2.4 nm S-G coated ITO sample, as shown in Figure 6.7(d). This is attributed to the reduction of the ITO surface areas without coating, which are preferential sites for NPB nucleation.

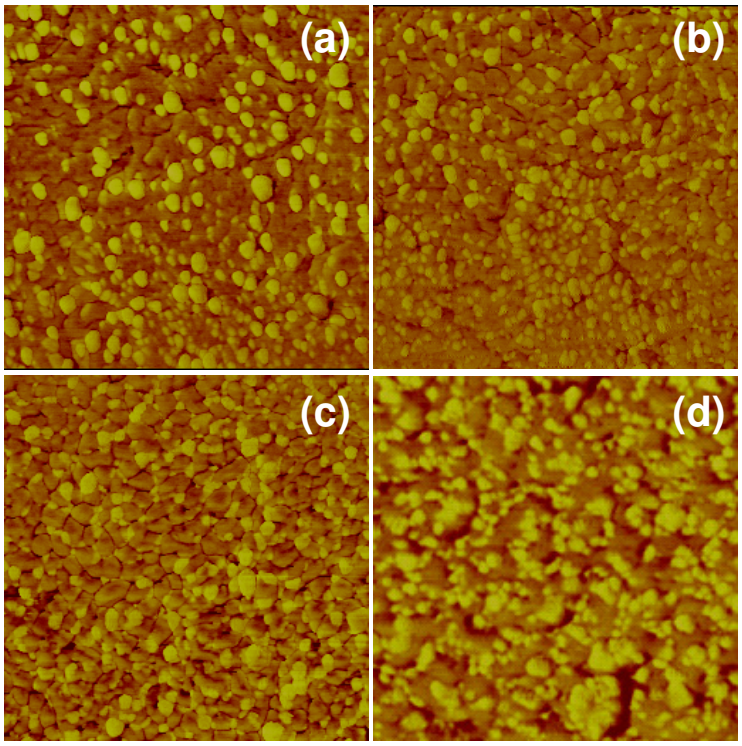

Figure 6.8. AFM (phase mode) images of 2 nm thick NPB thin film on the ITO surfaces modified by (a) 0.5 nm, (b) 1 nm, (c) 2 nm, and (d) 5 nm TE SiO_2 buffer layers. The dark phase on the images is NPB thin film. The scan area is 1×1 μm^2.

Similar to the S-G coated ITO samples, the morphological dependence of NPB thin film on the buffer layer thickness were also observed on the ITO surface modified by thermally evaporated (TE) SiO_2 layers, as shown in Figure 6.8 and Figure 6.9. When the film thickness is increased from 0.5 to 1 nm, the uniformity of 2 nm NPB film is slightly improved, with less island-like feature. However, the island-like characteristics of 2 nm NPB film become more perceptible with increasing the TE SiO_2 layer thickness, in particular, for the sample with 5 nm SiO_2 buffer layer, as shown in Figure 6.8(d).

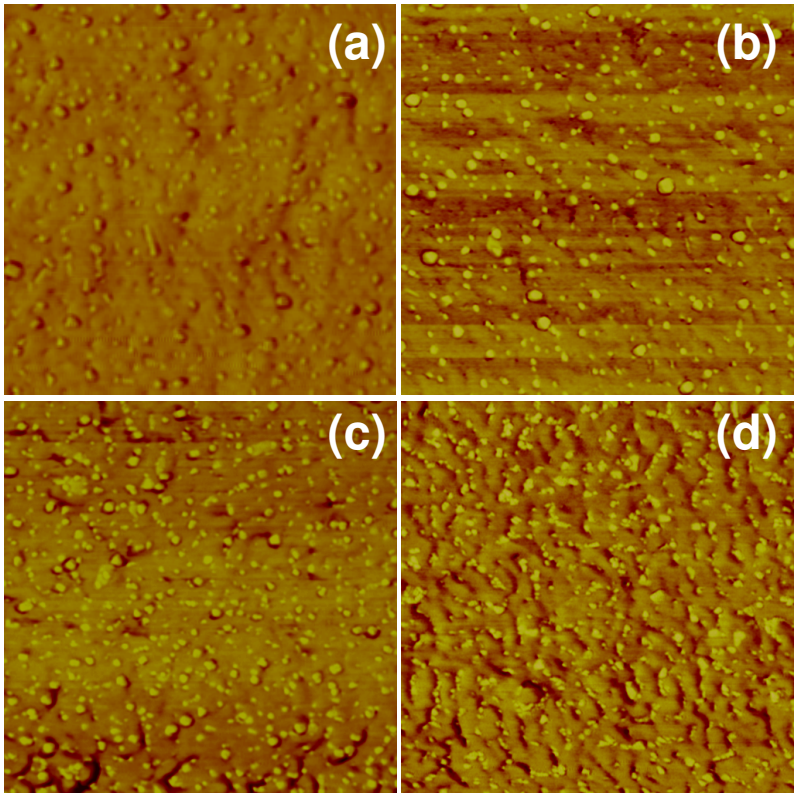

Figure 6.9. AFM (phase mode) images of 7 nm thick NPB thin film on the ITO surfaces modified by (a) 0.5 nm, (b) 1 nm, (c) 2 nm, and (d) 5 nm TE SiO_2 buffer layers. The dark phase on the images is NPB thin film. The scan area is 1×1 μm^2.

This effect of TE SiO_2 buffer layers on NPB nucleation and growth is enlarged when 7 nm thick NPB thin film is applied on the modified ITO surfaces. Figure 6.9 shows that with increasing S-G layer thickness, the NPB film becomes more crimpled and more substrate surface is exposed. This is attributed to incompatibility of SiO_2 film with the NPB film, as the coarsest NPB film was observed on the 5 nm SiO_2 coated ITO surface, where the ITO surface is fully covered by the TE SiO_2 buffer layer, as shown in Figure 5.1.

Chapter 5 has revealed that SiO_2 thin film thermally evaporated on ITO surface at room temperature takes island growth mode, and that the SiO_2 phase in a form of particle scatters across ITO surface. In the present study, the ITO surface could not be fully covered with a TE SiO_2 layer thinner than 5 nm. In particular, when 1 nm SiO_2 is deposited on to an ITO surface, as shown in Figure 6.10, the surface coverage seems to be much less than 10%. Because the ITO surface is not so flatten for clear identification of SiO_2 phase coverage, 1 nm thick SiO_2 was deposited on a Si wafer surface treated by Ar plasma as described in Chapter 3. Figure 6.10(b) shows that the 1 nm thick SiO_2 distributes on the Si surface in particles and the surface coverage is about 15%. More importantly, the presence of SiO_2 islands results in uniform distribution of NPB deposit on both ITO and Si surfaces. Figure 6.10(c) and 6.10(d) demonstrate that the initial deposit of NPB on the SiO_2 modified surfaces covers the exposed ITO or Si first, instead of TE SiO_2 deposit.

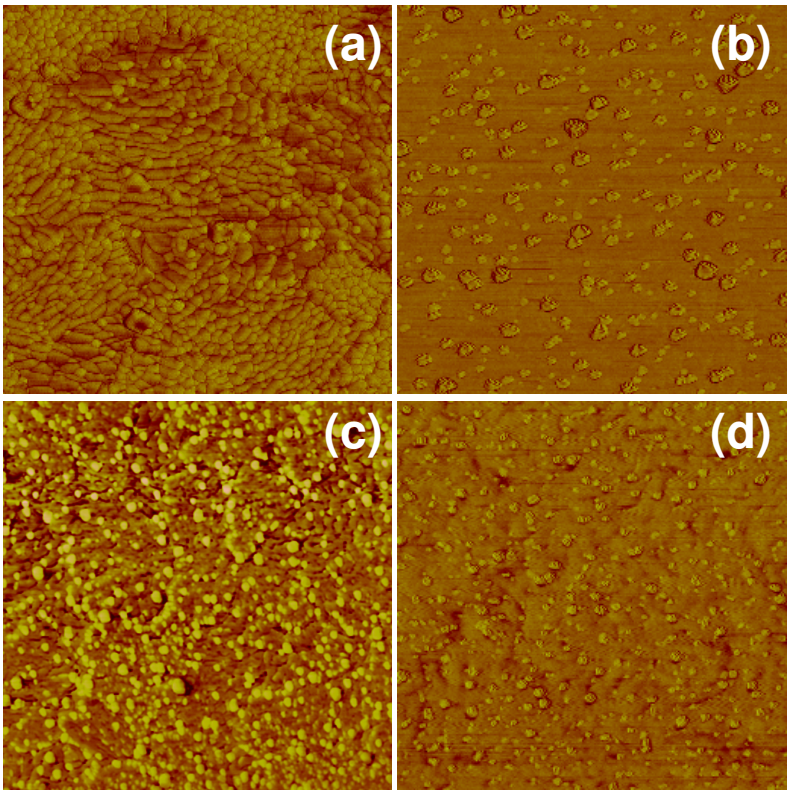

Figure 6.10. AFM (phase mode) images of 1 nm TE SiO_2 buffer layers on the ITO (a) and Si wafer (b) surfaces and of 2 nm NPB on the TE SiO_2 modified ITO (c) and Si wafer (d). The dark phase on the images is NPB thin film. The scan area is 1×1 μm^2.

The results in Chapter 3 have shown that NPB thin film grows on Ar-P treated Si surface in island mode. In comparison, the uniform NPB thin film shown in Figure 6.10(d) is clearly caused by the SiO_2 particles. It is reasonable to deduce that the SiO_2 particles increase the lateral diffusion energy barrier that confines the NPB molecules in a small area without further coagulations into islands. The SiO_2 particles, therefore, act as "anchors" to fix the organic molecules nearby. Moreover, the steps formed between the SiO_2 particles and the Si substrate are preferential sites for NPB nucleation.

In actual applications, the nominal thickness of the thermally evaporated insulating buffer layer is usually controlled within 1 nm for improving device performance. In this case, the

insulating materials are discontinuously distributed in a particle format, with covering percentage of less than 10-15%. In other words, more than 85-90% of the ITO surface coated with the ultra thin buffer layer exposes directly to the NPB molecules rather than the insulating materials. The coating coverage situation for S-G buffer layer is similar, although the differentiation in morphology. The findings suggest that the tunneling model frequently used for discussion over the effect of insulating buffer layer on hole injection efficiency is invalid in this study.

6.5 Conclusion

By using AMF analysis, nucleation and initial growth of NPB films on the ITO surfaces modified by different processes. The results show that the nucleation and initial growth modes of NPB films on the plasma- and electrochemically-treated ITO surfaces are correlated to the type of plasma and the electrochemical treatment voltage, respectively. For plasma and electrochemical treatments, the polarity of ITO surface affects the morphology of NPB thin film via governing the NPB nucleation and growth. More uniform and finer NPB deposit is corresponding to the higher surface polarity. However, the effect of the ITO surface property on NPB morphology is diminished once the ITO surface is fully covered by the NPB deposit.

More uniform NPB films on the ITO surfaces with ultra thin SiO_2 buffer deposits, which is attributed to the creation of more nucleation sites and shorten the lateral diffusion length of the adsorbed NPB molecules. However, with increasing the buffer layer thickness, the NPB films become coarser due to the incompatibility of NPB with SiO_2. It is also concluded that buffer layers thinner than 1 nm is not continuous on the ITO surface and its surface coverage is less than 10-15% for S-G and TE SiO_2 coatings, and therefore the tunneling model for hole injection is not applicable in this study.

Chapter 7

Discussion

Abstract

In this chapter, phenomenal models of ITO/NPB interface evolution are proposed to have good understanding of the mechanisms behind the improved device performance by different ITO surface modifications, in particular, the effect of surface modification the hole injection. The influence of hole injection on EL efficiency is also discussed.

7.1 Introduction

The results in this study show that the OLED device performance is correlated to the ITO surface properties that are suspected to have influence on the evolution of electrode/organic interface.

Chapter 3 and Chapter 4 demonstrate that plasma and electrochemical treatments of ITO surface introduce significant changes in chemical composition of ITO surfaces, which is generally believed to be the major factor controlling ITO surface WF by changing surface dipoles. Although WF is not the only surface property that is controlled by surface chemical states, change in WF is usually the first concern when the influence of surface treatment on device performance is discussed. This is because WF is the key parameter in modeling the electronic structure at ITO/organic interface. The influence of WF on the hole injection across ITO/organic has been well discussed in literature by using energy band theory [122,131,148,157,158]. It is generally accepted that the increased WF, i.e. lowering Fermi energy level (presented as the change in WF here, $\Delta\Phi$) via negative dipoles produced by surface treatments, reduces the energy barrier for holes' getting over the ITO/HTL interface, and therefore the driving voltage, as schematically shown in Figure 7.1.

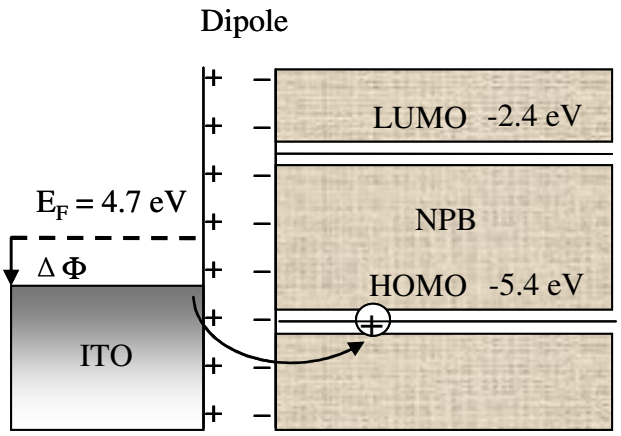

Figure 7.1. Schematic energy band diagram showing the reduced energy barrier for hole injection through increased surface WF by oxidative surface treatments.

It is clear that the intrinsic WF of the bulk ITO (Φ_{Bulk}) is conceptually different from the surface WF (Φ_{Surf}), as the former is entirely dependent of crystallinic structure rather than surface dipole. Therefore, surface WF can be presented as:

$\Phi_{Surf} = \Phi_{Bulk} + \Delta\Phi$

For negative dipole (point inwards) $\Delta\Phi$ is positive, and vice-versa for the positive dipole.

The $\Delta\Phi$ induced by surface treatments decays over time and returns to its original value within hours [120,128,259]. The ultimate cause of this erratic increase of WF is yet to be understood. Possible explanations include the diffusion of high concentration oxygen on ITO surface into the ITO bulk [299] and/or adsorption of ambient carbon during handling [300-302]. It is clear that the later can be avoided by preventing the treated samples from exposing to atmosphere. It is reasonable to deduce that if the former speculation is true, the improvements of OLED performance would be diminished correspondingly with the

decay of ITO WF, according to the energy band theory. However, there has been no such report on device instability attributed to the oxygen plasma treatment. Some results showed that oxygen-plasma treatment of the ITO anodes gives the highest operational stability and efficiency of polymer LEDs, even when an aqueous based PEDOT:PSS [Poly(3,4-ethylenedioxythiophene) poly(styrenesulfonate)] is used as the hole injection layer [115]. This result is clearly inconsistent with WF explanation, as ITO surface WF is independent of dehydoxylation and rehydroxylation [222].

Moreover, the WF elucidation has been intensively questioned partially due to the invalidity of Schottky-Mott model for organic semiconductors, which is mainly caused by vacuum shift at the ITO/organic interface [41,44], as shown in Figure 1.6, and no charge transfer cross the junction [49,63]. Years ago, in fact, surface WF was proven to be significantly changed as soon as atoms or molecules are deposited onto the surface under consideration [303]. The immediate consequence of the vacuum level shift is that the overall change in energy barrier is small or even zero, as the increased surface dipoles move downward not only the ITO Fermi level but also the vacuum level at the interface [162]. This conclusion is supported by many experimental results. For example, a markedly different performance was observed on the devices with ITO films being of similar work functions but different morphologies [160]. Chen et al. [161] recently reported their experimental results using different HILs being of varied HOMO levels, and concluded that the energy barrier difference at the ITO/HIL interface was not the main factor in determining the hole injection from the ITO anode to HIL. They proposed that besides the WF, other surface properties are also play an important role in influencing hole injection and device performance [115,124,211,212], one of which is surface energy [123].

Plasma treatments change not only ITO work function but also surface energy based on dipole theory [115,122,148]. Surface energy of a crystal is the energy required, per unit area of new surface formed, to split the crystal in two along a plane [304,305]; while WF is equal to the minimum work that must be done to remove an electron from the highest energy state of a solid to infinity at 0 K [306-308]. The two surface properties are conceptually different because WF is basically related to electromagnetic force, while surface energy is related to both electromagnetic force and nuclear force that has unknown quantitative expression. Although some efforts have been put to correlate the two surface properties [309,310], no quantitative expression for the correlation is yet reached. Furthermore, both theoretical calculations and experimental measurements over 40 closely-packed elemental metals [311] show that there is indeed no consistent relation existed between WF and surface energy. It is expected that the situation is much more complex in the study of compound systems, such as ITO. This suggests that the two surface properties may not be governed by the identical factors and in the same way.

In this chapter, the hole injection mechanisms behind ITO surface modifications with emphasis on the factors rather than WF.

7.2 Phenomenal Model of ITO/HTL Interface Evolution

The results in Chapter 6 clearly show that ITO surface properties have critical influence on the morphology of NPB film. In particular, the polarity of ITO surface controls the initial growth mode of NPB film, which thereafter is a determinant factor influencing OLED performance. Furthermore, the morphological studies suggest that the high density of nucleation sites and more uniform NPB layer promote hole injection from ITO to NPB layer. As discussed previously, the performance of OLEDs is strongly influenced by the properties of the interface between the organic layers and electrodes and a better electrical contact between the two materials is expected to enhance the charge carrier injection through the interface. From micro point of view, however, the interfacial properties are varied over the ITO surface due to the inhomogeneous HTL nucleation.

It is believed that a good contact is formed at the nucleation NPB sites on ITO surface, compared with the neighboring areas, in terms of mechanical, electrical and electronic properties. This is because, at preferential nucleation sites, the interaction between absorbing molecules and the substrate surface is stronger due to the higher overlap of electron clouds, resulting in more stable interface with lower energy. A better electrical contact at the preferential nucleation sites results in “active” spots being of lower barrier to hole injection and/or lower resistance to current flow. Driving voltage, a macro property of OLED associated with hole injection efficiency, is then controlled by the number of such active spots, i.e., the higher the spot density, the lower the driving voltage.

In addition, the electrical properties at the interface are also influenced by the effective interface area. As well-known, a deposition process producing islands on the surface inevitably leads to shadowing of portions of the surface from the incoming flux as islands come together. When atoms do not move sufficiently after deposition to fill gaps and shadows between coalescing islands, the result is narrow voids between adjacent grains in the film. This situation is severe in the case of large island on a rougher and poorly wetted surface. The interfacial voids obviously reduce the effective contact area between ITO and NPB, and therefore the number of active spots, which deteriorates hole injection further.

Another point should be addressed is the influence of ITO grain boundaries on carrier injection, where contains so large number of crystal misfits and defects that they are of properties of amorphous materials [232]. It was previously shown that polycrystalline ITO films allow for more efficient electron transfer than amorphous films [213]. Unfortunately, grain boundaries and other defects are often the preferential nucleation sites due to their higher surface energy than the polycrystalline surfaces. As a consequence, poor hole injection is frequently observed in the device based on an untreated ITO surface.

In regard of active spots, the actual situation is much more complicated, as the electrical properties of the active spots are varied from one to another due to the surface inhomogeneity. Therefore, the term of “active” is very conceptual and relative and the number of the active spots changes with electric field. This means that charge carriers can also be injected through other areas besides the indicated active spots, however, the voltage required to activate the so-called inactive areas is higher due to their higher interface barrier caused by poorer electrical contact.

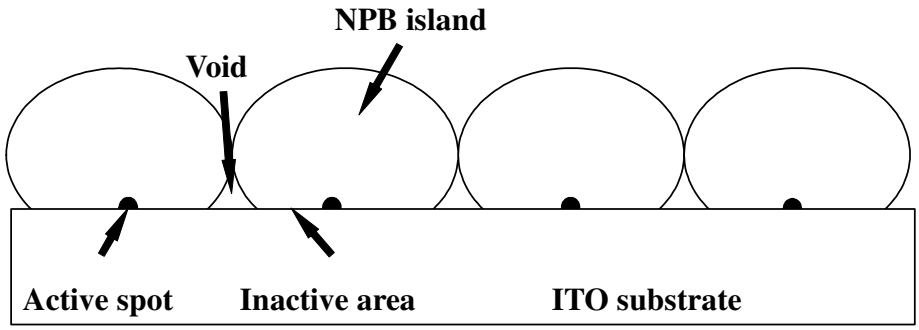

(a)

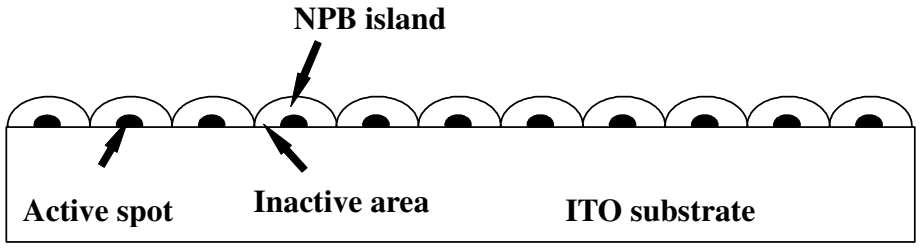

(b)

Figure 7.2. Schematic elucidation of active, inactive and void areas for NPB film on ITO substrates with lower surface energy (a) and higher surface energy (b).

For treated ITO surfaces with low surface polarity, the preferential nucleation sites are mainly located on the grain boundaries, as shown in Chapter 6, leading to fewer active spots for carrier passing through at a given voltage, as depicted in Figure 7.2(a). This is true for the samples of as-clean, H_2-P, ECT+1.2V and ECT+2.8V. On these samples, NPB film nucleates mainly along grain boundaries with low density of nucleation sites. The effectiveness of the "active" spots along the grain boundaries on hole injection is therefore discounted, as higher energy barrier exists on the grain boundaries.

By contrast, oxidative surface treatment, such as O_2 and CF_4 plasmas and electrochemical treatments at +2.0 and +2.4 V, significantly "passivate" ITO surface through removing the active sites on the grain boundaries. In other words, the high surface polarity obtained by the oxidative treatments can effectively suppress the preference of grain boundaries for nucleation. A result of the oxidative surface treatments is denser and more uniform nucleation over ITO surface, leading to smaller nucleus size and thus more active spots, as depicted in Figure 7.2(b). Furthermore, the resulted good wetting morphology can effectively reduce the possibility of voiding and therefore increase the actual contact areas. It is speculated that the void effect on device performance becomes more visible at high driving voltage, where carriers will be injected through both the active and the inactive areas but not the voids.

7.3 Phenomenal Models of EL Efficiency Controlled by Charge Injection

As described in Chapter 1, in an typical bilayer OLED device, the injected charges with opposite signs are transported in the applied field towards the counter electrode through HTL (e.g., NPB in this study) for holes and ETL (e.g., Alq_3) for electrons and finally recombine and form excitons in EML (e.g., Alq_3), which then decay either radiatively or nonradiatively. Understanding the charge transport is very important in discussion over the effect of hole injection on EL efficiency.

There are a number of factors influencing the charge transport. Due to the disorder of the organic semiconductors charge carrier transport in organic materials is to be described by hopping between sites with different energy and distance. Additionally, the injected charge carriers can be intermittently trapped in gap states originating from impurities or structural traps, which are mostly the exciton quenching sites. Both the intrinsic hoping transport and the presence of band-gap energy states are responsible to the resulted low carrier mobilities, which are typically between 10^{-3} and 10^{-7} cm^2/V s at room temperature and in many cases strongly depend on temperature and the magnitude of the applied electric field [327].

In addition, charge accumulation at interfaces must be taken into account. For a device with the typical structure of ITO/NPB/Alq_3/Al, it is unavoidable for the injected charges to accumulate at the NPB/Alq_3 interface due to the presence of energy barriers for holes and

electrons, as schematically shown in Figure 7.3 without consideration of the band gap states.

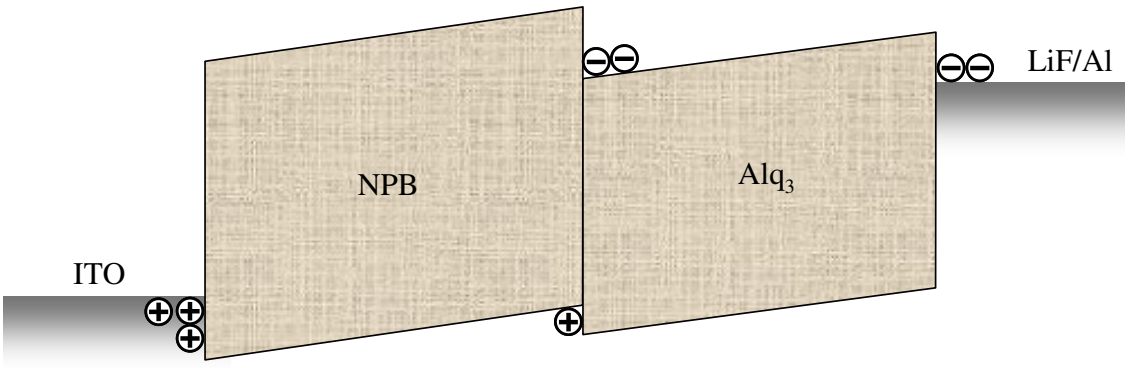

Figure 7.3. Schematic energy level diagram of an NPB/Alq_3 double-layer device with ITO as hole injection electrode and LiF/Al as electron injection electrode, showing the imbalanced charging at the NPB/Alq_3 hetero-junction.

As the overall device is neutral, the imbalance accumulation of the opposite charges at the interface is able to change the electric field redistribution. For instance, if the number of electrons exceeds that of holes at the interface as shown in Figure 7.3, the electric field strength will be increased in NPB but decreased in Alq_3. The field redistribution due to the imbalanced charging at the interface has influence of charge injection and mobility to certain extent. It should be kept in mind that the situation of imbalanced charging at the interface may be altered with changes in organic/electrode interfaces governing charge injection and overall field strength influencing both charge injection and mobility. Similarly, the space charge caused by the excessive charge injection with respect to the lower charge-drift mobility can also change the field redistribution.

It is conventionally accepted that turn-on voltage is controlled by hole injection; but EL efficiency by electron injection [25,26], and that an opposite effect of ITO surface modification on driving voltage and EL efficiency has been frequently reported. More

specifically, enhancement of hole injection generally results in lowering current efficiency, which has been attributed to excessive hole injection. Apart from previous reports, the results obtained from the devices with electrochemically treated ITO show that simultaneous improvement of both hole injection and EL efficiency is possible by using optimized pre-treating processes. The mechanism behind is clearly important for device design and fabrication aiming at high performance.

Besides the nonradiative triplets in fluorescent materials, which set a theoretical top limit of 25% in quantum efficiency [328,329], exciton quenching in particular at interfaces has a great influence on device efficiency [13]. Therefore, the location of recombination zone in the emitting layer takes a critical role in EL efficiency for a given device structure, which is highly correlated to the mobilities of the opposite charges as well as the position and density of the exciton quenching sites. As mentioned above, in Alq_3 layer, there are a lot of electron traps near NPB/Alq_3 and Alq_3/LiFAl interfaces, which are most likely formed due to the interaction between the two electron systems and/or their structural changes during the interface evolution. These electron traps possess varied energies located between LUMO and HOMO levels, i.e., band gap states. The injected higher energy electrons at LUMO level are inclined to filling the lower energy traps. In addition, the electrons trapped in the band gap states are also transfer mutually, most likely from higher energy traps to the lower ones. If the trapped electrons are unable to be re-excited into LUMO level by higher electric field, they will be captured by the holes from the counter electrode with nonradiative decay to the ground state. Therefore, recombination in the trap concentrated zone, such as zone A and zone C in Figure 7.4, definitely leads to lower EL efficiency. In contrast, an ideal recombination zone is in such an area that is far

enough from the interfaces, such as zone B shown in the same figure, as more excitons in this region will decay radiatively.

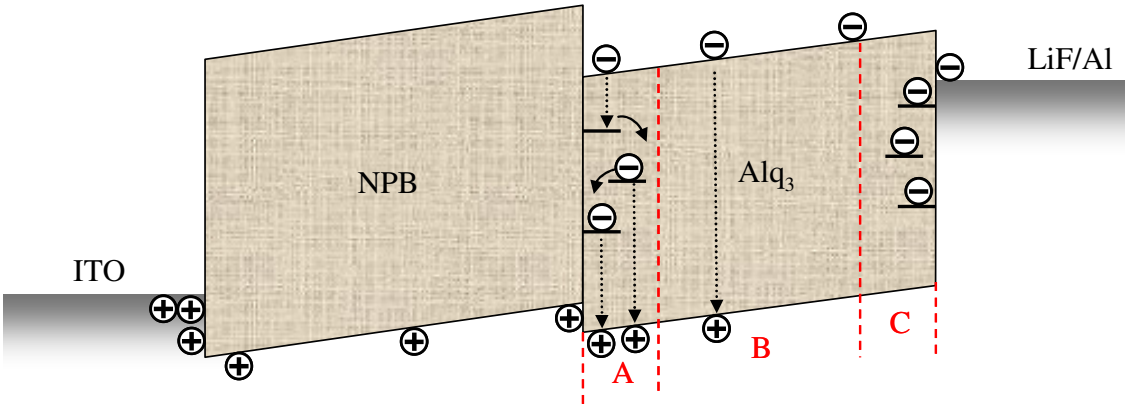

Figure 7.4. Schematic energy level diagram of an NPB/Alq_3 double-layer device with ITO as hole injection electrode and LiF/Al as electron injection electrode, showing the recombination zone shift towards the NPB/Alq_3 interface.

If hole injection is insufficient, as shown in Figure, the injected electrons fill the traps near Alq_3/cathode interface with first priority, then transport across Alq_3 layer, and finally fill the traps near the NPB/Alq_3 interface. Meanwhile, the excessive electrons accumulate at the interface due to the large energy barrier for electron surmounting the interface. In comparison, the accumulation of holes at the interface is not as serious, as the energy barrier for holes to overcome are small. As a consequence, a substantial number of injected holes will capture the low energy electrons trapped in zone A, without contribution to light emission. Meanwhile, the accumulated high energy electrons at LUMO level successively fill the vacated low energy traps. This situation becomes more serious with increasing driving voltage, as the mobility of electron in Alq_3 has stronger dependence of the electric field than that of holes in NPB [327,330,331]. This is the reason why declining EL efficiency at high driving voltage is generally observed. In addition, hole mobility in Alq_3 is much lower than electron mobility in Alq_3 [332]. It is

therefore speculated that the lower current density and EL efficiency obtained from a hole limited device (i.e., insufficient hole injection) is due to the shift of recombination zone towards the HTL/EML interface. Typical examples for this case in this study are the devices based on ITO surfaces modified by thicker buffer layers.

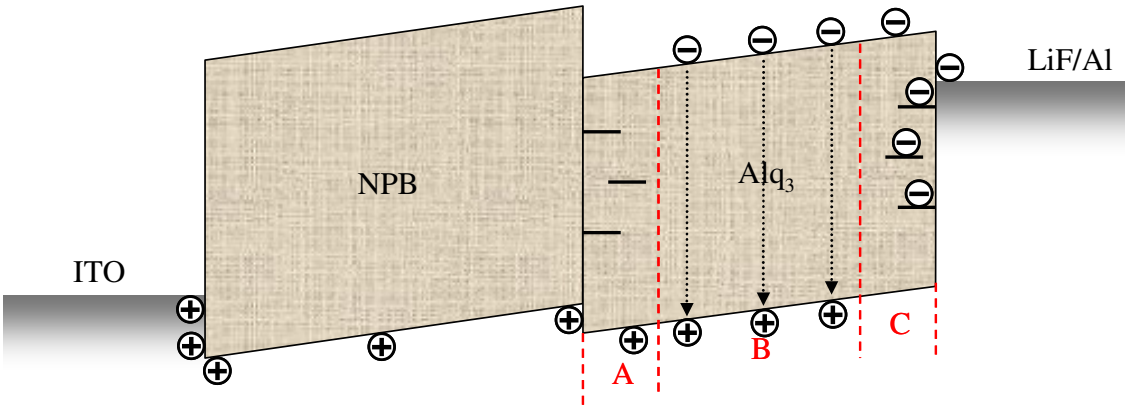

Figure 7.5. Schematic energy level diagram of an NPB/Alq_3 double-layer device with ITO as hole injection electrode and LiF/Al as electron injection electrode, showing the position of recombination zone for the best performance in EL efficiency.

With improved hole injection, as shown in Figure 7.5, more holes will diffuse into zone B being of less energy traps, leading to more radiative exciton decays and then high EL efficiency. Ideally, if the number of holes approaching zone B is sufficient that the majority of incoming electrons will be captured by the holes, the injected electrons have small probability to reach zone A. The ideal condition has been schematically displayed in Figure, which is rarely achieved in practice. Concurrent enhancement in both current density and current efficiency for the samples ECT+2.0V and ECT+2.4V suggests that electrochemical treatment of ITO is a useful technique to balance charge carrier injections to tune the position of combination zone for high EL efficiency at higher current density.

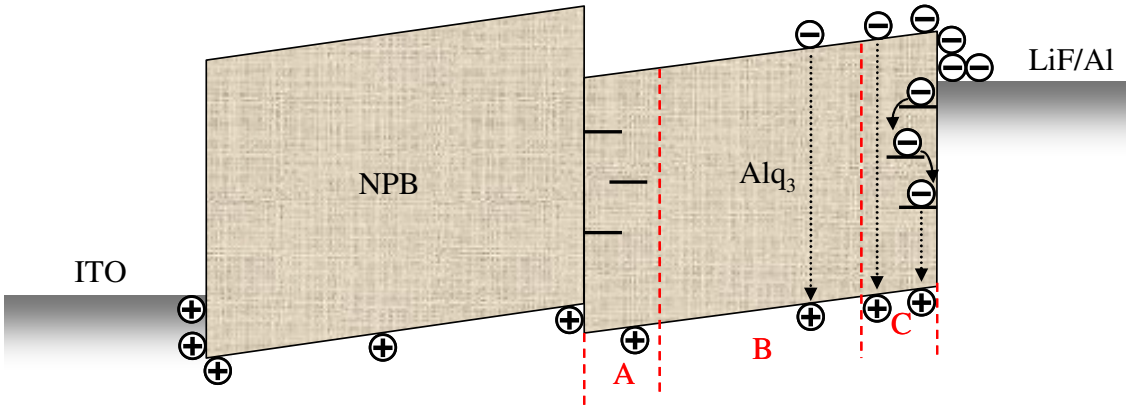

Figure 7.6. Schematic energy level diagram of an NPB/Alq_3 double-layer device with ITO as hole injection electrode and LiF/Al as electron injection electrode, showing the recombination zone shift towards the Alq_3/cathode interface.

Following the same model, it is easy to deduce an immediate consequence if excessive holes are injected. From Figure 7.6, it can be seen that the relative surplus holes will push the recombination zone towards zone C near Alq_3/cathode interface, where high density of lower energy traps exist. In this case, the number of electrons diffused into the effective recombination zone B is reduced, resulting in lower efficiency accompanying high current density. A typical example is the oxygen plasma treatment of ITO surface, where the reduced turn-on and driving voltages are obtained at a cost of lowering current efficiency. The loss of EL efficiency due to excessive hole injection will be worsened at high driving voltages, as hole mobility in Alq_3 is much more sensitive to electric field than electron mobility [332].

Chapter 8

Conclusion and Further Work

8.1 Summary of the Work

The aim of this work is to investigate the influence of various surface modifications on, in turn, ITO surface properties, hole injection efficiency, and finally device performance. This research is expected to provide important information on good understanding of hole injection mechanisms in OLED devices.

In this study, extensive work involving surface modifications of ITO was carried out, including gas plasma treatments, electrochemical treatments, and insulating buffer layers. In order to understand the governing factors of ITO surface properties, ITO samples were treated with different types of plasma (i.e., H_2, Ar, O_2, and CF_4) and characterized in terms of surface morphology by AFM, chemical states by XPS, electron transfer kinetics by CV, and surface energy by contact angle measurements. Electrochemical process was first proposed as a new approach for ITO surface treatment. Similar to the plasma treatments, the electrochemically treated ITO surfaces were also characterized in the surface properties. SiO_2 buffer layers produced by thermal evaporation (TE), self-assembled-monolayer (SAM), and sol-gel (S-G) processes were applied on to ITO surfaces as well, and characterized by AFM and CV techniques. OLED devices based on the modified ITO electrodes, in configuration of ITO/NPB(60nm)/Alq_3(60nm)/LiF/Al, were fabricated and

characterized in terms of L-I-V behavior and EL efficiencies. More importantly, nucleation and initial growth of hole transport layer on the treated ITO surfaces were morphologically investigated to understand the influence of surface modification methods on interface property and therefore hole injection. Based on the results of surface properties and device performance, phenomenal interface models were proposed for discussing the hole injection mechanism and the influence of hole injection on EL efficiency.

8.2 Findings and Conclusions

AFM analysis showed that plasma treatments at the working conditions used in this study did not cause detectable change in ITO surface morphology. ITO surface composition and chemical states were found by XPS to be sensitive to the plasma types. O:In ratios on the ITO surfaces were in a sequence of CF_4-P > O_2-P > Ar-P > as-clean > H_2-P, indicating the plasma-induced oxidation/reduction of the ITO surface. The highest O:In ratio on CF_4-P ITO surface was an evidence of In-etching. In addition, In/Sn-F species were also detected on the CF_4 plasma treated ITO surface, leading to ITO surface passivation. Both the surface oxidation and the passivation were clearly verified by CV experiments. Interestingly, ITO surface polarity was also plasma type sensitive and ranked in the same sequence as O:In ratio. The distinguished change in surface polarity after plasma treatments was attributed to the different contents of the polar species. Furthermore, surface polarity was correlated to the hole injection efficiency of the corresponding OLED device. More specifically, the higher the surface polarity, the higher the hole injection efficiency. However, the current efficiency based on the O_2-P and CF_4-P ITO samples were lowered due to the excess hole injection in comparison with the electron injection from the counter electrode.

Similar to plasma treatment, electrochemical treatment also led to significant changes in ITO surface properties, especially surface polarity, and in OLED performance. The surface polarity was sensitive to the treatment voltage, being of a max. value for the ITO sample treated at +2.0V and small values for those treated at +1.2 and +2.8V. The high

surface polarities of ITO samples treated at a voltage from +1.6 to 2.4 V were attributed to the anodic oxidation verified by XPS, which was caused by the water electrolysis requiring ITO polarized at a voltage more than +1.23 V. When a voltage higher than +2.4V was applied, however, significant surface corrosion ITO surface was clearly observed by AFM. Furthermore, XPS analysis confirmed the existence of insulating In/Sn phosphate on the ITO surface treated at +2.8V, which was the main reason causing the lowest surface polarity. More importantly, the electrochemical treatment at +2.0V provided ITO sample with much stable surface properties, compared with the most frequently used O_2 plasma treatment in OLED fabrication. Furthermore, the electrochemical treatment improved not only hole injection but also current efficiency of the corresponding ITO device. This finding suggested that electrochemical treatment could be used to tune hole injection by changing treatment voltage for improved device performance.

In comparison, insulating buffer layers affected hole injection and device performance in a different way from the plasma and electrochemical surface treatments. Buffer layer morphology on ITO surface was related to coating process. AFM and CV analyses revealed the coating density was in a rank of SAM SiO_2 > S-G SiO_2 > TE) SiO_2. More importantly, the L-I-V characteristics of the OLED devices based on the ITO modified by the SiO_2 buffer layers demonstrated that insulating buffer layers retarded hole injection. Denser buffer layer was consistent with lower hole injection efficiency. For the same coating process, thicker buffer layers blocked more holes. In addition, ~1 nm thick SiO_2 could not fully cover the rough ITO surface regardless of the coating processes used in

this study, implying that both tunneling and image force models might not be suitable for discussing the effect of insulating buffer layer on hole injection.

By using AMF analysis, nucleation and initial growth of NPB films on the ITO surfaces modified by plasma and electrochemical surface treatments and insulating SiO_2 buffer layers were investigated to understand the mechanisms behind the effect of the ITO surface modifications on hole injection and then OLED performance. The results showed that NPB thin film morphologies on the plasma- and electrochemically-treated ITO surfaces were correlated to the type of plasma and the electrochemical treatment voltage, respectively, which was attributed to the governing effect of surface polarity on the nucleation and growth of the NPB thin film. The higher the surface polarity, the finer and more uniform the NPB deposit. As a consequence, the improved adhesion of NPB film onto the ITO surfaces led to good electric contacts and therefore the enhanced hole injection.

In contrast, the uniform NPB films on the ITO surfaces coated with ultra thin (~ 1 nm thick) SiO_2 layers were attributed to the increased nucleation sites and the shorten lateral-diffusion length of the adsorbed NPB molecules, being beneficial to the adhesion of NPB film to ITO surface and then the hole injection. This positive effect of the ultra thin insulating buffer layer to hole injection, however, was limited to a layer thickness about 1 nm, and likely concealed by the reduced ITO/NPB contacts. In these cases, the majority of interfacial contacts were ITO/NPB rather than SiO_2/NPB. With increasing buffer layer thickness and therefore the ITO surface coverage with SiO_2, hole injection was significantly blocked due to the large fraction of SiO_2/NPB contacts at the interface.

8.3 Further Work

The findings in this thesis have demonstrated that CF_4 and O_2 plasma treatments and electrochemical treatments at a voltage of +2.0~+2.4V can significantly improve the hole injection across ITO/NPB interface (refer to Chapters 3 & 4). In contrast, almost all SiO_2 buffer layers blocked the hole injection (refer to Chapter 5). It is therefore an interesting topic to combine the three ITO surface modification techniques for balancing charge injection and improving OLED device performance.

This study has also shown that the ITO surface electrochemically-treated at +2.0V has much better stability in terms of surface energy than that of oxygen plasma treatment (refer to Section 4.3.1). The mechanisms behind the stable surface properties need to be further investigated. Furthermore, the work on lifetime and stability of the OLED devices after ITO surface modifications hasn't been carried out yet, and will be one of the focuses in the further work.

Reference

[1] S.M. Sze, Physics of Semiconductor Devices, 2nd ed., John Wiley & Sons, New York, 1981.

[2] A. Bernanose, "Electroluminescence of organic compounds," Brit. J. Appl. Phys. Suppl. 4 (1955) S54.

[3] M. Pope, H. Kallman and P. Magnante, "Electroluminescence in organic crystals," J. Chem. Phys. 38 (1963) 2042.

[4] W. Helfrich and W.G. Schneider, "Recombination radiation in anthracene crystals," Phys. Rev. Lett. 140 (1965) 229.

[5] D.F. Williams and M. Schadt, "A simple organic electroluminescence diode," Proc. IEEE 58 (1970) 476.

[6] M. Pope and C.E. Swenberg, Electronic Processes in Organic Crystals, Oxford University Press, New York, 1982.

[7] J. Kalinowski, "Electroluminescence in organics," J. Phys. D: Appl. Phys. 32 (1999) R179.

[8] N.V. Vityuk and V.V. Mikho, "Electroluminescence of anthracence excited by shaped -voltage pulse," Sov. Phys. Semicond. 6 (1973) 1479.

[9] P.S. Vincett, W.A. Barlow, R.A. Hann and G.G. Roberts, "Electrical conduction and low voltage blue electroluminescence in vacuum-deposited organic films," Thin Solid Films 94 (1982) 171.

[10] G.G. Roberts, M. McGinnity, P.S. Vincett and W.A. Barlow, "Electroluminescence, photoluminescence and electroabsorption of a lightly substituted anthracene Langmuir film," Solid State Commun. 32 (1979) 683.

[11] P.H. Partridge, "Electroluminescence from polyvinylcarbazole films: Electroluminescent devices," Polymer 24 (1983) 748.

[12] C.W. Tang and S.A. VanSlyke, "Organic electroluminescent diodes," Appl. Phys. Lett. 51 (1987) 913.

[13] C.W. Tang and S.A. VanSlyke, "Electroluminescence of doped organic thin films," J. Appl. Phys. 65 (1989) 3610.

[14] H. Kubota, S. Miyaguchi, S. Ishizuka, T. Wakimoto, J. Funaki, Y. Fukuda, T. Watanabe, H. Ochi, T. Sakamoto, T. Miyake, M. Tsuchida, I. Ohshita and T. Tohma, "Organic LED full color passive-matrix display," J. Lumin. 87–89 (2000) 56.

[15] J. Kido, "Organic displays," Phys. World 12 3 (1999) 27.

[16] J.H. Burroughes, D.D.C. Bradley, A.R. Brown, R.N. Marks, K. Mackay, R.H. Friend, P.L. Burn and A.B. Holmes, "Light-emitting diodes based on conjugated polymers," Nature 347 (1990) 539.

[17] J.R. Visser, "Application of polymer light-emitting materials in light-emitting diodes, backlights and displays," Philips J. Res. 51 (1998) 467.

[18] R.H. Friend, J. Burroughes and T. Shimoda, "Polymer diodes," Phys. World 12 6 (1999) 35.

[19] I.H. Campbell and D.L. Smith, in: Semiconducting Polymers, Eds.: G. Hadziioznnou and P. F. van Hutten, Wiley-Vch, 2000.

[20] D.D.C. Bradley, "Conjugated polymer electroluminescence," Synth. Met. 54 (1993) 401.

[21] H. Antoniadis, J.N. Miller, D.B. Roitman and I.H. Campbell, "Effects of hole carrier injection and transport in organic light-emitting diodes," IEEE Trans. Elec. Dev. 44 (1997) 1289.
[22] P.E. Burrows, Z. Shen, V. Bulovic, D.M. McCarty, S.R. Forrest, J.A. Cronin and M.E. Thompson, "Relationship between electroluminescence and current transport in organic heterojunction light-emitting devices," J. Appl. Phys. 79 (1996) 7991.
[23] C. Shen, A. Kahn and J. Schwartz, "Chemical and electrical properties of interfaces between magnesium and aluminum and *tris*-(8-hydroxy quinoline) aluminum," J. Appl. Phys. 89 (2001) 449.
[24] M.A. Baldo and S.R. Forrest, "Interface-limited injection in amorphous organic semiconductors," Phys. Rev. B 64 (2001) 085201.
[25] M. Stössel, J. Staudigel, F. Steuber, J. Simmerer and A. Winnacke, "Impact of the cathode metal work function on the performance of vacuum-deposited organic light emitting-devices," Appl. Phys. A: Mater. Sci. Process. 68 (1999) 387.
[26] T.M. Brown, R.H. Friend, I.S. Millard, P.J. Lacey, J.H. Burroughes and F. Cacialli, "Efficient electron injection in blue-emitting polymer light-emitting diodes with LiF/Ca/Al cathodes," Appl. Phys. Lett. 79 (2001) 174.
[27] B. Choi, H. Yoon and H.H. Lee, "Surface treatment of indium tin oxide by SF_6 plasma for organic light-emitting diodes," Appl. Phys. Lett. 76 (2000) 412.
[28] L. Zuppiroli, L. Si-Ahmed, K. Kamars, F. Nüesch, M.N. Bussac, D. Ades, A. Siove, E. Moons and M. Grätzel, "Self-assembled monolayers as interfaces for organic opto-electronic devices," Eur. Phys. J. B. 11 (1999) 505.
[29] G.E. Jabbour, Y. Kawabe, S.E. Shaheen, J.F. Wang, M.M. Morrell, B. Kippelen and N. Peyghambarian, "Highly efficient and bright organic electroluminescent devices with an aluminum cathode," Appl. Phys. Lett. 71 (1997) 1762.
[30] V. Bliznyuk, B. Ruhstaller, P.J. Brock, U. Scherf and S.A. Carter, "Self-assembled nanocomposite polymer light-emitting diodes with improved efficiency and luminance," Adv. Mater. 11 (1999) 1257.
[31] S.F.J. Appleyard, S.R. Day, R.D. Pickford and M.R. Willis, "Organic electroluminescent devices: enhanced carrier injection using SAM derivatized ITO electrodes," J. Mater. Chem. 10 (2000) 169.
[32] P.K.H. Ho, M. Granstrom, R.H. Friend and N.C. Greenham, "Ultrathin self-assembled layers at the ITO interface to control charge injection and electroluminescence efficiency in polymer light-emitting diodes," Adv. Mater. 10 (1998) 769.
[33] J.E. Malinsky, G.E. Jabbour, S.E. Shaheen, J.D. Anderson, A.G. Richter, N.R. Armstrong, B. Kipplelen, P. Dutta, N. Peyghambarian and T.J. Marks, "Self-assembly processes for organic LED electrode passivation and charge injection balance," Adv. Mater. 11 (1999) 227.
[34] X. Zhou, M. Pfeiffer, J. Blochwitz, A. Werner, A. Nollau, T. Fritz and K. Leo, "Very-low-operating-voltage organic light-emitting diodes using a p-doped amorphous hole injection layer," Appl. Phys. Lett. 78 (2001) 410.
[35] I.D. Parker, "Carrier tunneling and device characteristics in polymer light-emitting diodes," J. Appl. Phys. 75 (1994) 1656.
[36] W.R. Salaneck, S. Stafström and J.L. Brédas, Conjugated polymer surface and interfaces, Cambridge University Press, 1996.

[37] Y. Park, V.E. Choong, Y. Gao, B.R. Hsieh and C.W. Tang, "Work function of indium tin oxide transparent conductor measured by photoelectron spectroscopy," Appl. Phys. Lett. 68 (1996) 2699.
[38] H. Ishii and K. Seki, "Energy level alignment at organic/metal interfaces studied by UV photoemission: breakdown of traditional assumption of a common vacuum level at the interface," IEEE Trans. Elect. Dev. 44 (1997) 1295.
[39] S.T. Lee, X.Y. Hou, M.G. Mason and C.W. Tang, "Energy level alignment at Alq/metal interfaces," Appl. Phys. Lett. 72 (1998) 1593.
[40] I.H. Campbell, J.D. Kress, R.L. Martin, D.L. Smith, N.N. Barashkov and J.P. Ferraris, "Controlling charge injection in organic electronic devices using self-assembled monolayers," Appl. Phys. Lett. 71 (1997) 3528.
[41] H. Ishii, K. Sugiyama E. Ito and K. Seki, "Energy level alignment and interfacial electronic structures at organic/metal and organic/organic interfaces," Adv. Mater. 11 (1999) 605.
[42] H. Ishii, K. Sugiyama, D. Yoshimura, E. Ito, Y. Ouch and K. Seki, "Energy-level alignment at model interfaces of organic electroluminescent devices studied by UV photoemission: Trend in the deviation from the traditional way of estimating the interfacial electronic structures," IEEE J. Selected Top. Quantum Electron. 4 (1998) 24.
[43] N.J. Watkins, L. Yan and Y. Gao, "Electronic structure symmetry of interfaces between pentacene and metals," Appl. Phys. Lett. 80 (2002) 4384.
[44] I.G. Hill, A. Rajagopal, A. Kahn and Y. Hu, "Molecular level alignment at organic semiconductor-metal interfaces," Appl. Phys. Lett. 73 (1998) 662.
[45] E.H. Rhoderick and R.H. Williams, Metal-Semiconductor Contacts, Clarendon Press, Oxford, 1988.
[46] E.H. Rhoderick, W.R. Frensley and M.P. Shaw, in Handbook on Semiconductors, Vol. 4, Device Physics (Ed.: C. Hilsum), North-Holland, New York 1993.
[47] J. Kalinowski, "Electronic Progresses in Organic Electroluminescence," in: Organic Electroluminescent Materials and Devices, Eds.: S. Miyata and H.S. Nalwa, Gordon and Breach Publishers, 1997.
[48] K. Seki, T. Tani and H. Ishii, "Electronic structures of organic-inorganic interfaces studied by UV photoemission," Thin Solid Films 273 (1996) 20.
[49] N. Hayashi, E. Ito, H. Ishii, Y. Ouchi and K. Seki, "Energy level alignment at TPD/metal interfaces studied by Kelvin method," Mat. Res. Soc. Symp. Proc. 558 (2000) 445.
[50] N.C. Greenham and R.H. Friend, "Semiconductor device physics of conjugated polymers," Solid State Physics 49 (1996) 1.
[51] J. Halls, J. Cornil, D. dos Santos, R. Silbey, D. Hwang, A. Holmes, J. Bredas and R. Friend, "Charge- and energy-transfer processes at polymer/polymer interfaces: A joint experimental and theoretical study," Phys. Rev. B 60 (1999) 5721.
[52] G.G. Malliaras and J.C. Scott, "The roles of injection and mobility in organic light emitting diodes," J. Appl. Phys. 83 (1998) 5399.
[53] L.D. Bozano, S.A. Carter, J.C. Scott, G.G. Malliaras and P.J. Brock, "Temperature and field dependent mobilities in polymer LEDs," Mat. Res. Soc. Symp. Proc. 558 (2000) 45.
[54] A. Rajagopal, C.I. Wu and A. Kahn, "Energy level offset at organic semiconductor heterojunctions," J. Appl. Phys. 83 (1998) 2649.

[55] J. Blochwitz, T. Fritz, M. Pfeiffer, K. Leo, D.M. Alloway, P.A. Lee and N.R. Armstrong, "Interface electronic structure of organic semiconductors with controlled doping levels," Org. Electron. 2 (2001) 97.
[56] D. Schlettwein, K. Hesse, N.E. Gruhn, P.A. Lee, K.W. Nebesny and N.R. Armstrong, "Electronic energy levels in individual molecules, thin films, and organic heterojunctions of substituted phthalocyanines," J. Phys. Chem. B105 (2001) 4791.
[57] F. Nüesch, K. Kamarás and L. Zuppiroli, "Protonated metal-oxide electrodes for organic light emitting diodes," Chem. Phys. Lett. 283 (1998) 194.
[58] X. Crispin, V. Geskin, A. Crispin, J. Cornil, R. Lazzaroni, W.R. Salaneck and J.L. Brédas, "Characterization of the interface dipole at organic/ metal interfaces," J. Am. Chem. Soc. 124 (2002) 8131.
[59] N. Koch, A. Kahn, J. Ghijsen, J.-J. Pireaux, J. Schwartz, R.L. Johnson and A. Elschner, "Thermodynamic equilibrium and metal-organic interface dipole," Appl. Phys. Lett. 82 (2003) 70.
[60] N.D. Lang, DFT Approach to the Electronic Structure of Metal Surface and Metal-Adsorbate Systems. In: Theory of the Inhomogeneous Electron Gas, S. Lundqvist and N.H. March Eds., Plenum Press, New York, 1983.
[61] L. Yan, N.J. Watkins. S. Zorba, Y. Gao and C.W. Tang, "Thermodynamic equilibrium and metal-organic interface dipole," Appl. Phys. Lett. 81 (2002) 2752.
[62] L. Yan, Y. Gao, "Interfaces in organic semiconductor devices," Thin Solid Films 417 (2002) 101.
[63] W. Erley and H. Ibach, "Vibrational spectra of tetracyanoquino-di- methane (TCNQ) adsorbed on the Cu(lIl) surface," Surf. Sci. 178 (1986) 565.
[64] E. Ito, H. Oji, H. Ishii, K. Oichi, Y. Ouchi and K. Seki, "Interfacial electronic structure of long-chain alkane/metal systems studied by UV-photoelectron and metastable atom electron spectroscopies," Chem. Phys. Lett. 287 (1998) 137.
[65] T.R. Ohno, Y. Chen, S.E. Harvey, G.H. Kroll and J.H. Weaver, "C60 bonding and energy-level alignment on metal and semiconductor surfaces," Phys. Rev. B44 (1991) 13747.
[66] K.C. Kao and W. Hwang, Electrical Transport in Solids, Pergamon, Oxford, 1981.
[67] P. Mark and W. Helfrich, "Space-charge-limited currents in organic crystals," J. Appl. Phys. 33 (1962) 205.
[68] A. Sussman, "Space-charge-limited currents in copper phthalocyanine thin films," J. Appl. Phys. 38 (1967) 2738.
[69] S. Egusa, A. Miura, N. Gemma and M. Azuma, "Carrier injection characteristics of organic electroluminescent devices," Jpn. J. Appl. Phys. 33 (1994) 2741.
[70] P.S. Davids, I.H. Campbell and D.L. Smith, "Device model for single carrier organic diodes," J. Appl. Phys. 82 (1997) 6319.
[71] I.H. Campbell, P.S. Davids, D.L. Smith, N.N. Barashkov and J.P. Ferraris, "The Schottky energy barrier dependence of charge injection in organic light-emitting diodes," Appl. Phys. Lett. 72 (1998) 1863.
[72] H. Vestweber, J. Pommerehne, R. Sander, R.F. Mahrt, A. Greiner, W. Heitz and H. Bassler, "Majority carrier injection from ITO anodes into organic light-emitting diodes based upon polymer blends," Synth. Met. 68 (1995) 263.
[73] M. Matsumura, T. Akai, M. Saito and T. Kimura, "Height of the energy barrier existing between cathodes and hydroxyquinoline-aluminum complex of organic electroluminescence devices," J. Appl. Phys. 79 (1996) 264.

[74] V.I. Arkhipov, E.V. Emelianova, Y.H. Tak and H. Bässler, "Charge injection into light-emitting diodes: Theory and experiment," J. Appl. Phys. 84 (1998) 848.
[76] J. Gmeiner, S. Karg, M. Meier, W. Riess, P. Strohriegl and M. Schwoerer, "Synthesis, electrical conductivity and electroluminescence of poly(p-phenylene vinylene) prepared by the precursor route," Acta Polymer 44 (1993) 201.
[77] R.N. Marks, D.D.C. Bradley, R.W. Jackson, P.L. Burn and A.B. Holmes, "Charge injection and transport in poly(p-phenylene vinylene) light emitting diodes," Synth. Met. 55-57 (1993) 4128.
[78] E.M. Conwell and M.W. Wu, "Contact injection into polymer light-emitting diodes," Appl. Phys. Lett. 70 (1997) 1867.
[79] M.A. Abkowitz, H.A. Mizes and J.S. Facci, "Emission limited injection by thermally assisted tunneling into a trap - free transport polymer," Appl. Phys. Lett. 66 (1995) 1288.
[80] I. Esaki, Tunneling Phenomena in Solids, Eds.: E. Burnstein and C. Lundqvist, Plenum, New York, 1969.
[81] P.R. Emtage and J.J. O'Dwyer, "Richardson-Schottky effect in insulators," Phys. Rev. Lett. 16 (1966) 356.
[82] J.C. Scott and G.G. Malliaras, "Charge injection and recombination at the metal–organic interface," Chem. Phys. Lett. 299 (1999) 115.
[83] P.M. Borsenberger and D.S. Weiss, Organic Photoreceptors for Xerography, Optical Engineering, Marcel Dekker Inc., New York, 1998.
[84] Y. Roichman and N. Tessler, "Generalized Einstein relation for disordered semiconductors – implications for device performance," Appl. Phys. Lett. 80 (2002) 1948.
[85] C. Tanase, E.J. Meijer, P.W.M. Blom and D.M.de Leeuw, "Unification of the hole transport in polymeric field-effect transistors and light-emitting diodes," Phys. Rev. Lett. 91 (2003) 216601.
[86] Y.N. Gartstein and E.M. Conwell, "Field-dependent thermal injection into a disordered molecular insulator," Chem. Phys. Lett. 255 (1996) 93.
[87] U. Wolf, V.I. Arkhipov and H. Bässler, "Current injection from a metal to a disordered hopping system. I. Monte Carlo simulation," Phys. Rev. B59 (1999) 7507.
[88] P.E. Burrows and S.R. Forrest, "Electroluminescence from trap – limited current transport in vacuum deposited organic light emitting devices," Appl. Phys. Lett. 64 (1994) 2285.
[89] Z. Shen, P.E. Burrows, V. Bulovic, D.Z. Garbuzov, D.M. McCarty, M.E. Thompson and S.R. Forrest, "Temperature dependence of current transport and electroluminescence in vacuum deposited organic light emitting devices," Jpn. J. Appl. Phys. 35 (1996) L401.
[90] M.A. Lampert and P. Mark. Current Injection in Solids, Academic Press, New York, 1970.
[91] M. Higuchi, S. Uekusa, R. Nakano and K. Yokogawa, "Postdeposition annealing influence on sputtered indium tin oxide film characteristics ," Jpn. J. Appl. Phys. 33 (1994) 302.
[92] K. Sreenivas, T. S. Rao, A. Mansnigh and S. Chandra, "Preparation and characterization of RF sputtered indium tin oxide films," J. Appl. Phys. 57 (1985) 384.

[93] J.S. Kim, M. Granström, R.H. Friend, N. Johansson, W.R. Salaneck, R. Daik, W.J. Feast and F. Cacialli, "Indium-tin oxide treatments for single – and double-layer polymeric light-emitting diodes: The relation between the anode physical, chemical, and morphological properties and the device performance," J. Appl. Phys. 84 (1998) 6859.
[94] T. Osada, T. Kugler, P. Broms and W. Salaneck, "Polymer-based light-emitting devices: investigations on the role of the indium – tin oxide (ITO) electrode," Synth. Met. 96 (1998) 77.
[95] M. Kamei, Y. Shigesato and S. Takaki, "Origin of characteristic grain-subgrain structure of tin-doped indium oxide films," Thin Solid Films 259 (1995) 38.
[96] R.W.G. Wyckoff, Crystal Structures, 2nd ed., Wiley, New York, 1964, Vol. 2, p2.
[97] J.C.C. Fan and J.B. Goodenough, "X- ray photoemission spectroscopy studies of Sn-doped indium-oxide films," J. Appl. Phys. 48 (1977) 3524.
[98] H.K. Müller, "Electrical and optical properties of sputtered In_2O_3 films. I. Electrical properties and intrinsic absorption," Phys. Status Solidi. 27 (1968) 723.
[99] Y. Shigesato and D.C. Paine, "A microstructural study of low resistivity tin-doped indium oxide prepared by d.c. magnetron sputtering," Thin Solid Films, 238 (1994) 44.
[100] I. Hamberg and C.G. Granqvist, "Evaporated Sn-doped In_2O_3 films: Basic optical properties and applications to energy-efficient windows," J. Appl. Phys. 60 (1986) R123.
[101] J. L. Vossen, "Transparent conducting films," Phys. Thin Films 9 (1977) 1.
[102] N. Balasubramanian and A. Subrahmanyam, "Electrical and optical properties of reactively evaporated indium tin oxide (ITO) films-dependence on substrate temperature and tin concentration," J. Phys. D: Appl. Phys. 22 (1989) 206.
[103] L. Gupta, A. Mansingh and P.K. Srivastava, "Band gap narrowing and the band structure of tin-doped indium oxide films," Thin Solid Films 176 (1989) 33.
[104] Y.S. Jung, D.W. Lee and D.Y. Jeon, "Influence of dc magnetron sputtering parameters on surface morphology of indium tin oxide thin films," Appl. Surf. Sci. 221 (2004) 136.
[105] M. Scholten and J.E.A.M. Van Den Meerakker, "On the mechanism of ITO etching: the specificity of halogen acids," J. Electrochem. Soc. 140 (1993) 471.
[106] J.E.A.M. van den Meerakker, P.C. Baarslag and M. Scholten, "On the mechanism of ITO etching in halogen acids: The influence of oxidizing agents," J. Electrochem. Soc. 142 (1995) 2321.
[107] S. Fletcher, L. Duff and R.G. Barradas, "Nucleation and charge-transfer kinetics at the viologen/SnO_2 interface in electrochromic device applications," J. Electroanal. Chem. 100 (1979) 759.
[108] N.R. Armstrong, A.W.C. Lui, M. Fijihira and T. Kuwana, "Electrochemical and surface characteristics of tin oxide and indium oxide electrodes," Anal. Chem. 48 (1976) 741.
[109] B.J. Baliga and S.K. Ghandhi, "Electrochemical patterning of tin oxide films," J. Electrochem. Soc. 124 (1977) 1059.
[110] C.A. Huang, K.C. Li, G.C. Tu and W.S. Wang, "The electrochemical behavior of tin-doped indium oxide during reduction in 0.3 M hydrochloric acid," Electrochimica Acta 48 (2003) 3599.

[111a] G. Folcher, H. Cachet, M. Froment and J. Bruneaux, "Anodic corrosion of indium tin oxide films induced by the electrochemical oxidation of chlorides," Thin Solid Films 301 (1997) 242.
[111b] H. Cachet, M. Froment and F. Zenia, "Corrosion of tin oxide at anodic potentials" J. Electrochem. Soc. 143 (1996) 442.
[112] J.E.A.M. van den Meerakker, E. A. Meulenkamp and M. Scholten, "(Photo)Electrochemical characterization of tin-doped indium oxide," J. Appl. Phys. 74 (1993) 3282.
[113] C.C. Wu, C.I. Wu, J.C. Sturm and A. Kahn, "Surface modification of indium tin oxide by plasma treatment: An effective method to improve the efficiency, brightness, and reliability of organic light emitting devices," Appl. Phys. Lett. 70 (1997) 1348.
[114] C. Qiu, H. Chen, Z. Xie, M. Wong and H.S. Kwok, "Praseodymium oxide coated anode for organic light-emitting diode," Appl. Phys. Lett. 80 (2002) 3485.
[115] J.S. Kim, R.H. Friend and F. Cacialli, "Surface energy and polarity of treated indium-tin-oxide anodes for polymer light-emitting diodes studied by contact-angle measurements," J. Appl. Phys. 86 (1999) 2774.
[116] Y. Yang, E. Westerweele, C. Zhang, P. Smith and A.J. Heeger, "Enhanced performance of polymer light-emitting-diodes using high-surface-area polyaniline network electrodes," J. Appl. Phys. 77 (1995) 694
[117] E.W. Forsythe, M.A. Abkowitz, and Y. Gao, "Tuning the carrier injection efficiency for organic light-emitting diodes," J. Phys. Chem. B104 (2000) 3948.
[118] S.T. Lee, Z.Q. Gao and L.S. Hung, "Metal diffusion from electrodes in organic light-emitting diodes," Appl. Phys. Lett. 75 (1999) 1404.
[119] S.A. Van Slyke, C.H. Chen and C.W. Tang, "Organic electroluminescent devices with improved stability," Appl. Phys. Lett. 69 (1996) 2160.
[120] S.K. So, W.K. Choi, C.H. Cheng, L.M. Leung and C.F. Kwong, "Surface preparation and characterization of indium tin oxide substrates for organic electroluminescent devices," Appl. Phys. A68 (1999) 447.
[121] L.S. Hung, C.W. Tang and M.G. Mason, "Enhanced electron injection in organic electroluminescence devices using an Al/LiF electrode," Appl. Phys. Lett. 70 (1997) 152.
[122] M.G. Mason, L.S. Hung, C.W. Tang, S.T. Lee, K.W. Wong and M. Wang, "Characterization of treated indium-tin-oxide surfaces used in electroluminescent devices," J. Appl. Phys. 86 (1999) 1688.
[123] J.S. Kim, R.H. Friend and F. Cacialli, "Improved operational stability of polyfluorene-based organic light-emitting diodes with plasma-treated indium–tin–oxide anodes," Appl. Phys. Lett. 74 (1999) 3084.
[124] K. Furukawa, Y. Terasaka, H. Ueda and M. Mtsumura, "Effect of a plasma treatment of ITO on the performance of organic electroluminescent devices," Synth. Met. 91 (1997) 99.
[125] F. Nüesch, L.J. Rothberg, E.W. Forsythe, Q.T. Le and Y. Gao, "A photoelectron spectroscopy study on the indium tin oxide treatment by acids and bases," Appl. Phys. Lett. 74 (1999) 880.
[126] Q.T. Le, F. Nüesch, L.J. Rothberg, E.W. Forsythe and Y. Gao, "Photoemission study of the interface between phenyl diamine and treated indium–tin–oxide," Appl. Phys. Lett. 75 (1999) 1357.

[127] J.T. Yates, N.E. Erickson, S.D. Worley and T.E. Madey, in: The Physical Basis for Heterogeneous Catalysis, Eds.: E. Drauglis and R.I. Jaffee, Plenum, New York, 1975.
[128] A. Berntsen, Y. Croonen, R. Cuijpers, B. Habets, C. Liedenbaum, H. Schoo, R.J. Visser, J. Vleggaar, P. van de Weijer, in Organic Light-Emitting Materials and Devices, Vol. 3148 (Ed.: SPIE), SPIE, 1997, p264.
[129] K. Sugiyama, H. Ishii, Y. Ouchi and K. Seki "Dependence of indium-tin-oxide work function on surface cleaning method as studied by ultraviolet and X-ray photoemission spectroscopies," J. Appl. Phys. 87 (2000) 295.
[130] J.S. Kim, M. Granström, R.H. Friend, N. Johansson, W.R. Salaneck, A. Cola, G. Gigli, R. Cingolani and F. Cacialli, "Characterization of the physico-chemical properties of surface-treated indium-tin oxide anodes for organic light-emitting diodes," Mat. Res. Soc. Symp. Proc. 558 (2000) 427.
[131] H.Y. Yu, X.D. Feng, D. Grozea, Z.H. Lu, R.N. Sodhi, A.-M. Hor and H. Aziz, "Surface electronic structure of plasma-treated indium tin oxides," Appl. Phys. Lett. 78 (2001) 2595.
[132] I.M. Chan, T.Y. Hsu and F.C. Hong, "Enhanced hole injections in organic light-emitting devices by depositing nickel oxide on indium tin oxide anode," Appl. Phys. Lett. 81 (2002) 1899.
[133] R.A. Hatton, S.R. Day, R.D. Pickford and M.R. Willis, "Organic electroluminescent devices : enhanced carrier injection using an organosilane self assembled monolayer (SAM) derivatized ITO electrode," Thin Solid Films 394 (2001) 292.
[134] Y. Shirota, Y. Kuwabara, H. Inada, T. Wakimoto, H. Nakada, Y. Yonemoto, S. Kawami and K. Imai, "Multilayered organic electroluminescent device using a novel starburst molecule, 4,4',4"-tris(3-methylphenylphenylamino)triphenylamine, as a hole transport material," App. Phys. Lett. 65 (1994) 807.
[135] W.P. Hu, K. Manabe, T. Furukawa and M. Matsumura, "Lowering of operational voltage of organic electroluminescent devices by coating indium-tin-oxide electrodes with a thin CuOx layer," Appl. Phys. Lett. 80 (2002) 2640.
[136] W.P. Hu, M. Matsumura, K. Furukawa and K. Torimitsu, "Oxygen plasma generated copper/copper oxides nanoparticles ," J. Phys. Chem. B108 (2004) 13116.
[137] I.M. Chan and F.C. Hong, "Improved performance of the single-layer and double-layer organic light emitting diodes by nickel oxide coated indium tin oxide anode," Thin Solid Films 450 (2004) 304.
[138] J. Li, M. Yahiro, K. Ishida, H. Yamada and K. Matsushige, "Enhanced performance of organic light emitting device by insertion of conducting/insulating WO_3 anodic buffer layer," Synth. Met. 151 (2005) 141.
[139] S. Tokito, K. Noda and Y. Taga, "Metal oxides as a hole-injecting layer for an organic electroluminescent device," J. Phys. D: Appl. Phys. 29 (1996) 2750.
[140] F. Nüesch, L. Si-Ahmed, B. François and L. Zuppiroli, "Derivatized electrodes in the construction of organic light emitting diodes," Adv. Mater. 9 (1997) 222.
[141] J.M. Bharathan and Y. Yang, "Polymer/metal interfaces and the performance of polymer light-emitting diodes," J. Appl. Phys. 84 (1998) 3207.
[142] T.M. Brown, J. S. Kim, R.H. Friend, F. Cacialli, R. Daik and W.J. Feast, "Built-in field electroabsorption spectroscopy of polymer light-emitting diodes incorporating a doped poly(3,4-ethylene dioxythiophene) hole injection layer," Appl. Phys. Lett. 75 (1999) 1679.

[143] J. Morgado, A. Charas and N. Barbagallo, "Reduction of the light-onset voltage of light-emitting diodes based on a soluble poly(p-phenylene vinylene) by grafting polar molecules onto indium–tin oxide," Appl. Phys. Lett. 81 (2002) 933.
[144] I.H. Campbell, S. Rubin, T.A. Zawodzinski, J.D. Kress, R.L. Martin, D.L. Smith, N.N. Barashkov and J.P. Ferraris, "Controlling Schottky energy barriers in organic electronic devices using self-assembled monolayers," Phys. Rev. B54 (1996) R14321
[145] R.W. Zehner, D.F. Parsons, R.P. Hsung and L.R. Sita, "Tuning the work function of gold with self-assembled monolayers derived from $X–[C_6H_4–CC–]_nC_6H_4–SH$ (n = 0, 1, 2; X = H, F, CH_3, CF_3, and OCH_3)," Langmuir 15 (1999) 1121.
[146] J. Krüger, U. Bach and M. Grätzel, "Modification of TiO_2 heterojunctions with benzoic acid derivatives in hybrid molecular solid-state devices," Adv. Mater. 12 (2000) 447.
[147] P. He, S.D. Wang, W.K. Wong, C.S. Lee and S.T. Lee, "Vibrational and photoemission study of the interface between phenyl diamine and indium tin oxide," Appl. Phys. Lett. 79 (2001) 1561.
[148] S.F.J. Appleyard and M.R. Willis, "Electroluminescence: enhanced injection using ITO electrodes coated with a self assembled monolayer," Opt. Mater. 9 (1998) 120.
[149] J.E. Malinsky, J.G.C. Veinot, G.E. Jabbour, S.E. Shaheen, J.D. Anderson, P. Lee, A.G. Richter, A.L. Burin, M.A. Ratner, T.J. Marks, N.R. Armstrong, B. Kippelen, P. Dutta and N. Peyghambarian, "Nanometer-scale dielectric self-assembly process for anode modification in organic light-emitting diodes. consequences for charge injection and enhanced luminous efficiency," Chem. Mater. 14 (2002) 3054.
[150] Y. Kurosaka, N. Tada, Y. Ohmori and K. Yoshino, "Improvement of electrode/organic layer interfaces by the insertion of monolayer-like aluminum oxide film," Jpn. J. Appl. Phys. 37 (1998) L872.
[151] Z.B. Deng, X.M. Ding, S.T. Lee and W.A. Gambling, "Enhanced brightness and efficiency in organic electroluminescent devices using SiO_2 buffer layers," Appl. Phys. Lett. 74 (1999) 2227.
[152] Y. Qiu, D.Q. Zhang, L.D. Wang, and G.S. Wu, "Performance improvement of organic light emitting diode by low energy ion beam treatment of the indium tin oxide surface," Synth. Met. 125 (2002) 415.
[153] H. Jiang, Y. Zhou, B.S. Ooi, Y. Chen, T. Wee, Y.L. Lam, J. Huang and S. Liu, "Improvement of organic light-emitting diodes performance by the insertion of a Si_3N_4 layer," Thin Solid Films 363 (2000) 25.
[154] L.S. Hung, L.R. Zheng and M.G. Mason, "Anode modification in organic light-emitting diodes by low-frequency plasma polymerization of CHF_3," Appl. Phys. Lett. 78 (2001) 673.
[155] Y. Qiu, Y. Gao, L. Wang and D. Zhang, "Efficient light emitting diodes with Teflon buffer layer," Synth. Met. 130 (2002) 235.
[156] F. Zhu, B.L. Low, K. Zhang and S.J. Chua, "Lithium–fluoride-modified indium tin oxide anode for enhanced carrier injection in phenyl-substituted polymer electroluminescent devices," Appl. Phys. Lett. 79 (2001) 1205.
[157] J.S. Kim, F. Cacialli, A. Cola, G. Gigli and R. Cingolani, "Increase of charge carriers density and reduction of Hall mobilities in oxygen-plasma treated indium–tin–oxide anodes," Appl. Phys. Lett. 75 (1999) 19.

[158] V. Christou, M. Etchells, O. Renault, P.J. Dobson, O.V. Salata, G. Beamson and R.G. Egdell, “High resolution x-ray photoemission study of plasma oxidation of indium-tin-oxide thin film surfaces,” J. Appl. Phys. 88 (2000) 5180.
[159] C. Adachi, K. Nagai and N. Tamoto, “Molecular design of hole transport materials for obtaining high durability in organic electroluminescent diodes,” Appl. Phys. Lett. 66 (1995) 2679.
[160] N.G. Park, M.Y. Kwak, B.O. Kim, O.K. Kwon, Y.K. Kim, B. You, T.W. Kim and Y.S. Kim, “Effects of indium-tin-oxide surface treatment on organic light-emitting diodes,” Jpn. J. Appl. Phys. 41 (2002) 1523.
[161] S.F. Chen and C. Wu. Wang, “Influence of the hole injection layer on the luminescent performance of organic light-emitting diodes,” Appl. Phys. Lett. 85 (2004) 765.
[162] S.M. Tadayyon, H.M. Grandin, K. Griffiths, P.R. Norton, H. Aziz and Z.D. Popovic, “CuPc buffer layer role in OLED performance: a study of the interfacial band energies,” Org. Electron. 5 (2004) 157.
[163] Q. Huang, J. Cui, H. Yan, J.G.C. Veinot and T.J. Marks, “Small molecule organic light-emitting diodes can exhibit high performance without conventional hole transport layers,” Appl. Phys. Lett. 81 (2002) 3528.
[164] G. Binnig, C.F. Quade, and C. Gerber, “Atomic force microscope,” Phys. Rev. Lett. 56 (1986) 930.
[165] C. Chen, Introduction to Scanning Tunneling Microscopy, Oxford University Press, 1993.
[166] R.W.H. Guentherodt, Theory of STM and related scanning probe methods, Springer Verlag, 1993.
[167] D. Bonnell, Scanning probe microscopy and spectroscopy: theory, techniques and applications, Wiley, 2001.
[168] S. Myhra, Introduction to Scanned Probe Microscopy, in: Handbook of Surface and Interface Analysis: Methods in Problem Solving, Eds. J.C. Rivière and S. Myhra, Marcel Dekker, Inc., New York, 1998, Chapter 10.
[169] S.N. Magonov and M.-H. Whangbo, Surface Analysis with STM and AFM: Experimental and Theoretical Aspects of Image Analysis, VCH, Weinheim, New York, 1996.
[170] R. Howland and L. Benatar, Scanning Probe Microscopy (Manual), Digital Instruments, 1997.
[171] J. Israelachvili, Intermolecular and Surface Forces, 2nd edition, Academic Press, London, 1997.
[172] H.C. Hamaker, “The London-van der Waals attraction between spherical particles,” Physica 4 (1937) 1058.
[173] G.B. Hoflund, "Spectroscopic Techniques: X-ray Photoelectron Spectroscopy (XPS), Auger Electron Spectroscopy (AES) and Ion Scattering Spectroscopy (ISS)," in Handbook of Surface and Interface Analysis: Methods in Problem Solving, edited by J.C. Rivière and S. Myhra, Marcel Dekker, Inc., New York, pp57-158, 1998.
[174] C.D. Wagner, W.M. Riggs, L.E. Davis, J.F. Moulder and G.E. Muilenberg (eds.), Handbook of X-ray Photoelectron Spectroscopy, Perkin-Elmer Corp., Physical Electronics Division, Eden Prairie, MN, 1979.

[175] NIST X-ray Photoelectron Spectroscopy Database, data compiled by C.D. Wagner, Surfex Co, Program written by D.M. Bickham, Distributed by Standard Reference Data, NIST, Gaithersburg, MD, 1989.
[176] G. Beamson and D. Briggs, High Resolution XPS of Organic Polymers, Wiley, Chichester, 1992.
[177] D. Briggs, M.P. Seah, Practical Surface Analysis by Auger and X-ray Photoelectron Spectroscopy, Wiley, New York, 1983.
[178] E.F. Bowden, F.M. Hawkridge and H.N. Blount, Comprehensive Treatise of Electroanalytical Chemistry, Vol. 10, Ed. S. Srinivasan, Y.A. Chizmadshev, J.O'M. Bockris, B.E. Conway and E. Yeager, Plenum Press, New York, 1985.
[179] P.H. Riger, Electrochemistry, Chapman & Hall, New York, 1994.
[180] T. Riley and C. Tomlinson, Principles of Electroanalytical Methods, John Wiley & Sons, New York, 1987.
[181] A.J. Bard and L.R. Faulkner, Electrochemical Methods: Fundamentals and Applications, John Wiley & Sons Inc., New York, 2001.
[182] D. Halliday and R. Resnick, Physics, 3rd Edition., Wiley, New York, 1978, p644.
[183] R. Greef, R. Peat, L.M. Peter, D. Pletcher and J. Robinson, Instrumental Methods in Electrochemistry, John Wiley & Sons, New York, 1985.
[184] D.T. Sawyer, A.J. Sobkowiak, and J. Roberts, Jr., Electrochemistry for Chemists, 2nd Edition, John Wiley & Sons, New York, 1995, Section 5.2.
[185] E.P. Friis, J.E.T. Andersen, L.L. Madsen, N. Bonander, P. Moller and J. Ulstrup, "Dynamics of pseudomonas aeruginosa azurin and its Cys3Ser mutant at single-crystal gold surfaces investigated by cyclic voltammetry and atomic force microscopy," Electrochim. Acta. 43 (1998) 1113.
[186] K.N. Tu, J.W. Mayer, L.C. Feldman, Electronic Thin Film Science, Macmillan Publishing Company, New York, 1992, Chap. 2.
[187] A.W. Neumann and R.J. Good, Surface and Colloid Science, Vol. II, R.J. Good and R.R. Stromberg (Eds), Plenum Press, New York, 1979.
[188] R.J. Good, Aspect of Adhesion – 7, Ed. D J. Alner and K.W. Allen, Transcripta Books, London, 1973, p182.
[189] D.H. Bangham and R.I. Razouk, "Adsorption and the wetability of solid surfaces," Trans. Faraday Soc. 33 (1937) 1459.
[190] F.M. Fowkes, "Attractive forces at interfaces," Ind. Eng. Chem. 56 (1964) 40.
[191] A.W. Neumann, "Contact angles and their temperature dependence: thermodynamic status, measurement, interpretation and application," Adv. Colloid Interface Sci. 4 (1974) 105.
[192] D. Li, M. Xie and A.W. Neumann, "Vapor adsorption and contact angles on hydrophobic solid surfaces," Colloid Polym. Sci. 271 (1993) 573.
[193] W.A. Zisman, "Relation of the equilibrium contact angle to liquid and solid constitution," ACS Adv. Chem. Ser. 43 (1964) 1.
[194] D.Y. Kwok and A.W. Neumann, "Contact angle measurement and contact angle interpretation," Adv. Colloid Interf. Sci. 81 (1999) 167.
[195] D.K. Owens and R.C. Wendt, "Estimation of the surface free energy of polymers," J. Appl. Polym. Sci. 13 (1969) 1741.
[196] D.H. Kaelble and K.C. Uy, "A reinterpretation of organic liquid–polytetrafluoroethylene surface interactions," J. Adhesion 2 (1970) 50.

[197] S. Wu, in: Adhesion and Adsorption of Polymers, Polymer Science and Technology, Vol. 12A, Plenum Press, New York, 1980.
[198] R.J. Good, "Contact angle, wetting and adhesion: A critical review," J. Adhesion Sci. Technol. 6 (1992) 1269.
[199] F.M. Fowkes, "Additivity of intermolecular forces at interfaces. I. Determination of the contribution to surface and interfacial tensions of dispersion forces in various liquids," J. Phys. Chem. 67 (1963) 2538.
[200] F.M. Fowkes, J. Colloid. "Calculation of work of adhesion by pair potential summation," Interf. Sci. 28 (1968) 493.
[201] J. Schultz, K. Tsutsumi and J.B. Donnet, "Surface properties of high-energy solids: II. Determination of the nondispersive component of the surface free energy of mica and its energy of adhesion to polar liquids," J. Colloid. Interf. Sci. 59 (1977) 277.
[202] F.M. Fowkes, Treatise on Adhesion and Adhesives Vol. 1, Ed. R.L. Patrick, Marcel Dekker, New York, 1967, p325.
[203] Y. Tamai, K. Makuuchi and M. Suzuki, "Experimental analysis of interfacial forces at the plane surface of solids," J. Phys. Chem. 71 (1967) 4176.
[204] J.R. Dann, "Forces involved in the adhesive process : II. Nondispersion forces at solid-liquid interfaces," J. Colloid. Interf. Sci. 32 (1970) 321.
[205] A.J. Kinloch, "The science of adhesion," J. Mater. Sci. 15 (1980) 2141.
[206] E. Ruckenstein and S.V. Gourisankar, "Surface restructuring of polymeric solids and its effect on the stability of the polymer—water interface," J. Colloid Interf. Sci. 109 (1986) 557.
[207] S. Wu, "Calculation of interfacial tension in polymer systems," J. Polym. Sci. Part C 34 (1971) 19.
[208] S. Wu, Polymer Interface and Adhesion, Marcel Dekker Inc, New York, 1982
[209] S.R. Wasserman, G.M. Whitesides, I.M. Tidswell, B.M. Ocko, P.S. Pershan and J.D. Axe, "The structure of self-assembled monolayers of alkylsiloxanes on silicon: a comparison of results from ellipsometry and low-angle X-ray reflectivity," J. Am. Chem. Soc. 111 (1989) 5852.
[210] S.R. Wasserman, Y.T. Tao and G.M. Whitesides, "Structure and reactivity of alkylsiloxane monolayers formed by reaction of alkyltrichlorosilanes on silicon substrates," Langmuir 5 (1989) 1074.
[211] A. Andersson, N. Johansson, P. Bröms, N. Yu, D. Lupo and W.R. Salaneck, "Fluorine tin oxide as an alternative to indium tin oxide in polymer LEDs," Adv. Mater. 10 (1998) 859.
[212] Y.H. Liau, N.F. Scherer and K. Rhodes, "Nanoscale electrical conductivity and surface spectroscopic studies of indium−tin oxide," J. Phys. Chem. B105 (2001) 3282.
[213] N.D. Popovich, S.-S. Wong, S. Ufer, V. Sakhrani and D. Paine, "Electron-transfer kinetics at ITO films," J. Electrochem. Soc. 150 (2003) H255.
[214] C. Donley, D. Dunphy, D. Paine, C. Carter, K. Nebesny, P. Lee, D. Alloway and N. R. Armstrong, "Characterization of indium−tin oxide interfaces using X-ray photoelectron spectroscopy and redox processes of a chemisorbed probe molecule: effect of surface pretreatment conditions," Langmuir 18 (2002) 450.
[215] J.S. Kim, F. Cacialli and R. Friend, "Surface conditioning of indium-tin oxide anodes for organic light-emitting diodes," Thin Solid Film 445 (2003) 358.
[216] A.M. Ferraria, J.D.L. da Silva, A.M.B. do Rego, "XPS studies of directly fluorinated HDPE: problems and solutions," Polymer 44 (2003) 7241.

[217] J.S. Kim, P.K.H. Ho, D.S. Thomas, R.H. Friend, F. Cacialli, G.W. Bao, and S.F.Y. Li, "X-ray photoelectron spectroscopy of surface-treated indium-tin oxide thin films," Chem. Phys. Lett. 315 (1999) 307.
[218] M. P. Seah, P. Swift and D. Shuttleworth, in: Practical Surface Analysis: (1) Auger and X-ray Photoelectron Spectroscopy, D. Briggs and M. P. Seah Eds., 2nd Edition., Wiley, Chichester, 1990, p541.
[219] D. Shuttleworth, "Preparation of metal-polymer dispersions by plasma techniques. An ESCA investigation," J. Phys. Chem. 84 (1980) 1629.
[220] F.M. Fowkes, "Additivity of intermolecular forces at interfaces. I. Determination of the contribution to surface and interfacial tensions of dispersion forces in various liquids," J. Phys. Chem. 67 (1963) 2538.
[221] J. Lyklema, Fundamentals of Interface and Colloid Science, Academic Press, 1991.
[222] D.J. Milliron, I.G. Hill, C. Shen, A. Kahn, and J. Schwartz, "Surface oxidation activates indium tin oxide for hole injection," J. Appl. Phys. 87 (2000) 572.
[223] N. Johansson, F. Cacialli, K.Z. Xing, G. Beamson, D.T. Clark, R.H. Friend and W.R. Salaneck, "A study of the ITO-on-PPV interface using photoelectron spectroscopy," Synth. Met. 92 (1998) 207.
[224] M.L. Gordon, G. Cooper, C. Morin, T. Araki, C.C. Turci, K. Kaznatcheev and A.P. Hitchcock, "Inner-shell excitation spectroscopy of the peptide bond: comparison of the C 1s, N 1s, and O 1s spectra of glycine, glycyl-glycine, and glycyl-glycyl-glycine," J. Phys. Chem. A107 (2003) 6144.
[225] C.M.T. Sanchez, M.E.H. Maia da Costa, R.R.M. Zamora, R. Prioli, and F.L. Freire Jr., "Nitrogen incorporation into hard fluorinated carbon films: nanoscale friction and structural modifications," Diamond Relat. Mater. 13 (2004) 1366.
[226] S.A. Visser, C.E. Hewitt, J. Fornalik, G. Braunstein, C. Srividya and S.V. Babu, "Surface and bulk compositional characterization of plasma-polymerized fluorocarbons prepared from hexafluoroethane and acetylene or butadiene reactant gases," J. Appl. Polym. Sci. 66 (1997) 409.
[227] P. Gröning, O.M. Küttel, M. Cooaud-Coen, G. Dietler and L. Schlapbach, "Interaction of low-energy ions (< 10 eV) with polymethylmethacrylate during plasma treatment," Appl. Surf. Sci. 89 (1995) 83.
[228] Handbook of X-ray Photoelectron Spectroscopy, Perkin-Elmer Corporation, 1992.
[229] S. Mori and W. Morales, "X-ray photoelectron-spectroscopy peak assignment for perfluoropolyether oils," J. Vac. Sci. Technol. A8 (1990) 3354.
[230] J.F. Moulder, W.F. Stickle, P.E. Sobol and K.D. Bomben, Handbook of X-ray photoelectron spectroscopy, Phys. Electron., MN, 1995.
[231] A.B. Nelson and H. Aharoni, "X-ray photoelectron spectroscopy investigation of ion beam sputtered indium tin oxide films as a function of oxygen pressure during deposition," J. Vac. Sci. Technol. A5 (1987) 231.
[232] T. Ishida, H. Kobayashi and Y. Nakato, "Structure and properties of electron-beam-evaporated indium tin oxide films as studied by X-ray photoelectron-spectroscopy and work function measurements," J. Appl. Phys. 73 (1993) 4344.
[233] M.B. Hugenschmidt, L. Gamble and C.T. Campbell, "The interaction of H_2O with a TiO_2(110) surface," Surf. Sci. 302 (1994) 329.
[234] M.A. Henderson, S.A. Joyce and J.R. Rustad, 'Interaction of water with the (1×1) and (2×1) surfaces of α-Fe_2O_3(012)," Surf. Sci. 417 (1998) 66.

[235] W.F. Wu, B.S. Chiou, "Effect of oxygen concentration in the sputtering ambient on the microstructure, electrical and optical properties of radio-frequency magnetron-sputtered indium tin oxide films," Semicond. Sci. Technol. 11 (1996) 196.
[236] Z. Wang and X. Hu, "Structural and electrochemical characterization of 'open-structured' ITO films," Thin Solid Films 392 (2001) 22.
[237] E. McCafferty and J.P. Wightman, "Determination of the concentration of surface hydroxyl groups on metal oxide films by a quantitative XPS method," Surf. Interf. Anal. 26 (1998) 549.
[238] P.P. Fedorov, R.M. Zakalyukin, L.N. Ignatéva, and V.M. Bouznik, "Fluoroindate glasses," Russ. Chem. Rev. 69 (2000) 705.
[239] R.W. Hewitt and N. Winograd, "Oxidation of polycrystalline indium studied by XPS and static SIMS," J. Appl. Phys. 51 (1980) 2620.
[240] E. Paparazzo, G. Fierro, G.M. Ingo and N. Zacchetti, "XPS studies on the surface thermal modifications of tin oxides," Surf. Interf. Anal. 12 (1988) 438.
[241] H. Kobayashi, T. Ishida, K. Nakamura, Y. Nakato and H. Tsubomura, "Properties of indium tin oxide films prepared by the electron-beam evaporation method in relation to characteristics of indium tin oxide silicon-oxide silicon junction solar-cells," J. Appl. Phys. 72 (1992) 5288.
[242] E. Rutner, P. Goldfinger and J.P. Hirth (Eds.), Condensation and Evaporation of Solids Gordon and Breach, New York, 1966, p255.
[243] Th. Kugler, Å . Johansson, I. Dalsegg, U. Gelius and W.R. Salaneck, "Electronic and chemical structure of conjugated polymer surfaces and interfaces: applications in polymer-based light-emitting devices," Synth. Met. 91 (1997) 143.
[244] M. Lögdlund, T. Kugler, E. Rebourt, U. Getius and W.R. Salaneck, Proc. ECASIA'97, Göteborg, Sweden, 16-20 May 1997.
[245] E. Paparazzo, G. Fierro, G.M. Ingo and N. Zacchetti, "XPS studies on the surface thermal modifications of tin oxides," Surf. Interf. Anal. 12 (1988) 438.
[246] G.E. Mullenberg (Ed.), Handbook of X-ray Photoelectron Spectroscopy, Perkin-Elmer, Eden Prairie, MN, 1979.
[247] C.D. Wagner, in: D. Griggs and M.P. Seah (Eds.), Practical Surface Analysis by Auger and X-ray Photoelectron Spectroscopy, Wiley, NY, 1983, pp. 477-514.
[248] M.S. Lee, W.C. Choi, E.K. Kim, C.K. Kim and S.K. Min, "Characterization of the oxidized indium thin films with thermal oxidation," Thin Solid Film 279 (1996) 1.
[249] N.D. Popovich, B.K.H. Yen and S.-S. Wong, "Effect of tin-doped indium oxide electrode preparation methods on the mediated electrochemical detection of nucleic acids," Langmuir 19 (2003) 1324.
[250] K.L. Purvis, G. Lu, J. Schwartz and S.L. Bernasek, "Surface characterization and modification of indium tin oxide in ultrahigh vacuum," J. Am. Chem. Soc. 122 (2000) 1808.
[251] A.R. Span, E.L. Bruner, S.L. Bernasek and J. Schwartz, "Surface modification of indium tin oxide by phenoxytin complexes," Langmuir 17 (2001) 948.
[252] L.-Q. Wang, K.F. Ferris, P.X. Skiba, A.N. Shultz, D.R. Baer and M.H. Engelhard, "Interactions of liquid and vapor water with stoichiometric and defective TiO_2(100) surfaces," Surf. Sci. 440 (1999) 60.
[253] S.K. Vanderkam, E.S. Gawalt, J. Schwartz and A.B. Bocarsly, "Electrochemically active surface zirconium complexes on indium tin oxide," Langmuir 15 (1999) 6598.

[254] I.M. Chan and F.C. Hong, "Plasma treatments of indium tin oxide anodes in carbon tetrafluorinde (CF_4)/oxygen (O_2) to improve the performance of organic light-emitting diodes," Thin Solid Films 444 (2003) 254.
[255] M. Ishii, T. Mori, H. Fujikawa, S. Tokito and Y. Taga, "Improvement of organic electroluminescent device performance by in situ plasma treatment of indium–tin-oxide surface," J. Lumin. 87 (2000) 1165.
[256] F. Li, H. Tang, J. Shinar, O. Resto and S.Z. Weisz, "Effects of aquaregia treatment of indium–tin–oxide substrates on the behavior of double layered organic light-emitting diodes," Appl. Phys. Lett. 70 (1997) 2741.
[257] F. Cacialli, J.S. Kim, T.M. Brown, J. Morgado, M. Granström, R.H. Friend, G. Gigli, R. Cingolani, L. Favaretto, G. Barbarella, R. Daik and W.J. Feast, "Surface and bulk phenomena in conjugated polymers devices," Synth. Met. 109 (2000) 7.
[258] Q.T. Le, E.W. Forsythe, F. Nuesch, L.J. Rothberg, L. Yan and Y. Gao, "Interface formation between NPB and processed indium tin oxide," Thin Solid Films 363 (2000) 42.
[259] P.M.S. Monk and C.M. Man, "Reductive ion insertion into thin-film indium tin oxide (ITO) in aqueous acidic solutions: the effect of leaching of indium from the ITO ," J. Mater. Sci.: Mater. Electronics 10 (1999) 101.
[260] F. Nüesch, E.W. Forsythe, Q.T. Le, Y. Gao and L.J. Rothberg, "Importance of indium tin oxide surface acido-basicity for charge injection into organic materials based light emitting diodes," J. Appl. Phys. 87 (2000) 7973
[261] T. Osada, Th. Kugler, P. Bröms and W.R. Salaneck, "Polymer-based light-emitting devices: investigations on the role of the indium-tin oxide (ITO) electrode ," Synth. Met. 96 (1998) 77.
[262] H. Gerischer, Solar photoelectrolysis with semiconductor electrodes. In B.O. Seraphin (ed.), Topics in Applied Physics, Solar Energy Conversion, Springer, Berlin, 1979, Chapter 4.
[263] Ch. Comninellis and A. Nerini, "Anodic oxidation of phenol in the presence of NaCl for wastewater treatment," J. Appl. Electrochem. 25 (1995) 23.
[264] B. Correa-Lozano, Ch. Comninellis and A. de Battisti, "Physicochemical properties of SnO_2-Sb_2O_5 films prepared by the spray pyrolysis technique," J. Electrochem. Soc. 143 (1996) 203.
[265] W.E. Morgan, J.R. Van Wazer and W.J. Stec, "Inner-orbital photoelectron spectroscopy of the alkali metal halides, perchlorates, phosphates, and pyrophosphates," J. Am. Chem. Soc. 95 (1973) 751.
[266] R. Franke, Th. Chasse, P. Streubel and A. Meisel, "Auger parameters and relaxation energies of phosphorus in solid compounds," J. Electron Spectrosc. Relat. Phemon. 56 (1991) 381.
[267] D. Lide (Ed), CRC Handbook of Chem. Phys., 8^{th} edition, CRC Press, 2000.
[268] Z.F. Zhang, Z.B. Deng, C.J. Liang, M.X. Zhang and D.H. Xu, "Organic light-emitting diodes with a nanostructured TiO_2 layer at the interface between ITO and NPB layers," Displays 24 (2003) 231.
[269] J.M. Zhao, Y.Q. Zhan, S.T. Zhang, X.J. Wang, Y.C. Zhou, Y. Wu, Z.J. Wang, X.M. Ding and X.Y. Hou, "Modification of the hole injection barrier in organic light-emitting devices studied by ultraviolet photoelectron spectroscopy," Appl. Phys. Lett. 84 (2004) 5377.

[270] X.M. Ding, L.H. Hung, L.F. Cheng, Z.B. Deng, X.Y. Hou, C.S. Lee and S.T. Lee, "Modification of the hole injection barrier in organic light-emitting devices studied by ultraviolet photoelectron spectroscopy," Appl. Phys. Lett. 76 (2000) 2704.
[271] Y.E. Kim, H. Park and J.J. Kim, "Enhanced quantum efficiency in polymer electroluminescence devices by inserting a tunneling barrier formed by Langmuir–Blodgett films," Appl. Phys. Lett. 69 (1996) 599.
[272] E. Tutiš, M.-N. Bussac and L. Zuppiroli, "Image force effects at contacts in organic light-emitting diodes," Appl. Phys. Lett. 75 (1999) 3880.
[273] C.J. Brinker and G.W. Scherer, Sol-gel Science, The Physics and Chemistry of Sol-gel Processing, Academic Press, 1990
[274] K. Reichelt, "Nucleation and growth of thin films" Vacuum 38 (1988) 1083.
[275] M.A. Herman and H. Sitter, Molecular Beam Epitaxy - Fundamentals and Current Status, Springer, New York, 1989.
[276] A. Zangwill, Physics at Surfaces, Cambridge University Press, Cambridge, 1988.
[277] M. Mandai, K. Takarda, K. Takarda, T. Aoki, T. Fujinami, Y. Nakanishi and Y. Hatanaka, "AFM observation for the change of surface morphology of TPD thin films due to thermal annealing ," Synth. Met. 91 (1997) 123.
[278] L.F. Cheng, L.S. Liao, W.Y. Lai, X.H. Sun, N.B. Wong, C.S. Lee and S.T. Lee, "Effect of deposition rate on the morphology, chemistry and electroluminescence of tris-(8-hydroxyqiunoline) aluminum films," Chem. Phys. Lett. 319 (2000) 418.
[279] C.S. Smith, "Microstructure," Trans. Am. Soc. Metals 45 (1953) 533.
[280] T. Furuhara and T. Maki, "Variant selection in heterogeneous nucleation on defects in diffusional phase transformation and precipitation," Mater. Sci. Eng. A312 (2001) 145.
[281] J.W. Cahn, "Nucleation on dislocations," Acta Metall. 5 (1957) 169.
[282] Y. Han, D. Kim, J.S. Cho, Y.W. Beag and S.K. Koh, "Study of the substrate treatment effect on initial growth of indium tin-oxide films on polymer substrate using in situ conductance measurement," Thin Solid Films 496 (2006) 58.
[283] C. Ratsch and J.A. Venables, "Nucleation theory and the early stages of thin film growth," J. Vac. Sci. Technol. A21 (2003) S96.
[284] J.N. Barisci, R. Stella, G.M. Spinks and G.G. Wallace, "Study of the surface potential and photovoltage of conducting polymers using electric force microscopy ," Synth. Met. 124 (2001) 407.
[285] M. Harsdorff, "Heterogeneous nucleation and growth of thin films," Thin Solid Films 90 (1982) 1.
[286] Q.D. Wu, "Nucleation and growth of vapor phase deposition on solid surfaces," Vacuum 41 (1990) 1431.
[287] J.A. Venables, G.D.T. Spiller and M. Hanbücken, "Nucleation and growth of thin films," Rep. Prog. Phys. 47 (1984) 399.
[288] R. Kern, G. LeLay and J.J. Métois, in "Current Topics in Materials Science", Vol. 3, edited by E. Kaldis, North-Holland, Amsterdam, 1979, p139.
[289] M.H. Grabow and G.H. Gilmer, "Thin film growth modes, wetting and cluster formation," Surf. Sci. 194 (1988) 333.
[290] Y. Han, D. Kim, J.S. Cho, Y.W. Beag, S.K. Koh and V.S. Chernysh, "Effects of substrate treatment on the initial growth mode of indium-tin-oxide films," J. Appl. Phys. 97 (2005) 024910.

[291] S.K. Mishra, P.K.P. Rupa and L.C. Pathak, "Nucleation and growth of DC magnetron sputtered titanium diboride thin films," Surf. Coat. Technol. 200 (2006) 4078.
[292] J. Drelich and J.D. Miller, "The effect of solid surface heterogeneity and roughness on the contact angle/drop (bubble) size relationship," J. Colloid Interf. Sci. 164 (1994) 252.
[293] M. Kamei, H. Enomoto and I. Yasui, "Origin of the crystalline orientation dependence of the electrical properties in tin-doped indium oxide films," Thin Solid Films 392 (2001) 265.
[294] Z.C. Wang and X.F. Hu, "Structural and electrochemical characterization of 'open-structured' ITO films," Thin Solid Films 392 (2001) 22.
[295] Y.S. Jung and S.S. Lee, "Development of indium tin oxide film texture during DC magnetron sputtering deposition," J. Cryst. Growth 259 (2003) 343.
[296] E. Terzini, P. Thilakan and C. Minarini, "Properties of ITO thin films deposited by RF magnetron sputtering at elevated substrate temperature ," Mater. Sci. Eng. B77 (2000) 110.
[297] P. Thilakan and J. Kumar, "Studies on the preferred orientation changes and its influenced properties on ITO thin films," Vacuum 48 (1997) 463.
[298] C.H. Yi, I. Yashi and Y. Shigesato, "Effects of tin concentrations on structural characteristics and electrooptical properties of tin-doped indium oxide films prepared by RF magnetron sputtering," Jpn. J. Appl. Phys. 34 (1995) 600.
[299] K. Otsuka, T. Yasui and A. Morikawa, "Rapid diffusion of oxygen ions in indium oxide during reduction-oxidation," Bull. Chem. Soc. Jpn. 56 (1983) 2161.
[300] J.A. Chaney and P.E. Pehrsson, "Work function changes and surface chemistry of oxygen, hydrogen and carbon on indium tin oxide," Appl. Surf. Sci. 180 (2001) 214.
[301] Z.Y. Zhong, Y.X. Zhong, C. Liu, S. Yin, W.X, Zhang and D.F. Shi, "Study on the surface wetting properties of treated indium-tin-oxide anodes for polymer electroluminescent devices," Phys. Stat. Sol. A198 (2003) 197.
[302] Z. Ovadyahu, B. Ovryn and H.W. Kraner, "Microstructure and electro-optical properties of evaporated indium-oxide films," J. Electrochem. Soc. 130 (1983) 917
[303] P.A. Cox, The electronic Structure and Chemistry of Solids, Oxford University Press, New York, 1987, pp. 230-232.
[304] N.D. Lang and W. Kohn, "Theory of metal surfaces: charge density and surface energy," Phys. Rev. B1 (1970) 4555.
[305] V. Sahni, J.P. Perdew and J. Gruenebaum, "Variational calculations of low-index crystal face-dependent surface energies and work functions of simple metals," Phys. Rev. B23 (1981) 6512.
[306] N.D. Lang and W. Kohn, "Theory of metal surfaces: work function," Phys. Rev. B3 (1971) 1215.
[307] N.W. Ashcroft and N.D. Mermin, Solid State Physics, Hole, Reinehart, and Winston, New York, 1976.
[308] R.F. Tiner, "Stress dependence of ion and thermionic emission," J. Appl. Phys. 39 (1968) 355.
[309] Y.P. Li and D.Y. Li, "Experimental studies on relationships between the electron work function, adhesion, and friction for 3d transition metals," J. Appl. Phys. 95 (2004) 7961.

[310] D.Y. Li and W. Li, "Electron work function: A parameter sensitive to the adhesion behavior of crystallographic surfaces," Appl. Phys. Lett. 79 (2001) 4337.
[311] H.L. Skriver and N.M. Rosengaard, "Surface energy and work function of elemental metals," Phys. Rev. B46 (1992) 7157.
[312] D.H. Buckley, Surface Effects in Adhesion, Friction, Wear and Lubrication, Elsevier, New York, 1981.
[313] D.Y. Li and W. Li, "Electron work function: A parameter sensitive to the adhesion behavior of crystallographic surfaces," Appl. Phys. Lett. 79 (2001) 4337.
[314] J. Kollár, L. Vitos and H.L. Skriver, "Surface energy and work function of the light actinides," Phys. Rev. B49 (1994) 11288.
[315] C.J. Fall, N. Binggeli and A. Baldereschi, "Theoretical maps of work-function anisotropies" Phys. Rev. B65 (2001) 045401.
[316] R. Smoluchowski, "Anisotropy of the electronic work function of metals," Phys. Rev. 60 (1941) 661.
[317] A.L. Zharin, E.L. Fishbejn and N.A. Shipisa, "Effect of contact deformation upon surface electron work function," Soviet J. Friction Wear 16 (1995) 66.
[318] W. Li and D.Y. Li, "Effects of dislocation on the electron work function of a metal surface," Mater. Sci. Technol. 18 (2002) 1057.
[319] D.Y. Li, "Kelvin probing technique: A promising method for the determination of the yield strain of a solid under different types of stress," Phys. Stat. Solidi. A191 (2002) 427.
[320] F. Cyrot-Lackmann, "On the calculation of surface tension in transition metals," Surf. Sci. 15 (1969) 535.
[321] M.C. Desjonqueres and F. Cyrot-Lackmann, "On the anisotmpy of surface tension in transition metals," Surf. Sci. 50 (1975) 257.
[322] V.E. Henrich and P.A. Cox, "Functionals of gas-surface interactions on metal-oxides," Appl. Surf. Sci. 72 (1993) 277.
[323] C.F.J. Baes and R.E. Mesmer, The Hydrolysis of Cations; John Wiley & Sons: New York, 1976.
[324] M. Utsumi, N. Matsukaze, A. Kumagai, Y. Shiraishi, Y. Kawamura and N. Furusho, "Effect of UV treatment on anode surface in organic EL displays," Thin Solid Films 363 (2000) 13.
[325] H.-N. Lin, S.-H. Chen, G.-Y. Perng and S.-A. Chen, "Nanoscale surface electrical properties of indium–tin–oxide films for organic light emitting diodes investigated by conducting atomic force microscopy," J. Appl. Phys. 89 (2001) 3976.
[326] M. Higuchi, M. Sawada and Y. Kuronuma, "Microstructure and electrical characteristics of sputtered indium tin oxide-films," J. Electrochem. Soc. 140 (1993) 1773.
[327] P.M. Borsenberger and D.S. Weiss, Organic Photoreceptors for Imaging Systems, Marcel Dekker, New York, 1993.
[328] M.A. Baldo, S. Lamansky, P.E. Burrows, M.E. Thompson and S.R. Forrest, "Very high-efficiency green organic light-emitting devices based on electro-phosphorescence ," Appl. Phys. Lett. 75 (1999) 4.
[329] T. Tsutsui, M.J. Yang, M. Yahiro, K. Nakamura, T. Watanabe, T. Tsuji, Y. Fukuda, T. Wakimoto and S. Miyaguchi, "High quantum efficiency in organic light-emitting devices with iridium-complex as a triplet emissive center," Jpn. J. Appl. Phys. 38 (1999) L1502.

[330] R.G. Kepler, P.M. Beeson, S.J. Jacobs, R.A. Anderson, M.B. Sinclair, V.S. Valencia and P.A. Cahill, "Electron and hole mobility in tris(8-hydroxyquinolato) aluminum," Appl. Phys. Lett. 66 (1995) 3618.
[331] T. Tsutsui, H. Tokuhisa and M. Era, "Charge carrier mobilities in molecular materials for electroluminescent diodes," Proc. SPIE 3281 (1998) 230.
[332] W. Brütting, S. Berleb and A.G. Mückl, "Device physics of organic light-emitting diodes based on molecular materials," Organic Electronics 2 (2001) 1.